2001

Integral and pulse mode silicon dosimetry for dose verification on radiation oncology modalities

Grigori I. Kaplan
University of Wollongong

INTEGRAL AND PULSE MODE SILICON DOSIMETRY FOR DOSE VERIFICATION ON RADIATION ONCOLOGY MODALITIES

A thesis submitted in fulfilment of the requirements for the award of the degree

DOCTOR OF PHILOSOPHY

from

UNIVERSITY OF WOLLONGONG

by

Grigori I. Kaplan, MSc

Department of Engineering Physics

2001

Statement of Originality

I hereby declare that this submission is my own work and that, to the best of my knowledge and belief, it contains no material previously published or written by another person nor material which to a substantial extent has been accepted for the award of any degree or diploma of a university or other institution of higher learning, except where due acknowledgement is made in the text.

G.I. Kaplan

6th December, 2001

Acknowledgements

Firstly I would like to thank my supervisor, Professor Anatoly Rosenfeld, for all his valuable intellectual guidance, support and help during the past few years. His encouragement, belief in my abilities and excellent advice made this thesis possible.

I am grateful to Professor Barry Allen, from the St. George Cancer Care Centre, Sydney for many fruitful discussions, valuable advice and encouragement.

I would like to thank Professor Bill Zealey, Head of the Department of Engineering Physics, University of Wollongong for encouragement and for support during the course of this project. My many thanks to Mr. Peter Ihnat, from the Department of Engineering Physics, for electronic design of the MOSFET reader and to Mr. Peter Anthony, from the same Department, for assembling the reader. I also would like to thank Mr. John Burke, from the Mechanical Workshop of the Faculty of Science, for manufacturing the perspex phantoms and the detector holders. I also appreciate assistance with detector measurements by Jeremy Booth, Peter Bradley and Michael Bailey from the Centre of Medical Radiation Physics of the University of Wollongong.

I am grateful to Professor Rick Kefford, Director of the Westmead Institute for Cancer Research, for support and for fostering an atmosphere of scientific research. A/Professor Christine Clarke and Dr. Graham Mann, senior scientists of the Westmead Institute for Cancer Research, for encouragement and support. I also would like to thank A/Professor Clarke for helping me to overcome a brief decrease in motivation during the writing of this manuscript. I would like to thank Dr. Patricia Mote, from the Westmead Institute for Cancer Research, for reading this manuscript.

I appreciate support of the following people for assistance and use of radiation oncology facilities: Professor Peter Metcalfe, Dr. Martin Butson and Martin Carolan from the Illawarra Cancer Care Centre; Dr. Jeffey Coderre and the reactor staff, Avraham Dilmanian and the synchrotron staff at the Medical Department of the Brookhaven National Laboratory, Long Island, USA; Dr. Richard Maughan, Dr. Chandrasekhar Kota and Dr. Mark Yudelev from the Gershenson Radiation Oncology Centre, Harper Hospital, Detroit, USA; Dr. Tooru Kobaysahi from the Kyoto University Research Reactor. I am grateful to SPO Detector, Kiev, Ukraine for manufacturing of MOSFET detectors and ion-implanted silicon detectors.

I am very grateful and am in debt to my parents, Professor Ilya Kaplan and Dr. Lara Popova, for showing me, by their own example, the excitement of scientific endeavours, for encouraging a critical scientific thinking, and for believing in me and taking pride in my achievements.

Finally I must acknowledge my wife, Elena, for her total support, interest in my study and for the input of her artistic talent in enhancing some of the illustrations in this manuscript.

Publications

1. **Kaplan, G. I.**, Rosenfeld, A. B., Booth, J. T., Allen, B. J., Carolan, M. G., and Holmes-Siedle, A. "Improved spatial resolution by MOSFET dosimetry of an x-ray microbeam", *Medical Physycs*, v. 27, pp. 239-244, (2000)

2. **Kaplan, G. I.**, Rosenfeld, A. B., Allen, B. J., Coderre, J. A., and Liu, H. B. "Fission converter and metal-oxide-semiconductor field effect transistor study of thermal neutron flux distribution in an epithermal neutron therapy beam", *Medical Physics*, v. 26, pp. 1989-1994, (1999)

3. **Kaplan, G. I.**, Rosenfeld, A. B., Allen, B. J., Maughan, R. L., Coderre, J. A. and Kobayashi, T.,"Semiconductor detectors for in-phantom thermal neutron flux and boron dose measurements in BNCT and Fast Neutron Therapy". In: *Fronties in Neutron Capture Therapy*, Hawthrone (ed.), pp. 1175-1180, Kluver Publisher, (2001)

4. Rosenfeld, A. B., **Kaplan, G. I.**, Kron, T., Allen, B. J., Dalmanian, F. A., Orion, I., Ren, B., and Holmes-Siedle, A. "MOSFET dosimetry of x-ray microbeam", *IEEE Transactions on Nuclear Science*, v. 46, pp. 1774-1780, (1999)

5. Rosenfeld, A. B., **Kaplan, G. I.**, Carolan, M. G., Allen, B. J., Anokhin, I., Zinets, O., Khivrich, V., and Litovchenko, P. "Application of p-i-n diodes and MOSFETs for dosimetry in gamma and neutron radiation fields", *Radiation Protection and Dosimetry*, v. 84, pp. 349-352, (1999)

6. Rosenfeld, A. B., **Kaplan, G. I.**, Carolan, M. G., Allen, B. J., Kota, C., Maughan, R. L., and Yudelev, M. "New approach to simultaneous micro and macro dosimetry in neutron therapy with a MOSFET probe", *International Journal of Brachytherapy*, v. 13, pp. 129-136, (1997)

7. Rosenfeld, A. B., **Kaplan, G. I.**, Carolan, M. G., Allen, B. J., Kota, C., Maughan, R. L., Yudelev, M., and Coderre, J. A. "Simultaneous macro and micro dosimetry for boron neutron capture therapy with a MOSFET probe". In: B. Larsson, J. Crawford, and R. Weinreich (eds.), *Advances in Neutron Capture Therapy*, vol. 1, pp. 346-352. Lausanne: Elseiver, (1997)

8. Rosenfeld, A. B., **Kaplan, G. I.**, Carolan, M. G., Allen, B. J., Maughan, R. L., Yudelev, M., Kota, C., and Coderre, J. A. "Simultaneous macro and micro dosimetry with MOSFETs", *IEEE Transactions on Nuclear Science*, v. 43, pp. 2693-2700, (1996)

9. Rosenfeld, A. B., Carolan, M. G., **Kaplan, G. I.**, Allen, B. J., and Khivrich, V. I. "MOSFET dosimeters: role of encapsulation on dosimetric

characteristics in mixed gamma-neutron and megavoltage x-ray fields", *IEEE Transactions on Nuclear Science*, v. 42, pp. 1870-1877, (1995)

10. Kron, T., Duggan, L., Smith, T., Rosenfeld, A., Butson, M., **Kaplan, G.**, Howlett, S., and Hyodo, K. "Dose response of various radiation detectors to synchrotron radiation", *Physics in Medicine and Biology*, v. 43, pp. 3235-3259, (1998)

11. **Kaplan, G. I.**, Rosenfeld, A. B., and Maughan, R. L. "Thermal neutron dosimetry in fast neutron therapy and californium-252 brachytherapy radiation fields", in preparation

Abstract

Radiation oncology is an important part of cancer therapy. In 1996 a Committee of the Australian National Health and Medical Research Council recommended that 50-55% of all the new cancers include radiotherapy as part of their treatment. Cancer patients are treated with different radiation oncology modalities and while most are treated by conventional x-ray therapy a growing number is treated by hadron therapies such as fast neutron therapy (FNT), brachytherapy, proton therapy, heavy ion therapy and boron neutron capture therapy (BNCT). A new radiation oncology modality, microbeam radiation therapy (MRT), is currently under development. The outcome of radiation treatment in a hadron therapy is highly dependent on an accurate knowledge of both dose distribution and the quality of the radiation beam.

Aim of this project was to develop new semiconductor probes for applications in hadron therapy and in synchrotron MRT and for validation of quality assurance on these modalities.

A. Metal oxide semiconductor field effect transistor (MOSFET) dosimeters have been investigated in this study and new applications for dosimetry in radiation oncology have been introduced.

- A novel dual use of a MOSFET detector has been proposed, which is based on simultaneous mini and microdosimetry by a single MOSFET detector.
- The count mode response of a MOSFET detector has been investigated for correlation with its integral response in a high lineal energy transfer (LET) radiation field for separation, by a single MOSFET detector, of low and high LET doses in a mixed radiation field.
- A paired integral MOSFET detector technique, for dosimetry in a thermal neutron field, has been proposed and investigated. This technique has allowed determination of a relative boron depth dose in BNCT and evaluation of the boron enhancement in FNT.
- A novel "edge-on" MOSFET mini dosimetry has been introduced, investigated and its micron scale spatial resolution proven. It was successfully demonstrated that the "edge-on" MOSFET probe can be used for accurate measurements of the dose profile of a 30 μm wide synchrotron microbeam for MRT.
- The role of a MOSFET package for detector response was investigated for x-ray beams with energy range from 20 keV to 6 MV.
- High spatial resolution MOSFET dosimetry, in strong electron non-equilibrium x-ray fields of a conventional medical linac, has been proved using optimal packaging.

B. A pulse method has been introduced for neutron clinical dosimetry

- A small sized ion-implanted silicon detector with a thick ^{235}U converter, for absolute thermal neutron dosimetry, has been theoretically simulated and developed.

- Successful applications of the probe for thermal neutron flux and boron dose measurements in BNCT, FNT and californium-252 brachytherapy have been demonstrated with thermal neutron flux measurements being within 5% agreement with Monte Carlo calculations.

The semiconductor probes that have been developed during this project are accurate, reliable, have a high spatial resolution, require low operating voltage, are of low cost, versatile and offer significant advantages when compared with conventional detectors currently in use in radiation oncology.

Figures

Tables

Chapter 1. Introduction. Principles of MOSFET dosimetry

1.1. Introduction

Radiation therapy requires an advance clinical dosimetry. Any physical system which properties experience a change caused by an irradiation can be utilised as a radiation dosimeter. An ideal dosimeter has to have a linear response in a wide range of radiation dose, demonstrate negligible or well characterised dependence on type and energy of radiation, it has to be accurate with high resolution and offer a possibility of *in-vitro* and *in-vivo* measurements. While an ideal dosimeter does not exists, a semiconductor detector is a promising radiation sensor which can address and resolve dosimetry problems in clinical applications.

1.2. Radiation effects and charge traps in silicon dioxide

The effect of ionising radiation on electrical characteristics of a silicon transistor was first reported by (Green *et al.*, 1965) in January 1965. The observation was made during a scanning electron microscope investigation of a transistor structure. The irradiation was performed by low energy (10 keV to 20 keV) electrons. This first observation has triggered further research into radiation effects in semiconductor structures.

A test metal-oxide-semiconductor (MOS) capacitor was irradiated by 10 keV to 16 keV electrons (Szedon & Sandor, 1965). It was shown that electrical characteristics of the MOS structure changed with the radiation. The MOS

capacitance was measured in that experiment as a function of metal-to-silicon bias before and after irradiation. It was also noted that the radiation effect could be removed by 15 minutes annealing at 150-200°C with the MOS capacitor shorted. The change in C-V characteristics was attributed to accumulation of the positive charge in silicon oxide and/or in the silicon oxide/silicon interface. Several models were suggested to explain the charge trapping and annealing (Gwen, 1969; Kooi, 1967). The models explained the observed phenomena by hole trapping in the broken bonds of silicon oxide which were associated with a donor trapping level containing a trapped hole. The deficiency of this earlier model was that it assumed low mobility of holes and considered that the holes were trapped in the bulk silicon.

Further investigations focused on the mobility of a hole drifting through the silicon dioxide under the applied electric field, and on the distribution of the hole traps. Experiments with electron-hole pairs, created in silicon dioxide by low energy electron irradiation, demonstrated that holes were mobile in the SiO_2 (Srour *et al.*, 1974). The mobility, μ, of a hole was measured by a time resolution current method at a temperature range from 75 K to 298 K (Hughes, 1977). Hole mobility in SiO_2 at room temperature is 2×10^{-9} $m^2 \cdot V^{-1} \cdot sec^{-1}$, while the mobility of more mobile electrons is 2×10^{-4} $m^2 \cdot V^{-1} \cdot sec^{-1}$ (Curtis *et al.*, 1974). The product of hole mobility and lifetime, $\mu\tau$, is not less than 1×10^{-10} $m^2 \cdot V^{-1}$ (Curtis *et al.*, 1974). This product determines the schubweg , w, which is the mean distance that an excited carrier moves under the action of an applied electric field before it disappears through recombination or is immobilised by permanent trapping

$$w = \mu\tau E$$

where E is the electric field in the silicon dioxide.

The energy of creation of an electron-hole pair was measured to be about 18 eV (Srour *et al.*, 1974). This value agrees reasonably well with unpublished energy of a plusmon, calculated at a value of 17 eV, as it was cited by (Curtis *et al.*, 1974). Even when the electric field in the silicon dioxide is up to 10^8 $V \cdot m^{-1}$, approximately fifty percent of generated holes and electrons recombine in the radiation track. The density of the holes trapped in the thermally grown silicon oxide was measured to be 4×10^{12} cm^{-2}. The same value of density of the trapped holes was obtained by Woods and Williams (Woods & Williams, 1976) for oxides grown at 900°C in the presence of HCl and charge carriers injected into SiO_2 by a corona discharge. The density was calculated from C-V measurements. The trap density of vacant holes, N_0, may be estimated from a known value of a capture cross section by a neutral centre, S_0, which is typically (Woods & Williams, 1976) about 10^{-15} - 10^{-16} cm^2. The measurements showed that between 10 to 50% of all holes are captured. This means that the product $N_0 \cdot S_0$ is in the range of 0.1 to 0.5. Thus N_0 is of the order of 10^{15} cm^{-2}. The measurements of the hole-trapping cross-section by the avalanche injection technique demonstrated a higher trapping cross-section of 10^{-13} cm^2 (Aitken & Young, 1977). The higher cross-section value may be caused by an additional trapping of holes in the surface layer of silicon oxide. The holes were found to be located not further than 350 Å from the SiO_2/Si

interface. Measurements by DiMaria *et al.* (DiMaria *et al.*, 1977) put the upper limit for the centroid of trapped holes distribution at 50 Å from the interface.

Woods and Williams (Woods & Williams, 1976) suggested that the hole traps were formed during intermediate steps in the thermal growth of the silicon dioxide. Composition defects of silicon excess near the interface were registered by (Sigmon *et al.*, 1974) by an ion back scattering method. The excess silicon has a concentration of 10^{15} cm^{-2} and is found mainly within 20-30 Å from the SiO_2/Si interface. It is interesting to note that the excess silicon concentration is similar to the independently measured trap density. In silicon dioxide each silicon atom is covalently bounded to four oxygen atoms. If a neutral oxygen atom is removed, it leaves behind one electron on each of the two orbitals bound to the silicon atom. Each of the orbitals now contains a single non-bound electron where previously it was a covalent pair. This centre now forms a neutral hole trap.

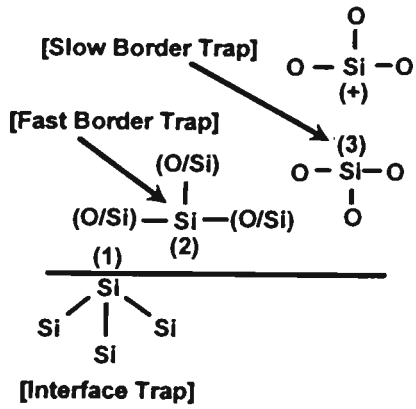

Figure 1-1. Schematic illustration of interface and border traps in SiO_2. Trap (1) is an interface trap, (2) and (3) are border traps. (After (Fleetwood *et al.*, 1995)).

Three types of traps were identified in MOS structures. There are oxide traps, border traps and interface traps (Fleetwood, 1992; Fleetwood, 1996). Similar trap characteristics were obtained by a charge pumping method (Djezzar *et al.*, 1999). The interface traps are found on the SiO_2/Si interface (Figure 1-1). The majority of the border traps are located in the narrow layer, of a few nanometers thick, directly above the interface (Figure 1-1). Trap sites (1) and (2) in Figure 1-1 are charged positively at negative gate bias and negatively at positive gate bias. Trap site (3) is neutral at negative gate bias and negative at positive gate bias. Thus all the interface and border trap sites are negatively charged at positive bias applied to silicon dioxide. The silicon dioxide layer in a metal-oxide-semiconductor field effect transistor (MOSFET) is an isolation layer above the transistor gate. As explained in Chapter 3, the positive gate bias is the operational mode of the MOSFET detector. Negatively charged interface traps are efficient in trapping positive holes produced by ionising radiation in silicon dioxide.

It should be mentioned, before proceeding any further, that there are two types of MOSFETs: n-type and p-type. The N-type, or n-channel MOSFET, has a p-type substrate silicon (majority charge carriers are holes) with n-type source and drain. An n-type conductivity channel is formed in n-MOSFET between its source and drain underneath the MOSFET gate. In the p-type, or p-channel MOSFET, the substrate material is n-type silicon while the channel conductivity is p-type. For more details on the structure and physics of MOSFETs see, for example, a monograph by (Nicollian & Brews, 1981).

1.3. Application of metal-oxide-silicon structure for radiation dosimetry

In 1974 Andrew Holmes-Siedle published a paper on the general principles of a new method of radiation detection by the space-charge dosimeter (Holmes-Siedle, 1974a). The new solid state dosimetry approach was originally published by Poch and Holmes-Siedle in 1970 in a hard to find RCA engineering journal (Poch & Holmes-Siedle, 1970). Holmes-Siedle suggested to use the property of a shift in current-voltage characteristic of metal oxide semiconductor field effect transistors for radiation dosimetry.

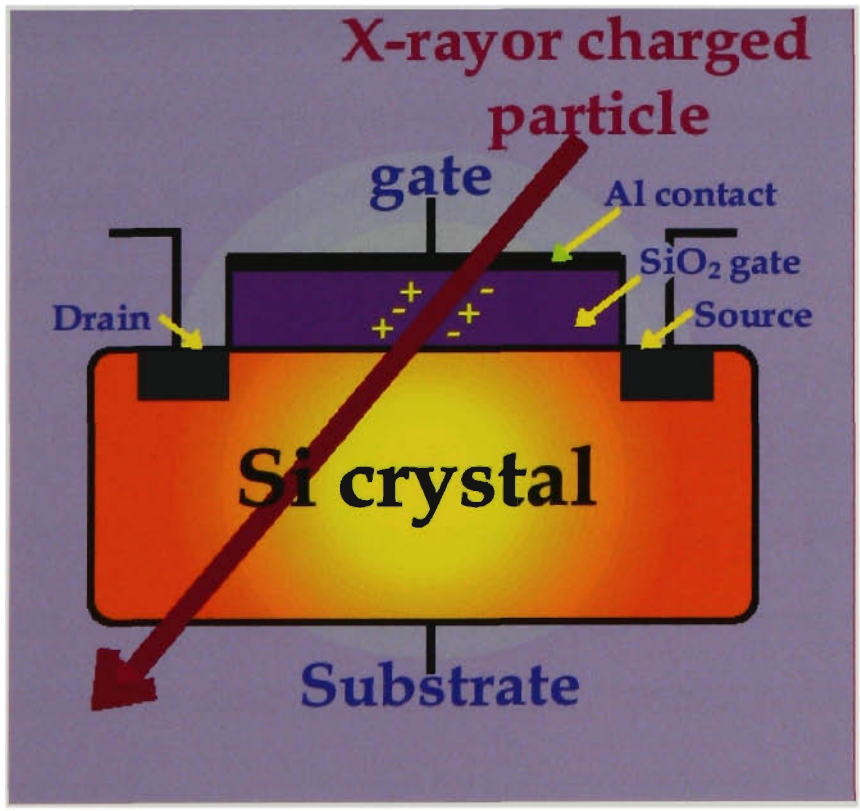

Figure 1-2. Structure of a MOSFET dosimeter.

When ionising radiation penetrates the silicon dioxide of a MOSFET gate, it creates electron-hole pairs along its path (Figure 1-2). The high density of electron-hole pairs in the vicinity of the radiation track leads to a high probability of recombination. Some holes escape recombination and migrate to the SiO_2/Si interface where they are trapped by the negative traps in the interface and border region (see Chapter 1.2). To increase electron and hole separation in the radiation track, and to direct hole diffusion towards the interface, a positive potential can be applied to the gate electrode. Four kinds of charge were identified in silicon dioxide (Deal, 1980): mobile ionic charge of K^+ and Na^+ ions, oxide trapped charge, fixed oxide charge and the interface trapped charge. The extra charge at the interface changes the electric field in the MOSFET channel. The channel's electric field affects source to drain conductivity of MOSFET. As a result, the source to drain current-voltage characteristic of MOSFET changes (Figure 1-3a). The most easily measured parameter of the MOSFET current-voltage characteristic is the source to drain voltage at which the source to drain current reaches some set level, I_0. This voltage is normally termed as the threshold voltage, V_{th}. Criteria for choosing the I_0 will be discussed later in this Chapter and in Chapter 3.2. The change in the threshold voltage, ΔV_{th}, is a measure of the radiation dose absorbed in the silicon dioxide gate. A circuit diagram for measurement of the threshold voltage of a p-channel MOSFET is shown in Figure 1-3b. To measure the threshold voltage for n-channel MOSFET the polarity is to be reversed, i.e. the drain and gate are connected to a positive potential, while the source and substrate are grounded.

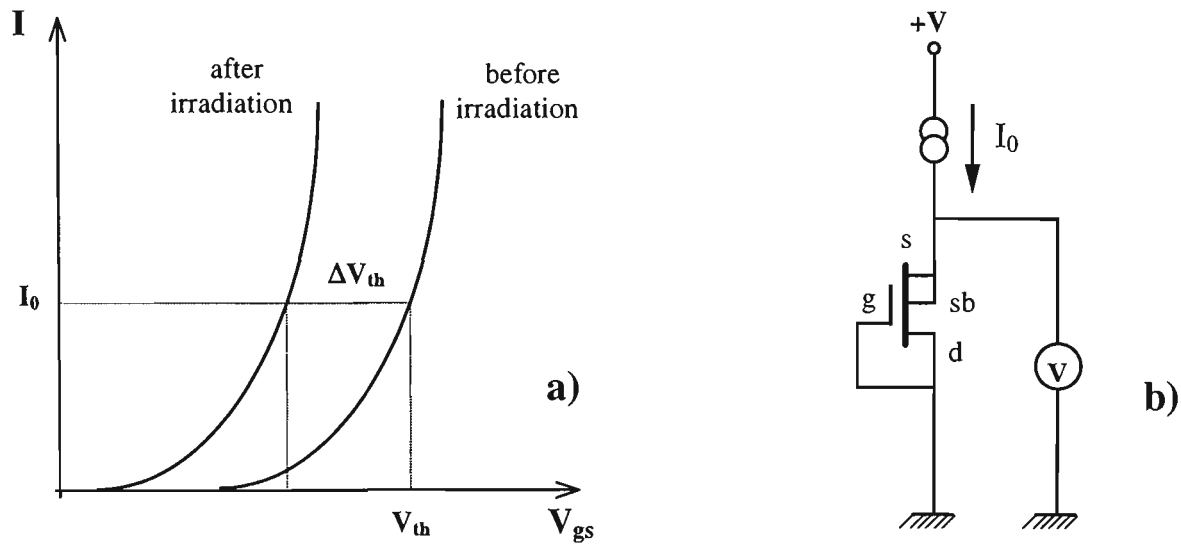

Figure 1-3. a) Change of MOSFET current-voltage characteristic due to the exposure to ionising irradiation; b) Diagram of the p-channel MOSFET read out circuit, where s - source, sb - substrate, d - drain and g - gate.

In 1978 Freeman and Holmes-Siedle published a model of the MOSFET threshold voltage shift due to exposure to ionising radiation (Freeman & Holmes-Siedle, 1978). Based on previous experimental studies, they assumed that the holes, released by radiation ionisation, are trapped in a thin layer in the silicon oxide. Our current understanding is that the charge is trapped in the vicinity of the SiO_2/Si interface. The oxide charge, Q_{ox}, produces a mirror charge, Q_s, in the silicon, ($Q_s = - Q_{ox}$). In order to restore the state of the MOSFET to be the same as before irradiation, a charge of - Q_s must be applied to the gate. The potential required to balance the threshold shift, ΔV_{th}, is

$$\Delta V_{th} = -\frac{Q_s d_{ox}}{\varepsilon_{ox}\varepsilon_0} = -\frac{eN_{ox}d_{ox}}{\varepsilon_{ox}\varepsilon_0} \qquad (1\text{-}1)$$

where d_{ox} is the oxide thickness, e is electron charge, N_{ox} is the number of holes trapped in oxide per unit area, ε_{ox} is dielectric constant of SiO_2 and ε_0 is dielectric permittivity of free space ($\varepsilon_0=8.854\times10^{-12}$ F·m^{-1}).

A rate of generating of electron hole pairs per unit of radiation dose in silicon dioxide, g, can be calculated from the mean energy of 18 eV for creating a pair and the density of SiO_2 ($2.27\cdot10^3$ kg·m^{-3}), by using the SI definition of radiation dose, 1 Gray, as the energy of 1 Joule deposited in 1 kilogram of material.

$$g = 7.9\cdot10^{20}\ \mathrm{m^{-3}\cdot Gy^{-1}}$$

or

$$g = 7.9\cdot10^{12}\ \mathrm{cm^{-3}\cdot rad^{-1}}$$

Recombination of electron-hole pairs occurs immediately after ionisation in the radiation track. This recombination reduces the amount of holes available for transport to Si/SiO_2 interface. The probability of escape from recombination or fractional yield, f, depends on the density of the radiation track or the lineal energy transfer (LET) of the radiation and dose rate. It also depends on the locally controlled parameter of the applied electric field in the silicon dioxide layer or the gate potential. Thus the number of holes trapped in oxide, N_{ox}, is given by

$$N_{ox} = g\cdot x_c\cdot f\cdot P \qquad (1\text{-}2)$$

where x_c is the thickness of the trap layer in the SiO_2/Si interface, P is probability for a hole to be trapped. P depends on the density of vacant traps and on the value of a capture cross section. By combining equations (1-1) and (1-2):

$$\Delta V_{th} = -\frac{eg}{\varepsilon_{ox}\varepsilon_0} x_c \cdot d_{ox} \cdot f \cdot P \cdot D \tag{1-3}$$

where D is SiO_2 radiation dose. When only a small fraction of available traps is occupied by the trapped holes and when the electron-hole separation in the SiO_2 due to the applied electric field is efficient, then from Equation (1-3) we can derive that change of MOSFET threshold voltage is proportional to radiation dose

$$\Delta V_{th} \propto D \tag{1-4}$$

Equation (1-4) forms the basis of MOSFET dosimetry. McGarrity (McGarrity, 1980) showed that MOSFET sensitivity to radiation dose is proportional to d_{ox}^2. This was later confirmed experimentally (Sarrabayrouse *et al.*, 1986). It can be shown (Ensell *et al.*, 1988) that the threshold voltage shift caused by trapped oxide charge, ΔV_{not}, is

$$\Delta V_{not} = 0.04 \cdot D \cdot t^2 \cdot f$$

where t is the oxide thickness in microns and V_{not} is in Volts.

The fractional yield was investigated for ^{60}Co gamma rays (Srour & Chiu, 1977), for 4 to 6 keV electrons (Curtis *et al.*, 1974), for 12 MeV electrons (Boesch & McGarrity, 1976) and for 8 to 10 keV x-rays (Dozier *et al.*, 1987). The fractional yield was measured at a range of electric fields in the silicon dioxide layer. For any given electric field, the fractional yield was smallest for the highest LET radiation of 5 keV electrons. The fractional yield, without an applied electric field, for carriers created by 5 keV electrons, was less than 5%, while for 12 MV electrons, the fractional yield was about 20%. The fractional yield for x-rays at an electric field of 1×10^{8} $V\cdot m^{-1}$ was 74%. The fractional yield increased with the increase of the oxide electric field. In accordance with Equation (1-3), the increase in fractional yield leads to an increase in the sensitivity of the MOSFET detector. For oxide electric fields of 5×10^{8} $V\cdot m^{-1}$ the fractional yield for all the radiation fields used in the experiments approached the theoretical limit of 1. This electric field corresponds to a gate bias voltage of 500 V for 1 μm thick silicon dioxide, which is a typical thickness of the gate oxide of the MOSFETs used in this research. A 10 V gate bias, typical for MOSFET dosimetry applications, creates an electric field of 1×10^{7} $V\cdot m^{-1}$ across 1 μm thick gate oxide.

The fractional yield data were confirmed by sensitivity measurements of the MOSFET dosimeter (August, 1982). The sensitivity of the MOSFET dosimeter (threshold voltage shift per unit dose) depends on the gate bias voltage since the fractional yield depends on the oxide electric field. As the electric field increases, the fractional yield approaches 100%. A saturation in sensitivity versus gate bias voltage was observed for Cu tube x-ray (operation voltage 45 kV) at about 20 V

bias. This bias corresponds to an electric field of 1.8×10^{8} V·m^{-1} in the reported oxide thickness of 0.11 μm. The saturation of 37 MeV protons and 7 MeV electrons commenced at the maximum applied bias of 30 V, while saturation of ^{60}Co gamma rays was not reached.

The radiation-induced change in threshold voltage depends on the recombination efficiency of the holes and on the density of the available interface traps. The application of a positive bias to a MOSFET gate leads to an increase in the fractional yield by decreasing the recombination efficiency of the holes. The electric field also improves the linearity of MOSFET measurements. ^{60}Co measurements with an unbiased MOSFET demonstrated that, for gate oxides of different thicknesses ranging from 0.69 to 2.30 μm, the threshold voltage shift is a power function of the dose

$$\Delta V_{th} \propto D^{n}$$

where n = 0.8 - 0.9. When a bias of 20 V·μm^{-1} was applied, the exponent approached 1, n = 0.99 ± 0.03 (Ensell *et al.*, 1988). The dose response of a MOSFET becomes linear when it operates under bias.

The change in threshold voltage per unit dose was investigated for both n- and p-channel MOSFETs in ^{60}Co and electron radiation fields (electron energies of 5 MeV and 20 MeV) as a function of the angle between an applied gate electric field and incident radiation (Tallon *et al.*, 1987). No angular dependence was observed

for electron irradiation. The effect of the incident radiation angle on the MOSFET threshold voltage change in ^{60}Co was moderate. The effect showed that, for a low density ionisation track, the direction of the electric field has no effect on the fractional yield. This result is important for medical dosimetry, where the dosimeter may not always have a single orientation in regards to the incident radiation.

The dose at a medical radiation facility is measured with reference to the dose in water. The conversion of Gy in SiO_2 to Gy in water was established for a p-channel MOSFET operated under zero gate bias (Adams & Holmes-Siedle, 1978). The measurements were performed in a ^{60}Co beam with a dose rate of 2000 $rad \cdot min^{-1}$ in water, and in a solid water-equivalent phantom for the x-ray beam of 8 MV hospital x-ray machine. The reference dose was measured by ionisation chamber and by lithium fluoride thermo luminescent dosimeter (TLD) calibrated in water. The conversion coefficient was measured to be:

$$\text{Dose in Gy } (SiO_2) = 0.9 \times \text{Dose in Gy (water)}$$

A MOSFET detector can store a radiation induced threshold voltage change for a long time after the irradiation, with a relatively small amount of fading. The observed change in threshold voltage is due to a room temperature annealing of the device. The threshold voltage increase of a p-channel MOSFET radiation detector, after 8 years of storage, was about 10% (Blamires *et al.*, 1986). This is very different to the post-radiation annealing of radiation hardened CMOS devices, where room temperature annealing reduced the threshold voltage shift by

up to 90% in the first 3 hours after irradiation (Winokur *et al.*, 1983). It shows that radiation hardening treatment reduces the deep trap concentration, where the trapped charge can be stored for a long period of time. The long term storage of trapped charge depends on the technological processes of growing and annealing of the gate oxide of the MOSFET. Devices with the oxide layer grown in dry conditions demonstrated greater long-term stability compared to devices with the oxide layer grown in wet conditions (Thomson *et al.*, 1984).

Soon after the introduction of the MOSFET as a radiation dosimeter, it was established that the MOSFET is dose rate independent for photon radiation dose rates of up to 10^4 Gy per second (Sanders, 1986; Thomson *et al.*, 1984). It was also shown, that while varying temperature during irradiation does not affect MOSFET sensitivity, changing temperature during the read out does affect the threshold voltage. More accurate measurements using a wide range of temperatures from -20°C to 100°C in a 10 keV electron beam demonstrated that the distribution of trapped charge within the silicon dioxide changes with the irradiation temperature (Shaneyfelt *et al.*, 1998).

A different design of MOSFET dosimeter was patented by Knoll and Braunig (Knoll & Braunig, 1988). This design was described by (Kassabov *et al.*, 1991). The proposed device is a p-channel MOSFET with a large polysilicon gate which extends over the field oxide. The gate is not electrically connected to a electrode, but is "floating". A charge can be injected into the floating gate. The charge produced in the silicon oxide during irradiation is attracted to the floating gate and neutralises part of its charge. The change in electrical potential of the floating gate

changes the MOSFET threshold voltage which is measured by a control gate. An advantage of the floating gate MOSFET is that it does not require bias during irradiation. One of the proposed applications of the floating gate MOSFET was radiation dose monitoring on board a space ship. To compensate for temperature change, a dual floating gate MOSFET was designed and tested (Tarr *et al.*, 1998). A sensitivity of about 0.5 mV per cGy was obtained. This device requires further investigation to continue evaluation of its linearity, temperature dependence, fading and possibility of re-use.

A design similar to the floating gate MOSFET detector was recently suggested by (Scheick *et al.*, 1999). These authors proposed to use the floated gate design of a commercial programmable read only memory (PRAM) chip. The chip contains tens of thousands of floating gate avalanche injection metal-oxide-silicon transistors. It is used for permanent storage of computer programs where each transistor stores one bit of information. The charge on the gate controls its conductivity and the information is normally erased by exposure to UV light. Radiation can knock an electron off the floating gate or create a hole-pair in the oxide, and the hole neutralises one electron on the gate. A decrease in the gate charge reduces the time necessary for memory erasing by UV. The erasure can be registered as a transistor flip from the non-conductive to the conductive state of the transistors. The concept was tested and proven and the dosimeter was shown to be reusable.

1.3.1. Dose enhancement. Energy dependence.

As the LET of x-ray radiation changes with energy, it was expected that the MOSFET radiation response would depend on incident photon energy. MOS capacitors with an oxide thickness of 0.5 μm were irradiated by x-rays with energies of 70 eV, 1.49 keV, 8.04 keV and 17.4 keV (Dozier & Brown, 1981). The responses were compared with the response caused by ^{60}Co irradiation. The electric field in the silicon dioxide ranged from 1×10^{3} V·cm^{-1} to 5×10^{6} V·cm^{-1}. The changes in C-V characteristics were measured and it was shown, that the recombination dynamics of electrons and holes varies with photon energy. The minimum recombination, of approximately 60% of the ^{60}Co level, was observed for 1.49 keV x-rays. For 70 eV x-ray the recombination was about the same as for ^{60}Co. The experimental data fitted the Brown and Dozier theory (Brown & Dozier, 1981). The equation is

$$N_c^{-1} = A + B \times E^{-1}$$

where N_c is the number of electron-hole pairs collected, E is the electric field across the oxide and A and B are constants. It was also shown that low energy radiation dose enhancement depends on the energy of radiation, as well as the electric field across the oxide (Fleetwood *et al.*, 1986).

Dose enhancement in a MOSFET occurs at the interface of silicon and of material with a high atomic number (Z), like metallisation on silicon. The dose

enhancement is greater for x-rays than for the higher energy gamma rays. X-rays interact with higher Z material more strongly and most of the interaction is due to photoelectron processes. The emission of photoelectrons is an isotropic process. The gamma rays interact with matter predominantly by the Compton process. Dose enhancement of gamma rays is directionally dependent due to the predominance of the forward scattered electrons in the Compton process. Some of the extra electrons, released in photon interactions with high Z materials, deposit their energy in the silicon dioxide layer. This additional absorbed energy increases the dose measured by the MOSFET.

The dose enhancement caused by the silicon chip metallisation (to provide electrical contacts) and the housing material was investigated by (Long *et al.*, 1982). The dose enhancement was not observed in the case of aluminium metallisation with a ceramic top lid. Most of the MOSFETs we have used in this study had ceramic housing or a Kovar housing with the lid removed. In the case for a Kovar lid, an enhancement of a factor of 1.2-1.6 was found for ^{60}Co radiation and of 1.4-2.6 for x-rays (Long *et al.*, 1982). The x-ray dose enhancement due to a Kovar lid was avoided in this study by removal of the lid before a measurement. The dose enhancement in the gamma field was resulted from the dose build up, caused by a production of delta electrons in the lid material (Johns & Cunningham, 1983), and did not affect measurements under the conditions of electron equilibrium (Rosenfeld *et al.*, 1995).

In many of the MOSFET housings (eg. TO-18 and TOT500) used in the study by (Long *et al.*, 1982), the back of 300 μm thick silicon chip was attached by gold

eutectic binding. Due to the high atomic number of gold, there is a possibility of a significant dose enhancement in the x-ray beam, since the photoeffect depends strongly on atomic number. The measurements proved that this was not the case (Long *et al.*, 1982). The extra photoelectrons were absorbed in the substrate silicon and did not affect the gate oxide of the MOSFET structure, which is on the top surface of the silicon chip.

The material of a MOSFET housing is an important factor in dose enhancement. It was demonstrated by (Brucker *et al.*, 1995) that the MOSFET housing material significantly affects dose enhancement for x-ray energies from 14 to 250 kV. The effect of Kovar and ceramic packagings on dose enhancement was investigated in that work. The dose enhancement for Kovar packaging was higher than for ceramic packaging by a factor of 2 to 3. The filling of a Kovar packaging with silicon grease prevented Compton scattered electrons, from the Kovar lead, from reaching the chip and dose enhancement was reduced by a factor of 4. The role of gold coating in dose enhancement was also confirmed. Ceramic packaging with a gold coating demonstrated a higher dose enhancement than without the coating.

The energy dependence of a p-channel MOSFET was compared with the energy dependence of a semiconductor diode and LiF TLD (Edwards *et al.*, 1997). No detailed information was given by the authors on the MOSFET housing material. The MOSFET dose enhancement peaked at a mean x-ray energy of between 30 to 40 kV. The maximum dose enhancement was about 4.5. The dose enhancement of the semiconductor diode occurred in a similar energy range and was measured to

be greater than 7. TLD dose response peaked at a slightly lower energy and was equal to approximately1.3.

As indicated in a number of studies, the MOSFET response is energy independent under electron equilibrium conditions for x-ray or electron beam energy in excess of 250 kV (Gladstone *et al.*, 1994a; Kron *et al.*, 1998) and (Rosenfeld *et al.*, 1995).

1.3.2. MOSFET dosimetry of hadron beams

The MOSFET threshold voltage was found to be sensitive to fast neutron radiation. Blamires *et. al.* (Blamires *et al.*, 1986) reported on 3 MeV and 15 MeV neutron irradiation of p-channel MOSFET dosimeters. The response to 15 MeV neutrons per Gy (silicon kerma) was about 30% lower than for 3 MeV neutrons. This energy dependence can be explained by a stronger interaction of ^{16}O with lower energy neutrons. The higher ^{16}O cross-section of interaction with neutrons leads to a higher kerma (Kinetic Energy Released in MAtter) . For this reason the dose deposited by neutrons in the MOSFET gate oxide is higher.

The ionisation cross-section of silicon oxide by neutrons is generally low so that the tissue-equivalent sensitivity of a MOSFET to neutron radiation is also low. It was suggested to place a fission fragment radiator over the MOSFET gate to increase the detector sensitivity (Streubel *et al.*, 1989; Tommasino *et al.*, 1977). Examples of fission radiator material for thermal and low energy neutrons are boron-10 and uranium-235. A MOSFET with a ^{6}LiF converter was used in an

epithermal neutron beam by (Carolan *et al.*, 1997). Experimental results were compared with MCNP4 Monte Carlo calculations and a good agreement was reported. However, all the reports in the literature have described the use of MOSFETs with fission converters in count mode. Passage of a fission fragment or an alpha particle through the MOSFET produced a breakdown in the gate oxide under high voltage. Current pulses were counted by an external circuit. The disadvantages of this approach include a need for an external circuit during the irradiation, dead time of the circuit and problems with separation of two nearly simultaneous impulses.

Change in the MOSFET threshold voltage was found to be dependent on the angle between the incident proton irradiation and the direction of electric field in the MOSFET silicon dioxide gate (Tallon *et al.*, 1987). It was demonstrated for 2 MeV and 16 MeV proton beams that the threshold voltage change per unit dose increased with an increase in the incident angle from 0 to 80 degrees.

1.3.3. MOSFET dosimeter applications in radiation oncology and other fields

The dose verification of a patient therapy plan and planning software are important parts of treatment procedure and of quality assurance in a radiation oncology facility. Ionisation chambers, thermoluminescent dosimeters (TLD) and semiconductor diodes are currently the most commonly used dosimeters for these purposes. Nevertheless the medical applications of the MOSFET detectors are

growing. The advantages of MOSFETs include the small size of the detector, an extremely thin sensitive volume, total dose accumulation, easy non-destructive readout and the possibility of on-line measurement. An extensive evaluation of the MOSFET at radiation oncology modalities was needed prior to its introduction to clinical practice.

A commercially available dual p-MOSFET dosimetry system (Soubra *et al.*, 1994) was tested with 6 MV to 25 MV x-rays and 5 MV to 14 MV electron beams produced by a medical linac (Ramani *et al.*, 1997). The dual MOSFET system utilises two identical MOSFETs on the same silicon chip. The MOSFETs are irradiated under different bias voltages. The difference in threshold voltage change between two MOSFETs is used as a measure of the radiation dose deposited in SiO_2. This technique improves linearity and reduces temperature dependence of the p-MOSFET response (Soubra *et al.*, 1994).

The dual p-MOSFET dosimetry system was characterised for angular dependence, energy response and accumulated dose effect. The dose was calibrated by an ionising chamber. The sensitivity of MOSFET changed within 5% at the 95% confidence limit in an x-ray energy range of 6 to 25 MV (Ramani *et al.*, 1997). The temperature effect in the range from room temperature to 37°C was within 3%. The MOSFETs were tested for patient *in-vivo* dosimetry and the general acceptance of MOSFET detectors by patients was reported to be good (Ramani *et al.*, 1997).

A threshold voltage "creep-up" effect was observed when a MOSFET threshold voltage was measured by a constant current readout system. The effect was explained by (Soubra *et al.*, 1994) who suggested that the charge injected by the measuring electronics during the previous measurement changes the electric field in the silicon dioxide which then causes a temporary change in threshold voltage. The effect becomes noticeable if a second measurement is performed on a MOSFET irradiated to a total dose in excess of 20 Gy. The maximum effect of 4 mV change was observed when the second measurement was performed less than 10 seconds after the initial one. Readings taken more than 60 seconds after the initial one showed no "creep-up" effect. An alternative explanation of the "creep-up" effect is that it is caused by the on-line measurement. The voltage on the gate became less positive, thus reducing sensitivity. The effect was eliminated by a new read-out design suggested by A. Rosenfeld and implemented by the Centre of Medical Radiation Physics of the University of Wollongong.

The calibration measurements of a similar dual p-MOSFET system revealed a low angular dependence (Scalchi & Francescon, 1998). The accuracy of the MOSFET satisfied the requirements of clinical dosimetry. The difference between a MOSFET and a graphite wall Farmer-type ionisation chamber measurement of midplane dose in a total body irradiation set up was within 2%. The difference between a MOSFET and TLD measurements did not exceed 5% (Scalchi & Francescon, 1998).

MOSFET sensitivity in operational mode, ie. under applied bias, is between 1 mV per cGy to 15 mV per cGy. However, applications of the MOSFET for patient

dosimetry in diagnostic x-ray imaging require a significantly higher sensitivity. In order to increase the dose response of the detector, several MOSFETs were produced on a single chip and connected in series. Study of this structure revealed a high temperature dependence and high noise, therefore a temperature compensation circuit was suggested (Conneely *et al.*, 1998).

An automated MOSFET dosimetry system was developed by (Gladstone & Chin, 1991). A computer control system was proposed for use in low dose brachytherapy and radioimmunotherapy applications. The system corrects for threshold voltage drift at a low dose rate. Threshold voltage was defined as the gate potential at which the MOSFET just begins to pass the source-gate current. This method requires measurement, plotting and extrapolating to zero using the relationship $\sqrt{I}$ vs V_{gate}. Apart from being time consuming, it adds extrapolation uncertainty and it lacks the benefit of measuring threshold voltage in a thermal-stable current (see Chapter 4.2).

The small size of the MOSFET detector makes it attractive for construction of miniature probes (Gladstone *et al.*, 1994a; Hughes *et al.*, 1988b). It is interesting to note that prior to introduction of the MOSFET as a radiation dosimeter, similar miniature instrument design principles were used in construction of needle type probes based on silicon diode (Lauber, 1972). In the miniature MOSFET probe instrument, a p-channel MOSFET manufactured by REM Semiconductors, Oxford, UK, of the same type as the p-MOSFET used during course of this PhD study, was reduced to the size of 0.6 mm and inserted into a standard 16 gauge flexineedle. The external diameter of the MOSFET probe was 1.6 mm. No

directional dependence was observed in megavoltage x-ray or electron beams when the detector was placed under conditions of electronic equilibrium. The temperature dependence of the MOSFET reading was rather high at 7.4 $mV \cdot °C^{-1}$. The temperature coefficient depends on the measuring current (Buehler *et al.*, 1993), but the current value was not quoted in the paper. The miniature probe was suggested for use in stereotactic radiation therapy, brachytherapy and radioimmunotherapy.

A MOSFET dosimeter is attractive for space applications due to its small size, low energy consumption and possibility of remote monitoring. The first launch of the MOSFET as a space radiation dosimeter took place in May 1978 on board a European satellite (Adams & Holmes-Siedle, 1978). The on-board electronics in a space radiation environment are under constant bombardment of cosmic radiation. An accumulated radiation dose or a passage of a high energy particle may change charge stored in a CMOS memory cell and invert it from logical 1 to 0 or otherwise. Monitoring of the total radiation dose is important for predicting changes in behaviour of integrated circuit (IC) components and for compensation of thosechanges. A MOSFET radiation monitor placed on the same silicon chip as an IC provides the advantage of the direct measurement of the dose absorbed in the silicon chip (Buehler *et al.*, 1993).

Chapter 2. Review of Boron Neutron Capture Therapy (BNCT) and Fast Neutron Therapy (FNT)

Within only four years after the discovery of the neutron in 1932 by James Chadwick (Chadwick, 1932), it was proposed to use neutron properties of interaction with nuclei, such as ^{10}B, ^{6}Li or ^{157}Gd (Chadwick & Goldhaber, 1935; Taylor & Goldhaber, 1935) in cancer radiation therapy (Locher, 1936). The clinical use of boron neutron capture therapy was suggested in 1950 by William Herbert Sweet, a neurosurgeon at the Massachusetts General Hospital (Javid *et al.*, 1952; Sweet, 1951). Sweet initiated collaboration with physicists from Brookhaven National Laboratory (BNL) and other institutions in search of new techniques for improving the diagnosis and therapy of brain tumours.

2.1. Physical, chemical and biological aspects of BNCT

Boron Neutron Capture Therapy (BNCT) is based on the nuclear reaction resulting from the capture of a slow neutron by the stable boron-10 isotope, leading to formation of unstable boron-11, which subsequently decays with the release of an alpha particle (^{4}He) and ^{7}Li nucleus. The advantage of BNCT is in the binary characteristic of the therapy, in that cancer cells are selectively loaded with a non-toxic agent which is then activated by subsequent irradiation. In BNCT the total dose in tissue originates from interactions of the medium with thermal, intermediate and fast neutrons, from gamma rays present in the beam and released

in some neutron capture reactions, and from recoil proton reactions. The major component of the biological dose in the tumour region is due to thermal neutron capture by a ^{10}B in the $^{10}B(n,\alpha)^{7}Li$ reaction. Both reaction products have a short range in tissue and high linear energy transfer (LET). Two other tissue nuclear reactions with thermal neutrons are possible in a biological tissue. They are $^{14}N(n,p)$ and $H(n,\gamma)$. Protons produced in a nitrogen neutron capture reaction have an energy of about 580 keV and deliver their dose locally. The gamma rays released in the hydrogen neutron capture reaction have an energy of 2.23 MeV and have a high range in tissue, contributing little to local tumour control. Epithermal and fast neutron components of the neutron beam deliver the dose to tissue mainly by recoil protons.

Boron-10 has a high thermal neutron capture cross section of 3840 barns (BNL, 1958) for 2200 m/s neutrons. The decay reaction proceeds in one of two modes

$$^{10}B + n \rightarrow [^{11}B^*] \rightarrow {}^{4}He + {}^{7}Li + 2.79 \text{ MeV (6\% of the reactions)}$$

or

$$^{10}B + n \rightarrow [^{11}B^*] \rightarrow {}^{4}He + {}^{7}Li + \gamma\,(0.48 \text{ MeV}) + 2.31 \text{ MeV (94\% of the reactions)}$$

The range of each of the decay particles in tissue does not exceed 10 μm and the particles produce a dense ionisation along their path. The track diameter for a 2 MeV alpha particle is less than 10 nm (Paretzke *et al.*, 1995). An alpha particle inflicts serious damage and destroys biologically active molecules such as DNA, RNA and proteins. The relative biological effectiveness (RBE) of alpha radiation

can be as high as 20. RBE of short range and high LET radiation of products of ^{10}B neutron capture decay depends strongly on microdistribution of boron atoms in the cell. Experimental measurements have been performed mostly *in vitro* on cell mono-layers and on suspension cells in a medium (Coderre & Morris, 1999). In these measurements it was assumed that boron-10 concentration in a suspension or in a mono-layer cell was the same as in the medium and no independent validation of the boron-10 concentration was performed. Because biological effectiveness of such a short range radiation depends not only on the radiation quality or LET, but also on the microdistribution of boron, the measured factor was called compound biological effectiveness or CBE (Gahbauer *et al.*, 1992; Morris *et al.*, 1994). CBE factors for different cell cultures and boron compound were reported in the range from 3.3. to as high as 9.8 (Coderre *et al.*, 1993; Fukuda *et al.*, 1987; Gabel *et al.*, 1984). An average RBE value of boron neutron capture reaction accepted in BNCT clinical trials is approximately 3.5 (Coderre & Morris, 1999).

Microscopic effects of alpha particles on cell survival were investigated in experiments with an alpha particle accelerator and cell cultures. It was established in experiments with mono-layers of mammalian cells that the mean number of alpha particle traversals required to kill a cell varied in the range of 2 for hamster HS-23 cells to 6 for a mouse cell line C3H 10T1/2 (Raju *et al.*, 1991). The number of traversals per unit area, as well as the total track length of analpha particle in a cell, necessary to inactivate the cell, were found to be constant for both mouse and hamster cells. Direct measurement of the lethality of an exact number of alpha particle traversals through mammalian cells showed that cell survival after a

single traversal of an alpha particle was 82%. The passage of alpha particles through the cell nucleus does not significantly change cell survival for a single alpha particle traversal (Miller *et al.*, 1999). Cell survival was reduced to about 10% after 8 alpha particles traversed the cell (Hei *et al.*, 1997).

If boron-10 is selectively delivered to a tumour, the radiation damage is localised to tumour cells and very little damage is done to normal tissue. The major advantage of a binary therapy system is that the two components of the therapy can be adjusted independently of each other. The components of neutron boron capture binary therapy are a boron compound and neutron radiation beam. An ideal boron compound will predominantly concentrate in a tumour sparing the healthy tissue. The time interval between a boron compound injection and irradiation can be varied to achieve a better tumour to tissue ratio of boron concentration. Furthermore the neutron beam can be collimated so that normal tissue can be excluded from the treatment.

An ideal boron compound for use in BNCT should have high specificity for malignant tumour cells, with low concentrations in blood and adjacent normal tissue. In the early stages of BNCT there were no specifically designed boron compounds. Compounds such as sodium borate and boric acid were selected because of their availability, known pharmacology and low toxicity (Pfeiffer & Jenney, 1950). Initially it was postulated that boron inorganic compounds could not pass blood-brain barrier and enter the normal brain tissue, but they would be able to penetrate brain tumour cells where the blood-brain barrier was absent or compromised. Studies of boron intake in mice showed that differences in boron

concentrations in tumour and brain were not large and that they disappeared one to two hours after the injection (Locksley & Sweet, 1954). This prompted more studies of boron compounds and sodium decahydrodecaborate ($Na_2B_{12}H_{10}$) was selected for further BNCT trials (Sweet *et al.*, 1963). This compound attained a tumour to brain ratio in mice of 8:1 which persisted for 2 hours. But naturally occurring compounds were not completely satisfactory and new compounds needed to be synthesised.

Synthesised sulfhydryl-containing boron hydrides such as $B_{12}H_{10}SH^{2-}$ showed a tumour to brain boron concentration ratio of 1.7-20:1 (Soloway *et al.*, 1967). One of the compounds of this class, $Na_2B_{12}H_{10}SH$, abbreviated as BSH, was selected for use in Japanese trials of BNCT because of its high concentration in tumours and low toxicity (Hatanaka, 1975). It was also studied for uptake by malignant melanomas. Melanoma, while being resistive to gamma radiation (Rofstad, 1986), is sensitive to alpha particles (Mishima, 1973; Nikanishi *et al.*, 1980).

Another class of boron compounds, that showed a promising potential as a BNCT drug, was an amino acid (Alam *et al.*, 1989). P-boronophenylalanine, or BPA, appeared to be more effective than BSH in cell studies and in brain tumour treatment studies in rats. BPA was more efficient in tumour targeting, but BSH caused proportionally less damage to tissue in BNCT (Coderre & Morris, 1999). The BPA compound was used in recent trials of epithermal BNCT for treatment of glioblastoma at the BNL and it is used in current trial at MIT for glioblastoma and melanoma, while BSH is used in a European Phase I trial of BNCT at High Flux Reactor (HFR) in Petten, in the Nederlands.

A new generation of boron containing drugs can target tumour cells by attaching boron to antibodies, or even by allowing the compound to enter the cell nucleus and become attached to DNA (Barth *et al.*, 1982; Soloway *et al.*, 1986). A series of boron-containing spermidine/spermine analogues were synthesised and tested for DNA targeting in *in vitro* studies using rat glioma cells. The polyamines retained an ability to displace ethidium bromide from calf thymus DNA and were taken up by the rat glioma cells (Cai *et al.*, 1997). However, these compounds require further development because of their toxicity.

An *in situ* detection of boron in patient tissues can be performed by a nuclear magnetic resonance (NMR) by using an imaging method or by a spectroscopy method. NMR detection method is capable of detecting of both isotopes of boron: ^{10}B and ^{11}B. Boron-11 provides a stronger signal and for this reason a majority of the detection was performed of ^{11}B (Bendel *et al.*, 1998; Bradshaw *et al.*, 1995). Boron compounds, which are used in BNCT, are up to 95% enriched in ^{10}B, thus reducing the signal used for mapping of boron distribution in a body. Another NMR approach is to detect ^{1}H covalently bound to ^{10}B in a boron compound. Justification for this approach is a higher sensitivity of NMR to ^{1}H than to ^{10}B (DeLuka *et al.*, 1991). For some compounds the boron-10 signal can be efficient in mapping of boron concentration. For example, evaluation of detection efficiency of BSH performed by (Bendel & Sauerwein, 2001) revealed no advantage in using ^{1}H instead of ^{10}B.

2.2. Early trials of thermal BNCT at the BNL and MIT (1951 to 1961)

An excellent account of early trials of BNCT can be found in a review by David Slatkin (Slatkin, 1991). In the fifties trials of BNCT were conducted at the BNL. The BNL Medical Department was formed on September 1, 1949 and in August 1950 the Brookhaven Graphite Research Reactor (BGRR) was commissioned. In 1950 a proposal was submitted to the Atomic Energy Commission to start BNCT treatment at BGRR (Sweet, 1986). The thermal radiation BNCT facility, including a treatment room, at BGRR was built on the top of the reactor. In order to perform an irradiation, a patient's head was positioned against the 5 cm × 10 cm rectangular neutron port. The initial BNCT study involved 10 patients. The study started only six months after BGRR was completed and it lasted for 24 months (Farr *et al.*, 1954a; Farr *et al.*, 1954b; Godwin *et al.*, 1955). In this first trial a 95% ^{10}B enriched borax was administrated over a period of several minutes followed by 17 to 40 minutes irradiation at full reactor power of 40 MW. The median thermal neutron fluence per treatment was 0.93×10^{12} cm^{-2}. No serious side effects were observed, despite borax being a slightly toxic compound.

The next group of 9 malignant glioma patients was irradiated at a modified 10 cm × 10 cm neutron port. A less toxic sodium pentaborate compound was used, but the boron concentration in the blood was found to be higher than in the first trial group. The median neutron fluence per irradiation was also increased to 3.38×10^{12} cm^{-2}. Radiation skin burns were caused due to the high thermal neutron fluence

and high concentration of boron in the skin. The median survival time was 147 days, which was an improvement on the 95-100 days of median survival after conventional radiotherapy treatment demonstrated by (Farr *et al.*, 1958). A third group of 9 patients was treated by injection of pentaborate directly into the carotid artery of the tumour-bearing hemisphere and thus reduced neutron fluence to 0.72×10^{12} cm^{-2}. This method of injection was developed in order to reduce the boron concentration in the blood and the radiation dose to the scalp. The median survival of 96 days was similar to conventional treatment (Slatkin *et al.*, 1986), but as a positive development, no patients developed severe radiation dermatitis.

As a result of BNCT trials at the BGRR, it was concluded that a shorter irradiation time should be used in order to deliver irradiation during the period when the tumour to brain ratio of boron concentration was highest. As this was impossible to achieve at any of the ports of the BGRR, a decision was made to build a new compact Brookhaven Medical Research Reactor (BMRR) with a BNCT facility. The BMRR is a light water cooled and moderated nuclear reactor with a maximum power of 5 MW. Seventeen patients were treated at the BMRR and the medium survival time was approximately 90 days (Slatkin, 1991). The trial was considered to be unsuccessful and the BNCT program at the BNL was terminated.

In the late fifties William Herbert Sweet became involved in development of BNCT in Boston, Massachusetts. A BNCT facility was established at the nuclear reactor of the Massachusetts Institute of Technology (MIT) (Brownell & Sweet, 1958). Clinical trials, in collaboration with the Massachusetts General Hospital, started in 1959 and lasted for 2 years. During this time 18 patients with brain

tumours were treated by BNCT. The p-carboxy derivative of phenylboronic acid was used as the boron-10 delivery agent. Average survival post BNCT was 6 months (Asbury *et al.*, 1972). This trial was also considered a failure, and for a long period from 1961 to 1994 there were no clinical trials of neutron capture therapy conducted in the USA.

There were several reasons responsible for the failure of the first boron neutron capture therapy trials. The boron compounds used could not guarantee a favourable tumour to brain ratio of boron concentration. The compounds could not freely enter glioma and at the same time not cross the blood-brain barrier. The tumour to brain boron ratio rapidly changed with time after the injection. A technique of rapid measurement of boron concentration in the patient's blood was not available at the time of the trials. A knowledge of boron concentration in the blood can help to plan treatment and to minimise a major complication of BNCT, the radiation damage to cerebral vasculature. Low molecular weight boron compounds were freely diffusible and could not achieve selective localisation in the tumour. The thermal neutron beam, used in the trial, was attenuated by the tissue with a half value layer of about 1.5 cm (Fairchild & Bond, 1985), and therefore, for delivering a lethal dose to the tumour, the skin and scalp were excessively irradiated, causing post-radiation complications. Deeper tumours could not be treated with a thermal neutron beam.

2.3. Development of thermal BNCT in Japan

In 1968 a neurosurgeon, Dr. Hiroshi Hatanaka, initiated a BNCT trial in Japan (Hatanaka, 1975). Dr. Hatanaka developed an interest in BNCT during his work with Dr. Sweet at the Massachusetts General Hospital in 1963-1968. The first irradiation of a patient with a malignant glioma took place in August, 1968 (Hatanaka & Urano, 1986). Later Dr. Mishima applied BNCT for the treatment of malignant melanomas (Mishima *et al.*, 1989). The trials were conducted at five different reactors. For the initial period from 1968 to 1975, the trails were performed at Hitachi training reactor. Later, from 1977 to 1989 majority of trials took place at a thermal neutron facility at the Mushashi Institute of Technology Reactor and from 1974 till present the trials have been performed at the Kyoto University Reactor (Kobayashi *et al.*, 1997). The reactor was remodeled in March 1996 (Kobayashi *et al.*, 2000b). 61 patients were treated before the remodeling. Among those patients, 47 were treated for malignant brain tumours and 14 were treated for melanomas (Ono *et al.*, 1997). Remodeling has increased the epithermal neutron component of a predominantly thermal neutron beam. After the remodeling to November 1999, 15 patients with brain tumours and 2 patient with melanomas were irradiated (Kobayashi *et al.*, 2000a).

Irradiations in Japanese trails were conducted after surgical removal of the tumour, often with the skull open. A thermal neutron fluence of $5.3\text{-}9.6\times10^{12}$ cm^{-2} was delivered to the tumour bed. As a way to improve access of thermal neutrons

to the tumour bed, a ping-pong ball or balloon was inserted into the tumour bed. The use of air-filled balloons was pioneered by the MIT team during the 1959-1961 trial (Slatkin, 1991). Sodium mercaptoundecahydrododecaborate or BSH ($Na_2B_{12}H_{11}SH$) was selected for the BNCT trials in Japan. For the first series of glioblastoma patients treated between 1968 and 1974 the average survival after BNCT was 28 months in contrast to only 5 to 17 months survival with conventional therapy (Hayakawa *et al.*, 1978). The quoted median conventional therapy survival time was longer in this study than in the BNL trial because of the differences in tumour stage and age of the patients. Some of the malignant glioma patients had very long survival times (Hatanaka *et al.*, 1986). For example, a patient treated in 1972, at the age of 50, was alive and well in 1990. In total, for the period from 1968 to 1997, 149 patients with brain tumours were treated by BNCT (Nakagawa & Hatanaka, 1997). Most of these patients were diagnosed with glioblastoma and their median survival time was reported to be 1.8 years. There was some controversy in the statistical treatment of the survival data. An analysis of the survival data of a subset of 12 patients from the USA showed no change in the median survival of 10.5 months and a non statistically significant increase from 13% to 22% in 3 year survival (Curran *et al.*, 1993). However, an increase in 3 year survival was still quite noticeable and the encouraging results of some of the patients in Japan helped to keep an interest in BNCT in the USA, Europe and in Australia.

2.4. Current clinical trials of BNCT

Trials of thermal BNCT of glioblastoma treatment are continuing in Japan at Kyoto University Reactor (Kobayashi *et al.*, 1997). Thermal neutrons are used to irradiate the tumour bed during intra-operative BNCT of brain tumours (Hayakawa *et al.*, 1978). Measurements of tumour uptake of BSH were performed by injection of the compound into newly diagnosed patients 2.5 to 16 hours prior to surgery for tumour removal (Takagaki *et al.*, 1997). The distribution of ^{10}B in the tumour was measured by gamma ray spectrometry or alpha autoradiography. The tumour to brain ratio was 11.0±3.2 and the blood to tumour ratio changed with time up to a maximum value of 1. Thermal BNCT treatment of shallowly located brain tumours (depth less than 3.3 cm) in 16 patients had a 31% 3-year survival and a 50% 2-year survival. A study of BSH and BPA compounds was undertaken in mice and cell lines with neutron irradiation (Masunaga *et al.*, 1998) and it was shown that the sensitivity of BPA treated cells was lower than BSH treated cells.

In 1994 the first modern clinical trials of epithermal BNCT were started at the Brookhaven Medical Research Reactor (BMRR), Brookhaven National Laboratory (BNL), New York (Chadha *et al.*, 1998), the MIT reactor in Cambridge, Massachusetts (Busse *et al.*, 1997), and, in October 1997, at the High Flux Reactor (HFR) in Petten, in the Netherlands (Sauerwein, 1997). All the

patients participating in the trials undergo surgical removal of the bulk of the tumour prior to BNCT treatment.

In the BNL Phase I/II clinical trial the patients were administrated intravenously with a BPA-fructose complex at a dose of 290 mg per 1 kg of body weight (Barth *et al.*, 1999). A dose of 15 to 60 Gy, depending on depth, was delivered to residual infiltrating tumours during single irradiation. The maximum dose delivered to a small volume of the brain of the size of 1 cm^3 was 12 Gy. A similar treatment plan was applied in the MIT phase I epithermal BNCT trial. As of August 1998, 40 patients were treated at the BNL and 13 at the MIT. At this initial stage, the median survival time of 14 months is similar to that of conventional therapy, but the survival data are based on Phase I of the trials. In 2000 the medical program at the Medical Research Reactor at BNL was suspended and the clinical trials of BNCT have been ceased there.

In a European Phase I trial (Protocol 11961) of epithermal BNCT, for glioblastoma treatment at the HFR in Petten, a BSH compound has been used (Sauerwein *et al.*, 1999). The compound is administered intravenously at a dose of 100 mg per 1 kg of body weight and irradiation is performed 12 to 18 hours after injection. Boron concentration in the blood is close to 30 μg per ml during irradiation. The initial study involved 10 patients (Barth *et al.*, 1999). A dose escalation of 10% has been planned to start in at least 6 months after the first stage is completed.

All the clinical trials of BNCT have been run so far at nuclear reactor facilities. An attractive alternative to a nuclear reactor is an accelerator based neutron source for BNCT. An accelerator-based BNCT facility is more acceptable for a large city hospital location than a nuclear reactor. Several charged-particle neutron production reactions have been investigated for production a therapeutic epithermal neutron beam. In these reactions, a proton or deuterium beam hits a ^{7}Li or ^{9}Be target, producing a neutron flux by one of the reactions: ^{9}Be(*p*,*n*), ^{9}Be(*d*,*n*) and ^{7}Li(*d*,*n*) (Klinkowstein *et al.*, 1997; Yanch *et al.*, 1997). Accelerator-base neutron irradiation facilities, suitable for BNCT, have been under development at the Lawrence Berkeley National Laboratory (Bleuel *et al.*, 1998), at the Ohio State University (Woollard *et al.*, 2001), at the Massachusetts Institute of Technology (Guerga *et al.*, 2000), the University of Birmingham and some other locations.

2.5. FNT and the possibility of boron enhancement of FNT

In 1938, in California, Dr. Robert Stone started the first clinical trial of fast neutron therapy (FNT). Patients with inoperable tumours were irradiated in a fast neutron beam from a Lawrence 60 in. synchrotron at Berkeley (Stone & Larkin, 1942). The trial continued through to 1943 during which time 13 patients were treated (Stone, 1948). The results of the trial were disappointing, there was no improvement compared to conventional radiation therapy and late complications of the treatment were much more severe than for x-ray therapy. After analysis of the trial results and the late sequelae, Stone recommended that the fast neutron therapy trial to be discontinued.

The reason for the failure of the first FNT trial was due to insufficient knowledge of radiobiology and the relative biological effectiveness (RBE) of fast neutron irradiation. Stone used RBE data obtained for high doses of irradiation (Marshak, 1939; Stone *et al.*, 1940) and applied them to devise a schedule of treatment using fractioned small doses. It was later recognised that that RBE should be considered, not in the relation to total dose, but to the dose per fraction (Field & Hornsey, 1971). When RBE was compared for acute and delayed reactions, it was higher for a large number of small dose fractions than for fewer fractions at larger doses. The RBE decreased with increased dose. It shows a difference in the sparing effect for normal tissue of fractionation radiation schedules with x-rays and fast neutrons for most of normal tissues (Denekamp, 1994). The acute and late effects of fast neutrons on living organisms have been experimentally studied with monkeys and small mammals. The experimental data for skin effects on mice, rats, pigs and humans showed that the RBE, if expressed in dose per fraction, was comparable in all four species for both acute and late effects (Denekamp, 1994). Investigations of RBE and dose fractionation for damage to the brain and spinal of rats and rhesus monkeys (Hornsey *et al.*, 1981; Stephens *et al.*, 1983) concluded that fractionation of neutron dose irradiation had a minimal effect on tolerance levels.

Other reasons for the failure of the first FNT trial were technical shortcomings. The 7 MeV neutron beam energy was low and as a result penetration of the neutrons was also low, being comparable to a 250 kV_p x-ray beam. Furthermore, the Lawrence accelerator was not designed for use as a medical therapy machine

and was therefore located outside the hospital. The beam had only one fixed horizontal direction and it could not be rotated around a patient.

Radiation biology investigations established a rationale for use of fast neutron beams in cancer therapy. Oxygen deficient hypoxic cells are found in most solid tumours (Adams, 1990) and these hypoxic cells are resistant to x-ray radiation. This resistance is described by the Oxygen Enhancement Ratio (OER). For x-rays the OER equals approximately 3. High LET radiation, such as fast neutrons, reduces the OER to about 1.6 Thus the therapeutic gain factor when using fast neutrons is 3:1.6 = 1.9 (Wambersie *et al.*, 1994). Another important advantage of using fast neutrons is that they reduce the difference in radio sensitivity of the cells dependent upon their position in mitotic cycle (Chapman, 1988). This can be an advantage for FNT of slow growing tumour with cells spending long periods of time in the G1 phase of the cycle, which is known to be radio resistant.

At the end of 1960's a FNT clinical trial started at Hammersmith Hospital in London. The neutron beam was produced by deuterons accelerated by a cyclotron to the energy of 16 MeV onto a beryllium target. In total 238 patients had been treated by 1973 and the results were very encouraging. Neutron treatment achieved 76% local control compared to 19% using x-rays for head and neck tumours (Catterall, 1974; Catterall *et al.*, 1975). Late reactions, however, were observed over a period of 3 years, where neutron treated patients showed a significantly greater number of severe complications (Catterall *et al.*, 1977).

In recent years delivery of FNT has greatly improved. Currently there are more than 20 medical centres world wide where the FNT facilities are installed and operational (Maughan, 1992). The new facilities operate higher energy cyclotrons, typically 45 to 60 MeV, with beam depth penetration and skin sparing effects similar to that of a 4 to 10 MV linear accelerator. They are equipped with gantry and multileaf or multirod collimators. FNT is applied for treatment of prostate, salivary gland and paranasal sinuse tumours, other head and neck tumours and soft tissue sarcomas. Fast neutron therapy of these types of cancer was found to be more efficient in providing local control compared to x-ray therapy.

The use a thermal neutron component of the beam could boost therapy with the boron capture reaction and so improve local control in FNT (Maughan *et al.*, 1997; Sauerwein *et al.*, 1989; Stelzer *et al.*, 1997). An *in vitro* study (Laramore *et al.*, 1994) of exposure of tumour cells loaded with 100 to 500 μg of ^{10}B per gram showed up to two orders of magnitude increased cell kill with boron neutron capture enhance fast neutron treatment, compared to fast neutron treatment without boron enhancement.

Chapter 3. Experimental procedures and materials

3.1. MOSFET detectors

The objective of this study is to research the novel applications of semiconductor detectors in radiation oncology. The Metal Oxide Semiconductor Field Effect Transistor (MOSFET) detector is the main subject of this study. Two types of MOSFETs were used in the research project. They were n-channel and p-channel MOSFETs.

3.1.1. N-channel MOSFETs

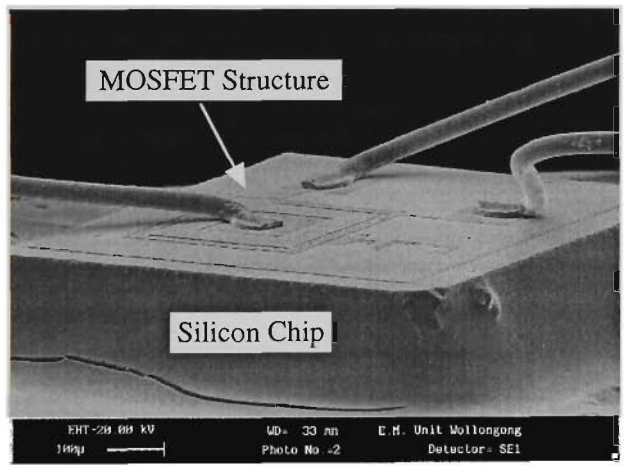

Figure 3-1. Electoron microscope photograph of the MOSFET structure on the silicon crystal of the MOSFET detector.

The n-channel MOSFETs were manufactured by SPA Detector Ltd, Ukraine. The development and testing of the devices was a joint project by Detector Ltd. and the Centre of Medical Radiation Physics of the University of Wollongong. The

MOSFET structure was built on a substrate of low resistivity (about 10 Ω centimetre) p-type silicon by multi-layer oxidation, masking, ion implantation and etching techniques. The majority charge carrier density in the substrate silicon was 1.35×10^{15} cm^{-3}. The thickness of the gate oxide was 1 μm. The gate, source and drain areas of the MOSFET were covered by approximately 1 μm thick aluminium pad contacts to which the contact wires were welded.

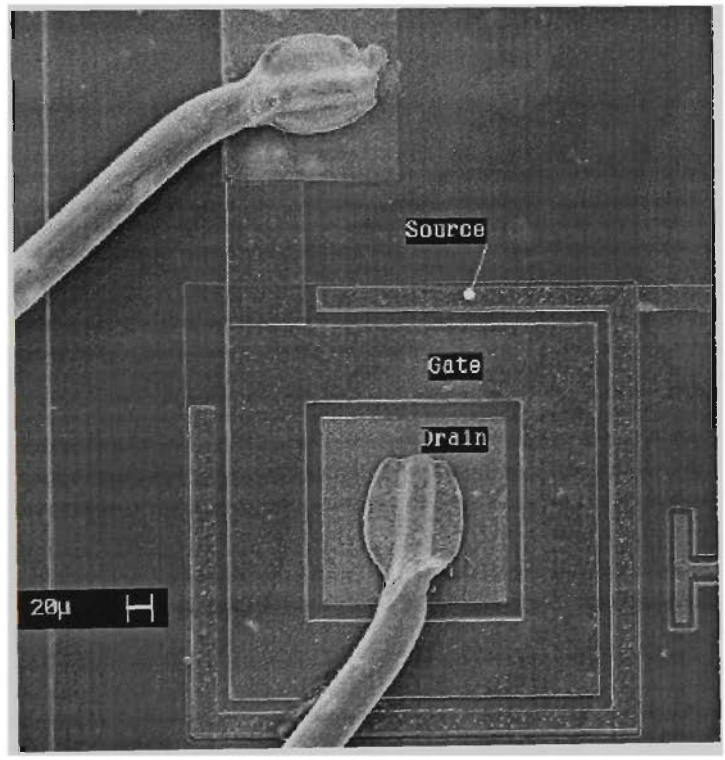

Figure 3-2. Surface topology of the n-channel MOSFET detector.

The position of the MOSFET structure on the silicon chip is shown in Figure 3-1. Three thin wires were welded to the aluminium pads to enable electrical connections to the MOSFET gate, drain and source. Connection to the substrate was achieved through ohmic contact at the back of the silicon chip. The drain of the MOSFET has a square shape with a side of 150 μm (Figure 3-2). The drain is surrounded by a square ribbon shaped gate, the width of which is 60 μm. The

outer, incomplete square ribbon in Figure 3-2 is the source of the MOSFET. This closed design geometry, when the drain is completely surrounded by the source, eliminates channel-edge leakage encountered in the linear design MOSFET.

The n-MOSFET chips were mounted in TO-18 Kovar housing which is standard for the electronic component industry. Each TO-18 housing contained a single MOSFET chip. The silicon chip was attached to the gold plated base of the TO-18 housing by conducting glue. Other major elements present in the housing material were iron and nickel.

3.1.2. P-channel MOSFETs

P-channel MOSFETs were supplied by Radiation Experiments and Monitors (REM), Oxford, UK. REM uses the brand name RADFET (Holmes-Siedle, 1986) for their MOSFETs. Four MOSFETs were grown on a single silicon chip. One pair of identical MOSFETs had a gate silicon oxide thickness of 0.13 μm each and the other pair of 1.24 μm each. MOSFETs with thicker gate oxide are more radiation sensitive and designed for cGy sensitivity. The thinner gate oxide MOSFETs are less radiation sensitive. The RADFETs were mounted in three different types of housings. All the MOSFETs in the large 14 pin TOT500 ceramic housing were individually connected to the contact pins. The smaller board mounted CC-3 housing allows only two MOSFETs to be electrically connected to on board contacts. The smallest board housing CC-5 has only four electrical contacts and only a single thick gate oxide MOSFET was wired to the CC-5 contacts.

3.2. MOSFET readers

A reader for n-channel MOSFETs, used in this study, was developed by the Centre of Medical Radiation Physics of the University of Wollongong (A. Rosenfeld). A schematic block diagram of a laboratory reader is shown in Figure 3-3.

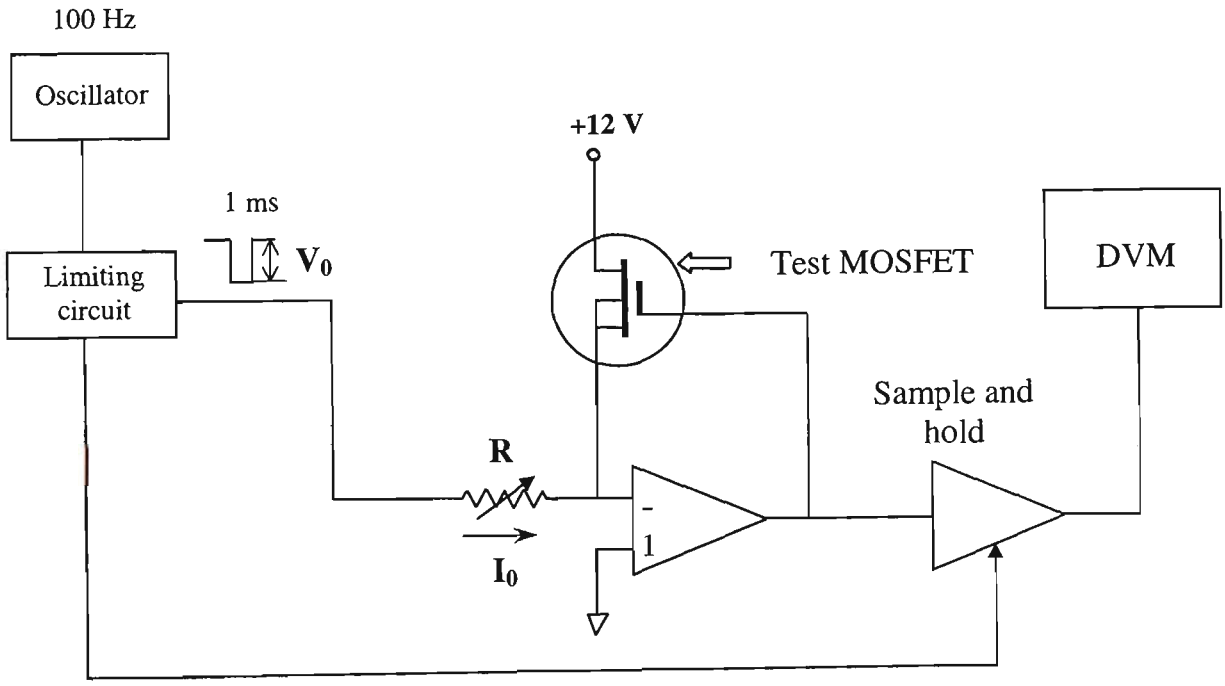

Figure 3-3. Schematic block diagram of n-MOSFET threshold voltage reader

The MOSFET source and substrate are connected to an operational amplifier in the threshold voltage measurement mode. The gate provides a negative feed back to the amplifier for measuring V_{th} at a setup current of $I_0 = \frac{V_0}{R}$. The threshold voltage measurement process is initiated when the "measure" switch is pressed on and a current flows between the drain and source contacts of the MOSFET.

During the reader development stage, we carefully considered the choice of the value of the operating current for the threshold voltage reading, and the method of the reading. In the majority of publications no reasons for choosing a particular current are given. Gladstone and Chin opted for measuring the actual threshold voltage as the gate potential at which the MOSFET begins to pass source-drain current (Gladstone & Chin, 1991). They argued that this definition of threshold voltage is superior to the arbitrary choice of measuring current. It is well established that the threshold voltage of a MOSFET depends on temperature. The temperature coefficient of the threshold voltage depends on the oxide thickness and may be in the order of ten millivolts per °C. It was shown that for some MOSFET designs a thermostable current exists at which the threshold voltage measurement is independent of temperature for a certain temperature range (Buehler *et al.*, 1993). A MOSFET with a gate surrounding the source or drain, as in the case of the n-channel MOSFET used in this study (Figure 3-2), is one of these designs. Investigation of the temperature dependency of current-voltage characteristics of n-channel MOSFETs (see Chapter 4.2) and consultations with the manufacturer, Detector Ltd, Ukraine, put the value of the thermal-stable current at 42 μA. At this current a small change in temperature has a very limited effect on threshold voltage. The current was set up by adjusting the value of the resistor R in Figure 3-3.

One of the main causes of MOSFET noise is $\frac{1}{f}$ noise which is typical for most semiconductor devices. The spectral density of noise, S_V, equals (Tarr *et al.*, 1996)

$$S_V = \frac{KF}{C_{ox} \cdot W \cdot L} \cdot \frac{1}{f}$$

where C_{ox} is the oxide capacitance per unit area, W is the width and L is the length of the MOSFET gate, and KF is a coefficient related to the MOSFET design and manufacturing process.

Constant current measurements increase the effect of spectral noise and this noise may be significant for low dose measurements. To reduce the $\frac{1}{f}$ noise, and mostly to reduce the instability of the MOSFET caused by creation of slow traps after irradiation, we chose to design a square wave current pulse power supply. The effective frequency of the square wave was set to 1 kHz and the threshold voltage at each pulse was measured by a voltage peak detector. Apart from reducing noise, the pulse current supply produces a more stable threshold voltage output by reducing the threshold voltage drift due to the drift of residual positive ions in the gate oxide. The pulse current also limits possible heating of the MOSFET due to energy dissipation.

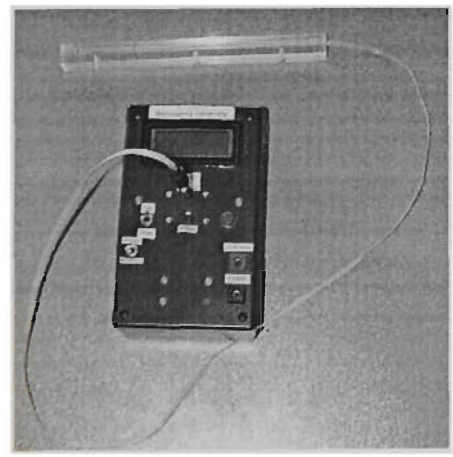

Figure 3-4. Combined n-channel MOSFET reader and gate bias power supply. A MOSFET probe embedded in a perspex slab is plugged into the gate bias terminal.

A simple reader for p-channel MOSFETs was used at currents specified by REM. The circuit diagram of the reader is similar to the one in Figure 1-3b. The readings were performed at constant currents of 90 μA or 160 μA, as recommended by REM.

3.3. Film dosimeter

Radiochromic (Gafchromic) film is a planar radiation dosimeter for low to high energy x-rays and electron beams. In November 1998 the American Association of Physicists in Medicine published the recommendations of Task Group 55 for the use of Radiochromic film for medical dosimetry (Niroomand-Rad *et al.*, 1998). Gafchromic film consists of a several micrometers thick, colourless aromatic hydrocarbon (diacetylene monomers) dye bounded to a polyester film base of approximately 100 μm thick. International Specialty Products (ISP), Wayne, NJ, USA manufactures the most commonly used Gafchromic film, MD-55. There are two types of the film, the less sensitive MD-55-1 and the more sensitive MD-55-2. The structure and composition of single-layer MD-55-1 and double-layer MD-55-2 films are given in Table 3-1. The effective atomic number of Gafchromic film is within the range of 6 to 6.5. The film's electron stopping power is similar to the stopping power of water and muscle tissue for secondary electron energy above 100 keV.

The film is practically grainless and its radiographic image gives a spatial resolution of 1200 lines/mm (McLaughlin *et al.*, 1991). Irradiation initiates a solid-state polymerisation reaction which induces a blue colour in the Gafchromic film. The film's optical density also changes. The polymerisation reaction and, as a result, the colour formation continues for several hours after irradiation. It is recommended that measurements of optical density are not performed within the first 24 hours after irradiation. After the initial set up period, the optical density of Gafchromic film does not change for many months. Since radiation response and optical density are temperature dependent, it is important to keep the dosimetry film at a constant temperature during irradiation and readout. Humidity is also an important factor affecting the response of the Gafchromic film dosimeter. It has to be kept constant during both irradiation and readout. It was shown that for 0% relative humidity, or in a vacuum, darkening within 10 minutes after irradiation was about 55% of the maximum value. When relative humidity increased to 25-35% the darkening became 77%, and for a relative humidity of 65-75%, the darkening reached 95% (Danchenko & Griffin, 1981).

Table 3-1. Structure and composition of MD-55 Gafchromic film.

Film type	Thickness		Composition	
	Sensitive layer (μm)	Base material (μm)	Polyester base	Sensitive layer
MD-55-1	15	67	Carbon 45 at% Hydrogen 36 at%	Carbon 31 at% Hydrogen 56 at%
MD-55-2	30	159	Oxygen 19 at%	Oxygen 8 at% Nitrogen 5 at%

Light absorption by the film is greatest if it is measured in the red part of the visible spectrum. The optical density spectrum in the visible and near-ultraviolet range has two principal absorption peaks at 596 nm and 650 nm (Figure 3-5). A greater non-linearity was reported for the minor absorption peak of 596 nm. The dose-response curve of Gafchromic film, model MD-55, is different for measurements of optical density at different wavelengths (Muench *et al.*, 1991). Some variations in sensitivity were also observed with the change in the equivalent proton energy. The dose response of double sided Gafchromic film MD-55-2 was measured using a He-Ne laser densitometer (wavelength 632 nm), a filtered red light densitometer (medium wavelength 670 nm, filter bandwidth 11 nm) and a broadband densitometer (Reinstein & Gluckman, 1997). The greatest response was shown by the filtered red light densitometer. The dose that creates a net optical density of 1 in red filtered light was nearly four times smaller then in He-Ne laser light. The broadband densitometer response to the absorbed dose was the poorest.

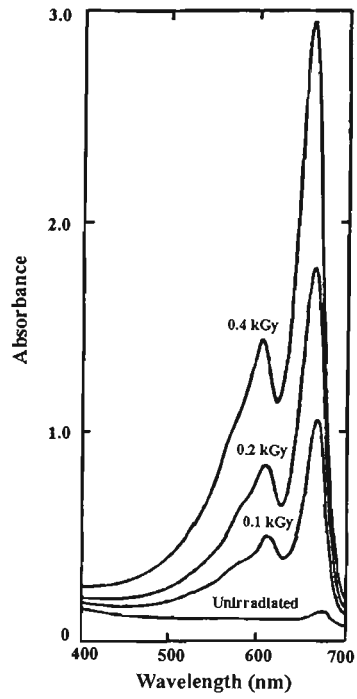

Figure 3-5. Absorption spectra of Gafchromic film irradiated at different doses (from McLaughlin *et al.*, 1991).

As a change in the optical density of Gafchromic film depends on radiation dose, a calibration of film response to radiation is required to determine radiation dose from optical density data. The shape of the calibration curve (optical density vs dose) depends on the wavelength of densitometer light. This is because optical density changes differently in different wavelengths (Figure 3-5). The calibration was close linear for the dose range up to 2 kGy for He-Ne laser light. For a longer wavelength, of 670 nm, the calibration curve becomes sub-linear (McLaughlin *et al.*, 1996). In one publication the calibration curve of Gafchromic film, with exposure up to 250 Gy, was obtained by fitting the curve to a second degree polynomial with a positive second derivative (Sanders *et al.*, 1993).

A limitation of the use of the laser light densitometers for measuring the optical density of Gafchromic film was recently discovered by (Sullivan *et al.*, 2000). A laser light can initiate polymerisation of the film dye thus changing the film's optical density. All the laser densitometers recommended by the Task Group 55 report (Niroomand-Rad *et al.*, 1998) are high speed units. A typical scanning speed of a 1 mW laser is 40-45 mm/s. The additional opacity of the film, due to the laser light, is equivalent to about 5 μGy. This dose is negligible as it is less than other uncertainties of the measurement. For a laser spot densitometer, the time for each measuring point may be as high as 3 s. This exposure time corresponds to a change in the calculated dose of about 20 cGy.

For a two dimensional dosimetry, a Gafchromic film must have a uniform response in a uniform radiation field. Non-uniformity of the optical density of up to 15% was reported (Meigooni *et al.*, 1996; Zhu *et al.*, 1997). For an improved MD-55 model of Gafchromic film the non-uniformity was different along different directions of optical density measurement. The smaller variations in uniformity along one of the directions were observed not to exceed 4%, while uniformity variations along the orthogonal direction were up to 15%. These directions did not correspond to orientations of the sides of the supplied sheets of Gafchromic film. 15% variations in uniformity were observed at a distance of 1 cm. Sharp spikes of up to 5% were also detected. The spatial resolution of the densitometer used for the optical density measurement was 0.25 mm. On a larger scale, Gafchromic film exhibited sinusoidal shape variation in optical density, with a period of about 1 cm. For a more accurate calibration and to minimise the effect of non-uniformity, a double exposure method was implemented (Zhu *et al.*,

1997). In this method a sheet of Gafchromic film was initially uniformly irradiated and optical density read in two dimensions by a computerised densitometer. The optical density after the first exposure was used for two dimensional calibration of the sheet response. The double exposure method to reduce a non-uniformity in Gafchromic film response to less than 5%.

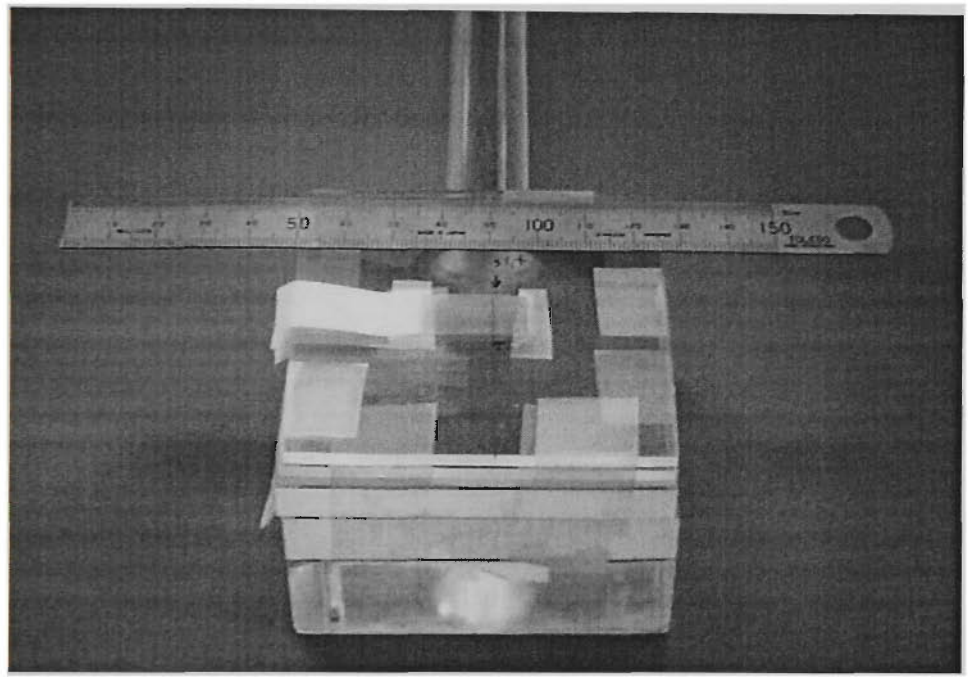

Figure 3-6. Perspex slab phantom with strips of Gafchromic film inserted between the slabs.

MD-55-1 and MD-55-2 Gafchromic films, by International Specialty Products, were used in this study to measure dose distribution in x-ray microbeam. A beam width of 200 μm corresponded to the reported resolution of MD-55 film. The darkening of the film was measured under strong magnification to obtain a high spatial resolution image of the radiation beam. It was found during microscopy investigation, that double layer film has air bubbles trapped between the layers.

The size of the bubbles was up to 0.05 mm. The bubbles reduced spacial resolution of the film. For this reason, only MD-55-1 film was used for high resolution dosimetry. After irradiation, the films were stored at room temperature in a light tight envelope for two days, to allow completion of the polymerization process.

For dose calibration measurement in air, the gafchromic film strip was suspended between two foam blocks to minimise back scattered radiation. The film strips were sandwiched between slabs of 7.5 cm × 7.5 cm perspex phantom (see Figure 3-6).

3.3.1. Film read out system

The radiation induced change in light transmission through the film was digitised and analysed by a two dimensional CCD image analysis system, originally designed for astronomical photographic plate image analysis, see Figure 3-8.

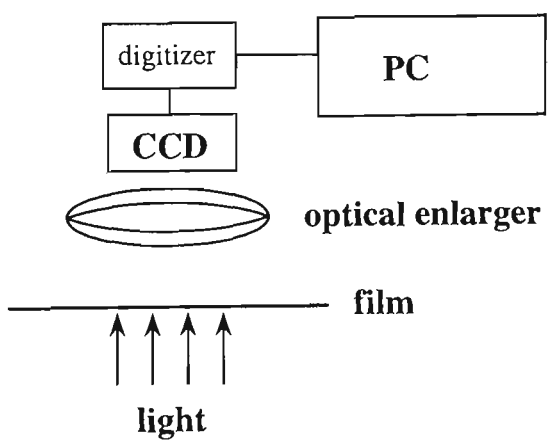

Figure 3-7. Block diagram of the image collection system

The system consists of a light source, enlarger lenses, CCD camera, digitizer and a computer with image analysis software (see Figure 3-7). The colour of the light can be changed by an cyan-magenta-yellow (CMY) filter set. In a comparative study of Gafchromic film dose response (Reinstein & Gluckman, 1997) for a He-Ne laser densitometer (wavelength 632 nm), a filtered red light densitometer and a broadband densitometer, the greatest response was demonstrated for filtered red light. For this reason, the light colour filter for Gafchromic film measurement was set to red. The CMY colour filtered light source was set to C=0, M=151 and Y=151. The median wavelength of the filtered light, as measured by a Jarrel-Ash diffraction spectrometer, was 620 ± 5 nm and the bandwidth was ±35 nm.

The system measures intensity of the transmitted light rather than optical density. An enlarger is used for projecting a magnified image of the film area to a high resolution CCD camera, the maximum optical magnification being used for film measurements. Optical resolution of the system was verified by a grating ruler as per Figure 7-7. No optical distortion was observed by using parallel lines of the ruler. The spatial resolution for this setting was measured to be 8 μm. The resolution was determined by counting the number of optical pixels per 1 mm of microscope grid. The spatial resolution of the readout system exceeded the best densitometer resolution, of 20 μm, reported in a review by Niroomand-Rad *et al.* (Niroomand-Rad *et al.*, 1998).

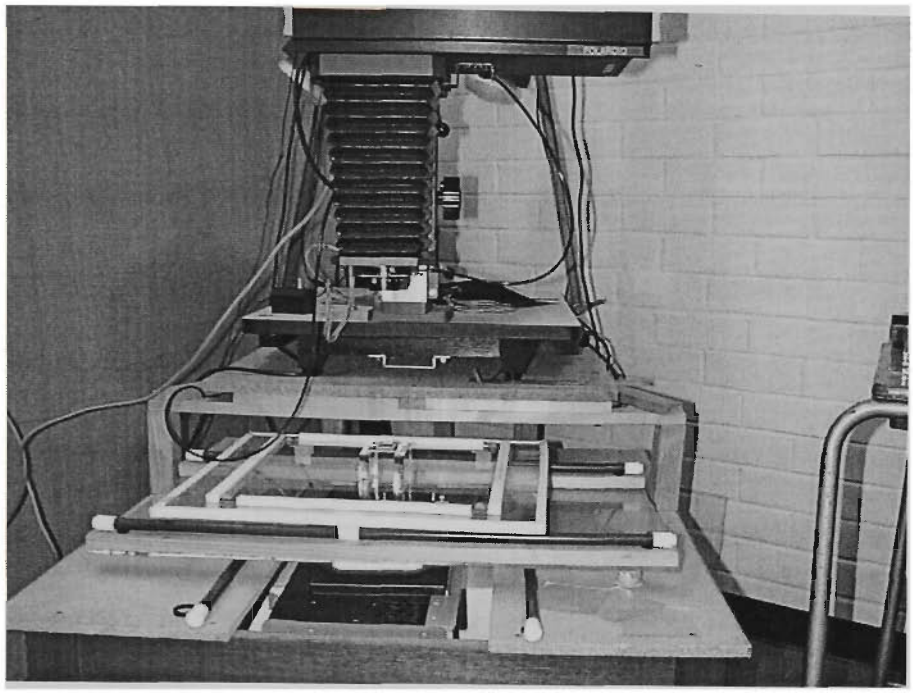

Figure 3-8. CCD image acquisition system.

3.4. Radiation Sources

3.4.1. Hospital based x-ray generators

A Therapax DXT300 orthovoltage x-ray machine was used for generation of x-ray beams with maximum energy in the range of 50 kV_p to 250 kV_p. A Therapax DXT300 contains an internal x-ray dosimeter (PTW Diamentor pancake chamber) located between the filter and collimator. The electron beam produced in the Therapax DXT300 hits a target at an angle of 45°. The size of the electron focal spot on the target is nominally 0.5 cm x 0.5 cm according to manufacturer specifications. More on the specific design of the machine and on the relevant medium x-ray energy is in Chapter 7 of this thesis.

High energy x-ray irradiation was performed in a megavoltage x-ray beam produced by the Varian, Clinac 2100C medical linear accelerator (linac). The linac accelerates electrons in pulses in envelopes of duration 5 μs, with a dose rate of 10^6 cGy(tissue)/s within a pulse. In x-ray mode the dose rate is significantly less, the dose during the pulse is approximately 10^2 Gy(tissue)/s. The linac dose rate can be adjusted by changing the number of pulses per second. The linac operated at an accelerating voltage of 6 MV. The mean energy of the x-ray beam was approximately 2 MeV.

3.4.2. Brookhaven Medical Research Reactor (BMRR)

The Brookhaven Medical Research Reactor (BMRR) is a research nuclear reactor facility of the Brookhaven National Laboratory (BNL), situated on Long Island, NY, USA. It became operational in 1959. BMRR is a light-water moderated and cooled, and graphite reflected research reactor with operating power of up to 3 MW. The reactor tank-type facility is fuelled with 31 elements of enriched uranium-235. It was purposely designed to provide a thermal neutron beam for BNCT study. As early experiments with thermal BNCT showed that the thermal neutron beam was inefficient in treating glioblastoma, the beam design was later modified (Sofar *et al.*, 1990) to produce an epithermal neutron beam (energy range of 0.4 eV to 10 keV). Until recently two irradiation facilities at BMRR were used for clinical trials of BNCT and radiobiology experiments. The epithermal neutron irradiation facility, on the east side, is equipped with a medical treatment room and since 1994 the clinical BNCT trials have been conducted there. In 2000 the

BNCT medical trials program at BNL was temporarily suspended. The thermal neutron irradiation facility on the east side of the reactor is used for experiments with small animals and cell cultures.

Fission neutrons from the reactor core initially travel through graphite reflectors and a bismuth shield 19 cm thick (see Figure 3-9). Bismuth is intended to shield the patient from the gamma rays originating in the reactor core. Al and Al_2O_3 are used as moderator and placed in the beam shutter to produce an epithermal neutron beam. Lithium poly shield lined the reactor wall of the medical treatment room and was designed to reduce stray neutrons. The epithermal irradiation port has an opening of 25.4 cm.

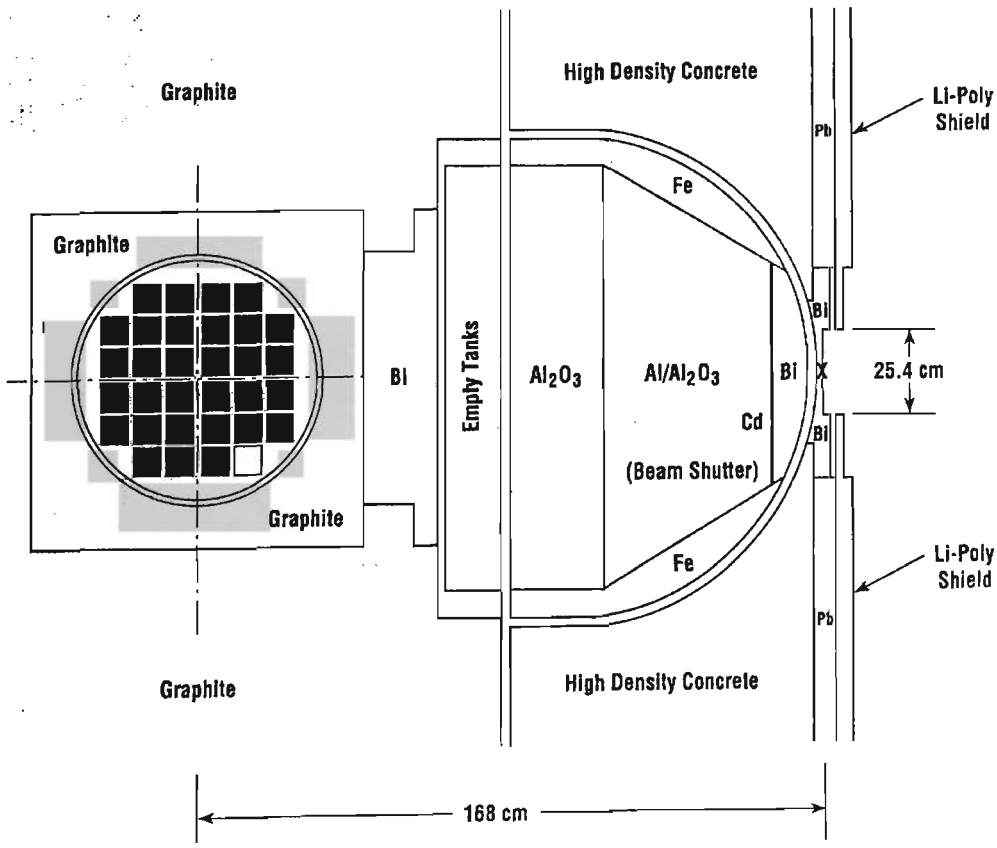

Figure 3-9. Horizontal cross-section view of the epithermal neutron irradiation facility of BMRR (after Liu *et al.*, 1996).

All the measurements at the BMRR epithermal neutron irradiation facility were performed with a 12 cm diameter collimator. The collimator was used to limit the whole body dose to the patient and at the same time to maintain an adequate dose to the brain tumour. The collimator was made from polyethylene with 45 wt. % of dispersed Li_2CO_3 powder. The lithium compound was the 93% enriched in ^6Li. The overall concentration of ^6Li in the collimator material was 7.0 wt. %.

Patient irradiation was conducted at the BMRR epithermal neutron irradiation facility at the full reactor power of 3 MW. The reactor power during our count mode measurements was set to 20 kW to avoid "pile up" for pulses, while during the MOSFET accumulated dose measurements the reactor power was 3 MW, the same as during BNCT treatment.

3.4.3. The Kyoto University Reactor

Kyoto University Reactor, Kyoto, Japan is a light water moderated tank type research reactor. It was commissioned in 1964 and reached a power of 1 MW. In 1967 the power was increased to 5 MW. The patients were treated at the reactor facility till November 1995 and in March 1996 the reactor was upgraded (Kobayashi *et al.*, 2000b). The upgrade made it possible to produce a quasi epithermal neutron beam (Kobayashi *et al.*, 1997). For irradiation in an quasi epithermal clinical mode, a cadmium filter reduces the thermal component of the beam. In a mixed clinical mode, the reactor beam is not filtered. The power of the reactor cannot be adjusted for a particular experiment, so to change the beam intensity the beam is filtered by heavy water. For fission detector measurements,

10 cm and 20 cm tanks were filled with heavy water. The total thickness of the heavy water filter was 30 cm, the diameter of the beam was 10 cm.

3.4.4. The Harper Hospital Fast Neutron Therapy Cyclotron

The isochronous superconducting cyclotron at Gershenson Radiation Oncology Centre at Harper Hospital accelerates deuterons to an energy of 48.5 MeV (Maughan *et al.*, 1994). At the spot where the deuteron beam hits a beryllium target it produces the fast neutrons by the d(48.5)+Be reaction. The mean energy of the neutrons in the beam is 20.4 MeV. The beam chamber is kept under $1\text{-}2\times10^{-5}$ Torr vacuum. One hundred litres of liquid helium per day are required to keep the magnet at the superconducting temperature. The weight of the superconducting cyclotron of 25 ton is supported by two support rings. It is balanced by a counter weight which also serves as a beam stopper. The gantry system allows 360° rotation of the neutron beam around the patient. A picture of the beam collimator and a water tank is on page 169, Figure 6-6. The gantry is equipped with a tungsten rod collimator for beam shaping and for changing the beam energy spectrum. The penetration characteristics of the Harper Hospital fast neutron beam are comparable to a 4 MeV X-ray beam from a conventional linac (Maughan & M.Yudelev, 1995). The beam is collimated by a tungsten multirod collimator. The typical beam operating current of 12.5 μA gives a dose rate of 40 $cGy{\cdot}min^{-1}$. The beam dose rate is monitored by an ionisation chamber.The dose can be delivered with an accuracy of 0.1 cGy.

3.4.5. The National Synchrotron Light Source (NSLS) at BNL

The superconducting wiggler beamline X17B1 of the National Synchrotron Light Source (NSLS) at BNL is used for the medical research. The electron energy inside the storage ring was 2.58 GeV, and the magnetic field strength of the wiggler was 4.7 T. The typical ring current was 200 mA during the experiment.

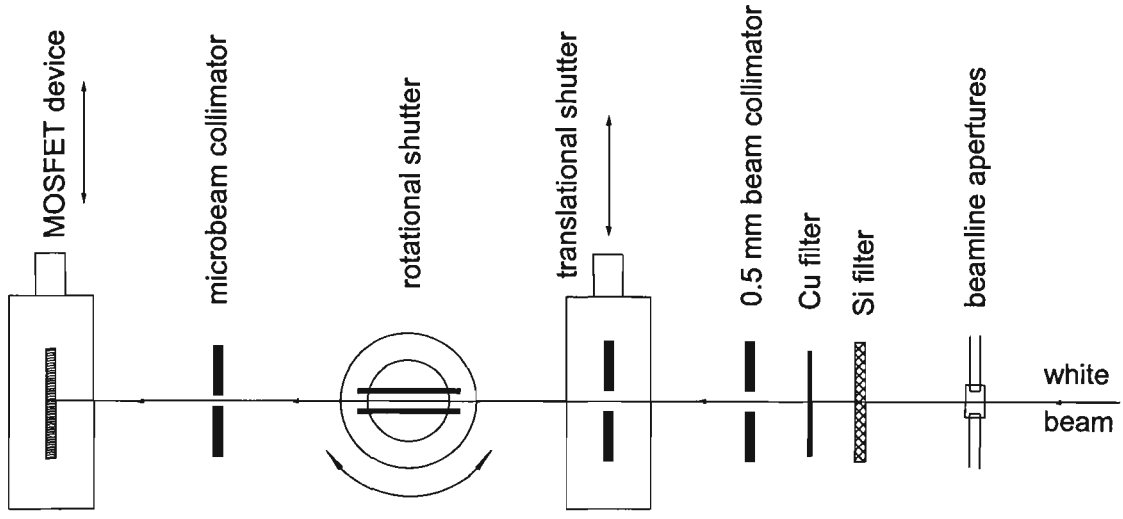

Figure 3-10. NSLS beam line and setup for MOSFET measurements.

The synchrotron produces a horizontal, partially plane-polarised beam. The horizontal divergence is ≈15 milliradian and the vertical divergence is ≈0.2 milliradian. The electron beam is emitted at a high-frequency of 53 MHz, a pulse duration is less than 2 nanoseconds. The electron beam had an energy of 2.584 GeV inside the storage ring, and the wiggler was running at 4.7 T magnetic field. The typical ring current was 200 mA during the MOSFET measurement. The central section of the white beam (3.5 milliradian horizontal and 0.143 milliradian vertical) from the source passes through a 3.7 mm Si filter, and 0.25 mm Cu filter, which produce an x-ray beam with a median energy of 64 keV, and a dose rate of

800 Gy per second. Because of such a high dose rate, very short exposure times were required during MOSFET irradiation. There were two alternative beam shutters in the experiment (see Figure 3-10). The rotational shutter served as a fast shutter for fast exposures of about 1 ms to the MOSFET. It was used for measuring dose with direct hitting beam. The transitional shutter acted as a slow shutter, to measure the tail of the beam intensity profile. The user's hutch is 27 metres away from the synchrotron wiggler. The beam is collimated through a microscopically narrow slit in a tantalum radiation shield approximately 1 metre into the hutch. The dimensions of the microplanner beam were set to be 30 μm x 0.7 mm horizontally versus vertically by the beamline apertures and two vertical beam collimators.

A multislit collimator (Slatkin *et al.*, 1995a) was designed for the X17 beam of NSLS to enable variation in beam widths and interbeam intervals for various conditions of microbeam radiation therapy. The collimator consists of a pair of identical foil stacks. Each stack is comprised of 100 μm or 150 μm tungsten foils alternating with beryllium foils of 50 μm or 100 μm thick. The beam line is parallel to the stacks and passes through both of them. One of the stacks is made movable. Translation of a movable stack parallel to the fixed one, in a direction perpendicular to the beam line, makes arrays of parallel microbeams at 200 μm intervals, with the width of the beam in the range 0 to 100 μm.

3.5. Phantoms

In-phantom measurements are used in radiation therapy for quality assurance of the radiation facility and for verification of a simulated model of dose distribution. Once the simulated model is validated by independent measurements, it can be used for calculation of a patient treatment plan. In our research we also used in-phantom measurements for testing and validation of the new dosimetry equipment, approaches and protocols.

3.5.1. The hadron therapy phantom

Two main types of phantoms have been applied for in-phantom characterisation of the neutron radiation therapy beams. One is a water tank and the other is a perspex phantom. A chemical name for perspex is polymethyl-methyacrylate (PMMA), the chemical formula is $[CH_2C(CH_3)(CO_2CH_3)]_n$.

Water tanks, usually with 6 to 8 mm thick perspex walls, were used as water head phantoms for dose component measurements at BNCT and FNT facilities around the world. For example, in the Birmingham accelerator beam in the UK, which was designed for an accelerator based BNCT, a perspex tank of 140×150×180 mm^3 with 8 mm thick perspex walls was used for dosimetric characterisation of the beam (Tattam *et al.*, 1998). Measurements of microdosimetry characteristics of the FNT beam at the Harper Hospital, Detroit, USA were performed in a similar size water tank (Maughan & M.Yudelev, 1995).

Perspex phantoms are widely used at radiation therapy facilities. The 15×15×15 cm^3 perspex phantom was used for measurements of epithermal BNCT beam characteristics at the High Flux Reactor in Petten, the Netherlands (Raaijmakers *et al.*, 1996a). In the epithermal beam of the BMMR, BNL, NY, USA a 14×14×14 cm^3 a perspex cube phantom was used for measurement of beam characteristics (Alburger *et al.*, 1998; Liu *et al.*, 1996). The volume of the phantom, of 2744 cm^3, was close to the volume of the head model described by Snyder *et al.* (Snyder *et al.*, 1969), the weight of the phantom was 3.230 kg which was 2.3 times greater than the average weight of a human brain, of 1.4 kg. A PMMA phantom was chosen for use in experimental verification of Monte Carlo calculations of an accelerator source for BNCT at the Ohio State University in USA (Dobelbower *et al.*, 1999).

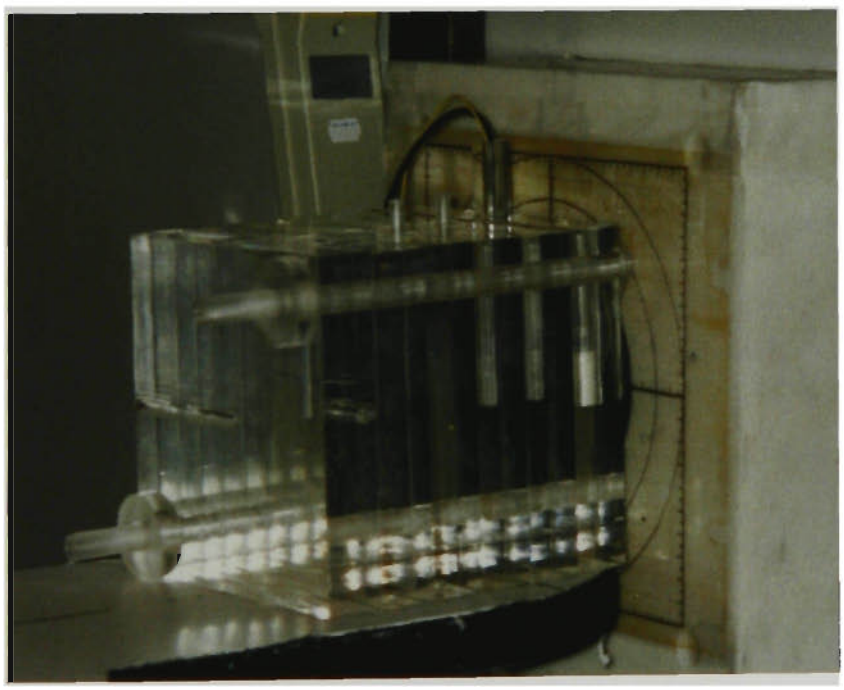

Figure 3-11. a perspex slab phantom placed next to the collimator of the epithermal neutron irradiation facility of the Brookhaven Medical Research

Reactor, BNL, NY, USA. The MOSFET dosimeter is inserted into the first slab facing the collimator.

A slab perspex phantom was designed and manufactured for our measurements of BNCT and FNT neutron beams. The material was chosen because pespex has been widely used previously in neutron measurements, it is easy to machine, non-toxic, and chemically and mechanically stable. The density of perspex is 1.17×10^{3} $kg{\cdot}m^{3}$. The phantom could be disassembled into separate slabs, making transportation to overseas radiation facilities easier. A radiation sensor can be held steady and with a minimum air gap in the pre-cut slots. The sensors do not require waterproofing.

The main configuration of the phantom consists of six 15 cm ×15 cm ×2.5 cm clear perspex slabs. Combining the slabs together makes a $15\times15\times15$ cm^{3} perspex cube (Figure 3-11). The slabs are held together by perspex screws and nuts. The radiation probes are inserted in the specially machined slots and hole. If a sensor slot is not in use, it is filled with a perspex filler rod. The depth-related radiation field characteristics can be measured by rearranging the slabs or/and by inserting a probe into the different slots. For obtaining a better depth resolution, 0.15 cm and 0.2 cm thick perspex plates were cut. By adding or removing the plates to/from the front plane of the phantom, a measurement can be performed with a step of 0.1 cm.

3.5.2. Micrometer jig and phantom for planar microbeam measurements

A measurement of dose distribution with a MOSFET detector has to be performed at a set of points in the region of interest. A high resolution measurement of a radiation dose distribution across a planar microbeam requires a positioning device capable of moving a detector with a micron accuracy. For making a jig, the chassis of a travelling microscope was modified and used. The device had a micrometer screw with 2 micron resolution. A brass holder was made, attached to the chassis and leveled with high precision (Figure 3-12). A 12 to 25 mm diameter rod can be inserted and secured in the holder. A detector can be attached to the end of the rod.

A 7.5 cm × 7.5 cm × 2.5 cm plate, and a 2.5 cm in diameter and 17.5 cm long rod were cut from a single block of perspex. The rod was attached to the jig and a perspex phantom was built on the base plate by adding 7.5 cm × 7.5 cm perspex plates of various thicknesses as per Figure 3-6. A MOSFET detector could be inserted in a machined slot between two plates. The air gaps around the dectector were filled with wax. Film detectors could be sandwiched between the plates. The palates were secured in the position by two nylon screws.

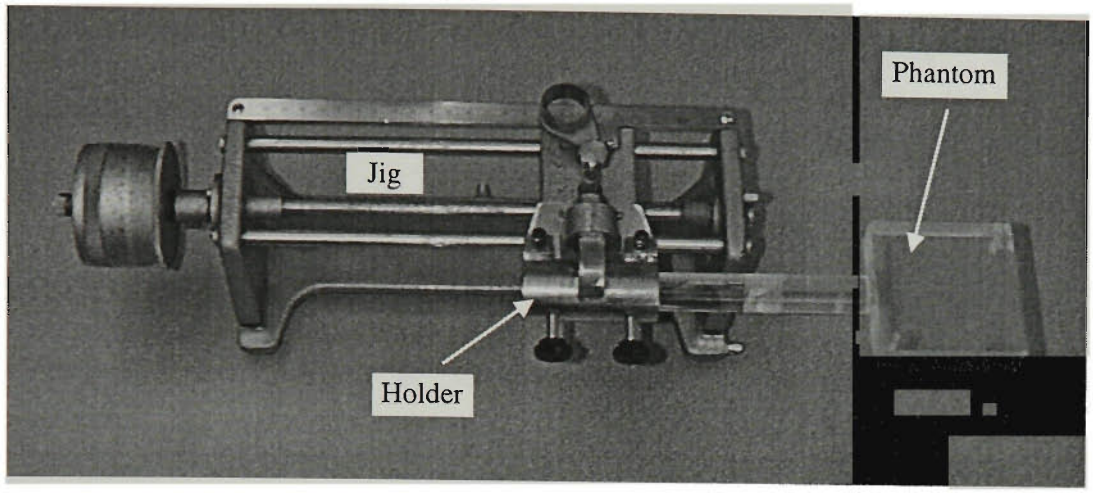

Figure 3-12. Micrometer jig with the attached phantom base plate.

3.6. Boron-10 coating of the radiation detectors

Therapeutic effect in BNCT depends on high LET doses delivered to the tumour by alpha and ^{7}Li particles released in ^{10}B decay. Boron-10 neutron capture cross-section depends on neutron energy and measurement of the thermal neutron flux will require further calculations to establish the boron dose enhancement. For measurements of boron response in BNCT and FNT, the MOSFETs and the silicon ion implanted detectors were covered by a layer of boron containing plastic. Because the majority of the measurements were performed in a perspex phantom, a perspex based coating was made. Perspex (polymethyl-methyacrylate) is a chemically resistant material but it dissolves in dichloroethane. Decaborane ($B_{10}H_{14}$) was chosen for the boron compound because it also dissolves in dichloroethane. The compound contains a naturally occurring boron which is a mix of 20 at. % of ^{10}B and 80 at. % of ^{11}B.

For preparation of a 1% weight ^{10}B perspex cover, the following calculation was performed:

Let us add m grams of $B_{10}H_{14}$ to perspex to have 1% concentration of ^{10}B in the converter. If M grams of perspex are taken then the total weight of perspex and decaborane is $M + m$ grams. One mole of $B_{10}H_{14}$ has a weight of 122 g. Because the compound contains naturally occurring boron, the weight of the boron-10 in one mole of decaborane equals 20 grams. In m grams of decaborane there is $20 \times m/122$ gram of ^{10}B. To find m, one has to solve an equation

$$0.01 = \frac{\frac{10}{61} \times m}{M + m}$$

For preparation of the boron converter, 10.000±0.005 g of perspex were dissolved in 300±0.1 ml of dichloroethane to which 0.625±0.005 g of decaborane were added.

The solution was deposited drop by drop on the surface of a MOSFET chip or a silicon detector. After deposition of each drop, a detector was left to dry for about half an hour and then the next drop was deposited. In total 6 coats were deposited. The requirement for the boron converter is for it to be thicker than the range of alpha particles and ^{7}Li ions produced in the $^{10}B(n,\alpha)^{7}Li$ reaction.

single coat of the boron containing perspex, the alpha particles peak shifted to the lower energy part of the spectrum and became a superposition of two broad maxima (Figure 3-13). Two maxima at an energy of about 2.8 MeV and 4 MeV were due to non-uniform coating. These energy loses of 5 MeV alpha particles correspond to the thickness of perspex layer of 16 μm and 8 μm, as calculated by TRIM software. After application of the second coat, no pulses were observed in the spectrum. Six coats were applied on every radiation detector dedicated to a boron response measurement. The thickness of the cover on a detector was estimated as between 50 μm to 100 μm.

Table 3-2. Change of MOSFET threshold voltage after deposition of several layers of ^{10}B enriched plastic

Number of coats	none	1	7
V_{th} (V)	7.637	7.637	7.637

Perspex is a good electrical isolator. Applying the boron-10 enriched coats on the surface and on the aluminium contacts of the silicon chip does not change the value of the MOSFET threshold voltage (Table 3-2).

For neutron therapy boron response measurement, a method of paired MOSFETs was applied. Both MOSFETs had their lids removed. One of the detectors was covered by perspex, containing 1% of ^{10}B while the other detector was a bare MOSFET (Figure 3-14).

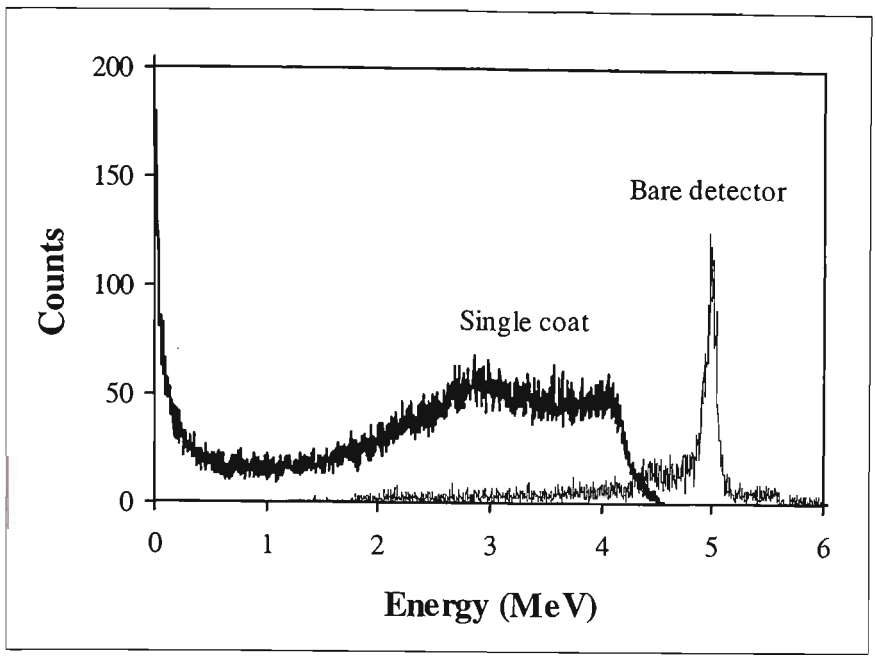

Figure 3-13. ^{210}Po alpha particles pulse height spectra recorded by a bare 3×3 mm^2 silicon detector and after deposition of a single coat of boron contained perspex.

In order to check the thickness and quality of the boron coating, we used a 3 x 3 mm^2 ion implanted silicon detector and a ^{210}Po alpha radiation source. A spectrum of ^{210}Po alpha particles was measured before and after the deposition of each layer of boron converter. The pulse height spectra were measured in air by connecting the probe to Canberra 7401 alpha spectrometer. A spectrum of ^{210}Po alpha particles, measured by a bare detector, has a narrow peak at an energy of approximately 5 MeV (Figure 3-13). The detector was mounted at the end of 0.9 m long shielded cable and it was placed on the laboratory bench outside the spectrometer chamber. A ^{210}Po source was placed on top of the detector. The air gap between the source and the detector was 1-2 mm. The higher than normal spectral noise in Figure 3-13 was caused by the 0.9 m cable. After deposition of a

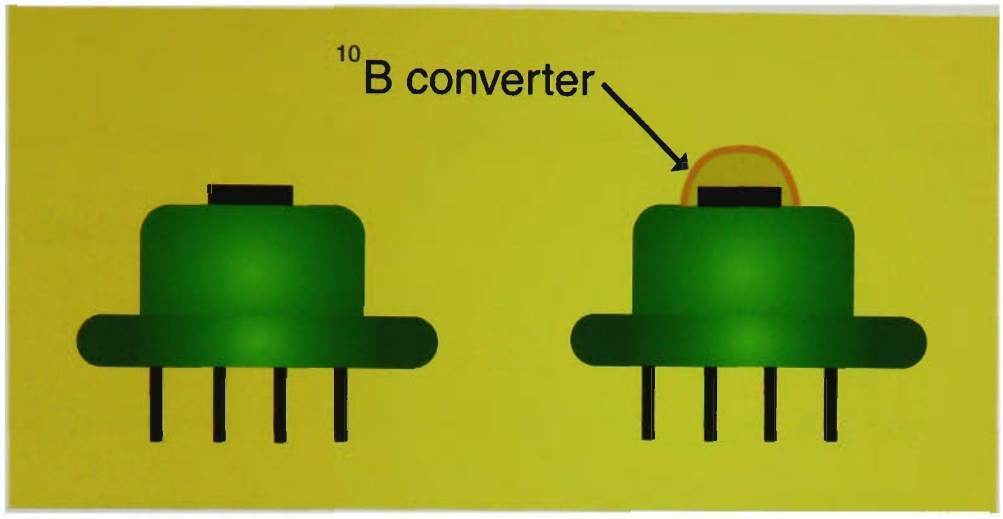

Figure 3-14. Paired MOSFET detectors. A bare MOSFET is on the left, the other MOSFET is covered by boron-10 containing perspex.

Chapter 4. Investigation of physical properties of the MOSFET dosimeter

MOSFET current-voltage characteristics and threshold voltage are temperature dependent (see discussion in Chapter 1.3). Clarification of this matter is important because the temperature of the MOSFET detector may change during measurement and readout, in medical applications of MOSFET, due to either thermal conductivity from the patient's body, or a temperature change in the treatment room. Choosing the threshold voltage readout current at its thermal-stable value may significantly reduce temperature drift of the MOSFET threshold voltage (Buehler *et al.*, 1993). An investigation of dependence of the MOSFET detector response on x-ray energy and on accumulated dose is equally important, as both these parameters may vary in the process of dose measurement. Response of the MOSFET detector may also depend on its housing material and in particular on the lid material. All these parameters need investigation prior to applying the detector to dosimetry at clinical facilities.

4.1. Aim

The aims of this research of the physical properties of the MOSFET detector were

⇒ To establish the temperature dependence of n-channel MOSFET current-voltage characteristics and determine the value of the thermal-stable current

⇒ To measure the x-ray energy dependence of MOSFET response and the significance of MOSFET dose enhancement

⇒ To evaluate the angular dependence of MOSFET response in an x-ray beam

⇒ To demonstrate the application of MOSFET detectors in high dose gradient regions

⇒ To evaluate the dependence of n-channel MOSFET detector response on accumulated dose

4.2. Temperature dependence of the MOSFET current-voltage characteristic: Thermal-stable current

It is well established that accumulated radiation dose produces a shift in the current-voltage characteristic of a MOSFET, with the change in threshold voltage being proportional to the absorbed radiation dose (see Chapter 1.2). It is also known that temperature change induces a similar effect on the MOSFET current-voltage characteristic. The current-voltage characteristic is measured as the MOSFET drain-source current versus drain-source voltage, the gate being kept at the same potential as the drain.

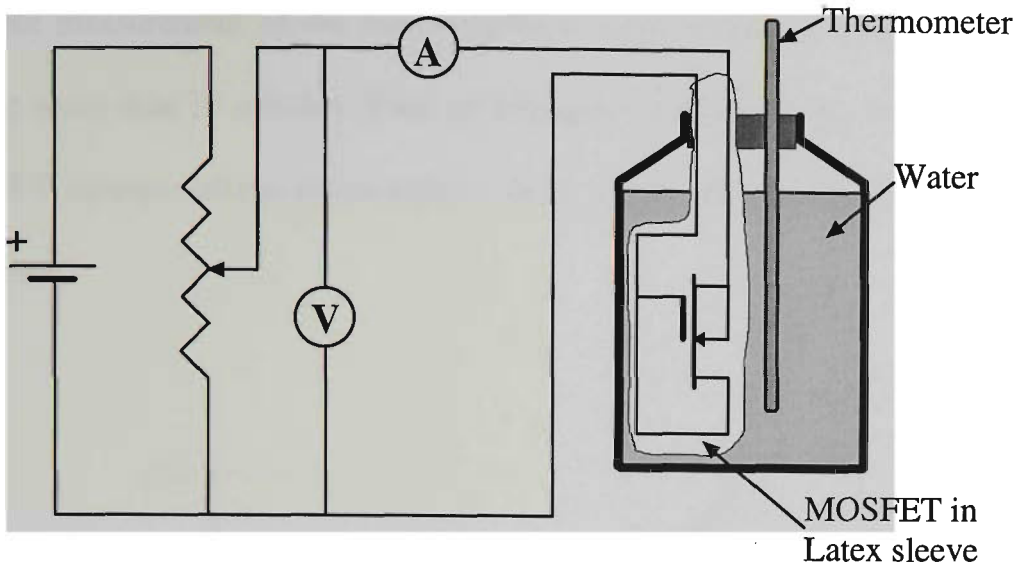

Figure 4-1. Schematic diagram of MOSFET temperature dependent current-voltage measurement.

To investigate the current-voltage characteristics of the MOSFET detector a circuit presented in Figure 4-1 was assembled. For current and voltage measurements two Keithley 177 digital multimeters were ued. The multimeters and power supply were kept on the laboratory bench at room temperature. A MOSFET was waterproofed and immersed in a vacuum flask filled with water to achieve a controlled temperature environment. The MOSFET and the connection wires were sealed in a long, thin Latex sleeve (see Figure 4-1). The sleeve was inserted into a water filled vacuum flask through an access hole in the lid. To monitor the temperature, a thermometer was inserted through another access hole. Measurements were performed in the temperature range 10°C to 40°C. The temperature interval was chosen for its relevance to patient and phantom dosimetry at radiation therapy facilities. In this temperature interval the rate of temperature change of the water in the flask was about 1-2°C per hour. A

complete measurement of the current-voltage characteristic at each temperature took no more than 10 minutes. Such an arrangement allowed measurement of the MOSFET current-voltage characteristic under stable and controlled temperature conditions.

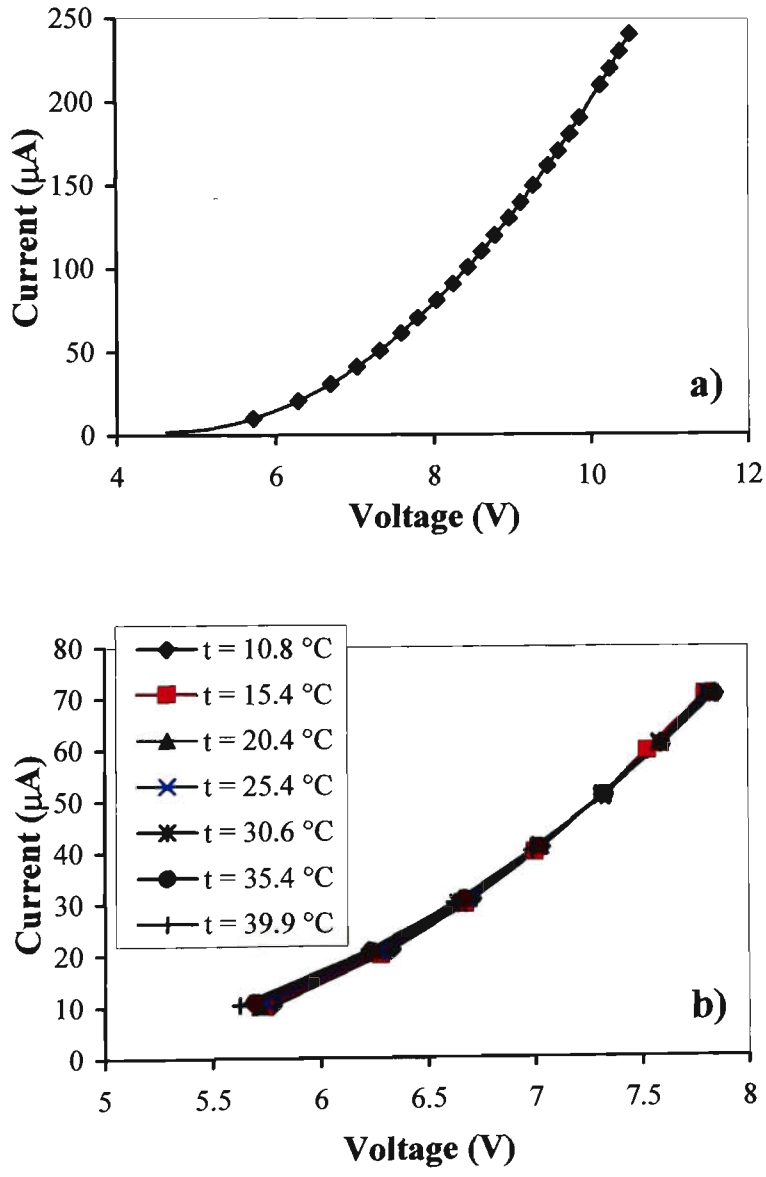

Figure 4-2. Current voltage characteristics of an n-channel MOSFET; a) - complete characteristics for a temperature of 20.4°C; b) region of intersection of current-voltage characteristics in the temperature range of 10°C to 40°C.

The temperature-dependent current-voltage characteristic measurements were performed with an n-channel MOSFET (for description see Chapter 3.1.1).

The current voltage characteristic of an n-channel MOSFET at 20.4°C is plotted in Figure 4-2a. It is a typical source-drain characteristic of a MOSFET (compare Figure 1-3a). The other characteristics measured at 10.8°C, 15.4°C, 25.4°C, 30.6°C 35.4°C and 39.9°C were very similar in shape. It was observed that all the curves intersect in a narrow current-voltage interval. A close up of the intersection region of all seven curves is shown in Figure 4-2b. The curves intersect at a current value of between 40 μA to 50 μA.

Threshold voltage temperature coefficients were calculated for currents of 20 μA, 40 μA, 50 μA and 100 μA. The temperature coefficients were calculated as change of threshold voltage, measured under constant current, with temperature. The threshold voltage change was plotted versus temperature and the experimental points were fitted by linear functions. The gradients of the slope of the lines at 20 μA and 40 μA are negative (see Figure 4-3). The gradient changes to positive for currents of 50 μA and 100 μA. The gradient increases with increase in current. This plot confirmed that a thermal-stable current for this particular design of MOSFET exists and its value lies between 40 μA and 50μA.

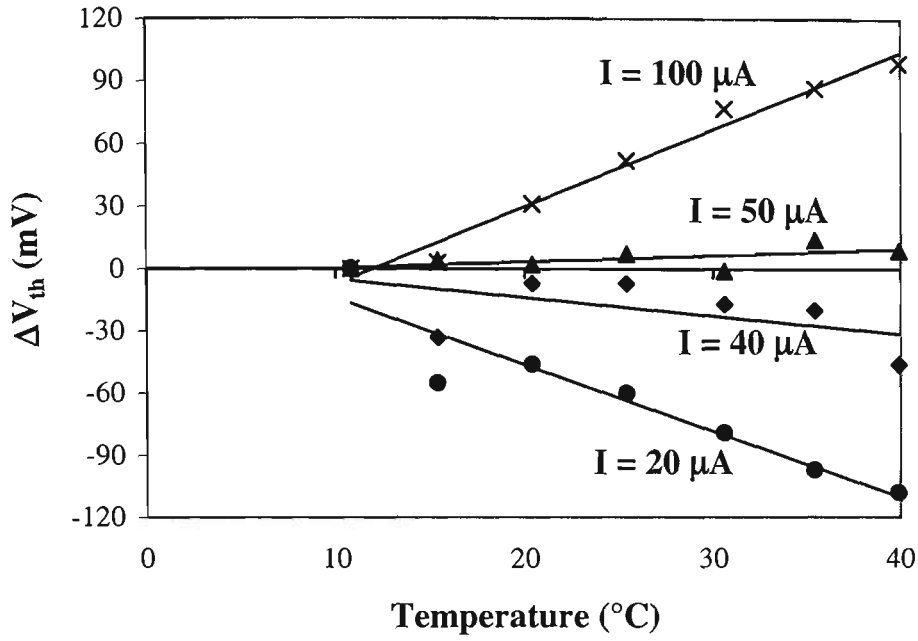

Figure 4-3. MOSFET threshold voltage change with temperature for source to drain current of 20 μA, 40 μA, 50 μA and 100 μA.

4.3. Energy and package material dependence of a MOSFET response to x-ray radiation

The material of MOSFET housing is an important factor in dose enhancement. A study by (Brucker *et al.*, 1995) demonstrated that MOSFET housing material significantly affects dose enhancement for x-ray energies from 14 to 250 kV.

Experiments were designed to investigate the energy and package material dependence of the response of a MOSFET dosimeter.

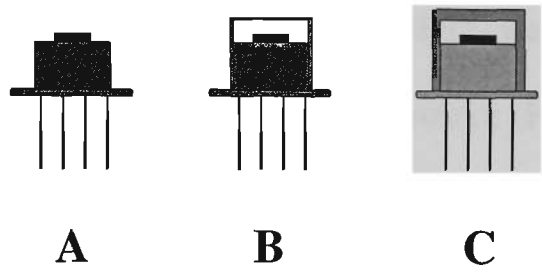

Figure 4-4. Three MOSFET packages used in energy dependence measurements; A – a bare MOSFET with removed lid, B - a MOSFET in its original TO-18 packaging with Kovar lid, and C – the Kovar lid was replaced by a plastic cap.

The energy dependence of a p-channel MOSFET was compared with the energy dependence of a semiconductor diode and LiF TLD by (Edwards *et al.*, 1997). No detailed information was given by the authors on the MOSFET housing material. The MOSFET dose enhancement peaked at a mean x-ray energy of between 30 to 40 kV.

As it was indicated in many studies, the MOSFET response is energy independent, under electron equilibrium conditions for x-ray or electron beam energies exceeding 250 kV (Gladstone *et al.*, 1994a; Kron *et al.*, 1998).

The dose enhancement of MOSFET radiation dose measurement at a low x-ray energy can be affected by the housing material. The n-channel MOSFET, in three different housings, was prepared for x-ray irradiation (Figure 4-4). The n-channel MOSFET was supplied by Detector Ltd in TO-18 Kovar housing. The housing contains nickel, cobalt and iron. The base of the Kovar lid was cut with a fine file

and was removed for some of the measurements (Figure 4-4a). The Kovar lid thickness is approximately 0.2 mm. This MOSFET was used with the cap removed and with the cap replaced to cover the detector (Figure 4-4b). For other measurements the Kovar cap was replaced with 1 mm thick plastic cap (Figure 4-4c). Thus the same MOSFET was irradiated in three different housings, so as to investigate the dose enhancement dependence on the housing material.

The MOSFETs were irradiated in an x-ray beam of the Therapax DXT300 orthovoltage x-ray machine (see page 56 for the x-ray machine description) at potentials of 50 kV_p, 75 kV_p, 100 kV_p, 125 kV_p, 150 kV_p, 200 kV_p and 250 kV_p. The corresponding mean x-ray energy is about $\frac{1}{3}$ of the accelerating potential. They were determined by a half value layer of cooper method. For each energy, the MOSFET was irradiated with the original Kovar cap, without the cap (bare) and with a plastic cap at the same gate voltage of 5.4 V. Threshold voltage was read about 20 seconds after each irradiation. The MOSFET was mounted on top of 25 cm long vertical perspex rod with 6 mm diameter. Thus the conditions of the experiment were close to free air irradiation.

In Figure 4-5 the sensitivity, in mV, of MOSFET threshold voltage change per cGy is plotted versus x-ray beam energy. The uncertainty in MOSFET sensitivity values is mostly due to the uncertainty of the delivered dose. The MOSFET was irradiated at low doses of 4 to 12 monitoring units, depending on x-ray energy, or at about 10 cGy. The dose monitoring was in whole monitoring units which make

dose delivery uncertainty as high as 15-20% for the lowest monitoring unit irradiation.

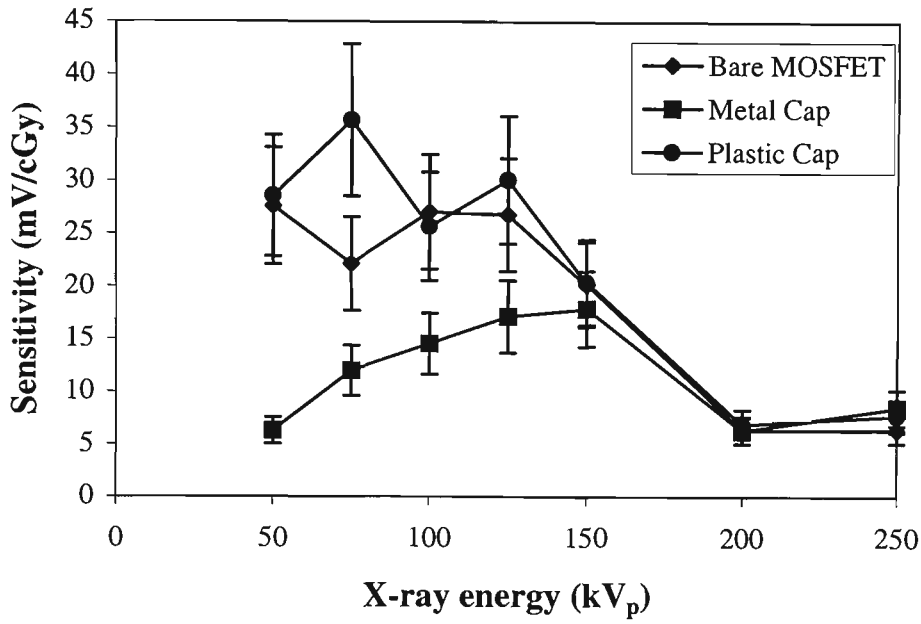

Figure 4-5. Sensitivity of an n-channel MOSFET detector as a function of x-ray energy for a bare detector, or a detector packaged in a metal or plastic cap.

The sensitivity of the MOSFET in all three housings rises initially as the x-ray energy increases from 50 kV_p. The sensitivity reaches a maximum at 75 kV_p for the plastic cap MOSFET, at about 100 kV_p for the bare MOSFET and at 150 kV_p for the metal cap MOSFET. The x-ray peak energy of 100 kV_p corresponds to the effective energy of 39 keV as determined by the half value layer method. The sensitivity of the bare and the plastic cap MOSFETs closely follow each other except for a single measurement at an x-ray energy of 75 kV_p. The sensitivity of the MOSFET in a Kovar cap was the lowest for low x-ray energy. This lower sensitivity can be explained by attenuation of low energy x-rays by the metal cap.

Penetration of x-rays of higher energy is greater and, together with production of secondary electrons, it is responsible for the increase in MOSFET response. The response of the detector in all three housings was the same for x-ray energy of 200 kV_p. As the energy increases, the MOSFET lid (metal or plastic) provides dose build-up material. A higher orthovoltage x-ray energy was not available for measurements. The next higher available energy was a megavoltage x-ray beam of a linac.

The x-ray energy response of a bare n-channel MOSFET and a MOSFET covered by a thin polystyrene layer, was investigated in the x-ray energy range of 10 keV to 72 keV. The irradiations were performed at a facility in Japan and the data were taken by Dr. Tomas Kron on his trip to the facility. The MOSFET probes were prepared for the irradiation by the author. MOSFETs were irradiated in an energy range of 10 keV to 26 keV in a mono-energetic synchrotron radiation beam and by a Siemens Stabilipan II orthovoltage x-ray machine for higher x-ray energies (Kron *et al.*, 1998). Synchrotron irradiations were conducted at BL14C experimental beam station at the National Laboratory for High Energy Physics in Tsukuba, Japan. The mono-energetic x-ray beam was produced from the wide spectrum beam by diffraction of a <111> plane of a silicon crystal-monochromator. The full width at half maximum of the diffracted beam was approximately 1%. Each diffraction angle corresponds to a certain energy of the beam. Both MOSFETs were irradiated in 10 keV, 15 keV, 20 keV and 26 keV beams.

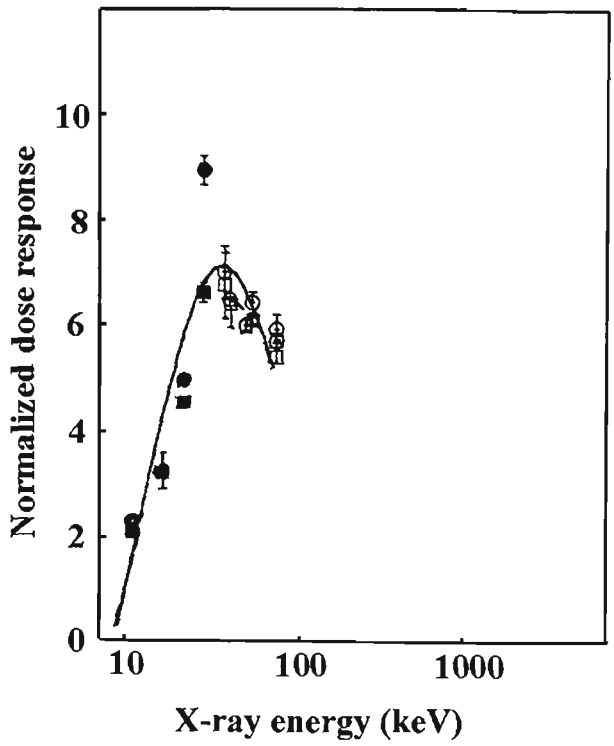

Figure 4-6. MOSFET sensitivity normalized to a 6 MV_p linac x-ray beam. Circles – a MOSFET with a thin polystyrene layer; squares – a bare MOSFET. Open symbols – x-ray machine irradiation with effective energy as per abscissa axis; closed symbols – monoenergetic synchrotron irradiation.

The MOSFET sensitivity was normalized to the sensitivity of a 6 MV_p x-ray beam produced by a medical linac. The sensitivity was plotted vs x-ray energy for synchrotron radiation and vs effective energy for orthovoltage x-ray machine beam. The maximum dose enhancement for both MOSFETs was observed for an x-ray energy range of 34 keV to 36 keV (see Figure 4-6). The enhancement was about 7 fold compare to the MOSFET response to a 6 MV linac beam. The energy of the peak enhancement and the enhancement ratio measured by combined synchrotron and orthovoltage irradiation are in good agreement with data obtained previously using an orthovoltage x-ray beam alone.

The measurements of dose enhancement dependence on MOSFET housing were also performed in a 6 MV beam of linac Varian 2100C (see page 56 for the beam description). The beam field was 10 cm × 10 cm. The measurements were performed in a 30 cm × 30 cm solid water phantom. The response of the MOSFET at the depth of the maximum dose of 1.5 cm and deeper was independent of housing. In the build-up region near the surface of the phantom, the MOSFET in the original TO-18 housing overestimated the dose by nearly 4 fold. This dose enhancement was due to secondary electrons produced in the metal lid. The thickness of the metal lid added up to dose build up (Rosenfeld *et al.*, 1995).

4.4. Phantom depth and angular dependence of MOSFET measurements

The knowledge of a surface dose is often required in medical oncology. Radiation treatment in a megavoltage x-ray beam is optimized to deliver a lethal dose to a target volume which is situated under the surface or sited deeper. An excessive skin dose may cause radiation burning and other undesirable skin reactions. The entrance dose for 6 MV_p x-rays in a solid water phantom is low then it increases steeply and reaches its maximum at a depth of 1.5 cm. The interface between the tissue and the air cavity, or simply between two tissues of different density, is another important application of surface dose measurement.

The MOSFET detector may be useful in high gradient x-ray radiation fields near the surface of a phantom because of its very thin sensitive volume. The thin

sensitive volume should also reduce the angular dependence of the MOSFET response when measurements are performed on a phantom surface or on the patient's skin.

The experimental data in a megavoltage x-ray beam of a medical linac, described in this section, were collected by Martin Carolan, with some contribution by the author, and were published by the Radiation Medical Physics Group, with the author as a co-author, and with an external collaborator, i.e. by A. Rosenfeld, M. Carolan, G. Kaplan, B. Allen and V. Khivrich (Rosenfeld *et al.*, 1995). The experimental orthovoltage x-ray measurements, as well as discussion of radiation detector angular dependence, are entirely my own. The medical linac measurements were performed in a 6 MV_p beam of a Clinac Varian 2100C linac (see page 56 for the linac description) in a 10 cm × 10 cm field in or on the surface of a 30 cm × 30 cm solid water phantom. The MOSFET data were compared with the Attix RMI 449 ionisation chamber measurements. The Attix chamber has a very thin entrance window of 2.5 μm and it is widely used as a reference surface dose dosimeter (Cross, 1992). The MOSFET detector mapped the build up region with a step of 1 mm. The MOSFET data were in good agreement with Attix ionisation chamber data (Figure 4-7a).

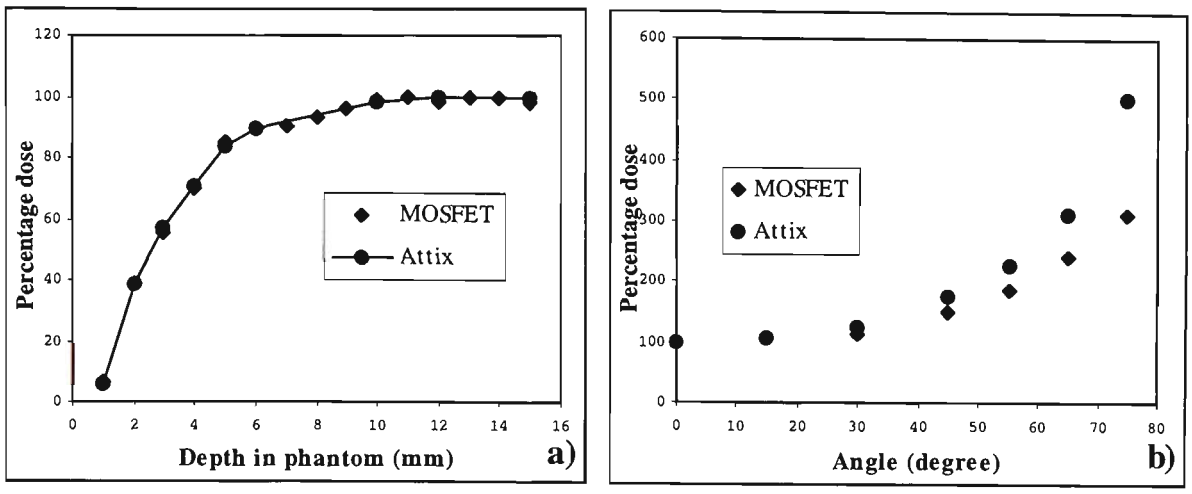

Figure 4-7. MOSFET and Attix ionisation chamber measurements in a 6 MV_p x-ray beam, 10 cm × 10 cm field. a) dose profile in build up region in a solid water phantom; b) angular dependence.

The angular dependence of the MOSFET was compared with that of the Attix chamber in a 6 MV_p x-ray beam. The measurements were performed on the surface of a solid water phantom. The beam was rotated around a detector, keeping the source-detector distance constant. It appears that the Attix chamber overestimated the dose more than the MOSFET with increase in incident angle (see Figure 4-7b), however the effective point of measurement affects actual dose build up in a condition of electron non-equilibrium and as such it has its effect on a detector angular dependence. The dose enhancement with incident angle in a high energy beam is related to the fact that more secondary electrons are entering the detector volume. The effective energy of the 6 MV_p x-ray beam is about 2 MeV. For the photons of this beam, most of the beam energy is transferred by Compton interaction. In a Compton collision, the incident photon energy is transferred to a recoil electron and to the scattered photon. The energy transfer to

the electron and the cross-section of the Compton process are angular dependent. If θ is the angle between the incident photon of energy $h\nu$ and the scattered photon, then the energy, E, transferred to the recoil electron is (Johns & Cunningham, 1983)

$$E = h\nu \cdot \frac{\alpha(1-\cos\theta)}{1+\alpha(1-\cos\theta)}$$

where α is the ratio of photon energy to the rest energy of the electron, i.e. $\alpha = \frac{h\nu}{m_0 c^2}$, m_0 is mass of the electron and c is the speed of light. The electron energy is maximum when a photon is scattered straight back. It happens if the photon makes a direct hit on the electron and the recoil electron continues in the direction of the incident photon.

The cross-section of a Compton collision per unit solid angle, $\frac{d\sigma}{d\Omega}$, was derived from the Klein and Nishina theory (Johns & Cunningham, 1983)

$$\frac{d\sigma}{d\Omega} = \frac{r_0^2}{2}(1+\cos^2\theta)\cdot F_{KN}$$

where r_0 is the classical radius of the electron and the factor F_{KN} depends on the scattering angle

$$F_{KN} = \left\{\frac{1}{1+\alpha(1-\cos\theta}\right\}^2 \left\{1+\frac{\alpha^2(1-\cos\theta)^2}{[1+\alpha(1-\cos\theta)](1+\cos^2\theta)}\right\}$$

Due to the conservation of linear momentum, an electron in the Compton process is never recoiled back. The highest probability of recoil is around the direction of the photon beam.

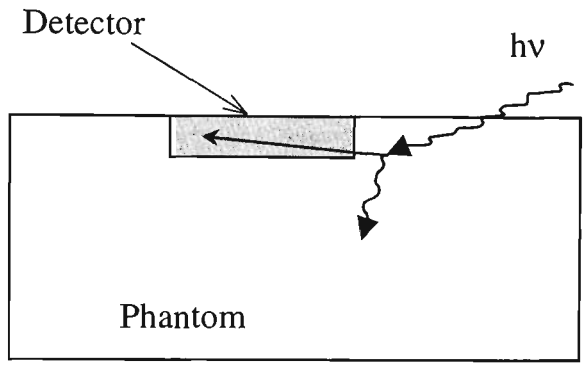

Figure 4-8. Diagram of Compton scattering of a photon entering the phantom at low incident angle. The recoil Compton electron enters the detector volume.

If a photon enters a phantom or any other scattering material at a low incident angle, the probability for the recoil electron to enter the detector volume is significantly higher than for the normal incidence of the photon beam (Figure 4-8). The physical dimensions of the Attix ionising chamber are significantly bigger than the sensitive volume of the MOSFET detector. Because of this, more electrons will enter the chamber volume and produce ionisation, than for the MOSFET detector. An important factor is the build up of the dose with depth (Figure 4-7a). Surface measurements in a high energy x-ray beam are performed in the absence of electron equilibrium. In non-equilibrium conditions, more delta

electrons are produced as photons travel extra parts of a millimeter in a phantom from the surface. For this reason the dose enhancement should be higher for the Attix ionising chamber, than for the MOSFET detector. The experiment confirmed this (Figure 4-7b).

A significance of secondary electrons in the angular response of a detector can be indirectly supported from the experiments of Tallon *et al.* (Tallon *et al.*, 1987). They measured a change in MOSFET threshold voltage, after irradiation at different angles, to ^{60}Co x-rays and to 5 MeV and 10 MeV electrons. The measurements were performed in a vacuum. The angular effect of the MOSFET response to electron radiation was below detection capability, while a significant effect was observed for ^{60}Co x-rays.

Photoeffect is the most important energy transfer process for low energy photons. The spatial distribution of photoelectrons for non-crystalline or polycrystalline media is nearly isotropic. For this reason, the angular dependence of detector response in a low energy x-ray beam is expected to be not so strong as in a megavoltage beam. This was confirmed in MOSFET measurements in a 100 kV_p x-ray beam. The measurements were performed at two incident angles: perpendicular and parallel to the surface (0° and 90°). The dose enhancement was only about 25% and is significantly lower than for 6 MV x-rays. The effective energy of 100 kV_p is 39 keV. For such photons about 20% of energy is transferred in water by the Compton process and 80% by photoeffect (Johns & Cunningham, 1983). This observation, together with measurements by Tallon *et al.* (Tallon *et*

al., 1987), confirms the validity of the suggested mechanism of angular dependence of dose enhancement.

4.5. Dependence of MOSFET sensitivity on total accumulated dose

Part of the charge produced in silicon dioxide by ionising radiation is trapped in the SiO_2/Si interface. The trapped charge causes a change in the MOSFET threshold voltage. Density of the trapped charge can be calculated by using Equation 1-1 (page 8). A trapped charge density of about 10^8 cm^{-2} causes a threshold voltage change of 1 volt. This density is relatively small compared to the total density of traps in silicon dioxide of 10^{12} to 10^{15} cm^{-2}. The vacant trap density depends on the technological process of growing and annealing of the silicon dioxide. The positive charge trapped in the Si/SiO_2 interface reduces the electric field in silicon oxide during MOSFET irradiation. The electric field is set up by applying a positive bias voltage to the gate electrode of the MOSFET. A decrease in the silicon oxide electric field makes initial charge separation and hole diffusion to the interface less efficient (see Chapter 1.2). When some traps are filled it changes the electric field in the silicon dioxide and also makes less vacant traps available, thus reducing the efficiency of further charge trapping and therefore reducing the fractional yield. As a result, the MOSFET sensitivity to radiation is also reduced. One can expect the change of MOSFET sensitivity with accumulated dose to be linear because the relative density of trapped charge is low.

To confirm the linear dependence and to measure the change in the MOSFET sensitivity with accumulated radiation dose, an n-channel MOSFET was irradiated under a 5 V gate bias in a 200 kV_p beam of an orthovoltage x-ray machine (for the description see page 56). The beam current was 13 mA. A dose of 20 MU was delivered during each radiation of 0.32 minutes in duration. In total 61 irradiations were performed. The initial threshold voltage of the MOSFET detector was 6.581 V. The threshold voltage was measured immediately after each irradiation. The threshold voltage after the final irradiation was –4.995 V. Thus the total change in threshold voltage was 11.586 V.

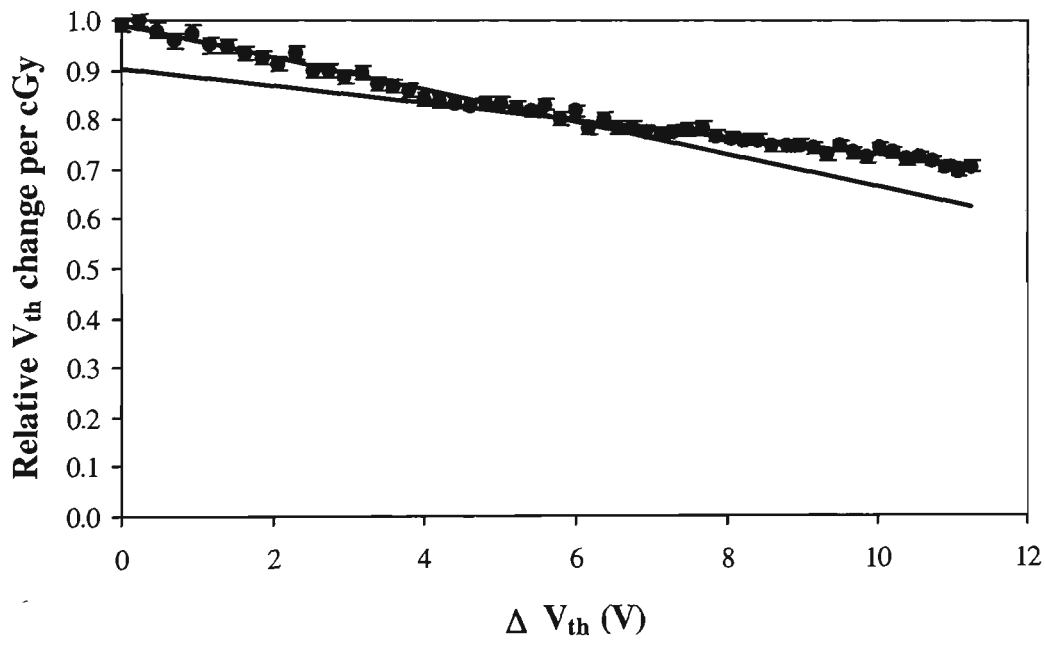

Figure 4-9. An n-MOSFET threshold voltage change per cGy of x-ray radiation versus the total threshold voltage change. Solid circles with error bars – experiment, solid lines – fitting of experimental data.

It was noted that sensitivity of the MOSFET detector decreased with accumulated dose. Maximum sensitivity was displayed by a "fresh" MOSFET. The relative

change of MOSFET sensitivity per unit dose was plotted versus the total change of threshold voltage (Figure 4-9). For reasons discussed above, a change of interface trapped charge density with dose depends exponentially on accumulated dose, D, or on the threshold voltage

$$\frac{dVth}{dD} \propto \exp(-\beta D)$$

The experimental points in Figure 4-9 were fitted by exponential function. The fitting parameter, β, was equal to –0.03 and the R^2 value was 0.98. It is also convenient for practical reasons to fit the experimental data using a linear function. A linear fit estimates percentage reduction in dose response and allows comparison with published data. The data in Figure 4-9 can be best fitted by two linear functions with slightly different gradients. The straight lines intersect at the point when the MOSFET threshold voltage turns zero. The change of MOSFET sensitivity for 1 volt of threshold voltage change in the positive threshold voltage range is 3.2%. In the negative threshold voltage range the sensitivity change is 1.7%. The average change of MOSFET sensitivity over the whole interval of threshold voltage is 2.5 %. The data were obtained for a 5 V gate bias. The sensitivity change should be different for a different bias, because the bias changes the electric field in the silicon oxide.

The response of a MOSFET detector of the same batch was measured in the 4 MV_p beam of Varian Clinac 600C, linear accelerator (Kron *et al.*, 1998). The MOSFET probes were prepared for the measurements by the author. The effective

energy of the beam was 1.3 MeV. The measurements were performed at the depth of the maximum dose in a solid water phantom. The measurements were performed over positive and negative threshold voltage ranges. The MOSFET sensitivity decreased with accumulated dose (Figure 4-10). The graph is very similar to Figure 4-9. In linear approximation, the change of MOSFET response was about 3% per 1 volt of threshold voltage change. This value is very similar to the one obtained for kilovoltage x-rays. The similarity of the results for two different x-ray energies proves that change in the MOSFET sensitivity with decrease in threshold voltage is caused by accumulation of charge in the interface traps, and there is no dependence on energy of incident x-rays. Similarly, the sensitivity change should be independent of the type of the radiation, as long as it causes the same trapped charge to be accumulated in Si/SiO_2 interface leading to the same threshold voltage.

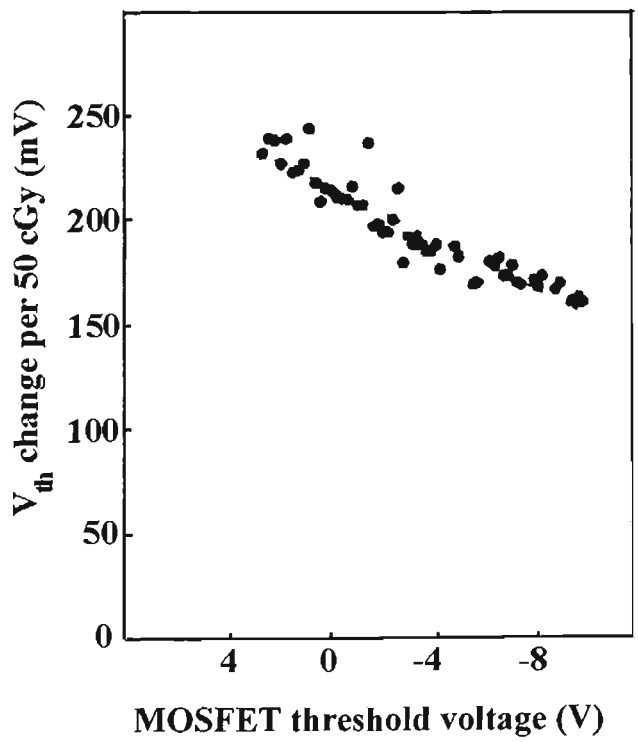

Figure 4-10. Change in n-MOSFET response. Irradiation in a 4 MV_p x-ray beam.

The MOSFET sensitivity change has to be taken into account when a measurement is performed over an extended range of threshold voltage change. The correction can be entered automatically by a microprocessor based MOSFET reader or by dose plotting software.

4.6. Conclusions

A range of physical properties and applications of the MOSFET detector were investigated. Current-voltage characteristics of an n-channel MOSFET source to drain current were measured for a temperature range from 10°C to 40°C. All the current voltage characteristics passed in close vicinity of the same point in a I-V plot. The thermal-stable current was in the range of 42 μA to 45 μA.

X-ray energy and packaging material dependence of the MOSFET response was investigated for a MOSFET in 3 different packagings. The MOSFET was irradiated in original n-channel MOSFET Kovar TO-18 packaging, in TO-18 packaging with the Kovar lid removed and with the Kovar lid replaced by a plastic cap. The MOSFET, with its lid removed, had the maximum dose enhancement in a 35 keV x-ray beam. The maximum enhancement for a MOSFET with a lid was observed at slightly higher energies. For measurements taken under conditions of electron equilibrium, the MOSFET, in all the housings, performed identically in the incident x-ray beam of energies above 250 kV_p. No dose enhancement was observed for the same range of energies above 250 kV_p.

The MOSFET was found to be a good dosimeter for applications in high energy x-rays in a region of high dose gradient, such as surface and interface. The angular dependence of the MOSFET response was found to be less significant than for an Attix ionisation chamber. The reduced angular dependence can be explained by the thinner sensitive volume of a MOSFET detector. Therefore, it can be expected that a MOSFET detector will measure the actual surface dose in an oblique incident x-ray beam more accurately.

The sensitivity of a MOSFET detector reduces with accumulated dose or with accumulated change in the MOSFET threshold voltage. The reduction in sensitivity is caused by an accumulation of trapped holes in the SiO_2/Si interface. The electric field of positively charged holes reduces the external electric field in silicon oxide. The reduction in the electric field causes a less efficient separation of electron-hole pairs in the oxide and a reduction in the fractional yield. The sensitivity of a MOSFET detector was reduced by about 2.5% for each 1 V change of threshold voltage. The change in MOSFET sensitivity was taken into account in analysis of further experiments.

Chapter 5. The MOSFET as a dual alpha-gamma detector and as a microdosimeter

The applications of a MOSFET detector for gamma dosimetry were introduced by Andrew Holmes-Siedle some 25 years ago (Holmes-Siedle, 1974a). Soon after, it was suggested to use MOSFETs for electron and neutron dosimetry (see Chapter 6.2). MOSFET p-n junctions had also been used previously for the collection of charge produced by ionising radiation, especially in the investigation of the single event upset phenomena in microelectronics (Knudson *et al.*, 1984; McNulty *et al.*, 1991; Sexton *et al.*, 1993), as MOSFET transistors are an integral part of a CMOS circuit. However, to the best of my knowledge, the use of the MOSFET detector for alpha dosimetry and the application of the MOSFET as a dual detector and as a microdosimeter was pioneered by our work at the Centre of Medical Radiation Physics at the University of Wollongong (Rosenfeld *et al.*, 1996). The separate measurements of high and low LET components of radiation dose are important for treatment planning and quality assurance in neutron therapy. In particular it is important to separate alpha and gamma contributions to radiation dose in boron neutron capture therapy.

5.1. Aim

The aims of this research into new applications for the MOSFET detector in alpha dosimetry and dual dosimetry were:

⇒ To prove essential sensitivity of the MOSFET dosimeter to alpha radiation.

⇒ To establish that the MOSFET threshold voltage changes linearly with alpha particle fluence.

⇒ To demonstrate the possibility of using MOSFET p-n junctions as micro-silicon detectors and to show that they can be used simultaneously with threshold voltage measurement.

⇒ To show that threshold voltage change is proportional to alpha particle fluence when measured simultaneously by the same MOSFET micro silicon detector .

⇒ To establish geometry of the charge collection volume of the MOSFET drain-substrate p-n junction.

⇒ To test MOSFET simultaneous macro and micro dosimetry at neutron therapy facilities.

5.2. MOSFET threshold voltage sensitivity to alpha particle fluence

New radiation therapy modalities, such as Boron Neutron Capture Therapy and Alpha Immunotherapy, use alpha particles for targeted delivery of a lethal dose to tumour cells. An introduction of such modalities requires the development of clinical alpha dosimetry. Because the MOSFET has emerged as a potentially promising radiation dosimeter for radiation oncology applications (Butson *et al.*, 1996; Ramani *et al.*, 1997; Rosenfeld *et al.*, 1995; Soubra *et al.*, 1994), we decided to research into its use as an alpha dosimeter.

The main principle of MOSFET dosimetry is that the holes produced by ionized radiation in the silicon dioxide layer are trapped in the SiO_2/Si interface and change the electric field in the MOSFET channel. This principle should also be applicable in the case of accumulation of the interface charge due to alpha particle irradiation. The difference is that the density of ionisation around the path of an alpha particle is higher than for gamma radiation. Because of the higher density of electron-hole pairs, the recombination of the charge carriers is more efficient. The distribution of the alpha particle tracks for a low radiation dose may not be as uniform as for gamma radiation.

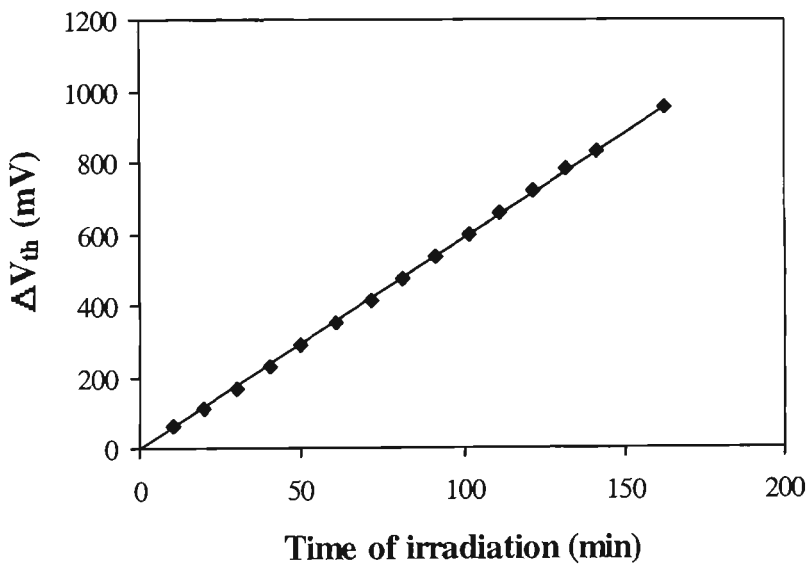

Figure 5-1. Change of the MOSFET threshold voltage versus alpha particle fluence. The MOSFET gate bias voltage was 18 V.

An experiment using an n-channel MOSFET and an ^{241}Am laboratory source was set up to test the MOSFET threshold voltage response to alpha particle irradiation. The source was a thick laboratory source with low activity of about 0.1 mCi. The

energy of americium-241 alpha particles is E_α = 5.48 MeV. The cap of a MOSFET in TO-18 housing was removed and the bare MOSFET chip was placed at a distance of 0.2 cm from the ^{241}Am source. The MOSFET gate bias voltage was set to 18 V. The MOSFET was repeatedly exposed to alpha irradiation for 10 minutes each time. The final irradiation lasted for 21 minutes. After each irradiation the threshold voltage was measured.

The accumulated change in the threshold voltage was plotted against accumulated time of irradiation (Figure 5-1). The total change in the threshold voltage was close to 1 V. Because the geometry of the experiment was kept constant for all measurements, the time of irradiation was directly proportional to alpha particle fluence. A linear function fitted the experimental data shown in the graph in Figure 5-1. It showed that the MOSFET threshold voltage change is proportional to the alpha particle fluence, therefore that the MOSFET can be used for alpha particle dosimetry.

In each act of alpha decay of ^{241}Am, a gamma ray with an energy of 60 keV is also released. The sensitivity of the MOSFET detector to gamma irradiation in this range of energy is relatively high (see Chapter 4). However, it was still expected that the observed change in threshold voltage would be mainly caused by alpha radiation. The reason for this was that an equal number of alpha particles and photons are released, but an alpha particle produces significantly more ionisations per micrometer of track length (higher $\frac{dE}{dx}$). Proof was still needed, however, that

the observed threshold voltage change was caused predominantly by alpha radiation.

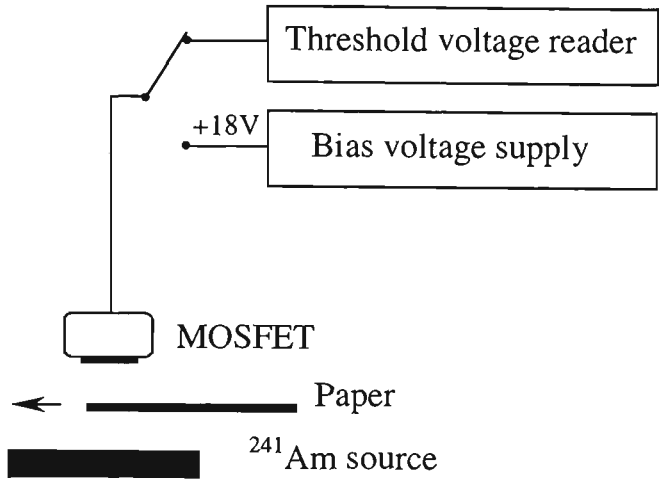

Figure 5-2. Diagram of experimental set up of alpha+gamma or pure gamma irradiation.

The range of 5.5 MeV alpha particle in paper does not exceed 50 μm. The alpha particle completely stops in a sheet of ordinary paper (thickness about 0.1 mm). This was checked by recording the alpha spectra by the Canberra ion implanted silicon detector in the Canberra 7401 alpha spectrometer. Measurements with a bare ^{241}Am source demonstrated a profound alpha peak, while there were no alpha counts for a paper-covered source.

An experiment was set up with a MOSFET detector placed above an ^{241}Am source. The MOSFET gate bias was set to 18 V. The MOSFET was exposed to alternate 10 minute cycles of irradiation by a bare and a paper covered source. The position of the MOSFET detector and the ^{241}Am source did not change during measurements. A strip of paper was placed between the source and the detector

(Figure 5-2). Threshold voltage was measured after each irradiation. The source was always covered during a threshold voltage measurement and a bias voltage was not applied. The interval between irradiations, during which threshold measurements were performed and the paper strip was replaced, did not exceed 20 seconds. Thus the change in the threshold voltage of the unbiased detector exposed to a paper covered source during read out was less than the detection limit of the readout system.

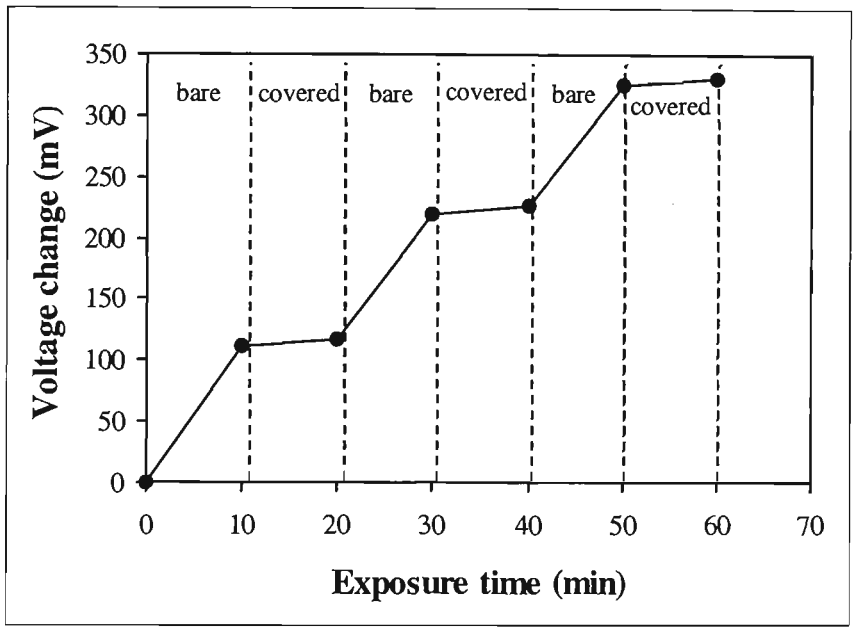

Figure 5-3. MOSFET threshold voltage change due to irradiation by a bare and covered by a sheet of paper ^{241}Am alpha source

The change in the MOSFET threshold voltage after 10 minutes exposure to an open americium source was about 100 mV. The threshold voltage change after exposure, of the same duration, to a paper-covered source, when the detector was exposed to 60 keV gamma radiation and no alpha particles penetrated through the paper, was only 6% of the change in the threshold voltage for a bare source, when

both gamma and alpha radiations were reaching the detector. Figure 5-3 presents changes in the MOSFET threshold voltage during irradiation by an open or covered ^{241}Am source. It is evident from this experiment that alpha radiation was the major contributor to the detector response. This experiment validates the data on MOSFET response to alpha radiation presented in Figure 5-1. The change in MOSFET threshold voltage was indeed due to americium-241 alpha particles and not to gamma radiation. The relative contribution of gamma radiation to the MOSFET threshold voltage change, in a mixed 5 MeV alpha-gamma field for a higher energy gamma component, is expected to be even less due to the lower sensitivity of the MOSFET to high energy gamma radiation (see Chapter 4.3).

The response of a MOSFET detector depends on the gate bias voltage. An ^{241}Am source makes it possible to compare the MOSFET threshold voltage change at different bias voltages for alpha and gamma radiation. The technique of a bare or paper-covered source was used. To obtain the contribution of pure alpha radiation, the threshold voltage change for a paper-covered source was subtracted from the bare source threshold voltage change.

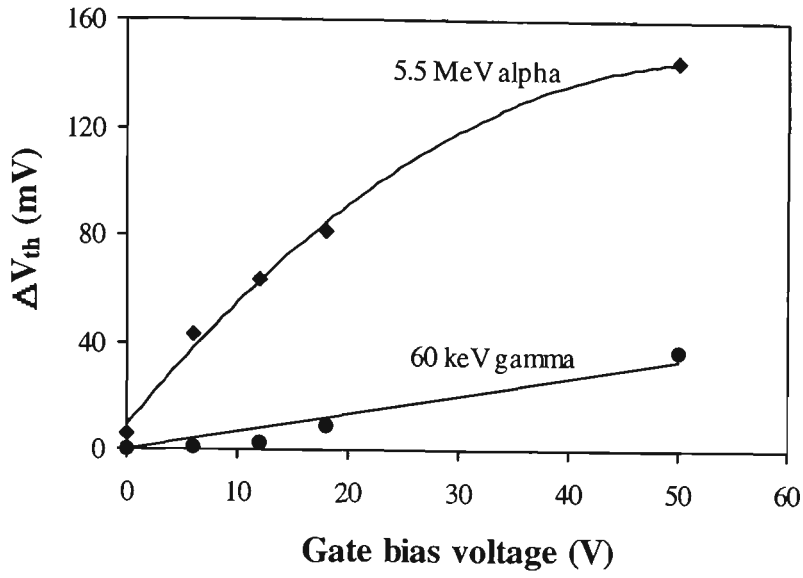

Figure 5-4. MOSFET threshold voltage change versus gate bias voltage for 10 minutes of ^{241}Am alpha and gamma radiations.

The data presented in Figure 5-4 demonstrate that, for bias voltages of up to 20 volts, the increase in MOSFET response to alpha radiation is significantly greater than for gamma radiation. An initial slope for 60 keV gamma is 0.68 mV/V while for 5.48 alpha particles the slope is 2.7 mV/V. An alpha particle produces a high density ionisation track, compared to gamma radiation and recombination of electron hole pairs in the track is very efficient. In the absence of an external electric field in silicon oxide, in the case of zero bias, holes diffuse to the SiO_2/Si interface where they are trapped. The probability of electron-hole recombination is high due to the high density of free charge carriers in the alpha particle track. For this reason, threshold voltage change in an unbiased MOSFET, due to alpha and gamma radiation, is not much different. Threshold voltage change due to alpha irradiation increases more significantly with the introduction of bias voltage, than due to gamma radiation. This experiment demonstrates that an increase in the

electric field in the silicon oxide layer efficiently separates positive and negative charge carriers in a dense alpha particle track and prevents their recombination. A slow down in the increase of threshold voltage change, due to alpha radiation, was observed at a higher bias. A possible reason for this is that charge separation was efficient and the fractional yield was high (see Chapter 1.3). The initial charge separation in a low density x-ray track was higher and its increase in a low electric field in silicon oxide was less significant than for alpha particle tracks.

5.3. Pulse height spectrum measurements by a MOSFET source and drain p-n junctions

A semiconductor (silicon or germanium) radiation detector operates by collecting free charge carriers produced by ionising radiation in the depletion layer. The depletion layer is extended by reverse biasing of the silicon detector p-n junction. A MOSFET structure has two p-n junctions. For an n-channel MOSFET, there is one p-n junction between the p-type substrate silicon and the n-type drain and another one between substrate and source (see Figure 5-5 and Figure 3-2). Thus one can consider that a MOSFET detector contains two silicon micro-detectors.

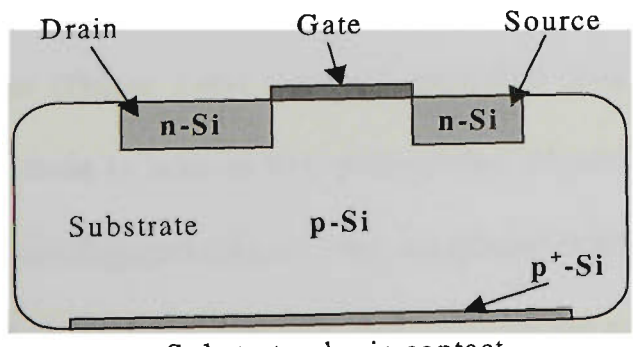

Figure 5-5. Diagram of a n-channel MOSFET structure, including drain-substrate and source-substrate p-n junctions.

The MOSFET p-n junctions can be stretched by applying positive reverse bias to the drain or source and a negative or earth potential to the substrate. If a reversed biased MOSFET p-n junction is connected to a spectroscopy set up, a pulse height spectrum of ionised radiation can be acquired. Si/SiO_2 interface trapping of holes, produced in the gate silicon oxide, is responsible for the MOSFET operation as an integral dosimeter. This process is independent of the charge production and collection in the p-n junctions. Thus the MOSFET can be simultaneously used for integral dosimetry of a radiation dose deposited in the silicon oxide and for differential spectroscopy by the drain and/or source p-n junctions. These were the original ideas which initiated our research into charge collection in MOSFET structure p-n junctions.

There are three possible ways of connecting the drain and source p-n junctions to the charge sensitive preamplifier of a spectroscopy system. For the best charge collection efficiency both of the p-n junctions can be connected to a charge sensitive preamplifier (Figure 5-6b). Another alternative is to connected only a single p-n junction (drain or source) to a preamplifier (Figure 5-6a). The gate is grounded in both of the diagrams (Figure 5-6). An independent bias voltage can be applied to the gate, because it is electrically isolated from the rest of the MOSFET structure. Another possibility is to connect the gate to the p-n junction bias voltage power supply.

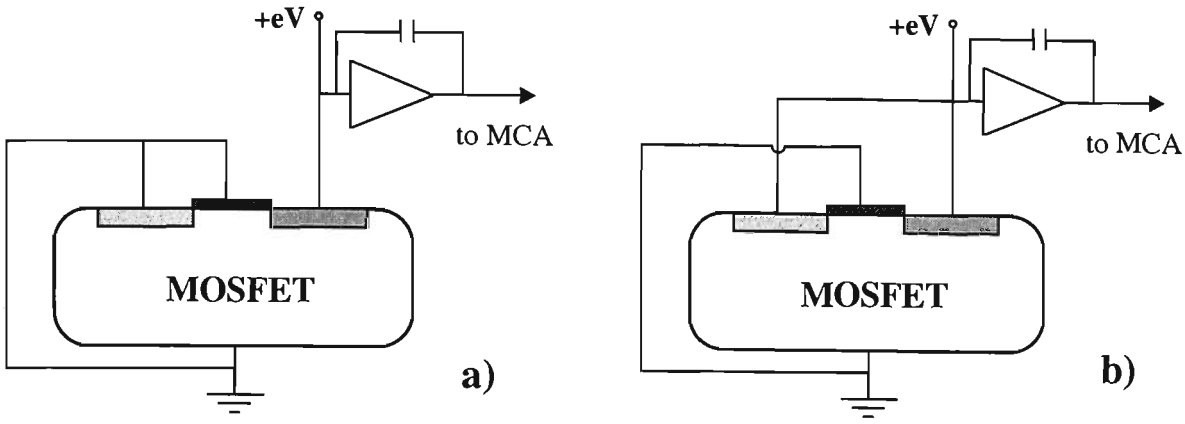

Figure 5-6. Diagram of possible connections of the MOSFET p-n junctions to a charge sensitive preamplifier and a Multichannel Analyzer (MCA). Connection of drain or source (a); connection of both, drain and source (b).

The following set of experiments was designed to establish the most effective type of connection of MOSFET p-n junctions to a preamplifier and spectroscopy set up. A MOSFET detector with the lid removed was placed inside the vacuum chamber of a Canberra 7401 alpha spectrometer and electrically connected to the preamplifier input socket. An ^{241}Am alpha source was placed under the MOSFET chip. The energy calibration of the spectrometer was performed with a Canberra ion implanted silicon detector (surface area 1 cm^2) and the system's pulse generator. The measurements were performed at a p-n junction reversed bias voltage of 6.1 V. The acquisition time varied between 75 and 85 minutes and all measurements were normalized to a constant acquisition time. Four different connections of the MOSFET to a preamplifier were used in the measurements: 1) and 2) the drain or source alone was connected to the preamplifier, while the rest of MOSFET elements, including gate and substrate, were grounded; 3) both drain

and source were reversed biased and connected to the preamplifier, while gate and substrate were grounded; and 4) drain and gate were biased and connected to a preamplifier, while source and substrate were grounded. The resultant pulse height spectra are presented in Figure 5-7.

The main peak in all four spectra was observed at an energy of about 4 MeV see Figure 5-7). This energy is less than the ^{241}Am alpha particle energy of 5.48 MeV. The reduction in observed energy was partly due to the loss of alpha particle energy in the MOSFET passivating film and in the aluminium contact pad, and partly because the effective charge collection layer was thinner than the alpha particle range in silicon. A substantial contribution to the reduced measured energy of alpha particles was through loss of collection charge due to surface recombination, diffusion and the capture of charge by the Si/SiO_2 interface and the other p-n junction. The topology of the MOSFET detector was not originally designed for spectroscopy charge collection measurements. Some of the elements of a silicon detector design, for example a guard ring, are not part of the MOSFET topology. For all of the above reasons a part of the charge is lost before reaching the preamplifier. It is important to note that a measurement of the exact energy of a charged particle is not the aim of MOSFET application for pulse height spectrum measurements. Moreover an exact energy measurement is often not possible as the charge collection layer of a biased MOSFET p-n junction is thin and in many cases is less than the range of a charged particle. In fact, it may be an advantage because it enables application of the MOSFET detector for microdosimetry (see more in Chapters 5.5.1 and 5.5.2). Charge collection for the

alpha particles of different energies and the geometry of the depletion layer, as probed by alpha radiation, are described in detail in Chapter 5.4.

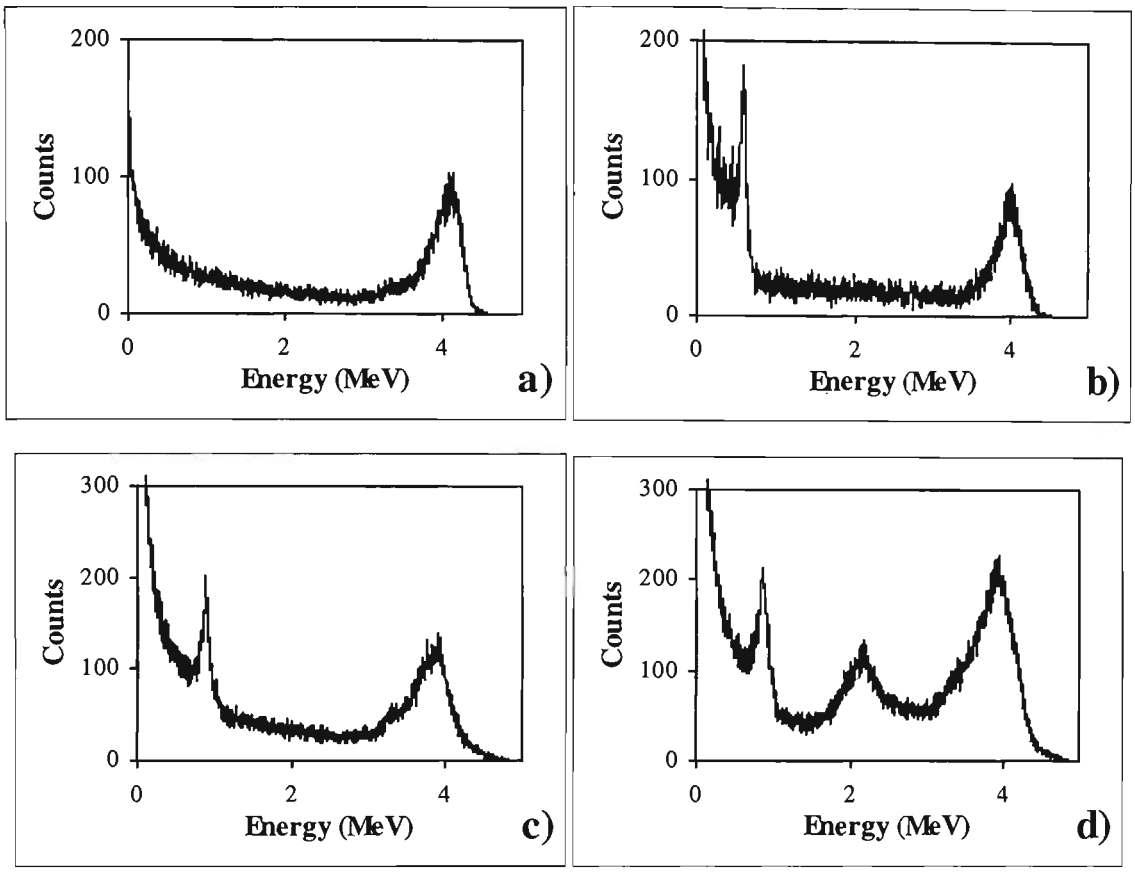

Figure 5-7. Pulse height spectra of ^{241}Am alpha particles measured by MOSFET structure p-n junctions. (a) - MOSFET drain alone is connected to preamplifier; (b) - drain and gate are connected to preamplifier; (c) - source is connected to preamplifier; (d) - source and drain are connected to preamplifier.

The spectrum collected by the MOSFET drain-substrate p-n junction (Figure 5-7a) is the only one among all the spectra which has a single peak at the energy of about 4 MeV. Only part of the drain area can be used for low and intermediate energy alpha particle detection. A contact wire with diameter of 40 μm is soldered

to the drain (Figure 3-2) and partly blocks alpha particle fluence. The exposed area of the drain was measured to be about A_{drain}=10,000 μm^2.

The spectrum collected by the source-substrate p-n junction has a second peak at lower energy of about 0.8 MeV (Figure 5-7c). The second peak is probably caused by the charge collected by the part of the drain ribbon which does not have an aluminium contact layer on top of it (top left corner in Figure 3-2). There was no external electric field and charge collection became less efficient.

The intensity of the 4 MeV peak collected by the MOSFET source-substrate p-n junction (Figure 5-7c) was greater than the intensity of the drain collected peak. The ratio of areas under the peak for the drain and source spectral measurements was 0.59. The source-substrate p-n junction was more efficient in charge collection because it has a larger surface area. The effective area of the source, measured from Figure 3-2, was A_{source}=19,000 μm^2, which is nearly twice the area of the drain, A_{drain}=10,000 μm^2. The ratio of A_{drain}/A_{source} = 0.52 and corresponds to the ratio of the peak intensities.

The spectrum measured by both drain and source p-n junctions connected to the preamplifier was clearly a superimposition of the drain and source spectra (Figure 5-7d). The intensity of the main peak was close to the sum of the intensities of the separate drain and source peaks. The third broad peak, at an energy of about 2.2 MeV, is an extra feature that probably appeared due to an expansion of the p-n charge collection depletion layer under the gate region. No additional research has been undertaken to clarify the origin of the third peak as it was outside the scope

of this study and it was clear that this combination of drain and source is not suitable for intended applications of the MOSFET.

After comparative analysis of the ^{241}Am alpha particle spectra (Figure 5-7), the drain-substrate p-n junction was chosen for use in alpha/high LET particle dosimetry with a MOSFET detector.

For simultaneous integral dosimetry and height pulse spectrum measurements the MOSFET drain-substrate p-n junction and the gate have both to be biased. If the bias voltage supply is common for the gate and drain, then the gate electrode is also connected to a charge-sensitive preamplifier. The alpha spectrum, with such a connection configuration, shows no change in position, shape or intensity of the 4 MeV peak (Figure 5-7b). However, an additional peak at an energy of about 0.6 MeV was observed. This peak was caused by charge collection in the silicon volume under the gate. A positive bias applied to the gate causes expansion of n-type Si under the gate. This expansion provided for an additional thin p-n junction which was responsible for the low energy peak in the spectrum. This peak should not cause concern since only the higher energy peak is used for dosimetry measurements. The low energy peak in no way interferes with the higher energy peak. There is no electrical connection of the MOSFET gate to a charge sensitive preamplifier if the gate is biased by a separate power supply. This type of connection does not cause a second peak at low energy. A MOSFET with two separate bias voltage suppliers was applied for experimental measurements at neutron therapy facilities.

The change in MOSFET threshold voltage due to irradiation is the basis of integral dosimetry with a MOSFET detector. Threshold voltage is sensitive to both low and high LET components of a mixed radiation field. However, low LET radiation, like gammas and electrons, does not contribute to a pulse height spectrum for energies above 0.1 MeV, as measured by a MOSFET p-n junction. This statement can be proved by MOSFET drain-substrate p-n junction pulse height spectrum measurements with ^{60}Co gamma and ^{137}Cs beta sources (see Figure 5-8). The spectra were recorded by a Canberra7401 alpha spectrometer connected to multichannel analyzer. All of the settings of the spectroscopy system were the same as for the alpha particle experiments previously described in this chapter. Thus application of a MOSFET detector in a mixed radiation field, with simultaneous measurement of the pulse height spectrum by the drain-substrate p-n junction, makes it possible to separate the contributions of high and low LET radiation to the total dose.

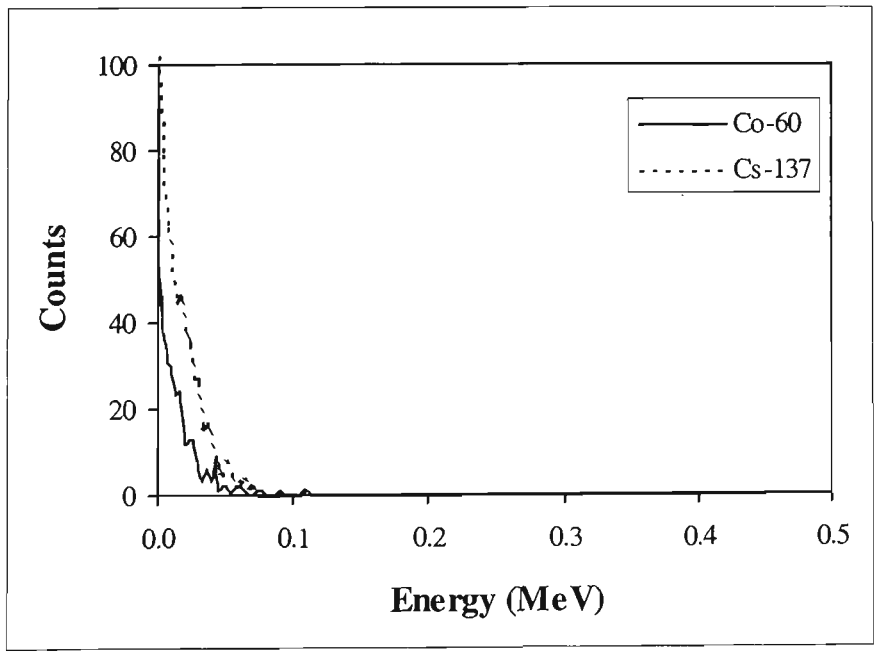

Figure 5-8. Pulse height spectra of ^{60}Co gamma and ^{137}Cs beta radiation measured by MOSFET drain-substrate p-n junction.

The next set of the experiments was designed to prove the principles of the application of a MOSFET detector for use in simultaneous dosimetry of high LET radiation and integral dosimetry of accumulated radiation dose in the MOSFET gate silicon oxide. The MOSFET detector was irradiated inside a Canberra 7401 alpha spectrometer vacuum chamber. The drain and gate of the MOSFET were biased at 6 V and connected to the spectrometer's charge-sensitive preamplifier. The height pulse spectrum of the alpha particles was measured at six different acquisition times of 20, 30, 45, 60, 90 and 120 minutes. After each irradiation the change in the MOSFET threshold voltage was also measured. The number of alpha counts was measured by integrating the area under the alpha peak in a pulse height spectrum. ^{241}Am emits a 60 keV X-ray for each alpha particle released and it was demonstrated in Chapter 5.2 that, for a gate bias voltage of 6 V, the contribution of X-rays to the threshold voltage change does not exceed 2% (see Figure 5-4). The accuracy of the threshold voltage measurement was between 2% and 4%. The accuracy of the alpha count measurements varied within the same limits and for this reason, the contribution of x-rays to the change in threshold voltage was neglected.

The change in the MOSFET threshold voltage increased linearly with the increase in alpha counts, measured by the drain-substrate p-n junction of the same detector (Figure 5-9). It proves that a MOSFET can be used as a dual dosimeter if the alpha

particle fluence can be considered uniform over the area of the MOSFET. This area itself is quite small, about 0.5×0.5 mm^2. The graph in Figure 5-9 can be used to calculate the alpha component of the MOSFET threshold voltage change of the detector in a mixed alpha-gamma field. The calibration was obtained for 5.48 MeV alpha particles, but for different alpha particle energies, the gradient of the calibration line may be different.

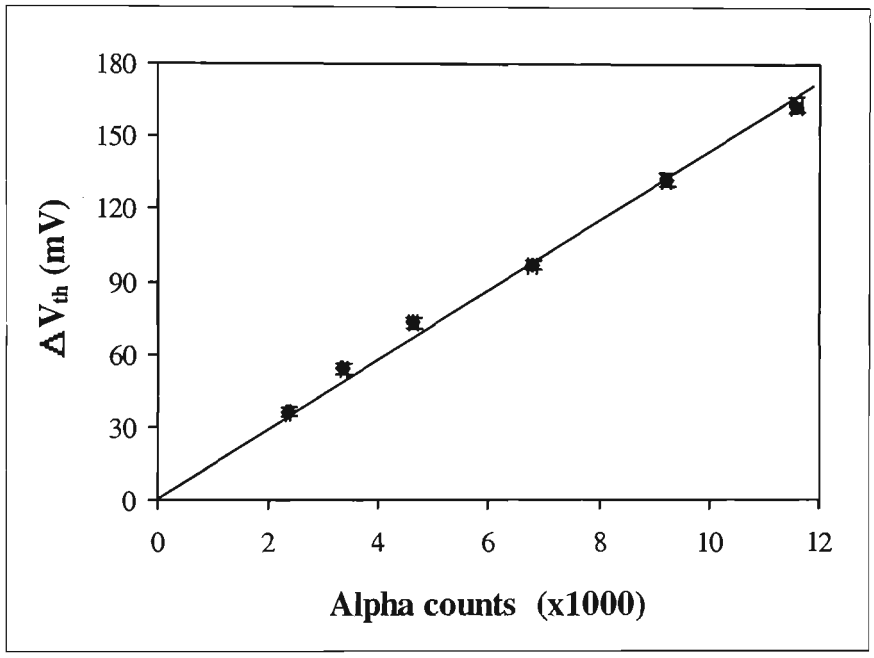

Figure 5-9. Change of MOSFET threshold voltage versus number of alpha counts measured by the MOSFET drain-substrate p-n junction. Gate bias $V_g = 18$ V.

5.4. Alpha particle probe of the charge collection of the biased drain-substrate p-n junction

For application of a MOSFET detector as a microdosimeter, the geometry of the charge collection volume has to be well defined. The charge collection volume can be probed by varying the energy of alpha particle irradiation. MOSFET applications in neutron capture therapy and alpha immunotherapy also require knowledge of MOSFET response to alpha radiation for a range of energies. For example, the energy of alpha particles in boron neutron capture therapy is about 1.5 MeV. All the data reported in Chapter 5.2 and Chapter 5.3 were obtained for ^{241}Am alpha particles from a thick laboratory source with a maximum energy of 5.46 MeV. The alpha particle energy from a ^{241}Am alpha source has to be modulated by a set of absorbers in order to obtain alpha particles of different energies.

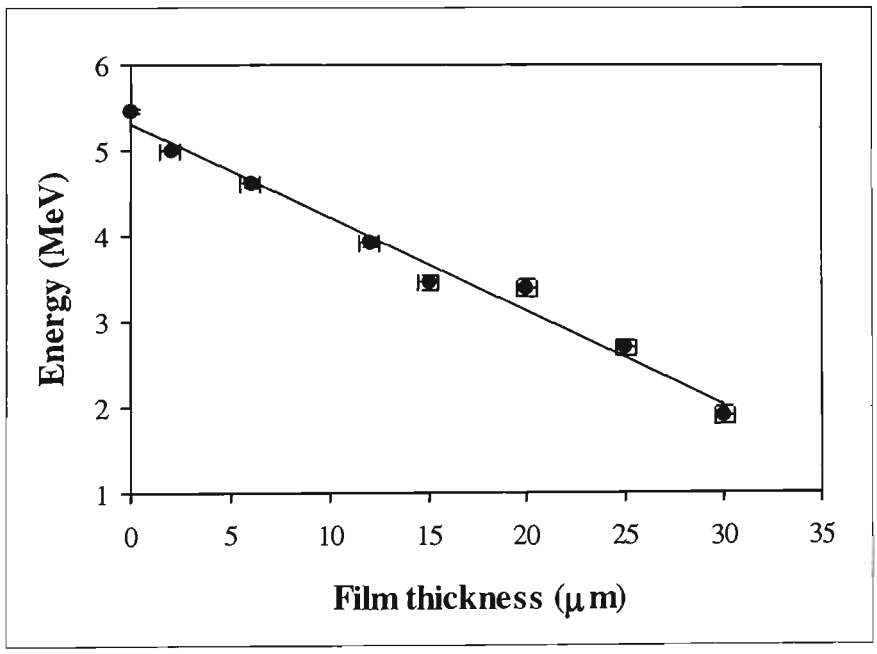

Figure 5-10. ^{241}Am alpha particle energy versus thickness of a Mylar film moderator.

The energy of alpha particles was modulated by a set of Mylar (Melanex) films (chemical formula $C_{10}H_8O_4$, density 1.3 g/cm^3) of different thickness. The film was stretched across an aluminium ring and placed on top of the alpha source. The accuracy in measuring the film thickness was better than 0.5 μm. The energy spectra of alpha particles passing through each of the films was measured by a Canberra ion implanted silicon detector in a Canberra 7401 alpha spectrometer. A calibration curve of alpha particle energy versus film thickness was obtained (Figure 5-10). The residual alpha particle energy changed linearly with film thickness. The straggling increased as the film thickness increased. The straggling effect leads to deterioration of alpha peak energy resolution and a decrease in the accuracy of determining the peak position (Figure 5-11). For the thickest films the accuracy of measurement was 0.2 MeV. However, the actual error might be greater than estimated one (see the error bars on Figure 5-10), because a source of additional error was the non-uniformity of film thickness due to wrinkles and stretching.

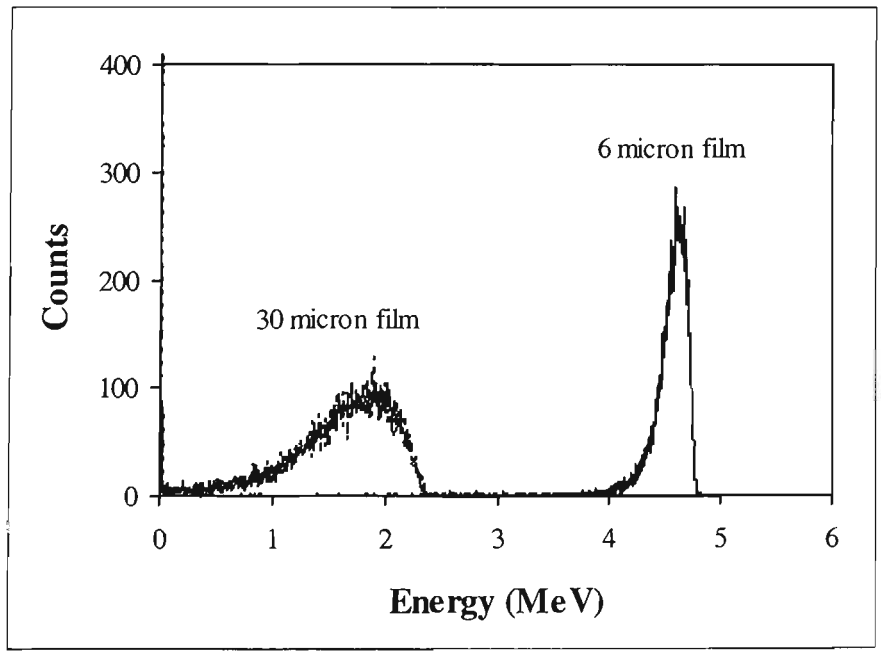

Figure 5-11. Pulse height spectra of ^{241}Am alpha particles after passing through 6 μm and 30 μm thick Mylar films measured by a Canberra ion-implanted silicon detector.

Pulse height spectra of moderated ^{241}Am alpha radiation were measured by the drain-substrate p-n junction of the MOSFET detector. The p-n junction was reversed biased at 6.1 V. The aim of this experiment was to probe the charge collection of the MOSFET detector at various incident energies of alpha particles and, as a result, to estimate the effective thickness of the charge collection layer. The energy collected by the MOSFET was consistently lower than the incident energy of the alpha particles. While for energies lower than 5 MeV the relationship between the incident and MOSFET measured alpha particle energy is nearly linear, for higher energies the rate of increase in the alpha particles energy deposited in the MOSFET sensitive layer slows down. The gradient of the best fit curve was reduced for higher alpha particle energies (Figure 5-12a); a trend that becomes even more apparent when the difference between the incident and MOSFET collected energies versus the incident energy is graphed (Figure 5-12b).

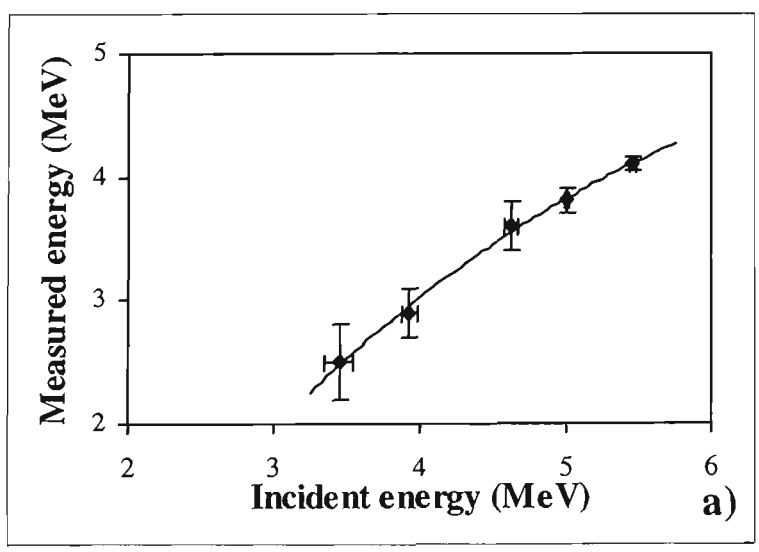

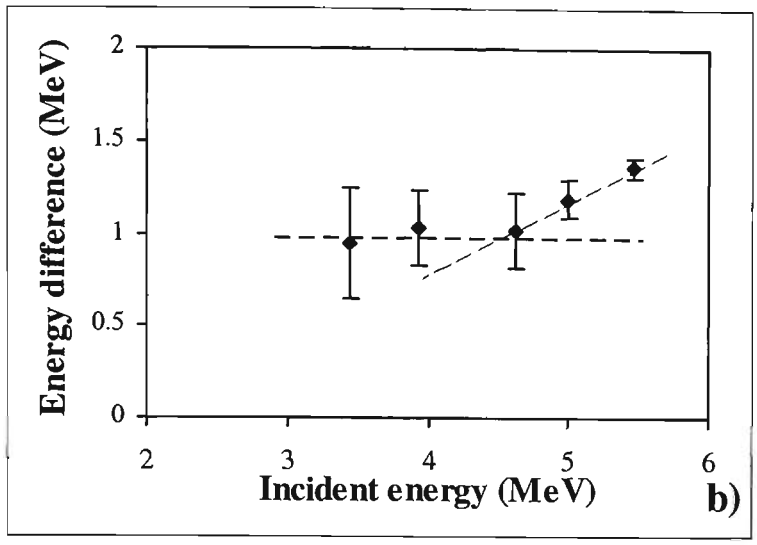

Figure 5-12. (a) - Alpha particle energy measured by a drain-source MOSFET p-n junction versus the mean energy of the incident alpha beam; (b) - difference between the alpha particles incident and MOSFET drain-source p-n junction collected energies versus the incident energy.

For incident energies of up to approximately 4.5 MeV, the difference between the incident and collected energies remains constant at about 1 MeV (Figure 5-12b). This means that about 1 MeV of the incident alpha particle energy was lost, partly in the detector entrance window and partly due to a deficiency in charge collection. The entrance window consists of a passive layer, aluminium pad contact and the n^+ silicon layer of the drain. Some charge produced by an alpha particle is lost due to non-efficient charge collection in the drain-substrate p-n junction and because of surface charge recombination and diffusion. The remainder of the alpha particle energy is collected if the range of the alpha particle does not exceed the effective thickness of the charge collection layer.

The charge produced by a high energy particle is collected in the silicon detector by three main processes:

1. Fast drift of charge in the depletion layer of a p-n junction. The drift in a reversed biased p-n junction proceeds under a high electric field produced by the bias voltage, as practically all of the bias voltage drop occurs in the thin high resistivity layer depleted of charge carriers.
2. Funneling. A high energy particle produces a hot electron plasma along its track through a semiconductor material. For example, a 5.5 MeV alpha particle has lineal energy transfer of 150 keV per μm (Shröder *et al.*, 1992). The extra free electrons released by the high energy particle produce a strong electric field which causes the external electric field in the particle track to collapse. A strong electric field of free electron plasma extends the depletion layer field and forms a funnel which transfers charge generated in the substrate into the depletion layer (see Figure 5-13). The funnel breaks down when the charge density in the track drops to the same order of magnitude as the doping charge density. The process is very fast, taking only a few picoseconds to complete (Kirkpatrik, 1979; Messenger, 1982). Because the funneling is restricted to a less than 1 nanosecond, it is not possible to separate the funneling component from the drift component of charge collection.
3. Diffusion. Diffusion charge collection, from substrate silicon, is driven by charge density gradient. The main component of the gradient is perpendicular to the particle track. A gradient component towards the p-n junction exists due to funneling. Diffusion length is determined by the carriers life time and diffusion coefficient.

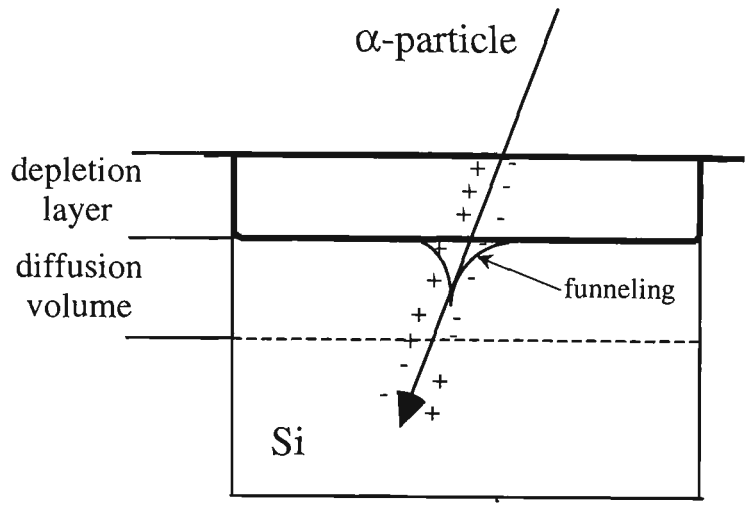

Figure 5-13. Diagram of silicon detector charge collection.

The full remainder of the alpha particle's energy, after charge loss accounting for 1 MeV energy, was collected for incident energies of up to approximately 4.5 MeV. This means that the effective thickness of the charge collection layer of the drain-substrate p-n junction is not less than the range of the alpha particle in silicon. The range of the alpha particle at 4.5 MeV energy is equal to the effective depth of the charge collection volume. This observation allows estimation of the depth of the detector's sensitive volume. A calculation of the range of 4.5 MeV alpha particles in silicon by a Monte Carlo TRIM (Transport and Range of Ions in Matter) software package (Ziegler *et al.*, 1985) provides a value of 14 μm for the depth of the charge collection volume. The thickness of the depletion layer of a reversed biased p-n junction is proportional to $\sqrt{\rho V}$, where ρ is the resistivity of bulk silicon (for MOSFET's p-type silicon ρ = 10 Ω·cm, see Chapter 3.1.1) and V is bias voltage. The depletion layer thickness for such silicon at a bias of 6 V does

not exceed 3 μm, and when the bias voltage is increased to 30 V, the depletion layer still does not exceed 6 μm (Nemec & Hofman, 1975). Only a fraction of observed charge can be collected in such a small volume. The depletion layer is relatively shallow because the silicon used in the manufacturing of MOSFET detectors is a low resistivity silicon. The funneling effect is also less prominent in low resistivity silicon compared to high resistivity silicon, as it is formed is by an excess of free charge produced by the ionising particle above the silicon doping level. The majority charge carrier density in the substrate silicon was 1.35×10^{15} cm^{-3}. While measurement or accurate calculation of the size of the funnel was not available, it is generally considered that the funnel depth is smaller than the thickness of the depletion layer. Funneling also depends on the LET of the charged particle. A higher LET particle releases more charge per unit track length and introduces a stronger electric field. Calculations for heavy ions showed that in 2.6 ps after an ion strike, an electric field of 5 V penetrates into the silicon substrate to a depth of 3 μm (Woodruff & Rudeck, 1993). The effective depth of the detector's sensitive volume exceeds the depletion layer and funneling. Thus diffusion is responsible for charge collection from a greater depth.

In the diffusion process, electrons diffuse towards the p-n junction where they are picked up by the electric field. The diffusion length, l, can be estimated as the square root of the product of diffusion coefficient, D, and the charge carrier life time, τ, or $l = \sqrt{D\tau}$. The life time of a minority charge carrier in p-type silicon is about 10 μs, and the diffusion coefficient of electrons D = 35 $cm^2 \cdot s^{-1}$. All values are quoted for room temperature (Baranskiy *et al.*, 1975). Therefore the diffusion

length of electrons in silicon of an n-type MOSFET, l, is approximately 180 μm. Not all the charge produced at depth $x < l$ will be collected and some charge will be collected from greater depths, due to the random nature of the diffusion process. The proportion of charge collected from depth x decrease exponentially with depth as per

$$Q \propto \exp(-\frac{x}{l})$$

where Q represents the collected charge.

Diffusion length, and as a result efficiency of the diffusion charge collection, depends on the minority carrier's life time. Defects in silicon crystal structure act as recombination centres and affect the carrier's life time. To test validity of the hypothesis of diffusion charge collection, a MOSFET detector was irradiated by fast neutrons. The fast neutron irradiation produces crystal structure defects in silicon. The MOSFET was irradiated to a neutron fluence of 2×10^{11} n·cm^{-2} and later to a total fluence of 1×10^{13} n·cm^{-2}. Neutron irradiation was carried out at the Van de Graaff accelerator at the Lucas Heights Laboratories of the Australian Nuclear Science and Technology Organisation (ANSTO) by Mr. Mark Reinhard. Americium-241 alpha particle spectra were recorded before irradiation and after each exposure to neutron irradiation. The pulse height spectra were measured by the MOSFET drain-substrate p-n- junction biased at 6.1 V. The MOSFET and the radiation source were placed in the vacuum chamber of a Canberra 7401 alpha spectrometer and the MOSFET was connected to the spectrometer preamplifier.

Table 5-1. Position of ^{241}Am alpha peak measured by the drain-substrate p-n junction of a MOSFET detector before and after two consecutive fast neutron irradiations.

Neutron fluence, $n \cdot cm^{-2}$	none	2×10^{11}	1×10^{13}
Peak position, MeV	3.94	3.83	3.62

The alpha peak moved to a lower energy range after each neutron irradiation (see Table 5-1). The move after the final irradiation is greater than the move after the first irradiation. The reduced alpha peak energy means that less charge was collected after exposure to fast neutron irradiation. Fast neutron irradiation introduces defects in Si crystal structure which reduce the charge carrier life time and diffusion length. Reduction in diffusion length caused reduction in charge collection. This experiment confirmed that of the charge collected by the drain-substrate p-n junction was collected by a diffusion process.

We can conclude that the effective depth of a detector's sensitive volume of 14 μm consists of the drift region of the depletion layer, funneling, and the diffusion region (Reed *et al.*, 1993). A model of a silicon detector p-n junction charge collection is in Figure 5-13. The figure is not to scale. Charge collection in the depletion layer and funneling, with its strong electric field, is rapid. The electric field in the rest of the silicon volume is close to zero. The charge released by ionising radiation below the p-n junction is collected by a slow diffusion process. The fast drift charge collection takes just one or two nanoseconds, while a slow diffusion charge collection may take tens of nanoseconds.

All the alpha particle measurements described in this section were performed in the vacuum chamber of a Canberra 7401 alpha spectrometer. The alpha spectrometer's built-in charge sensitive preamplifier is a general type preamplifier with a time constant of 2 microseconds. Because of the large time constant, the preamplifier integrates both fast (drift) and slow (diffusion) components of the current. A separation of the slow and fast components of charge collection was not possible.

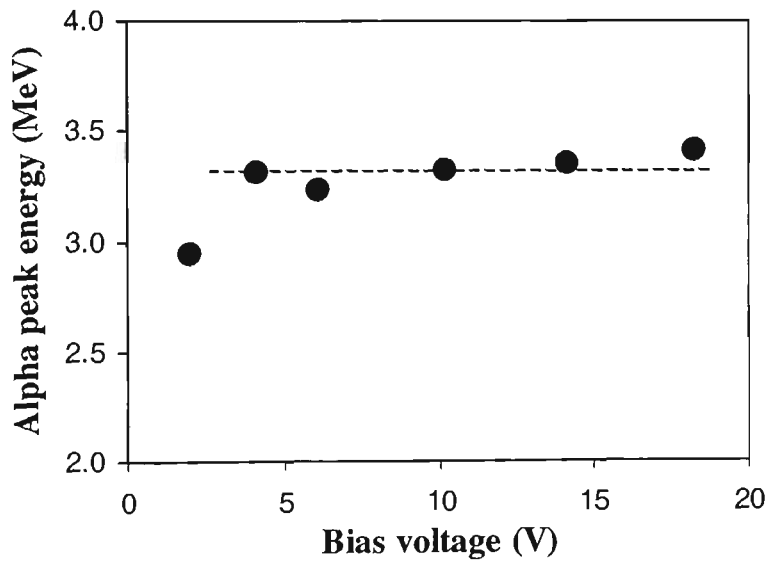

Figure 5-14. Alpha particle energy measured by the MOSFET drain-substrate p-n junction versus bias voltage

The total 14 μm effective depth of the effective charge collection volume of the MOSFET drain-substrate p-n junction was obtained for a bias voltage of 6.1 V. Increase of the bias voltage causes an increase in the thickness of the depletion

layer, and as a result, the charge collection volume may also increase. This increase is insignificant because a part of the charge collection depth is due to diffusion charge collection, which is affected only slightly by an increase in bias voltage, and a corresponding increase in the depletion layer. The depletion layer itself expands only marginally with an increase in the reverse bias voltage as it is proportional to the square root of the voltage. To test this statement, ^{241}Am alpha particle spectra were acquired in air by the MOSFET drain-substrate p-n junction under different bias voltages from 2 V to 18 V. The energy of the alpha peak was plotted versus bias voltage (Figure 5-14). The measured energy is directly related to the thickness of the charge collection volume, because the incident alpha particle energy is such that the alpha particle range exceeds the charge collection volume thickness. The measured alpha peak energy increased while the bias increased from 2 V to 4 V, then the peak energy stayed about the same for bias up to 15 V. It proves that the effective charge collection volume is not very sensitive to a change in bias voltage, and for this range of bias voltage it is about 14 μm thick. This parameter is important for conversion of pulse height spectrum to a microdosimetry spectrum as discussed in Chapter 5.5. The energy of alpha peak increased only slightly for a bias voltage of 18 V.

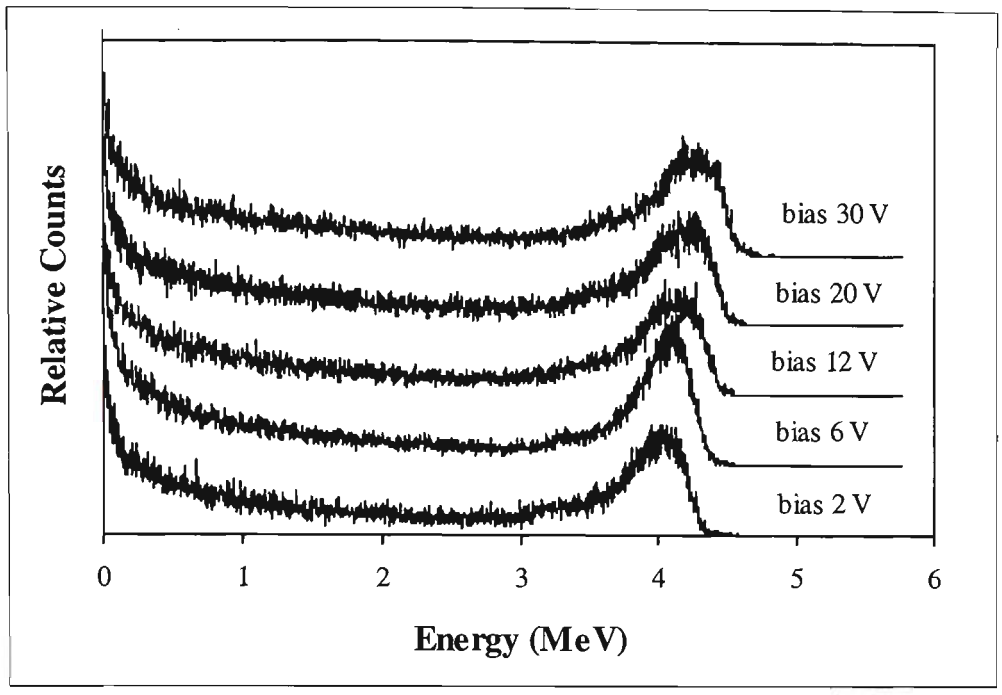

Figure 5-15. Change of ^{241}Am alpha particle peak position with change in the detector bias voltage. Spectra presented in the same graph for convenience and do not correspond to the absolute amplitude of different peaks.

The relatively low importance of bias voltage on the position of the alpha particle peak was confirmed in experiments using another MOSFET. The MOSFET drain-substrate p-n junction was irradiated in a vacuum with ^{241}Am alpha particles up to a bias of 30 V (Figure 5-15). An increase of charge collection at a higher bias voltage is expected and is caused by a more efficient charge collection in the diffusion process. A charge created by an ionising particle, at a certain depth below the depletion layer, diffuses through less distance before reaching the p-n junction. The reduction in distance makes charge collection more efficient, as the collected charge is proportional to $\exp(-x/l)$.

5.5. Application of a MOSFET detector for simultaneous macro and micro dosimetry at neutron radiation therapy facilities

A knowledge of total dose in radiation therapy is quite adequate for characterising the biological effects of radiation in a pure gamma field, as used in medical linac treatment. This dose is characterised by a shift in the MOSFET threshold voltage. The total dose becomes inadequate in mixed radiation fields where high lineal energy transfer (LET) radiation with its high relative biological effectivness (RBE) is present. The effect of the radiation field in such complicated mixed fields as used in boron neutron capture therapy (BNCT) and fast neutron therapy (FNT) demands both macrodosimetry and microdosimetry measurements. Microdosimetry yields a spectrum of the energies deposited at the cellular level, which is the LET spectrum (ICRU, 1983).

5.5.1. Basic principles of microdosimetry

A radiation dose, as measured by integral dosimetry, is a mean quantity. It characterises the total energy absorbed by a unit mass of irradiated medium. The biological and chemical effects of the ionising radiation are all caused by the single interactions or single transfers of energy from the radiation, mostly to electrons in the medium. In the case of a gas, an interaction leads to excitation which results in ionisation, in case of a semiconductor, it is usually due to transfer of an electron from a lower energy level to a conductivity band, creating an electron-hole pair. In a chemical compound or a biological molecule, an

interaction leads to a break or excitation of a chemical or electrostatic bond. Radiation damage to a biological cell is inflicted by damage to the cell's DNA. In all eukariotic cells, such as human and animal cells, genetic information of DNA is localized in chromosomes in the nucleus. The pattern of dose delivered to the nucleus or on even smaller scale to DNA, determines the radiation effect.

Microdosimetry addresses the regional and structural aspects of the interaction of ionising radiation with medium (Rossi & Zaider, 1996). Interaction of radiation with matter, or energy transfer, occurs at discrete transfer points and in discrete events. An event is a set of statistically correlated transfer points in a restricted volume of interest. An example is the ionisation track of a charged particle. Interaction introduces a change or alteration to the energy state of a system, which may be a crystal, molecule or biological system. These changes may result in a radiation effect if sufficient amount of energy is transferred to the system. The transferred energy depends on the total number of the transfer points which on average is proportional to the absorbed dose.

Two quantities are used in microdosimetry, they are specific energy, z, and lineal energy, y. The International Commission on Radiation Units and Measurements defines these quantities as (ICRU, 1980):

$$z = \frac{\varepsilon}{m}, \quad \text{and}$$

$$y = \frac{\varepsilon}{\bar{l}} \tag{5-1}$$

where ε is the energy imparted by ionising radiation to the volume of matter of mass m, and $\bar{l}$ is the mean chord length in that volume. The lineal energy is commonly measured in units of keV/μm.

Mean chord length for a convex shaped body is given by Cauchy's theorem (Cauchy, 1908)

$$\bar{l} = \frac{4V}{S} \tag{5-2}$$

where V is the volume and S is the surface area of the body. For the simplest spherical volume, $\bar{l} = \frac{2}{3} d$, where d is the diameter of the sphere. For the rectangular prism shape of a MOSFET sensitive volume with sides a, b and c

$$\bar{l} = \frac{4abc}{2(ab+ac+bc)} = \frac{2}{\frac{1}{a}+\frac{1}{b}+\frac{1}{c}} \tag{5-3}$$

The mean chord length calculation by Cauchy's theorem assumes random direction of the dosimetric volume transversal by radiation, or the assumption of a direction independent radiation field. Directional independence is required in and around the detector volume. The mean chord length calculated for an isotropic radiation field may still be applicable even in a directional beam. Biological cells are normally randomly oriented in a body or in a suspension cell culture. A

microdosimeter can rotate in all the possible directions within the field, to model the cells, or one can simply use the mean chord length.

Lineal energy is important in radiobiology and radiation oncology because together, with the type of radiation, it determines biological effectiveness. In general, it is true to say that radiation with a higher lineal energy will cause a greater effect than the same dose and type of radiation but with a lower lineal energy. An example may be an electron or neutron radiation at different energies, or a proton radiation at the end of its range in matter at Bragg's peak and at a higher energy.

In experimental microdosimetry, a pulse height spectrum is collected from a well characterised dosimetric volume with a known mean chord length. The energy axis can be converted to lineal energy by dividing the abscissa values by the mean chord length. Pulse height distribution is proportional to lineal energy distribution, $f(y)$ (Rossi & Zaider, 1996). $f(y)dy$ is the probability that the lineal energy produced in an event is in the interval $[y,y+dy]$ and fraction of events with lineal energy in this interval is given by

$$\int_{y_1}^{y_2} f(y)dy$$

A convenient way to represent a microdosimetry spectrum graphically is to plot $yf(y)$ vs $\log(y)$. This plot allows graphical estimation of the fraction of events with lineal energy in a given interval of y_1 to y_2, because

$$\int_{y_1}^{y_2} yf(y)d\log(y) = \int_{y_1}^{y_2} f(y)dy$$

The standard representation of microdosimetry data is a plot of $y^2f(y)$ vs $\log(y)$, or in another notation it is $yd(y)$ vs y (Rossi & Zaider, 1996). The area under the curve between two values of lineal energy represents the dose delivered by ionising radiation in this interval of lineal energies.

Traditional microdosimetry is based on the use of gas proportional counters. A gas proportional counter is spherical in shape and relatively large in size. The diameter of the counter may vary from a few centimeters to 10-15 centimeters, depending on the particular design. An effective tissue equivalent size is determined by the mass of the gas in the ionisation chamber. The effective size or, in microdosimetry terms, the site diameter, can be changed by variation of the pressure of the tissue equivalent gas inside the detector, to simulate energy deposition by ionising radiation in a site with diameter as small as 1 μm.

A microdosimetry spectrum $yd(y)$ vs $\log(y)$ shows a dependence on the site diameter. Investigation of an energy deposition of 1.5 MeV neutrons in site diameters of 1 to 8 μm by (Srdoc *et al.*, 1981) demonstrated that the microdosimetry spectrum moves towards lower lineal energies with an increase in site diameter. Similar results were obtained for ^{252}Cf radiation in 1 and 2 μm sites (Dicello *et al.*, 1972). The dose contribution of lower lineal energy radiation increased for the 2 μm site.

There are several hundred publications reporting on the use of gas proportional counters in microdosimetry. Gas proportional counters are also applied in mixed neutron - gamma fields of FNT, boron neutron capture enhanced FNT and BNCT (Kota *et al.*, 2000; Maughan *et al.*, 1992a; Wuu *et al.*, 1992). The size of a gas proportional counter limits the accuracy of measurement in a field with a high dose rate gradient or when the energy spectrum of radiation changes significantly at a distance equal to the size of the counter. The external diameter of a small gas proportional counter is about 2 cm. For this reason, the use of a tissue equivalent gas proportional counter for in-phantom measurement in radiation oncology may not always be adequate, because, due to its size of several centimeters, it may significantly perturb the radiation field itself. The dose rate may change significantly over a several centimeter range for many radiation fields in a phantom.

An optimal microdosimeter for radiation biology and radiation oncology should have geometrical dimensions of the sensitive volume comparable to cellular size, and ideally should even represent a cell on a subcellar level for modeling the pattern of energy deposition in nuclear and cytoplasmic cell structures. This approach to microdosimetry, based on actual cell morphology, using high resolution quantitative autoradiography and two dimensional Monte Carlo simulation, was first proposed for BNCT by Solaris and Zamenhof (Solaris & Zamenhof, 1995). However this method is time consuming and is limited to ^{10}B dose only. A different approach is to model a biological cell with a several micron size silicon cell. Quantitative measurement of a deposited energy pattern by charge

spectroscopy in a p-n junction with typically sized biological cell is a further step in the characterisation of a mixed radiation environment. This approach was suggested by Shröder *et al.* and was tested in personnel monitoring in radiation protection for separation of gamma and neutron components of a radiation field (Shröder *et al.*, 1992; Shröder *et al.*, 1994). Commercial CMOS memory chips were used for microdosimetry measurements of energy deposition spectra (Shröder *et al.*, 1994).

The rationale in using micro silicon volumes for tissue microdosimetry is that a numerical scaling coefficient of 0.63 can be applied to the re-scale volume of silicon to tissue to convert the pattern of energy deposition in silicon to energy deposition in tissue (Bradley *et al.*, 1999). The sensitive volume of the drain-substrate p-n junction of a MOSFET detector can be used for performing microdosimetric measurements. The volumes of the p-n junctions of the MOSFETs used in this study are larger than a typical microdosimetric volume. Because of this, the accuracy of the MOSFET microdosimetry can be reduced, compare to a well defined sphere of a proportional counter.

5.5.2. Microdosimetry application of a MOSFET at a FNT facility

A test run of a MOSFET detector as a microdosimeter was performed in the fast neutron therapy beam at Harper Hospital, Detroit, MI, USA. See page 60 for a description of the facility. The use of random access computer memory chips

(CMOS) for neutron beam microdosimetry has been previously reported (Shröder *et al.*, 1994). While a CMOS chip consists of an array of MOS transistors, our experiments at FNT facility were the first microdosimetry applications of a MOSFET radiation detector. Both threshold voltage and the pulse height spectra were recorded.

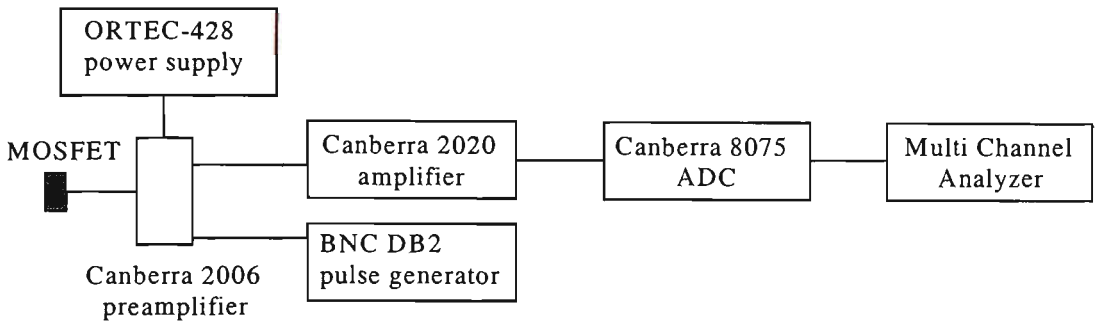

Figure 5-16. Block diagram of the experimental setup of MOSFET dosimetry measurements in a FNT beam at Harper Hospital.

The MOSFET probes had 6 mm external diameter perspex covers and were connected to a Canberra 2006 charge sensitive preamplifier via a 1.0 m length of cable. All probes were waterproof. The MOSFET drain-substrate p-n junction was reversed biased to 5 V by an ORTEC-428 spectroscopy power supply. The MOSFET gate was biased during the measurements to +5V. The pulse height analysis system (Figure 5-16) contained four sets of Canberra 2020 amplifiers and four sets of Canberra 8075 ADC, with relative gains chosen to cover the LET range from 0.2 keV/μm to 1050 keV/μm. The pulse height spectra were acquired by a 1024 channel multichannel analyser.

The energy calibration of the spectroscopy system was performed using a 1.0 x 1.0 cm^2 silicon ion implanted detector. The silicon detector was connected to a Canberra 2006 preamplifier instead of a MOSFET detector (Figure 5-16), using the same settings of the spectroscopy system for the calibration as for MOSFET microdosimetry measurements. A ^{210}Po alpha particle source was used for energy calibration measurement. A peak of 5.3 MeV ^{210}Po alpha particles was observed in channel number 940 of the multichannel analyser.

The water tank had 6 mm thick perspex walls. The detector depth in water was measured from the internal face of the perspex wall. The measurements in a fast neutron beam were performed in a water tank at the depths of 5 cm, 10 cm, 15 cm and 25 cm. The opening of the neutron beam collimator was 10 x 10 cm^2. Each irradiation was performed to the total monitored dose of 250 MU, as measured by an in-beam ionisation chamber.

The pulse height spectrum measured by a MOSFET drain-substrate p-n junction at 5 cm depth in a water phantom is presented in Figure 5-17. The spectra acquired at the deeper depths are of a similar shape. A feature of the spectrum in Figure 5-17 is a proton energy cut-off at an energy level of about 5.1 - 5.2 MeV.

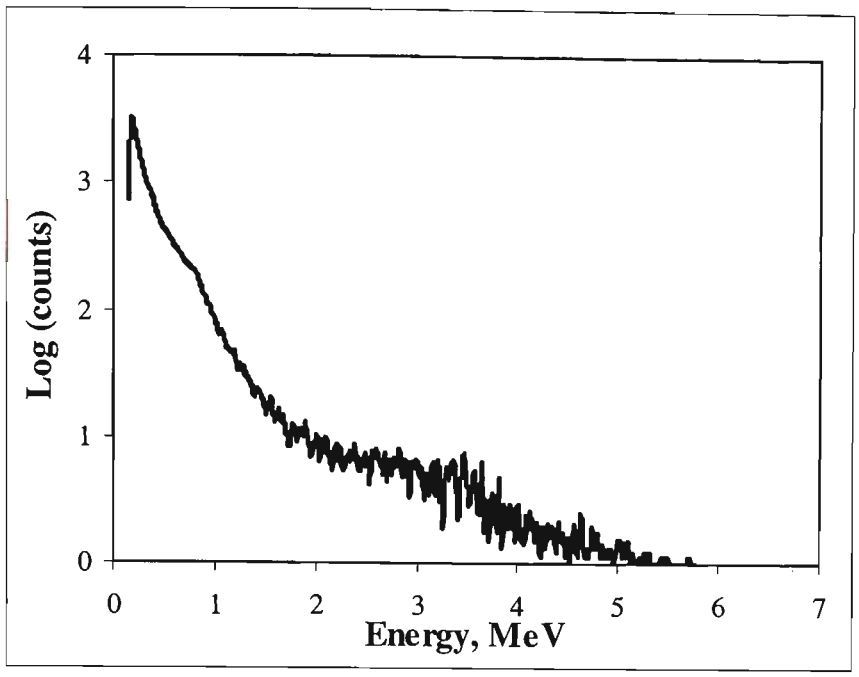

Figure 5-17. Pulse height spectrum measured by a drain-substrate p-n junction of a MOSFET detector in a fast neutron beam along the central axis of the beam at a depth of 5 cm in 10×10 cm^2 field in a water phantom.

The drain of a MOSFET detector has geometrical dimensions of 150 x 150 μm^2. The effective depth of the sensitive volume, as determined by an alpha particle probe, (Chapter 5.4) is 14 μm. The shape of the sensitive volume can be described as a rectangular prism with mean chord length of the sensitive volume $\bar{l} \doteq 23.5$ μm, as calculated by using equation 5-3. The maximum chord length equals 212 μm.

The Harper Hospital FNT beam has a maximum energy of approximately 48 MeV. These neutrons produce, by elastic scattering processes, a wide range of protons with energies of up to 48 MeV. The maximum energy of a recoil proton equals the energy of the incident neutron. This energy is reduced at a depth of 5

cm, because it is moderated by water. A proton with an energy of 40 MeV has a range in silicon of 8 mm, a range of 10 MeV proton is 600 μm, and 1.3 MeV protons have a range in silicon of 23.5 μm which is approximately equal the length of the average chord of the MOSFET drain-substrate p-n junction sensitive volume. These ranges were calculated by the TRIM software package (Ziegler *et al.*, 1985). Therefore, the mean chord of a MOSFET drain-substrate p-n junction sensitive volume is significantly smaller than the range of high energy protons in silicon and the MOSFET can be applied for measuring of microdosimetry spectra of protons with energies down to approximately 1.5 MeV.

The maximum energy a proton can deposit in a sensitive volume is when it traverses the sensitive volume along its longest chord. The LET of a proton depends on its energy, therefore the total energy deposited in a volume crossed by a proton depends on the energy of that proton. The lineal density of the deposited energy rises towards the end of the proton range in matter. The distribution of deposited energy by a monoenergetic proton beam is low at the entrance and is followed by a sharp increase called the Bragg peak. The ratio of LET in the proton entrance and in the Bragg peak in water is about 4-5 fold (Vanitsky *et al.*, 1999). Thus a proton deposits maximum possible energy along its path in a medium of length l only if its range in that medium equals l. Silicon is the material of the MOSFET p-n junctions. The range of 5.1 MeV protons in silicon is approximately 220 μm, as calculated by TRIM. The range of protons of the maximum energy registered in the spectrum in Figure 5-17 is in very good agreement with the length of the maximum chord of the detector sensitive volume of 213 μm, as

estimated by the alpha particle probe in Chapter 5.4. The proton energy cut off data confirmed the validity of the estimation of the effective depth of the sensitive layer.

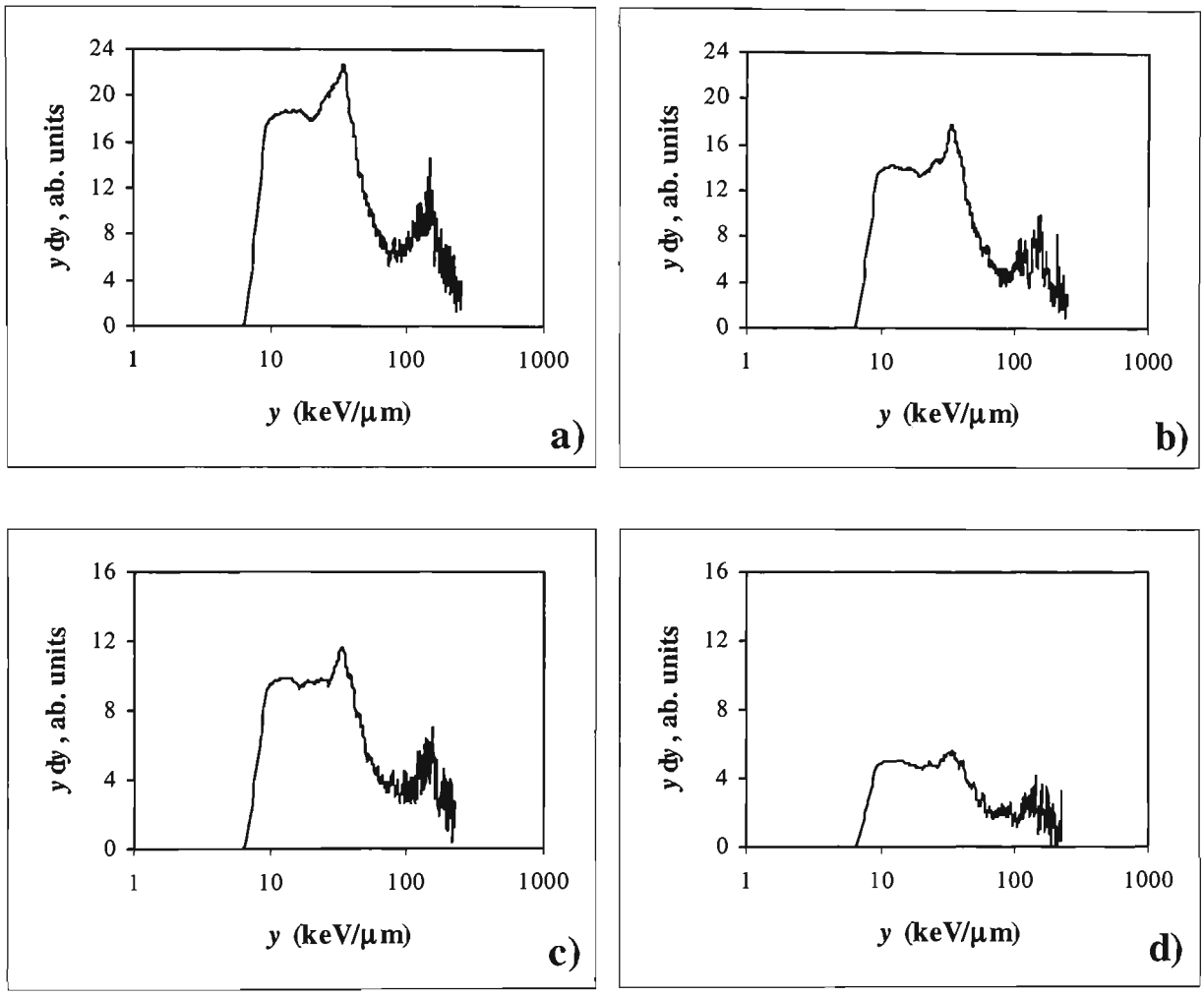

Figure 5-18. Microdosimetry spectra of a d(48.5MeV)+Be fast neutron therapy beam measured along the central axis of the beam in 10×10 cm^2 radiation field at the depths of a) 5 cm, b) 10 cm, c) 15 cm and d) 25 cm in a water phantom by the drain-substrate p-n junction of a MOSFET detector.

The pulse height spectra were converted to microdosimetry spectra by the method described in Chapter 5.5.1. The energy was converted to the lineal energy by dividing into the mean chord length of 23.5 μm. The microdosimetry spectra are presented in Figure 5-18. The spectra have all the features of microdosimetry spectra measured in the same beam by a tissue equivalent gas proportional counter (Kota *et al.*, 2000; Maughan *et al.*, 1992b). The main difference between microdosimetry spectra measured by a MOSFET or a proportional counter is a low energy shoulder, shown in Figure 5-18. This shoulder is caused by particles stopping or originating in the detector sensitive volume. The size of the MOSFET drain-substrate sensitive volume is relatively large compared with the 2 μm site of a tissue equivalent gas proportional counter. Thus a relatively larger number of secondary particles become stoppers or starters in the sensitive volume of the detector. These particles do not cross all of the sensitive volume and, as a result, they deposit less energy in it. When the reduced energy is converted to lineal energy by dividing by the mean chord length, it results in the observed low energy shoulder.

The peak at low lineal energy in microdosimetry spectra (Figure 5-18) corresponds to high energy protons, and the peak at high energy corresponds to low energy protons (Wambersie *et al.*, 1994). The high lineal energy peak consists of several overlapping peaks. The higher energy part of it is due to charged particles of greater mass. The neutron beam is moderated with depth in water. The energy spectrum of the neutrons in the beam shifts towards the low energies and this change is confirmed by the microdosimetry spectra because the ratio of a low lineal energy microdosimetry peak (corresponding to high energy protons) to a

high lineal energy peak (corresponding to low energy protons) decreases with depth in water (Figure 5-18 a to d).

The LET of gamma radiation is low and it is not registered in a MOSFET pulse height spectrum, as shown in Chapter 5.3. The area under the LET spectra in Figure 5-18 represents the neutron dose at each depth in water. Therefore a measurement of area under the curves in Figure 5-18 yields information on the relative neutron dose. A relative total dose at different depths in the water phantom was obtained by measurement of the MOSFET threshold voltage shift simultaneously with microdosimetry measurements at each depth. The fast neutron beam at the Gershenson Oncology Center of Harper Hospital is regularly monitored and dose components are measured during a routine quality assurance process. At around the time when the MOSFET microdosimetry measurements were performed, Dr. Mark Yudelev of the Gershenson Oncology Center of the Harper Hospital, measured the total dose, and the neutron and gamma components of the dose, in the water tank by a paired ionisation chamber method. These data were used as a reference for comparison with MOSFET data (Figure 5-19).

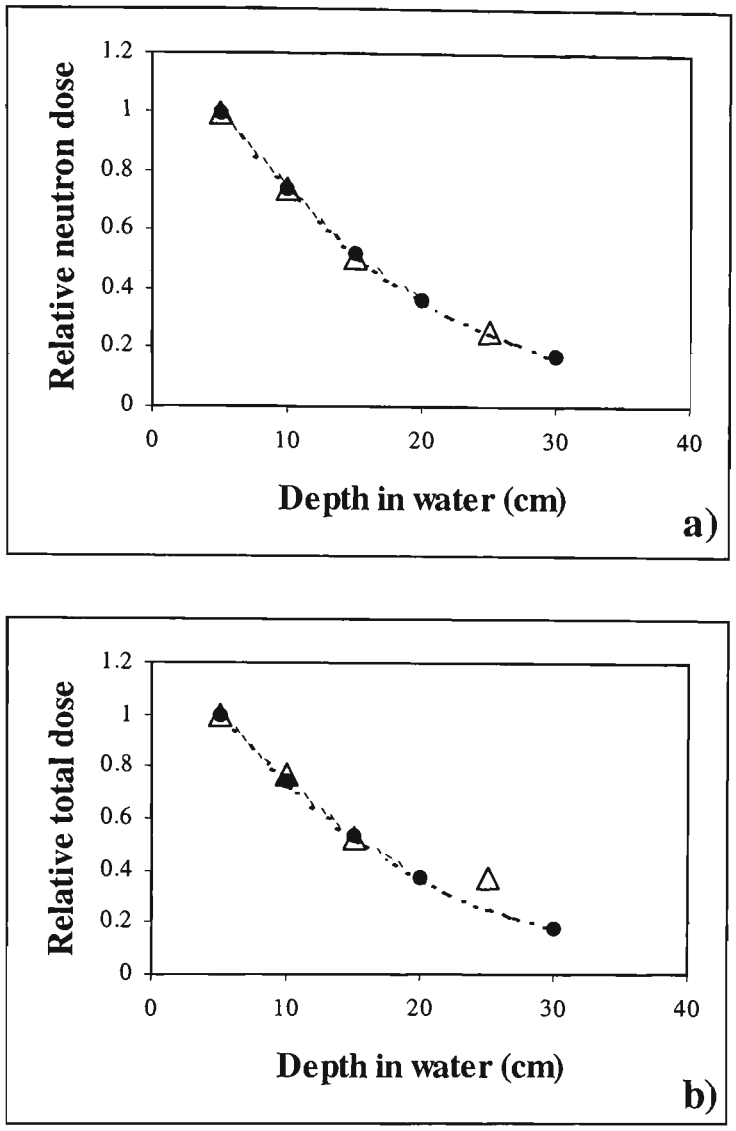

Figure 5-19. Neutron dose (a) and total dose (b) measured by a paired ionisation chambers (solid circles) and by a MOSFET detector (triangles) in along a central axis of a fast neutron beam in 10 cm × 10 cm radiation field, at different depths in the water tank.

The dose measured by MOSFET microdosimetry was compared to the dose obtained by the paired ionisation chamber method. The neutron dose in the water tank was normalised to the dose at 5 cm depth for both the paired ionisation chambers and for MOSFET microdosimetry method. The correlation between the two measurements was very good (Figure 5-19a).

Gamma radiation contributes about 3.5% to the total dose in FNT beam of the Harper Hospital facility at a depth of 5 cm in water, rising to 8.5% at a depth of 30 cm. Gamma dose data were measured by Mr. Mark Yudelev as part of a regular beam quality check. In order to evaluate the total dose from the MOSFET measurements, the MOSFET threshold voltage was measured simultaneously with microdosimetry measurements, that is at the start and at the end of each microdosimetry run. The total dose, as measured by an ionisation chamber and by the MOSFET threshold voltage shift, was normalised to the dose at 5 cm depth and it was plotted against depth in water (Figure 5-19b). Agreement between the two methods of measurement was good.

MOSFET dosimetry experiments at the fast neutron therapy facility demonstrated that a MOSFET can be applied as a microdosimeter. It was also demonstrated that a single MOSFET detector can measure both the total dose and microdosimetry quality of a neutron beam. A MOSFET detector, when applied simultaneously in count and in total dose modes, can efficiently separate a high LET dose, with its higher relative biological effectiveness, from the total dose.

5.5.3. Application of a MOSFET as a dual dosimeter at a BNCT facility

The application test of the MOSFET, as a dual radiation dosimeter, was conducted at the epithermal neutron irradiation facility of the Brookhaven Medical Research

Reactor, Brookhaven National Laboratory, NY, USA (see page 57 for the facility description).

The advantage of using a MOSFET detector in dual mode is that this dosimeter incorporates integral MOSFET dosimetry and charge collection spectroscopy in practically the same geometrical volume. The integral dose is measured using the threshold voltage shift, and the spectrum of deposited energy is measured using the drain-substrate p-n junction. Both low LET (gamma and electrons) and high LET (charged particles) radiation induce change to the MOSFET threshold voltage, while only high LET radiation is registered in the pulse height spectrum.

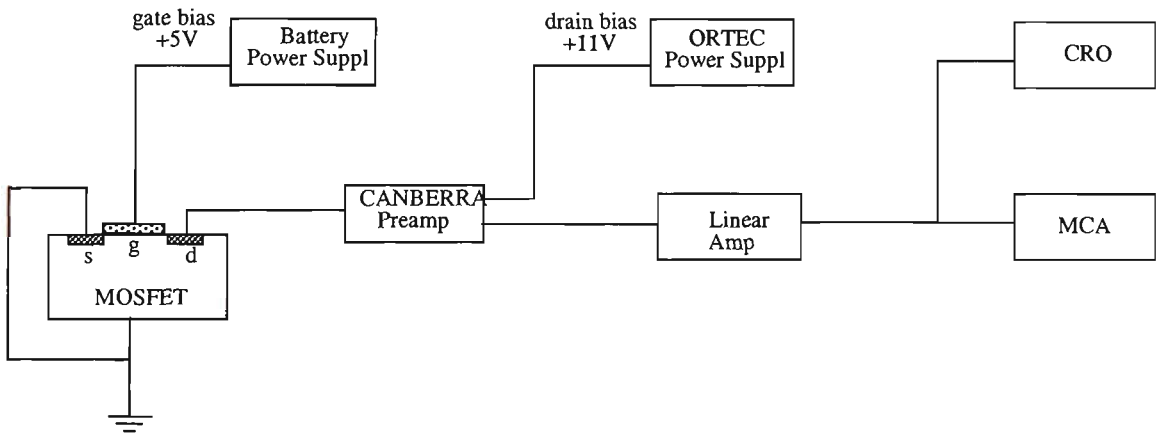

Figure 5-20. MOSFET connection diagram for simultaneous integral dosimetry and pulse height measurements at the epithermal neutron irradiation facility of BMRR.

The following set up was used for the spectroscopy measurements in the epithermal neutron irradiation facility at BMRR in a perspex phantom. The

MOSFET drain was connected to a standard spectroscopy setup and a charge sensitive preamplifier. The MOSFET gate was connected to an independently battery-operated bias voltage power supply (Figure 5-20).

A method using paired MOSFET detectors (see Chapter 3.6) was applied for boron response measurements in the BNCT beam at BNL. One of the MOSFETs had a boron-10 converter while the other did not. The MOSFETs were mounted in 6 mm diameter perspex rods. The lids of the MOSFETs were removed and replaced with perspex caps. One of the caps was loaded with epoxy containing ^{10}B enriched boric acid powder. The boron-10 concentration in the epoxy was about 1%, and the boron converter thickness was up to 0.5 mm. The epoxy did not make contact with the MOSFET chip surface, the air gap between the chip and the epoxy being about 1 mm. The detector rods were inserted into the holes in a perspex cube phantom with sides of 15 x 15 x 15 cm^3. A detailed description of the phantom is given in Chapter 3.5.1.

The paired MOSFETs were used simultaneously for pulse height spectrum and for threshold voltage measurements. The MOSFET drain-substrate p-n junction was biased to 11 V and the gate was independently biased to 5 V. The reactor power during irradiation was 3 MW, acquisition time for each pulse height spectrum was 20 minutes and all the measurements were performed at a depth of 1.25 cm along the central axis of the perspex cube phantom.

The pulse height spectrum acquired by the MOSFET without a boron converter shows very few counts with energy exceeding 200 keV (Figure 5-21a). The high

energy pulses are caused by the recoil nuclei. Pulses with energies between 200 keV and 500 keV are present in the spectrum acquired by the paired MOSFET with boron-10 converter (Figure 5-21b). These pulses were caused by the alpha particles of the boron neutron capture decay reaction. Both spectra were acquired at the same reactor power during the same acquisition time of 20 minutes. The difference of the two spectra shows a peak attributed to alpha particle pulses (Figure 5-21c). The maximum energy of the broad maximum is 0.5 MeV. The energy of an alpha particle of boron-10 decay is 1.5 MeV. It was demonstrated in Chapter 5.4, that an alpha particle with an incident energy of less than 4.5 MeV loses about 1 MeV of its energy due to ineffective charge collection in the MOSFET drain-substrate p-n junction. Thus the MOSFET collected energy of 1.5 MeV corresponds to the alpha particle incident energy of 2.5 MeV. The peak in the difference spectrum in Figure 5-21c has a lower energy, because the alpha particles originate from different depths in the thick boron converter and part of the energy is deposited inside the converter.

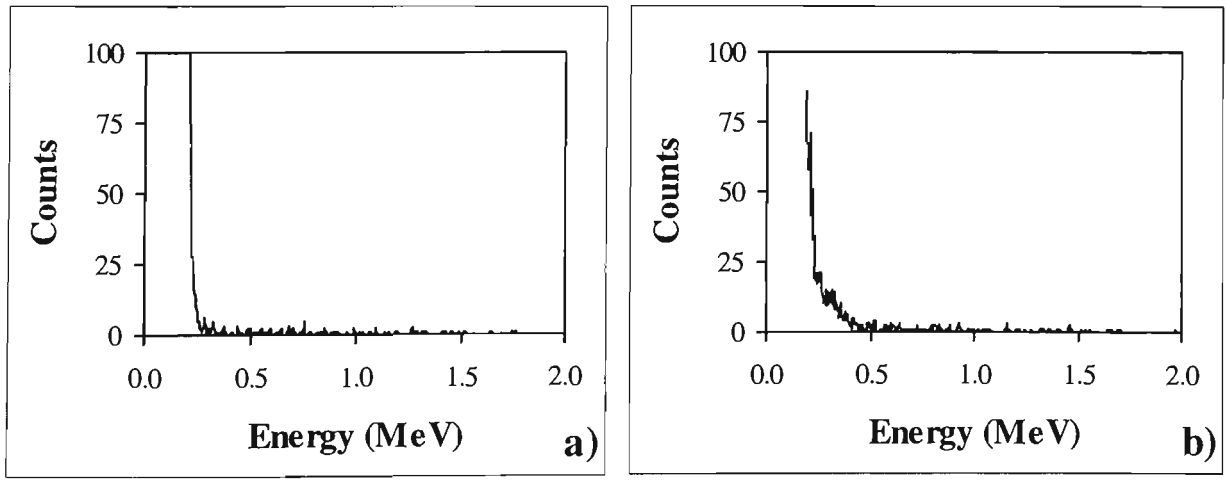

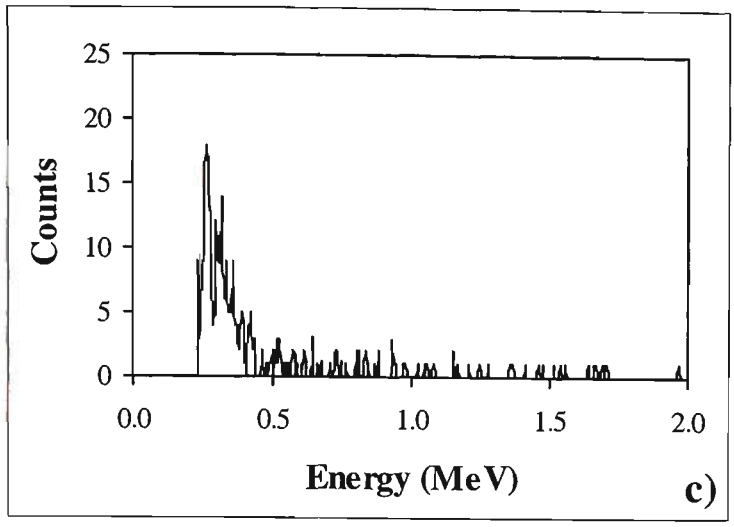

Figure 5-21. Pulse height spectra measured by a MOSFET drain-substrate p-n junction in a BNCT beam at a depth of 1.25 cm in a perspex phantom. a) - MOSFET without converter, b) - MOSFET with ^{10}B converter, and c) – difference spectrum b-a.

The total change in threshold voltage, during exposure in the epithermal neutron beam, of the MOSFET without the boron converter was 640 mV. The MOSFET with the boron-10 converter, after an exposure of the same duration, changed its threshold voltage by 1335 mV. Thus the difference in threshold voltage change of 695 mV was caused by boron dose enhancement. The boron dose threshold voltage change is caused by the high LET particles released in the boron neutron capture decay reaction and is proportional to the area under the curve in the difference spectrum (Figure 5-21c).

The dose enhancement measured by a MOSFET detector is a physical dose. The biological dose is significantly higher. The relative biological effectiveness (RBE) of products of boron neutron capture reaction is taken for BNCT calculations as

approximately 3.5 (Coderre & Morris, 1999). Thus the same physical dose is three and a half times more effective in producing biological damage if it is delivered by alpha particles than by low LET radiation.

The experiments at the BMMR demonstrated that an application of a MOSFET detector in dual mode, together with the paired MOSFET technique, can be applied for separation of high and low LET components in mixed neutron-gamma-alpha radiation field of BNCT. It is possible to calibrate paired MOSFET response in count mode to convert the area under the boron difference peak to a change in threshold voltage. Calibration measurements should be performed in a range of exposures and boron-10 concentrations. Calibration was outside the scope of this research project, which was to develop a dual detector technique and to demonstrate its application in BNCT. Calibration requires extra resources, including considerable reactor time, which were not available to us for the project.

5.6. Conclusions

It was demonstrated in the course of these studies that a MOSFET detector with 1 μm thick gate oxide is sensitive to alpha radiation. The MOSFET threshold voltage changed linearly with the exposure time in a beam of ^{241}Am alpha particles. Americium-241 emits a 60 keV gamma ray during each act of alpha decay. An experiment was designed to prove that most of the MOSFET threshold voltage change, after exposure to ^{241}Am, was caused by alpha radiation. Gamma radiation was responsible for less than 6% change in threshold voltage. These

experiments confirmed one of the initial hypothesis of this project, that a MOSFET can be used successfully as an alpha dosimeter.

High LET radiation deposits a measurable amount of energy in a reversed biased p-n junction of a MOSFET detector. There are two p-n junctions in a MOSFET structure: drain-substrate and source-substrate p-n junctions. Charge collection by each of them separately and by both of them simultaneously was investigated by measuring the pulse height spectra of alpha radiation. Energy spectra of ^{241}Am and ^{210}Po alpha particles were acquired for different connection configurations of the MOSFET dosimeter. Analysis of the experimental data revealed that the drain-substrate p-n junction is the most suitable for acquisition of a spectrum of energy loss of high LET radiation in the sensitive volume of the p-n junction. The gate contact of a MOSFET detector can be biased independently from the drain-substrate p-n junction or by the same power supply. A pulse height spectrum can be acquired by a p-n junction of a MOSFET detector simultaneously while measuring the total dose by change in the detector threshold voltage. Both measurements are performed independently of each other. The MOSFET gate surrounds the drain, with a gap between them of only a few micrometers. Thus the total absorbed dose and the pulse height spectrum are measured in practically the same silicon/silicon oxide volume of the MOSFET detector.

It was shown that low LET gamma and beta radiations deposit very little energy in the thin sensitive volume of the MOSFET drain-substrate p-n junction, while both high and low LET radiation induce change in the MOSFET threshold voltage. This makes it possible to separate doses delivered by low and high LET radiation.

High energy alpha particles or protons lose only a part of their energy in the sensitive volume of a MOSFET detector. The pulse heights spectrum measured by the MOSFET drain-substrate p-n junction is not an energy, E, spectrum, but rather an energy loss, $\frac{dE}{dx}$, or a microdosimetry spectrum. To convert energy, E, to lineal energy, l, used for microdosimetry representations, the geometrical dimensions of the sensitive volume are required. Alpha particles of different energies were applied in order to characterise the sensitive volume. The energy of alpha particles from an available ^{241}Am source was moderated by a set of several micron thick mylar films. The effective thickness of the sensitive volume of a MOSFET drain-substrate p-n junction, as measured by an alpha probe, is equal to the range in silicon of alpha particles of 4.5 MeV. Calculation of the range of 4.5 MeV alpha particles yielded, for the effective depth of the sensitive volume, the value of 14 μm.

This new approach to semiconductor microdosimetry and to dual high and low LET dosimetry by the same MOSFET detector was tested in the Fast Neutron Therapy beam of the Superconducting Cyclotron of Harper Hospital, Detroit, USA and in the BNCT epithermal neutron beam of the Brookhaven Medical Research Reactor of Brookhaven National Laboratory, NY, USA.

The microdosimetry spectra measured by the MOSFET drain-substrate p-n junction in a FNT beam were in a good agreement with tissue equivalent gas proportional chamber measurements. The measurements were performed at four

different depths in a water tank. The area under the microdosimetry spectra, at each depth, is proportional to neutron dose. The relative neutron dose depth distribution curve coincided with the neutron dose measured by a reference paired ionisation chamber method. The relative total dose depth distribution, measured simultaneously with microdosimetry spectra by MOSFET threshold voltage change, was in a good agreement with the relative total dose measured by an ionisation chamber. The relative total dose was measured simultaneously with the microdosimetry spectra by the same MOSFET detector. The relative total dose, measured by the MOSFET, was in a good agreement with independent ionisation chamber measurement.

Paired MOSFET measurements in an epithermal neutron beam at BNL allowed separation of boron-10 enhancement of the dose. One of the paired MOSFETs had a ^{10}B converter above the silicon chip. The other MOSFET was a reference detector without a converter. The MOSFETs were applied in dual mode with both pulse height spectra and threshold voltages were measured simultaneously.

In summary, the research presented in this chapter introduced a new dosimetry method of separating the high and low LET radiation contribution to total radiation dose in a mixed radiation field by a single MOSFET detector applied in dual mode.

Chapter 6. Semiconductor probes for thermal neutron flux and dose measurements in neutron therapy modalities

Boron Neutron Capture Therapy is a binary radiation oncology modality. In BNCT a tumour volume is selectively loaded with a boron-10 containing compound followed by irradiation by an epithermal or thermal neutron beam. A thermal neutron is captured by ^{10}B, which decays releasing a short range high LET radiation. BNCT is currently undergoing clinical trials in the USA, Japan and Europe. It was proposed to enhance the effect of Fast Neutron Therapy and Californium-252 Brachytherapy by boron neutron capture. Thermal neutron flux at target depth, combined with selctive introduction of ^{10}B into the cancer cells, is the main parameter which determines the therapeutic effect of a neutron capture therapy. Accurate determination of thermal neutron flux and boron dose is important for the above modalities.

6.1. Aim

The aims of studying the solid state detector response at neutron therapy facilities were :

⇒ Testing of new designs of detectors and fission converters applied to silicon detectors and MOSFETs

⇒ Testing and application of a novel absolute detector method of thermal neutron flux measurement by a silicon detector with a thick ^{235}U fission converter, and comparison with Monte Carlo calculations in epithermal BNCT

⇒ Application of a new method of using paired MOSFET detectors for in-phantom boron response measurement, and comparison of the response curve with depth distribution of thermal neutron flux.

⇒ Confirmation of the most efficient depth for tumour treatment in epithermal and thermal BNCT

⇒ Measurement of in-phantom depth and lateral thermal neutron flux distribution in thermal BNCT

⇒ Estimation of the boron response in boron neutron capture enhanced fast neutron therapy and an evaluation study of the feasibility of BNCEFNT

6.2. Methods of thermal neutron dosimetry at neutron radiation therapy facilities

As described in details in Chapter 2.1, tumour control in BNCT results from the exposure of cancer cells to the products of a $^{10}B(n,\alpha)^{7}Li$ reaction. Boron-10 captures a neutron and decays releasing an alpha particle and a ^{7}Li ion. Both reaction products have a short range, high linear energy transfer (LET) and are efficient in sterilising a biological cell. In FNT the therapeutic effect is due to the effect of high-LET secondary radiation which is produced by the interaction of fast neutrons with a tissue. Boron Neutron Capture Enhanced FNT (BNCEFNT)

has been proposed (Maughan *et al.*, 1997; Sauerwein *et al.*, 1989) for further improvement of effectiveness in tumour control.

The cross-section of the boron neutron capture reaction, σ, depends strongly on neutron energy. The cross-section has a maximum value for thermal neutrons and decreases as $\sigma \propto E^{-\frac{1}{2}}$ with increasing neutron energy (Lamarsh, 1966). For achieving optimal sterilisation, a tumour undergoing BNCT or BNCEFNT must be exposed to thermal neutrons. The problem is that thermal neutrons have a low penetration ability in tissue (the half value layer is less then 2 cm, dependent on field size (Fairchild & Bond, 1985)). To deliver a significant fluence of thermal neutrons to a deep tumour the irradiation has to be performed with an epithermal neutron beam. Epithermal neutrons are moderated in tissue, producing thermal neutrons at increased depth in the tumour. This makes experimental measurement of thermal neutron flux distribution at depth in a phantom important for dose planning and validation of Monte Carlo calculations. Measurement of the thermal neutron flux in a mixed neutron-gamma field is a complicated and time consuming task. Several dosimetry methods have been developed and applied to radiation therapy neutron beams.

6.2.1. Foil activation method

If the induced gamma activity of the fission products is measured after the irradiation, the fissile material can be used as an activation detector, like an activation foil (ICRU, 1969). However, induced gamma activity is often a low

intensity process which limits the accuracy of the measurement. Application of several foils of different compositions allows measurement of neutron flux in different ranges of neutron energies, including evaluation of neutron flux of a neutron source.

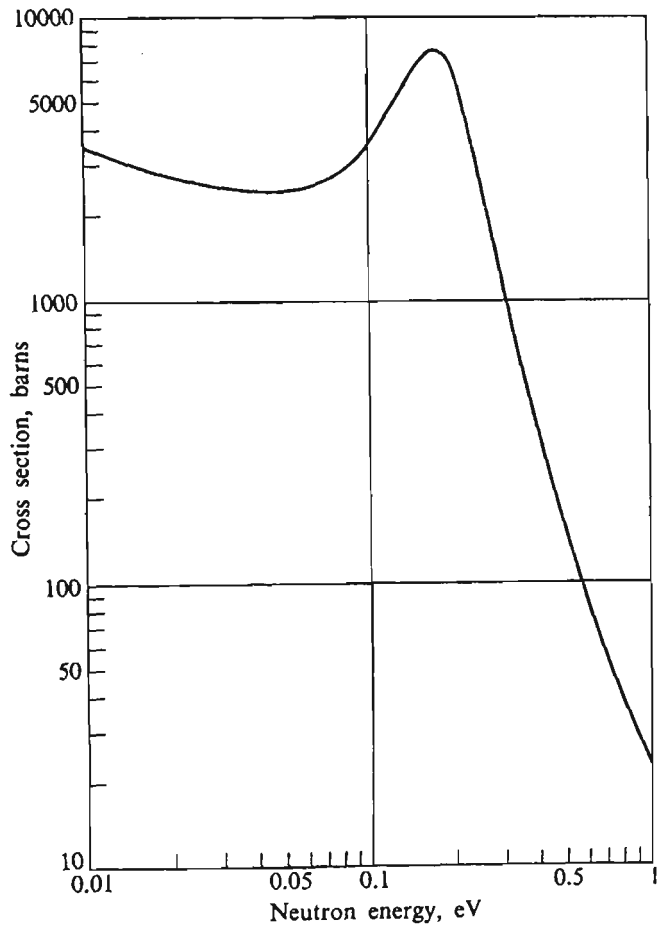

Figure 6-1. Cadmium neutron capture cross section for low energy neutrons (from (BNL, 1958)).

More often measurements of thermal neutron fluence are based on a cadmium difference method. Neutron induced activity of a thin foil is measured for a bare foil (A) and for the foil wrapped in cadmium (A_{Cd}). Cadmium neutron capture cross-section is very high for low neutron energies and drops sharply at an energy

of about 0.4 eV (see Figure 6-1). As a result, essentially all the neutrons with energies below a threshold of 0.4 eV to 0.55 eV are absorbed. The exact cutoff energy depends on the thickness of the cadmium foil. The thermal neutron flux (Φ) can be calculated as

$$\Phi = \frac{A - A_{Cd}}{N\sigma_0 g}$$

where N is the number of atoms available for activation, σ_0 is the neutron capture cross-section for neutron velocity (v) of 2200 ms^{-1} and g is a correction factor for deviation of the neutron cross-section from the $1/v$ law. In most cases g is close to unity.

The foil activation method is widely applied at neutron therapy facilities. In the majority of investigations of thermal neutron flux with activation foils, gold foils were used (Carolan *et al.*, 1994; Liu *et al.*, 1996; Raaijmakers *et al.*, 1997; Raaijmakers *et al.*, 1995; Raaijmakers *et al.*, 1996a; Sofar *et al.*, 1990; Tattam *et al.*, 1998).

Characterisation of the thermal neutron component of the High Flux Reactor beam in Petten, the Netherlands, was performed with a set of two activation foils, using the cadmium difference method (Raaijmakers *et al.*, 1995; Raaijmakers *et al.*, 1996b). The two foils were Au and Mg. The exact compositions of the foil were AuAl (5 wt % Au), thickness 0.2 mm, and MgNi (88 wt % Mg), thickness 0.1 mm. With the assumption that a simplified neutron energy spectrum which

consists of a Maxwell distribution of thermal neutrons coupled with an 1/E spectrum of higher energy neutrons, the saturation activation reaction rates are

$$\alpha_{Mn} = \varphi \cdot \sigma_{Mn} + \theta \cdot I_{Mn}$$
$$\alpha_{Au} = \varphi \cdot \sigma_{Au} + \theta \cdot I_{Au}$$

where α is the saturation reaction rate per unit mass of foil, σ is the thermal neutron cross section of the corresponding nuclear reaction, I is the reaction resonance integral, φ is the thermal neutron fluence and θ is the intermediate neutron fluence. For calculation of thermal and epithermal neutron fluxes the following values were used

$$\sigma_{Mn} = 1.330\times10^{-23}\ cm^2; \quad I_{Mn} = 1.400\times10^{-23}\ cm^2$$
$$\sigma_{Au} = 9.865\times10^{-23}\ cm^2; \quad I_{Au} = 1.550\times10^{-23}\ cm^2$$

Reaction rates were determined using a 846.7 keV line of ^{56}Mn and a 411.8 keV line of ^{198}Au. The cross sections of both foils, to neutrons with energy above 10 eV, are low. Measurements by the cadmium difference method with Au foil were affected by 4.9 eV neutron cross-section resonance. The agreement between the two foils and using the cadmium difference methods was within 2 %. The maximum thermal neutron flux was observed at a depth of 2 cm in water. For the reactor power of 45 MW the maximum flux was $7\times10^8\ n\cdot cm^{-2}\cdot s^{-1}$.

A foil activation cadmium difference method was applied at the BMRR epithermal neutron irradiation facility for in-phantom thermal neutron fluence

measurements (Liu *et al.*, 1996). The measurements were performed in a 14 cm side cube perspex phantom. The very thin Au foils of 0.0127 mm thickness with a diameter of 8 mm were used bare and Cd-covered. Induced activity of a 411.8 keV gamma line was measured after irradiation by a NaI(Tl) well-type detector. The estimated uncertainty of the measurements was 6%. Measurements were compared with MCNP Monte Carlo calculations of thermal neutron flux. Thermal neutron flux measurements along the central axis of the perspex cube exceeded computed values by 2.5%. The thermal neutron flux measured along the line parallel to the central axis, but shifted by 1/4 along the direction to the cube edge, parallel to the beam, was 4.5% to 6% less than the calculated flux.

The measurement of thermal neutron flux distribution in an epithermal beam of the M-057 port of an MITR-II reactor in an ellipsoidal water-filled phantom was performed by a gold foil activation method (Hardling *et al.*, 1994). Reactor power during measurements was 5 MW. A maximum in thermal neutron flux, of 7×10^{8} $n\cdot cm^{2}\cdot s^{-1}$, was observed in a depth of 1 cm to 3 cm in water.

6.2.2. Fission chamber

Fission methods for determination of neutron dosimetric characteristics, such as neutron flux or kerma, are based on neutron-induced fission reactions (ICRU, 1984). Direct counting of fission products allows absolute, and in some cases accurate, measurement of neutron fluence. To achieve this a fissile material is

incorporated into the walls of a detector or is placed/deposited as a thin converter on the entrance window of the detector.

Initially the fission chamber dosimetry method was developed for the monitoring of thermal neutron flux in the core of a nuclear reactor (Böck & Balcar, 1975). Later the fission chamber technique was adopted at neutron therapy facilities.

Two ^{235}U fission chambers covered with Cd were used for beam monitoring at the High Flux Reactor in Petten, the Netherlands (Raaijmakers *et al.*, 1996a). They were positioned between the main beam shutter and the gamma shutter and were used for relative comparison of the beam intensity. Two fission chambers with depleted uranium coating were used for in-air neutron beam intensity monitoring at the epithermal neutron irradiation facility at the Brookhaven Medical Research Reactor (Liu *et al.*, 1996). The chambers are covered by 2 mm thick lithium metal (95% ^{6}Li enrichment) to cut the thermal neutrons. A fission chamber was also used for in-air measurement of epithermal neutron flux across the neutron beam. In-air epithermal neutron flux in the collimator plane was measured as 8.4×10^{8} $n\cdot cm^{2}\cdot s^{-1}$.

Use of a $^{10}BF_3$ proportional counter is based on decay of boron-10 caused by thermal neutron capture and measurement of the count rate of the decay reaction $^{10}B(n,\alpha)^{7}Li$ or charge. A 12.7 mm diameter and 50 mm active length $^{10}BF_3$ tube was used in a Birmingham accelerator based BNCT beam (Tattam *et al.*, 1998). Measurement in proportional counter mode allows discrimination against gamma events. The large size of the counter may limit the spatial resolution of the

measurements and may disturb the in-phantom neutron flux. The agreement between experimental results and Monte Carlo calculation was within 10% for depths up to 9 cm and 20% for greater depths. A similar $^{10}BF_3$ chamber was used in an accelerator produced epithermal neutron beam at Ohio University during research of boron dose distribution in a water head phantom (Gupta *et al.*, 1994).

At BMRR, a $^{10}BF_3$ chamber was applied in 14×14×14 cm^3 and 11×11×11 cm^3 perspex cube phantoms for measurement of neutron flux (Alburger *et al.*, 1998). The chamber was 6 mm in diameter and 25 mm long and was filled with $^{10}BF_3$ gas at a pressure of 1350 Torr. The chamber was operating at a bias of 1250 V. Measurements were performed in a count mode at the reactor power of 50 W and scaled to the reactor power of 3 MW by applying a numerical factor of 60,000. The thermal neutron flux measured and converted to 3 MW power in a 14×14×14 cm^3 phantom at a depth of 2.5 cm was 1.5×10^9 $n\cdot cm^{-2}\cdot s$. The flux was not compared with an independent measurement or calculation. Our Monte Carlo MCNP calculations for a similar sized phantom exceeded the quoted value by 13% (see Figure 6-10). High operating voltage is another disadvantage of a $^{10}BF_3$ chamber, because it rules out chamber applications for patient dosimetry.

More recently a magnesium ionisation chamber, with ^{10}B coated walls (a 3 μm thick layer of ^{10}B), was used for measurements of thermal neutron flux around two brachytherapy ^{252}Cf sources (Schmidt *et al.*, 1999). The californium brachytherapy facilities were located at Harper Hospital in Detroit, MI, USA and at the University Hospital in Chiang Mai, Thailand. The doses were measured in water.

The chamber was operating with argon flow at a rate of 17 cm^3/min. The chamber was calibrated in a ^{60}Co beam and in a homogeneous thermal neutron flux of mean energy of 37 meV. The sensitivity to thermal neutrons was

$$R(4\pi, 37\ meV) = 1.02 \times 10^{-7}\ nC \cdot cm^2/neutron$$

The KERMA factor for muscle at a neutron energy of 37 meV was taken as 2.31×10^{-13} Gy·cm^2. The total KERMA for ^{10}B dose was taken as 4.30×10^{-12} Gy·cm^2 for a boron concentration of 50 ppm (Konijnenberg *et al.*, 1995). KERMA for the $^{10}B(n,\alpha)$ reaction was 4.27×10^{-13} Gy·cm^2 and for the $^{10}B(n,\gamma)$ reaction KERMA was 0.027×10^{-13} Gy·cm^2. The combined error of measurements was estimated to be 6.5%.

A method using paired tissue equivalent Rossi type gas proportional counters was applied for neutron dosimetry and microdosimetry in FNT and fast neutron ^{252}Cf beams at Harper Hospital, Detroit, MI, USA by Kota *et. al.* (Kota *et al.*, 2000). The counters were identical, with walls of tissue equivalent plastics A-150. The walls of one of the counters were loaded with 50 ppm of ^{10}B. The effective tissue equivalent energy loss volume of the chambers was 0.5 μm in diameter. The tissue equivalent volume can be adjusted by a change in the chamber gas pressure. The chambers were calibrated by proton edge energy loss calculated for the chamber volume. The total uncertainty of the chamber measurement was estimated at about 5%. The method allowed measurements of microdosimetry spectra as well as

gamma and neutron doses. The uncertainty in measurement of the boron dose was up to 40%.

The thermal neutron flux of the epithermal neutron beam of the Massachusetts Institute of Technology Research Reactor (MITR-II) was monitored by ^{3}He filled ion chambers operating in a current mode (Solares *et al.*, 1997). The chambers were about 1 cm in diameter and a few centimetres in sensitive length. They provided relative data on thermal neutron flux.

A ^{3}He filled proportional chamber was applied for characterising an accelerator produced neutron beam at the Ohio State University (Dobelbower *et al.*, 1999). The detector was 44 mm in length and 7 mm in diameter. The detector was filled with ^{3}He gas under pressure of 40 atm. The detector was calibrated in a Pu-Be neutron source radiation field using the gold foil activation method to measure the neutron flux. Measurements differed by an average of 10% from the Monte Carlo calculated data points.

The disadvantage of a fission chamber detector is its relatively large size, which may be responsible for radiation field perturbation. A fission chamber operating in current mode needs to be calibrated in known thermal neutron and gamma radiation fields. A fission chamber has to be used paired with a gamma chamber for separate measurement of dose components in the mixed neutron-gamma radiation field of a nuclear reactor or accelerator.

Other methods have also been applied for in-phantom measurements of the thermal neutron flux in a neutron therapy beam. Thermoluminescent dosimeters (TLDs) were used in the fast neutron therapy beam of the Biomedical Cyclotron in Nice, France (Pignol *et al.*, 1998) for dosimetry of boron neutron capture enhancement of FNT. One set of LiF TLDs was doped with ^{6}Li and the other one with ^{7}Li. The difference was taken to be a characteristic of thermal neutron fluence. This method does not appear to be very accurate as both lithium isotopes were actually present in each set of TLDs, however if both concentrations are known than the actual fluxes can be derived by solving simultaneously of two linear equations.

6.2.3. Solid state fission detector

A fission detector is an absolute radiation detector for measurement of a neutron fluence. A radiation dosimeter can be regarded as absolute if its construction and application allows measurement of a certain radiation quantity without calibration in a known radiation field. A solid state fission detector provides an alternative method of thermal neutron flux measurement, which has been used in nuclear reactor applications and described elsewhere (Kozlov *et al.*, 1977; McKenzie & Bromley, 1959; Pospisil *et al.*, 1993). A fission detector requires a single irradiation with no post-irradiation measurement of neutron induced activity, and it does not require a calibration in a known radiation field. It also offers a possibility of on-line monitoring of thermal neutron flux and of on-line testing of radiation damage to a silicon detector caused by neutrons and fission fragments.

A silicon alpha particle detector with a ^{6}Li converter was applied for thermal neutron flux measurements using the epithermal BNCT beam of the HFR, Petten (Raaijmakers *et al.*, 1997). The detector was a 10 mm^2 silicon alpha detector with a $^{6}Li_2CO_3$ converter. The converter plate was mounted in a 15×15×15 cm^3 perspex phantom and positioned opposite the detector chip. The air gap between the converter plate and the entrance window of the detector was 2 mm. The detector was calibrated against activation foil measurements and only relative measurements of thermal neutron flux were made.

The ^{235}U and ^{6}Li fission converters were used with a silicon diode for beam monitoring of the neutron therapy beam in Japan (Hayakawa *et al.*, 1996; Matsumoto & Aizava, 1988), but the application did not allow absolute measurement of thermal neutron fluence.

A solid state fission detector, with a uranium-235 converter for thermal neutron fluence measurements, utilises a high thermal neutron capture cross section of the uranium-235 nucleus. The cross section is maximal for the thermal neutron energies and it decreases as $1/v$, with one broad resonance, while energy increases to about 0.3 eV (see Figure 6-2). More resonances are observed in the energy range of 1 eV to 1000 eV.

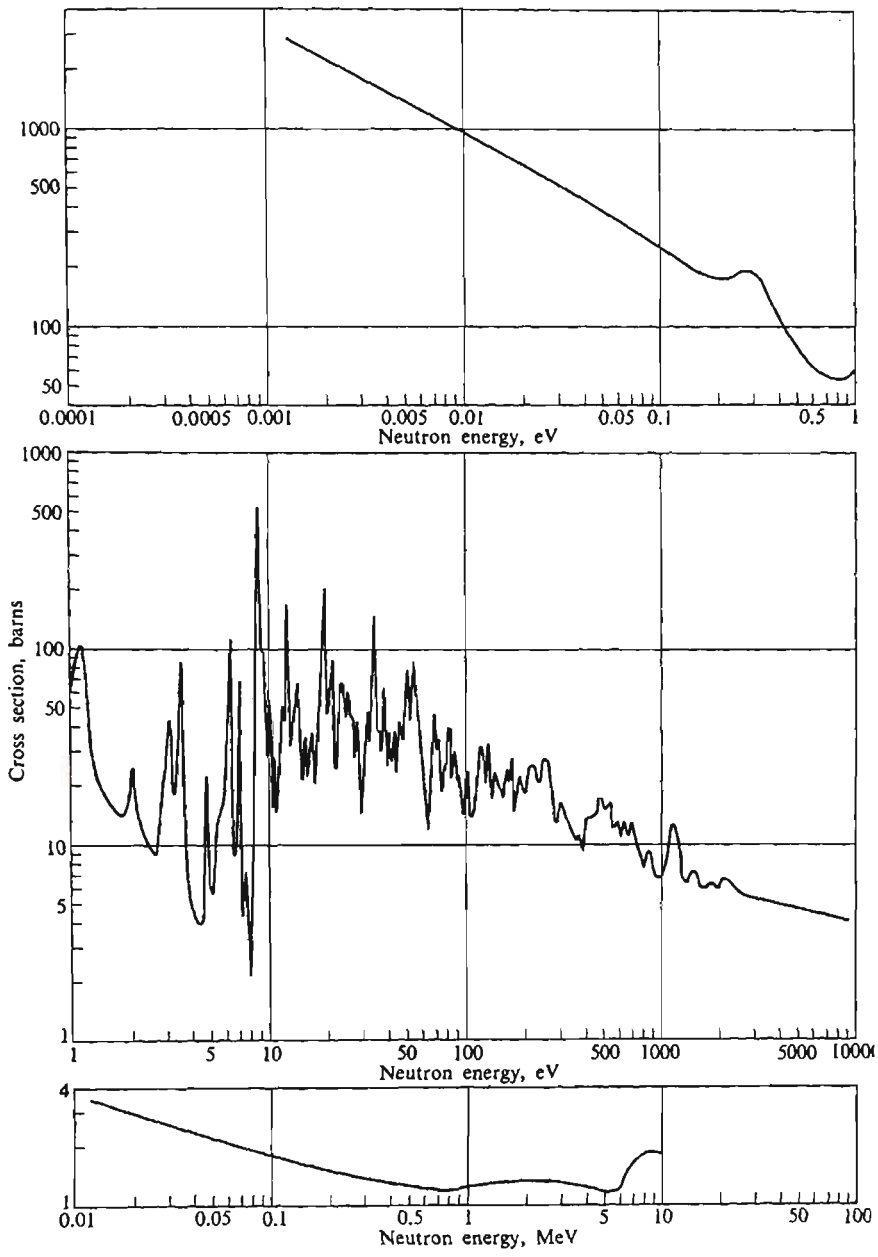

Figure 6-2. ^{235}U neutron capture cross section (from (BNL, 1958)).

After capture of a neutron, the ^{235}U nucleus decays releasing two fission fragments. Mass distribution of the fragments depends on the energy of the neutron (Figure 6-3). The energy resolution of a solid state ^{235}U fission detector and exact positions of the fragments peaks on the pulse height spectrum depends on the thickness of the converter (Lerche *et al.*, 1972). A uranium oxide deposit enriched to 93% ^{235}U was prepared by vacuum evaporation. The thickness of the

uranium oxide varied from 5 to 400 μg/cm^2. The energy resolution of the pulse height spectrum is decreasing and the peaks move to lower energy region. For minimal distortion of the spectrum the thickness of uranium a converter should not exceed 50 μg/cm^2, or about 0.06 μm.

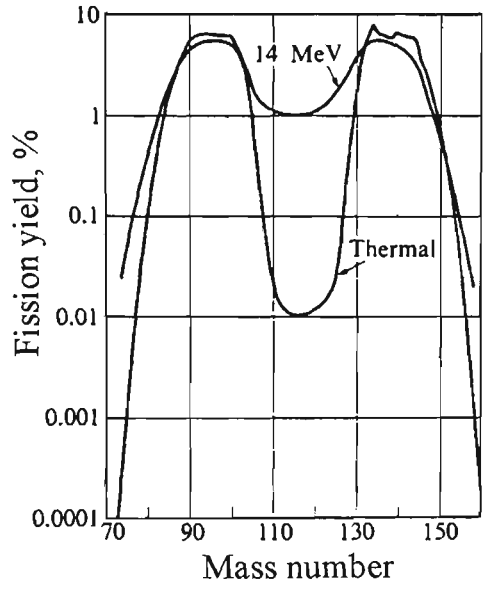

Figure 6-3. Mass distribution of fragments of ^{235}U neutron capture fission when irradiated by 14 MeV and thermal neutrons (from (Turner, 1992)).

6.3. Ion implanted silicon detectors

A 3×3 mm^2 ion implanted silicon detector, manufactured by SPA Detector Ltd, Ukraine, was used for measuring a pulse height spectrum. The energy resolution of the silicon detector was 15 keV, as measured for 5.48 MeV alpha particles.

Two other identical detectors were also used in this study. A uranium fission converter detector had a ^{235}U converter placed on its surface (see Chapter 6.3.1). A second fission detector had a boron converter made by depositing on its surface a plastic (perspex based) film containing 1% by weight of ^{10}B. The thickness of the film was about 0.1 mm. The third detector was a reference detector without a cover. It was used in a paired detector method for comparison with the fission detectors.

6.3.1. Fission detector with a thick uranium-235 converter

The main part of the fission detector used in this study was a 150 μm thick uranium oxide (99.25% ^{235}U enrichment) converter (Figure 6-4). The converter was deposited onto aluminium foil. A piece of approximately 1.5 mm × 2 mm in size was cut out of the foil and placed in contact with the surface of a small sized (3x3 mm^2) ion implanted silicon detector. The uranium coated side of the aluminium foil was in contact with the detector surface.

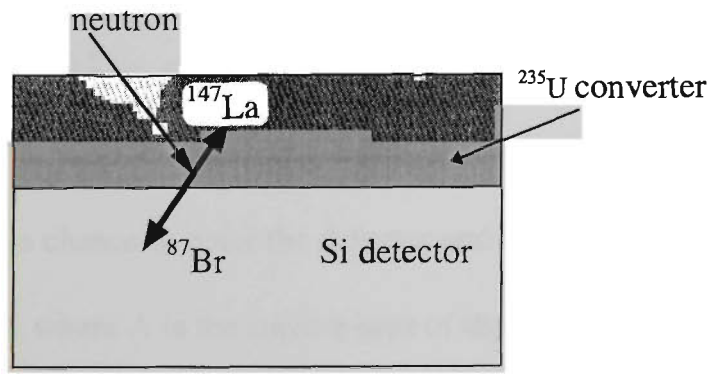

Figure 6-4. Sketch of a fission converter silicon detector

When ^{235}U captures a thermal neutron, it fissions with a probability of p=85% (Turner, 1992) into one of about 40 modes. A typical nuclear reaction is:

$$ {}^{1}_{0}n + {}^{235}_{92}U \rightarrow {}^{147}_{57}La + {}^{87}_{35}Br + 2{}^{1}_{0}n \qquad (6\text{-}1) $$

Two heavy fragments move in opposite directions and carry a total kinetic energy of 162 MeV (Turner, 1992). In a pulse height spectrum the high energy and high LET fragments will be well separated from low LET gamma background and recoil protons produced by neutron interactions with the phantom material. This separation makes the fission detector efficient for thermal neutron fluence measurements in a mixed radiation field. The fast neutrons, which are released in the ^{235}U fission reaction (Equation 6-1) with an energy of about 1 MeV, have a low cross-section of interaction with ^{235}U (see Figure 6-2) and for this reason are not re-captured by ^{235}U and do not trigger a further fission reaction in the converter.

The range of 4.5 MeV alpha particles in uranium released in spontaneous alpha decay of uranium-235, as calculated by TRIM (Ziegler *et al.*, 1985), is R_α=7.37 μm. Only an alpha particle originating within the layer of thickness R_α, adjacent to the detector, has a chance to enter the detector and to be registered. The volume of this layer is $R_\alpha \cdot A$, where A is the surface area of the converter. The total number of ^{235}U atoms in the R_α thick layer is $N_U = n_U \cdot R_\alpha \cdot A$, where n_U is the volume concentration of ^{235}U atoms in the converter. If a spontaneous alpha decay of a

uranium atom occurs at the depth x under the surface of the converter ($x \leq R_\alpha$), the alpha particle reaches the detector only if it is projected within the cone of solid angle Ω (Figure 6-5).

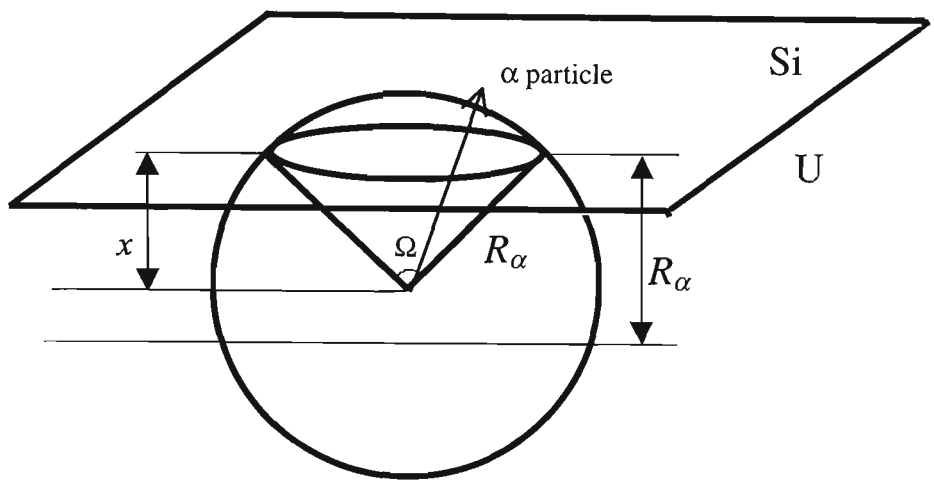

Figure 6-5. Sketch of the geometry of an alpha particle or decay particle production in the uranium converter of the fission detector (below the horizontal plane) and particle entering the silicon detector (above the plane).

We assume that the angular distribution of alpha particles is isotropic. The fraction of alpha particles, which is registered after being emitted from a depth x (Figure 6-5), equals the ratio of the part of the surface area of a sphere of radius R_α above the converter surface to the total surface area of the sphere

$$\frac{2\pi \cdot R_\alpha (R_\alpha - x)}{4\pi \cdot R_\alpha^2} = \frac{R_\alpha - x}{2R_\alpha}$$

If the rate per second of disintegrations within the layer of thickness R_α is A_t, then the detector registers N_α alpha particles per second, ie:

$$N_\alpha = \frac{A_t}{R_\alpha}\int_0^{R_\alpha}\frac{R_\alpha - x}{2R_\alpha}dx = \frac{A_t}{4}, \qquad \text{or}$$

$$A_t = 4N_\alpha \tag{6-2}$$

The number of uranium atoms in a R_α thick layer of the uranium converter can be calculated as

$$N_U = \frac{A_t \cdot \tau}{\ln 2}, \qquad \text{or}$$

$$n_U = \frac{4N_\alpha \cdot \tau}{R_\alpha \cdot A \cdot \ln 2} \tag{6-3}$$

where τ is the half life of ^{235}U, $\tau = 7.1\times10^8$ years (Turner, 1992).

For calculating the response of the fission detector we assume that in a radiation field of thermalised neutrons the angular distribution of ^{235}U fission fragments is close to isotropic. For simplicity we also assume that all of the fission reactions proceed in one mode and ^{147}La and ^{87}Br nuclei are released. Kinetic energy of each fragment separately can be calculated by applying conservation of kinetic energy and linear momentum laws; $E_{La} = 60$ MeV and $E_{Br} = 102$ MeV. Ranges of

the fragments, as calculated by TRIM, equal R_{La} = 4.35 μm and R_{Br} = 6.23 μm. Note: $R_\alpha > R_{Br} > R_{La}$. Only ^{147}La nuclei produced within R_{La} layer and ^{87}Br nuclei produced within R_{Br} layer can reach the detector. As for the above alpha particle consideration (Figure 6-5 and Equation (6-2)), only one quarter of the fragments produced within the corresponding layers will be registered. The number of ^{147}La nuclei, N_{La}, registered by the detector per second equals

$$N_{La} = \tfrac{1}{4}\Phi \cdot p \cdot \sigma \cdot n_U \cdot R_{La} \cdot A$$

where Φ is the thermal neutron flux and p is probability of decay. Similarly the number of ^{87}Br nuclei, N_{Br}, registered by the detector per second equals

$$N_{Br} = \tfrac{1}{4}\Phi \cdot p \cdot \sigma \cdot n_U \cdot R_{Br} \cdot A$$

Because both of the fragments have a spherically uniform distribution of the velocities, the total flux of fission products registered by the detector equals $N_f = N_{La} + N_{Br}$. Substituting N_U from Equation (6-3), the thermal neutron flux equals

$$\Phi = \frac{N_f \cdot R_\alpha \cdot \ln 2}{p \cdot \sigma \cdot N_\alpha \cdot \tau \cdot (R_{La} + R_{Br})} \qquad (6\text{-}4)$$

This equation will be later used for calculation of thermal neutron flux.

6.4. Experimental set up and calibration

Experimental measurements of thermal neutron flux and boron response in therapeutic neutron beams were performed at epithermal BNCT, thermal BNCT and at FNT facilities.

For measurements in neutron beams, MOSFETs, including RADFETs, and silicon detectors were mounted in perspex rods and were inserted into perspex blocks of a perspex cube phantom. The blocks were held together by two perspex screws with perspex nuts and washers. The phantom had linear dimensions of 15 x 15 x 15 cm^3 and the depth in the phantom was adjusted by changing the position of the blocks. The phantom is described in detail in Chapter 3.5.1. Measurements at the FNT facility at the Gershenson Oncology Center of Harper Hospital, Detroit, USA (see Chapter 3.4.4 for the facility description) were also performed in a water phantom (Figure 6-6). For waterproofing the detectors were inserted into thin latex sleeves.

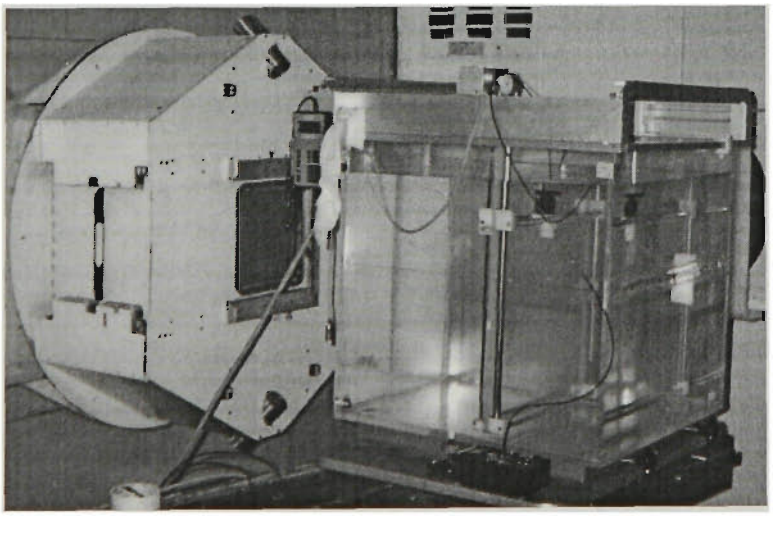

Figure 6-6. Water tank with inserted MOSFET detector positioned next to the neutron beam collimator of a superconducting cyclotron. Fast neutron therapy facility at Harper Hospital, Detroit, USA.

A +5 V gate bias was applied to the MOSFETs during the irradiations. The MOSFET threshold voltage was measured immediately after irradiation by a special reader under a constant current condition. The MOSFET threshold voltage reader and a gate bias power supply were developed and assembled by the Centre of Medical Radiation Physics, University of Wollongong. The reader operated in a pulse mode, see Chapter 3.2 for more details on the reader design. Threshold voltage was measured at the thermal-stable current, to minimise thermal drift of the detector reading. The theoretical considerations and an experimental method of determining the thermal-stable current are described in Chapter 4.2.

A paired MOSFET technique was applied for boron response measurements. The technique is described in Chapter 3.6. The measurements performed by a bare MOSFET were taken away from the measurements by the MOSFET with its sensitive element covered by plastic containung 1% of boron-10. The reading differences were normalised to the maximum in-phantom reading difference. The data provided a relative depth distribution of boron response.

A standard spectroscopy set-up of a Canberra 2003T preamplifier, Canberra 2024 fast spectroscopy amplifier and a computer-based multichannel analyser was used for pulse height spectra acquisition with the silicon detectors. A Canberra 2006 preamplifier, Canberra 2020 spectroscopy amplifier and a Canberra 8075 analog-to-digital converter were used at the FNT facility at the Gershenson Oncology Center of Harper Hospital. For initial calibration and measurement of ^{235}U alpha activity in an absence of an external radiation field, the fission probe was

connected to a Canberra 7401 alpha spectrometer. During data acquisition, the silicon detectors were reversed biased at 40 V. The depletion layer at such a bias was extended through the full depth of the silicon wafer.

At the Brookhaven Medical Research Reactor of the Brookhaven National Laboratory, NY, USA the very high count rate and consequent high dead time of the silicon detector, made it impossible to conduct spectroscopy measurements at full reactor power. Consequently, a reactor power of 20 kW was used for silicon detectors, assuming linearity of beam intensity as a function of reactor power. Using the FNT superconducting cyclotron the silicon detector measurements were performed with a reduced beam current of 0.7 μA. MOSFET measurements were performed at full reactor power and a cyclotron current of 12 μA.

Alpha particles released in the spontaneous decay of ^{235}U at an energy of 4.5 MeV were used as an internal energy reference for energy calibration of the detector. The pulse height spectrum was also used for measuring the alpha activity of the uranium converter, N_α, (see Equation (6-2), Chapter 6.3.1).

Because alpha particle emission originates from different depths in the converter and the particles originating from the deeper layers of the converter were losing part of their energy before escaping from it, the alpha particle peak was broadened and shifted to lower energies (Figure 6-7). The maximum energy of measured events corresponds to the energy of ^{235}U alpha particles of 4.5 MeV, however, the main peak is observed at an energy of about 3.9 MeV. The alpha particle count rate was measured to be $N_\alpha = 2.26$ counts per second.

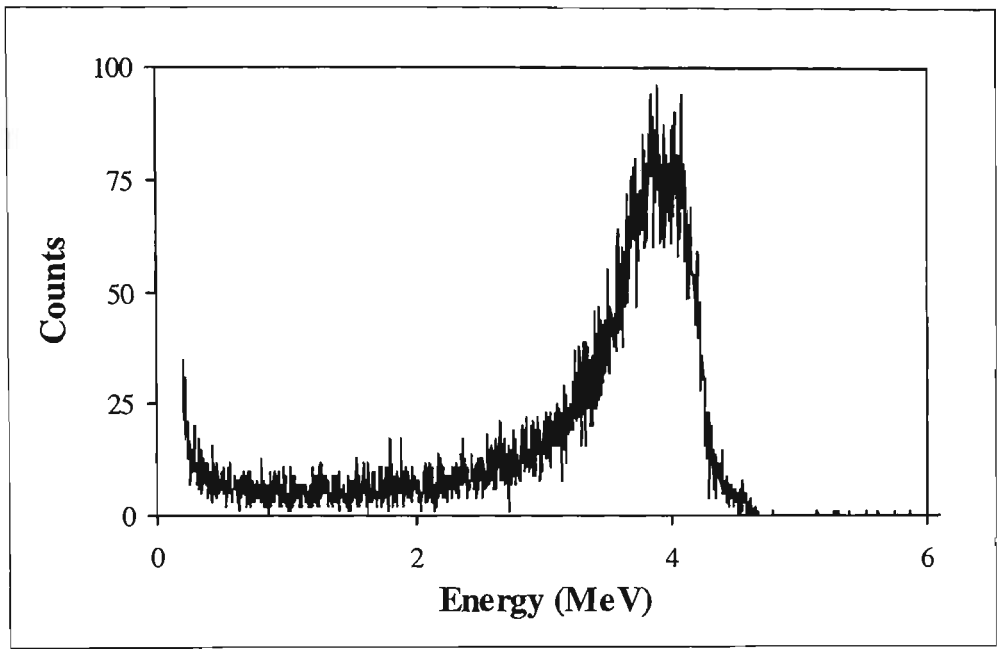

Figure 6-7. Energy spectrum of spontaneous alpha decay of ^{235}U in the fission converter.

6.5. Epithermal BNCT

The initial testing of the fission detector at the epithermal irradiation facility of BMRR had the advantage of being performed in a well characterised beam. The neutron spectrum of the beam was calculated and calculations were validated by foil activation and TLD measurements in a phantom similar to the one used in this study (Liu *et al.*, 1994; Liu *et al.*, 1996). Apart from testing, new knowledge on the in-phantom boron response distribution and on the suitability of a uranium converter fission detector for on-line applications in BNCT was gained.

6.5.1. Fission detector study

An advantage of the ^{235}U fission converter detector for thermal neutron fluence measurement in a mixed neutron-gamma field is that the fission fragment counts

are well separated from gamma and recoil proton counts in the pulse height spectrum. The pulse height spectrum of the epithermal neutron beam incident on the perspex phantom, i.e. energy spectrum of the secondary particles, was measured by the silicon detector without the ^{235}U converter (Figure 6-8) at a depth of 1.3 cm. The spectrum did not show any counts for deposited energies above 1 MeV. The spectrum in Figure 6-8 is typical for all phantom depths used in these experiments. Since the fission fragments have much greater energies and LET than recoil protons and Compton electrons produced by gamma rays, the fragment's pulse height spectrum did not overlap with the spectrum of low energy or low LET radiation present in the radiation field (compare Figure 6-8 and Figure 6-9).

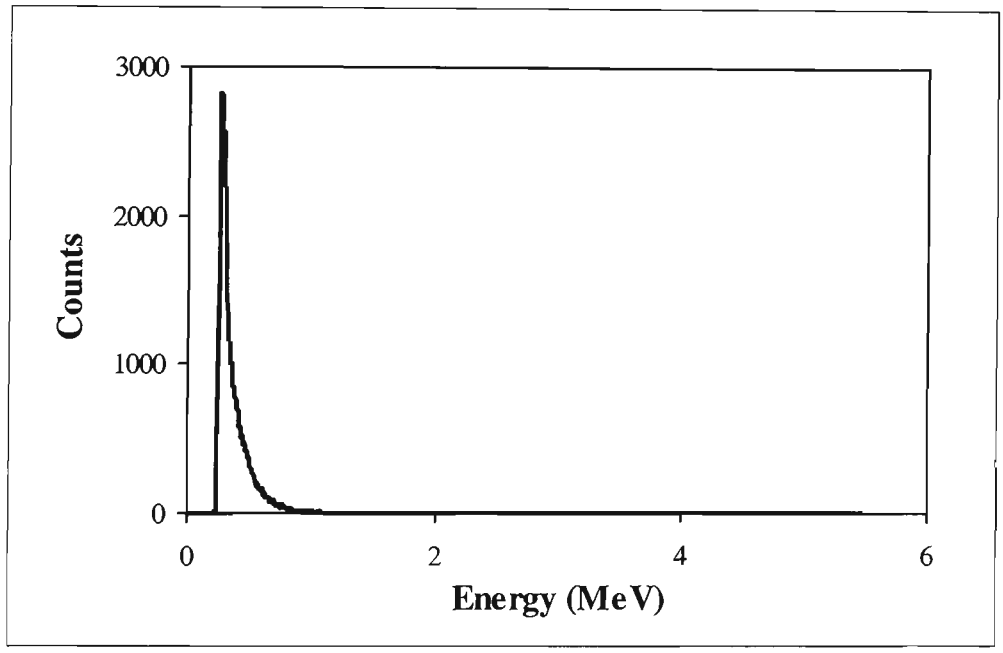

Figure 6-8. Gamma and recoil proton spectrum at 1.3 cm depth in perspex phantom at the epithermal neutron facility at the BMMR, reactor power 20 kW.

Measurements with a fission detector were performed at depths of 1.3 , 3.7 , 6.2 and 11 cm in the perspex phantom. A pulse height spectrum of the fission detector exposed to epithermal neutrons exhibits a broad double peak of fission fragments in the energy range up to 90 MeV (Figure 6-9). When the thermal neutron flux decreases with an increase in phantom depth, this double peak becomes lower in intensity and the alpha particle peak, originating from the spontaneous alpha decay of uranium, becomes more apparent (Figure 6-9b).

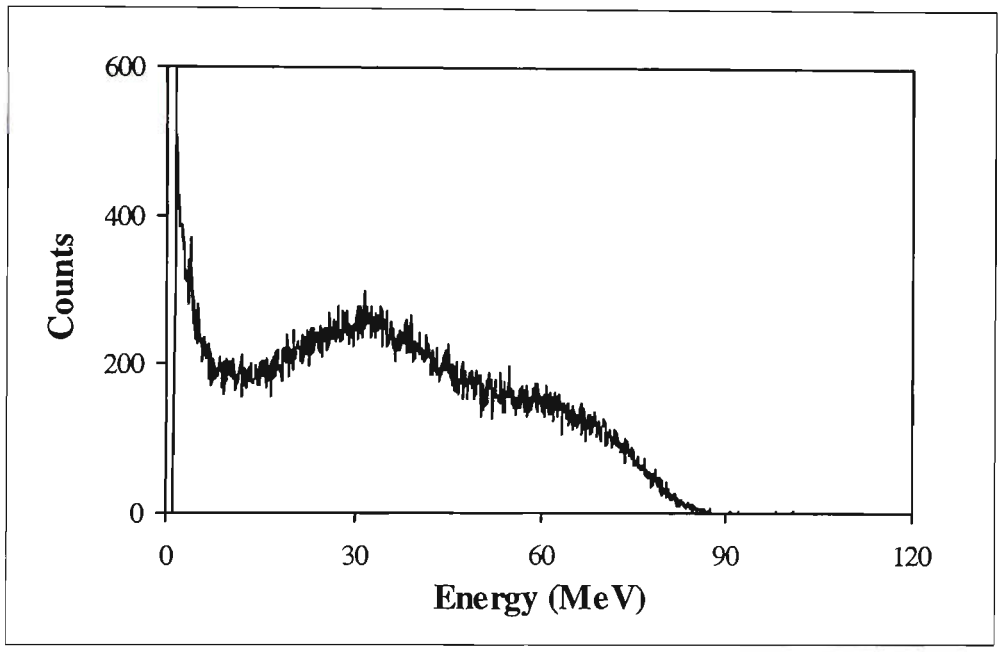

a)

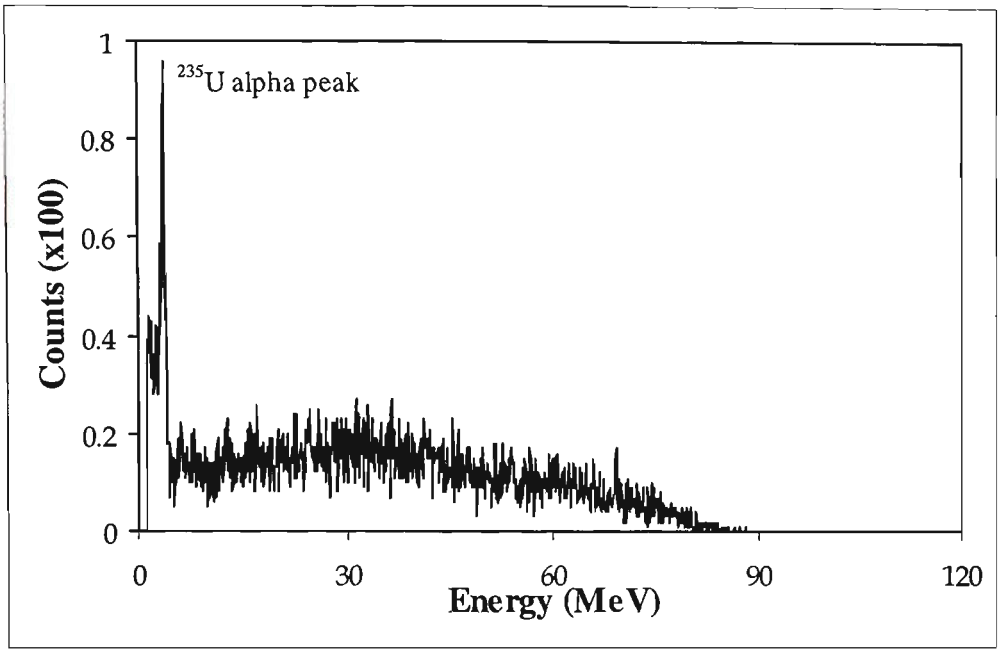

b)

Figure 6-9. Uranium fission fragment spectra at 1.3 cm (a) and 11 cm (b) depth in perspex phantom. (Epithermal neutron irradiation facility at the BMRR, reactor power 20 kW)

For calculation of thermal neutron flux in the phantom by applying Equation (6-4), Chapter 6.3.1, the following values for the constants were used (Turner, 1992):

$\Rightarrow$ Half life of ^{235}U $\tau = 7.1\times10^{8}$ years $= 2.2\times10^{16}$ seconds

$\Rightarrow$ $p = 0.85$

$\Rightarrow$ $\sigma = 580$ barns $= 580\times10^{-24}$ cm^{-2}

The exact composition of the uranium converter is not known. Fortunately, for the calculation of the thermal neutron flux by applying Equation (6-4) the absolute ranges of the alpha particle and the fission fragments separately are not required, only their ratio $R_{\alpha}/(R_{Br} + R_{La})$. To estimate the significance of a change in the

converter composition, the ranges were calculated by TRIM in a metallic uranium and in a uranium oxide (Table 6-1).

Table 6-1. Alpha particle and fission fragments ranges in uranium and uranium oxide.

	Uranium	**U_2O_5**
R_α (E = 4.48 MeV)	7.37 μm	15.85 μm
R_{Br} (E = 102 MeV)	6.23 μm	13.63 μm
R_{La} (E = 60 MeV)	4.35 μm	9.39 μm
$R_\alpha/(R_{Br}+R_{La})$	0.697	0.689

The ratio of alpha particle range to fission fragments range is practically insensitive to variations in the composition of the uranium converter (Table 6-1). For a pure uranium with a density of 19 g/cm^{-3} the ratio $R_\alpha/(R_{La}+R_{Br})$ = 0.697. For an oxide U_2O_5 with a density of 6.5 g/cm^{-3} the ratio $R_\alpha/(R_{La}+R_{Br})$ = 0.689. For further calculations this ratio is taken as 0.69.

Table 6-2. Alpha particle and fission fragments ranges in silicon and silicon oxide

	Silicon	**SiO_2**
R_α (E = 4.48 MeV)	20.26 μm	25.10 μm
R_{Br} (E = 102 MeV)	16.76 μm	21.23 μm
R_{La} (E = 60 MeV)	11.26 μm	14.80 μm
$R_\alpha/(R_{Br}+R_{La})$	0.723	0.694

In the fission detector model (Figure 6-5) the thickness of the dead layer of the detector was not taken into account. It is a simplification of the model, which can be justified by the following reasons:

- The silicon detector was of an ion implanted type with a thin entrance window produced by a low energy ion implantation technique.
- In the final Equation (6-4), Chapter 6.3.1, only the ratio of the ranges, not the absolute values, are included. In Table 6-2 the ranges of alpha particle and fission fragments in Si and SiO_2 are presented. The values were calculated by TRIM. As it can be seen from the data presented in Table 6-1, the ratio of ranges does not significantly depend on the composition of the media. The ratio $R_\alpha/(R_{La} + R_{Br})$ equals 0.697 for uranium and it equals 0.689 for uranium dioxide. The ratio of ranges equals 0.723 for silicon and 0.694 for silicon dioxide. SiO_2 is the typical composition of a passivating film on the surface of a silicon detector.

In spite of more than an order of magnitude difference in energies of ^{235}U alpha particles and uranium fission fragments, the difference in the corresponding ranges in silicon is less than 60% (see Table 6-2). The similarity in the values of ranges allows on-line monitoring of radiation damage to the silicon detector. Radiation damage causes a reduction in charge collection efficiency due to electron-hole recombination in the depletion depth of the detector. A decrease in charge collection will result in a change of ^{235}U alpha peak position towards lower energies. No change in the peak position was observed during the measurements, confirming reliability of the fission converter detector.

Fission fragments flux, N_f, as measured by a ^{235}U fission detector at different depths in a cube perspex phantom at the BNCT facility at the Brookhaven Medical Research Reactor, is presented in Table 6-3. Accuracy in the measurement of the area under the fragments' double peak was 4%.

Table 6-3. Fission detector fragments flux and thermal neutron flux at different depths along the central axis of a perspex cube phantom irradiated at the BMRR epithermal beam.

Depth (cm)	**Fragments flux (per second)**	**Thermal neutron flux in $n \cdot cm^{-2} \cdot s^{-1}$**
1.3	564	1.61×10^9
3.7	533	1.53×10^9
6.2	257	7.35×10^8
11	38.2	1.09×10^8

Note: Thermal neutron flux was scaled to the reactor power of 3 MW.

All the fission detector measurements were performed at a reduced reactor power of 20 kW. For calculating thermal neutron flux, experimental data were substituted into Equation (6-4), Chapter 6.3.1, and the flux was scaled up to a reactor power of 3 MW (see Table 6-3). The accuracy of the thermal neutron flux measurement was estimated at 7%. The clinically significant reactor mode, which is used for patient treatment, is the maximum operational reactor power of 3 MW. The accuracy of the reactor power setting was better than 5%. For converting the thermal neutron flux, measured at the reduced energy of 20 kW, to the full reactor energy of 3 MW a numerical scaling coefficient of 150 was applied, assuming

linearity of the beam intensity as a function of reactor power. As the BMRR is a light-water nuclear reactor, the power of the reactor is regulated by adjusting the positions of graphite and fuel rods. This changes the rate of the reactor nuclear fission reaction but does not change the energy spectrum of epithermal beam neutrons after the beam passes through the facility moderator filter system. A method of numerical factors for conversion of reactor dosimetry characteristics measured at a lower power to the full reactor power was also used by the BNL dosimetry group (Alburger *et al.*, 1998). A scaling factor of 60,000 was applied for converting measurements performed at 50 W power of the BMRR to the full power of 3 MW.

The linearity of the reactor dose rate with power was checked by a MOSFET detector. The detector was inserted at a 6.7 cm depth in the perspex phantom. For 5 minutes irradiation, at the reactor power of 3 MW, the change in threshold voltage was registered as 148 mV. In 16 minutes irradiation, with a reactor power of 300 kW, the corresponding change in threshold voltage was 47 mV. The 47 mV threshold voltage change change is expected from the ratio of irradiation times and powers.

$$47 = 148 \times \frac{16}{5} \times 0.1$$

The linearity of a MOSFET detector in this range of threshold voltage change was demonstrated previously, see Chapter 4.5.

The experimental thermal neutron flux data, scaled to 3 MW reactor power, are compared to Monte Carlo calculated thermal neutron flux (Figure 6-10). For the

calculations, a MCNP4A Monte Carlo code was used. The calculations were performed by Hungyan B. Liu of the BNL Medical Department. Thermal neutron flux was calculated along the central axis of the 15×15×15 cm^3 perspex cube phantom at the full reactor power of 3 MW. The flux was calculated with a step of 0.5 cm. An energy of 0.4 eV was used in the Monte Carlo calculation as a separator between thermal and intermediate neutrons. The statistical error estimate of all the calculated data was below 1%. The agreement between the calculations and experimental data was good (see Figure 6-10). The error bars on the graph represent 7% accuracy in the experimental measurement. This accuracy can be compared with the recent measurements by *Schmidt et al.* (Schmidt *et al.*, 1999), of thermal neutron flux around a ^{252}Cf source measured by a boron coated magnesium fission chamber. An error of 6.5% was obtained for measurements by the fission chamber, where response was calibrated in two known radiation fields prior to measurement.

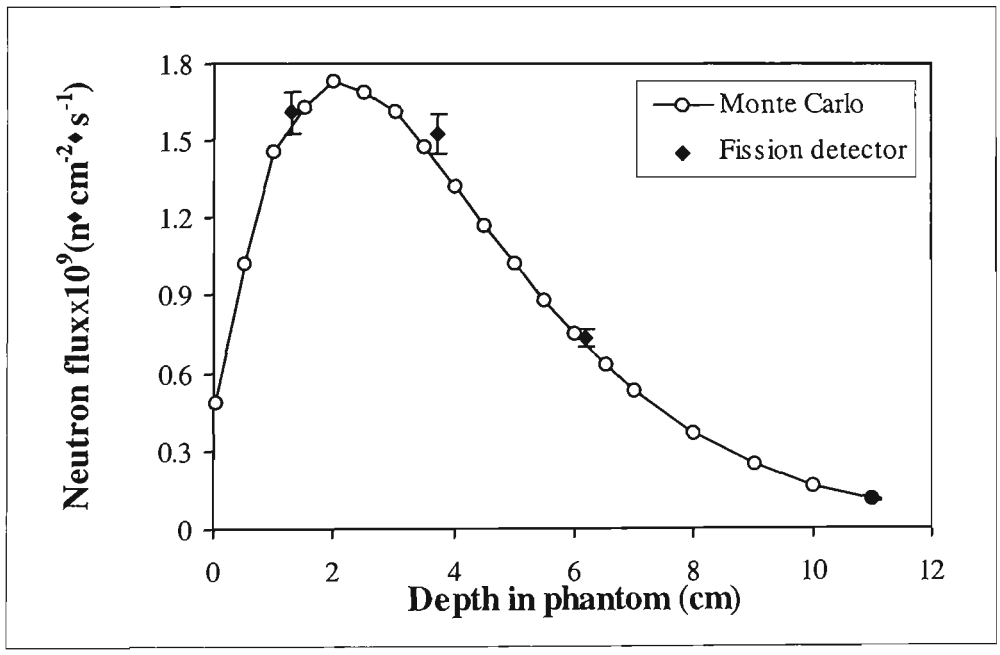

Figure 6-10. Monte Carlo (MCNP4A) calculated and Si(^{235}U) fission detector measured thermal neutron flux along the central axis of a perspex cube phantom irradiated at the epithermal BNCT facility at BMRR.

charge deposited for 2D and 5% for 3D simulations. If the charge conservation conditions are not met then insufficient discretization is almost always the reason.

Note however, that one should avoid excessive discretization if possible because the simulation time varies according to $O(n^{\alpha})$ where n is the number of nodes and α is between 1.5 and 2 [223]. The 2D simulations with 2000 nodes typically take less than 30 minutes whilst the 3D simulations with 20000 nodes take over 24 hrs running on a DEC alpha processor with 1 GByte memory. Currently, a reasonable limit for such a system is 50000 nodes.

6.2.2.2 Collection Efficiency Simulations

2D simulations were performed every 0.75 μm along the line (0,15) to (15,15) (referring to Figure 6.9), from the $p+$ to the $n+$ region. A 5.3 MeV alpha particle strike was modeled for each of the 21 simulations. Two different minority carrier lifetimes, corresponding to a normal device and a radiation damaged device, were simulated along with two sets of voltages (0 and 10 V). The lifetimes were calculated from proton microbeam measurements, described later in section 6.3.2. The substrate doping density for the undamaged device is 1.5×10^{15} cm^{-3} whilst the radiation damaged device has a lower doping density of 1×10^{15} cm^{-3}. In addition, the maximum mobility was adjusted to account for radiation damage effects as discussed in section 6.3.2.

The CE was calculated for each point with the results shown in Figure 6.32. Charge collection efficiency approaches 100% in the depletion region since drift collection is strong for an unirradiated device. As we move away from the depletion region a transition region occurs in which a combination of funneling and diffusion takes place. In this region, the charge carriers diffuse into the depletion region with a sufficient carrier density to cause depletion region collapse. The lateral funnel effect, confirmed by simulation voltage distribution plots, has been reported previously by Edmonds [218, 219]. Eventually we reach a point at which only diffusion occurs and the efficiency decays exponentially with a constant that is related to the effective recombination time, which depends on both surface and bulk recombination. The diffusion length is long relative to the device dimensions so the exponential decay is approximately linear as shown in Figure 6.32. However, simulations were performed with shorter lifetimes that confirmed the exponential drop in CE. The onset of funneling corresponds to the transition point between the exponential decay and the constant high CE as we move

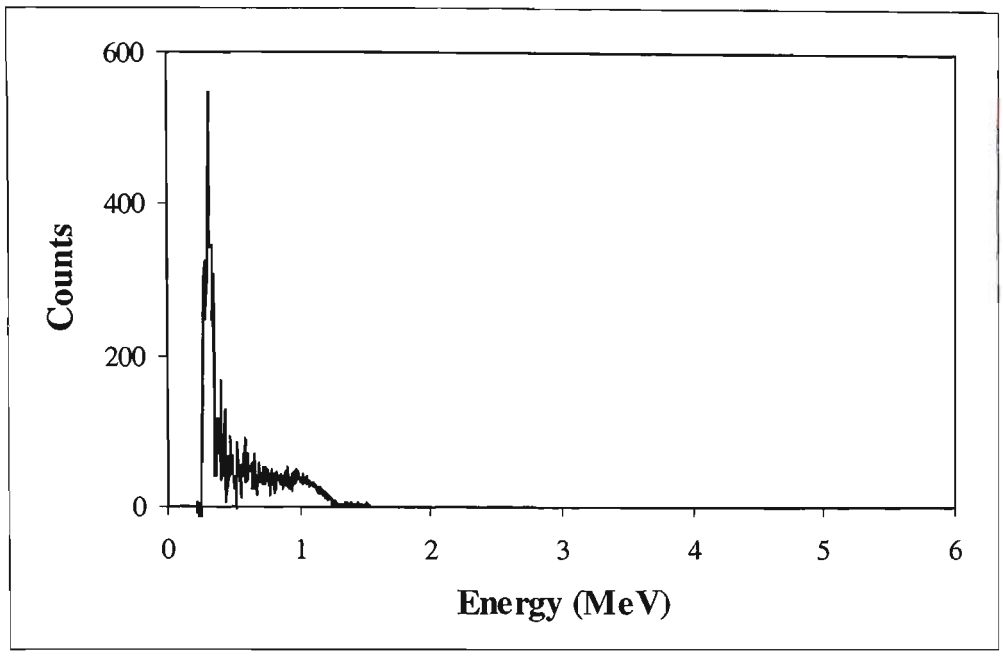

Figure 6-11. Difference spectrum between measurements by the silicon detector with and without a ^{10}B converter at a depth of 3.7 cm in perspex phantom at the epithermal facility of the BMRR, reactor power 20 kW.

Relative data on boron response were obtained by the paired detector method. The pulse height spectra were measured by the detector covered by a 1% ^{10}B converter at depths of 1.3 cm, 3.7 cm and 6.2 cm in the perspex phantom. At the same depths the spectra were measured by the identical reference silicon detector without a ^{10}B converter. After normalising to the acquisition time, a reference spectrum was subtracted from the corresponding boron converter spectrum. All the difference spectra were similar to the one measured at the depth of 3.7 cm and reproduced in Figure 6-11. The difference spectrum had a distinguished shoulder at a mean energy of 1 MeV which started at an energy of approximately 1.5 MeV. This shoulder was caused by the energy deposited in the detector by alpha particles and ^{7}Li ions, due to escape of the charged particles from various depths

in the converter. Low energy events are also more intense in the ^{10}B converter spectrum compared to the bare detector spectrum, as a result of the 478 keV gamma released in the boron neutron capture decay reaction.

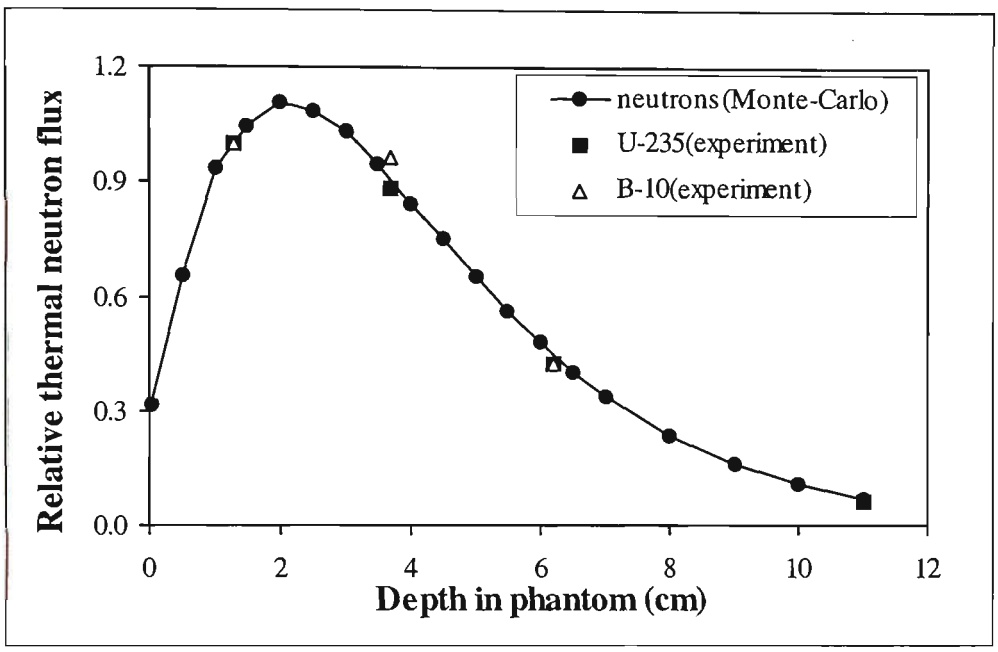

Figure 6-12. Relative thermal neutron flux (Monte Carlo) and relative response of detectors with ^{235}U and ^{10}B converters.

A relative boron response was calculated from the difference spectra and was compared to the measured and calculated relative in-phantom thermal neutron flux. All the fluxes were normalised to the measurement at a depth of 1.3 cm in the phantom. The relative boron response was in very good agreement with the relative thermal neutron fluxes measured by the uranium fission detector and calculated by the Monte Carlo code (Figure 6-12). This agreement is very important for applications of the uranium fission converter detector at an epithermal BNCT facility, as it shows that both boron capture and uranium fission

converter detectors have similar responses to the incident epithermal neutron beam.

Thermal neutron flux measurements are of importance in BNCT because they allow the calculation of a boron augmented dose. The boron dose rate D is equal to

$$D = \Phi \times \sigma \times N_B \times E_0$$

where σ = 3840 barn = 3840 $\times$ 10^{-24} cm^2 and is the ^{10}B thermal neutron capture cross section (BNL, 1958), N_B is a number of boron-10 atoms in 1 kg of medium and E_0 is the energy released in a single neutron boron capture reaction. The calculation procedure is described in more detail in Chapter 6.7. The boron dose rate in cGy per second in the perspex phantom is shown in Figure 6-13. The dose rate was calculated for the ^{10}B concentration of 50 ppm and with thermal neutron flux values measured by the uranium fission converter detector (see Table 6-3).

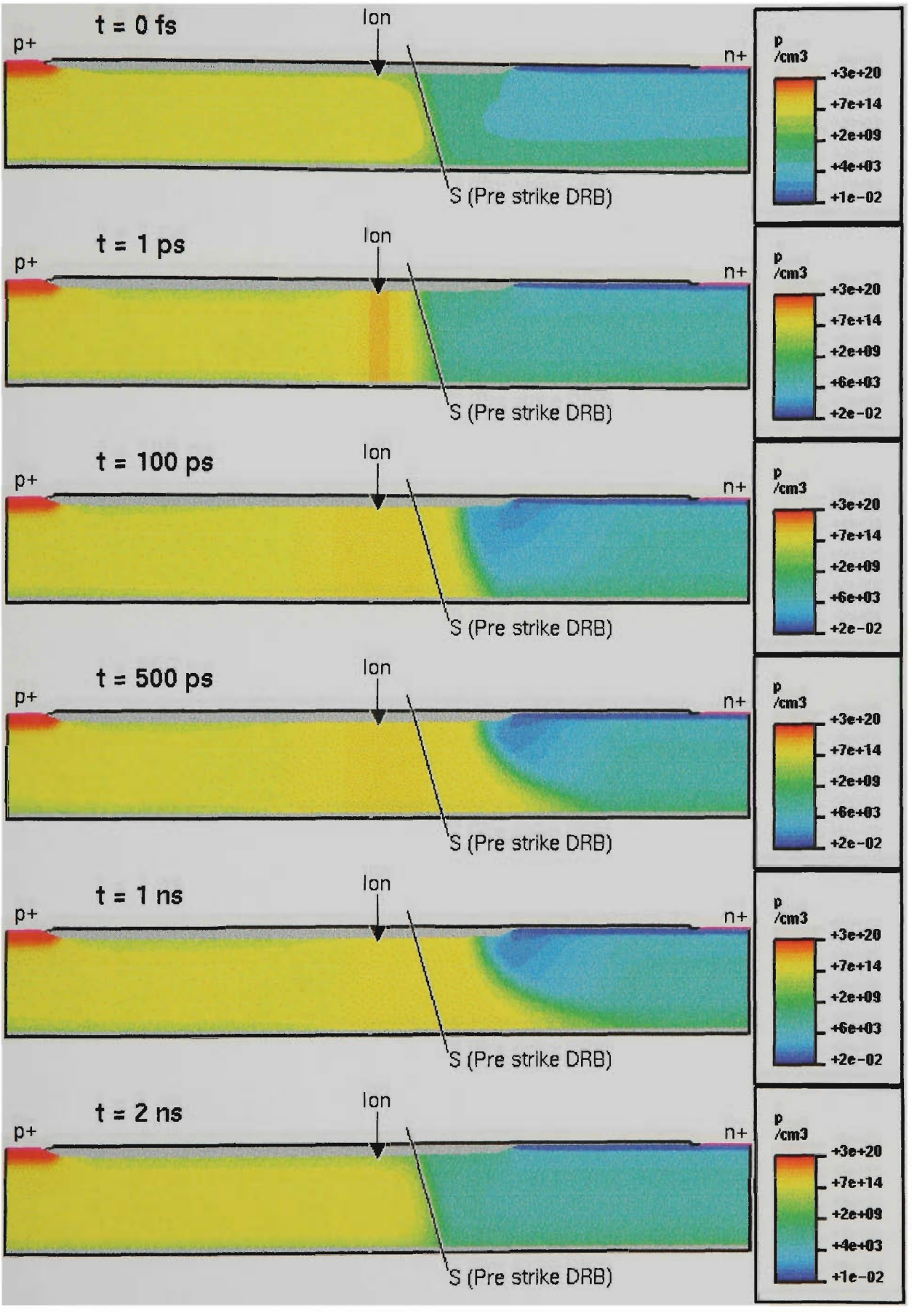

Figure 6.15. Hole density distribution for a 2D 5.3 MeV alpha particle transient simulation. Diode is the 10 × 10 μm junction size on 2 μm SOI substrate. The boundary denoted by S is the pre-ion strike (0 fs) depletion region boundary defined by the sharp transition in hole density.

cube phantom, as described in Chapter 3.5.1, and by inserting the detector in perspex, the air gap between the detector and the phantom was minimised. The gates of both types of MOSFETs were biased during the measurements to a positive bias of +5 V.

The method of using paired MOSFET detectors, as described in Chapter 3.1.1, with one n-channel MOSFET covered by boron contained plastic and the other identical MOSFET used without a cover (see Figure 3-14 on page 71), was employed for boron dose measurements. The measurements were performed at 0.5 cm, 1.3 cm, 2.0 cm, 3.0 cm, 3.7 cm, 6.2 cm, 8.7 cm and 11.2 cm depths in the phantom. At each of the depths both paired detectors were used. RADFET measurements were performed at depths of 0.3 cm, 2.5 cm, 5 cm and 7.5 cm.

Irradiation time for each of the measurements was 5 minutes and the reactor power was set to 3 MW. After 5 minutes irradiation the reactor shutter closed the beam line and the reactor power was reduced to 10 kW. The treatment room door was then opened and the reading of MOSFET threshold voltage was taken.

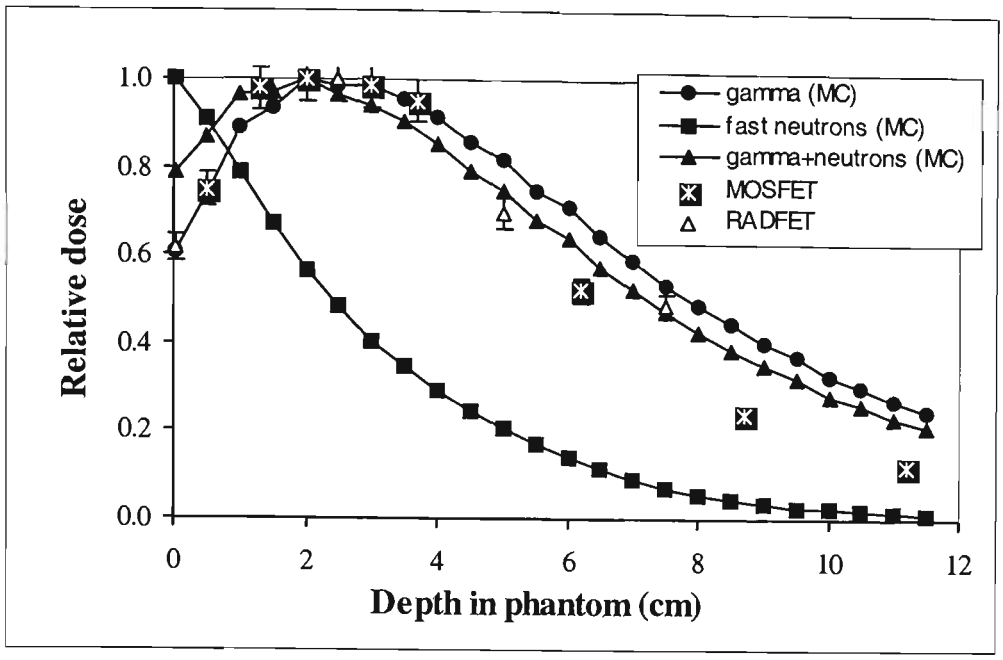

Figure 6-14. MCNP-calculated relative gamma and fast neutron dose and relative bare MOSFET measurements.

Experimental measurements were compared to data calculated for the same experimental setup by MCNP 4a Monte Carlo computer code run by Hungyuan Liu. Calculations were performed for two separate components : gamma dose and fast neutron dose (neutron energy in excess of 10 keV). The Monte Carlo-calculated depth dose distribution curve was compared with the bare MOSFET and RADFET measurements. In Figure 6-14 we plotted the relative Monte Carlo-calculated gamma and fast neutron doses separately, as well as their relative sum dose. The relative MOSFET/RADFET measurements are shown with 5% error bars. The experimental MOSFET and RADFET points follow the calculated relative gamma dose curve very closely from the surface to a depth of up to 4-5 cm. The MOSFET/RADFET measurements are below the calculated values for greater depths in the phantom. A similar Monte Carlo overestimate of a dose at a

greater depths in a 14 cm ×14 cm ×14 cm perspex cube phantom was observed by Dennis Greenberg of BNL for TLD depth dose data (Greenberg, 1997). The ratio of TLD measurements at a depth of 3.5 cm to 7 cm was 1.84, while for the Monte Carlo the ratio is smaller, at 1.73. For the MOSFET detector, the estimated ratio is even larger, while for the RADFET it is about the same, as for TLD.

The method of using paired MOSFET detectors (see Chapter 3.6) was applied for measuring the depth profile of the relative boron dose. Readings from the bare MOSFET were subtracted from the readings of a boron converter coated MOSFET. The difference between the readings was ascribed to the boron dose enhancement. The MOSFET measurements were adjusted to a small change in the detector sensitivity with accumulated dose. To the best of my knowledge, this was the first application of the paired MOSFET method in hadron radiation therapy dosimetry. The results were normalised to the maximum measured dose and are plotted in Figure 6-15. In the mixed epithermal neutron-gamma radiation field, the maximum boron dose enhancement occurs at depths of 2 to 4 cm from the surface. This is in agreement with the depth distribution of thermal neutron flux (Figure 6-10). The relative boron dose curve shape is also similar to the boron dose rate curve measured by the uranium fission converter method (Figure 6-13).

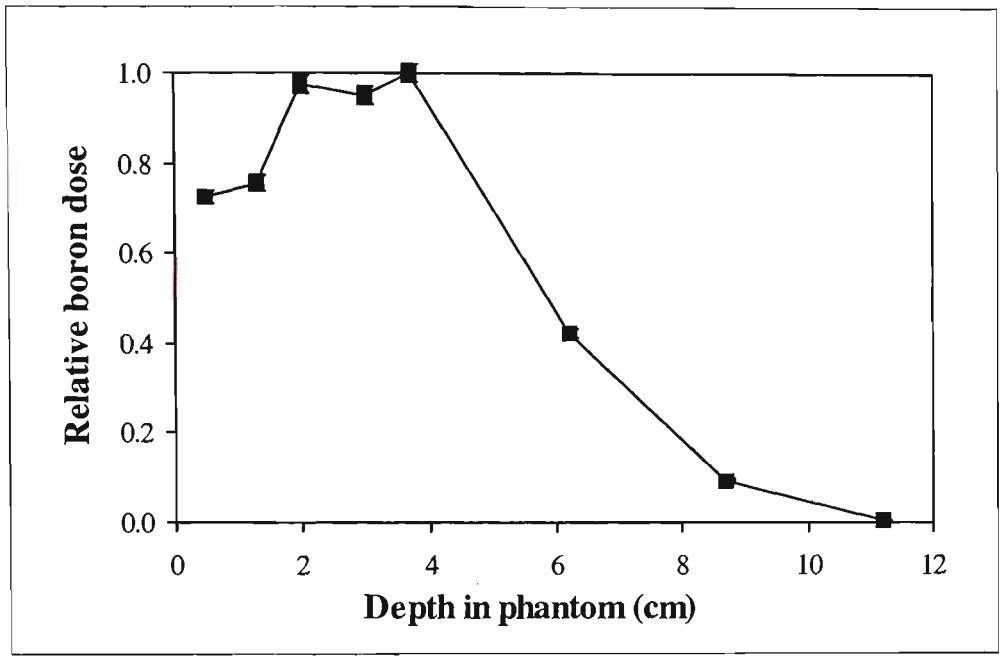

Figure 6-15. Relative boron dose depth distribution for the BMRR epithermal beam measured along the central axis of a cube perspex phantom by paired MOSFET detectors.

It is evident from the boron dose depth distribution that the optimal treatment depth in epithermal BNCT is from 1 cm to 5 cm.

6.6. Thermal and quasi epithermal BNCT

The in-phantom thermal neutron flux depth distribution was expected to be different in the thermal BNCT compared to an epithermal BNCT. The nuclear reactor at Kyoto University (the reactor is described in Chapter 3.4.3) and its filtering system also differ from the epithermal irradiation facility at the BMRR (this facility is described is in Chapter 3.4.2). It was necessary to test the uranium converter fission detector in the thermal neutron beam and to obtain data on thermal neutron flux distribution, in order to validate the dose planning

calculations at the facility. The measurements were performed in the facility's reference phantom. The phantom was water filled, cylindrical in shape, and was 18 cm in diameter and 20 cm in length. Thirty centimetres of a heavy water filter reduced the thermal neutron flux by about two orders of magnitude.

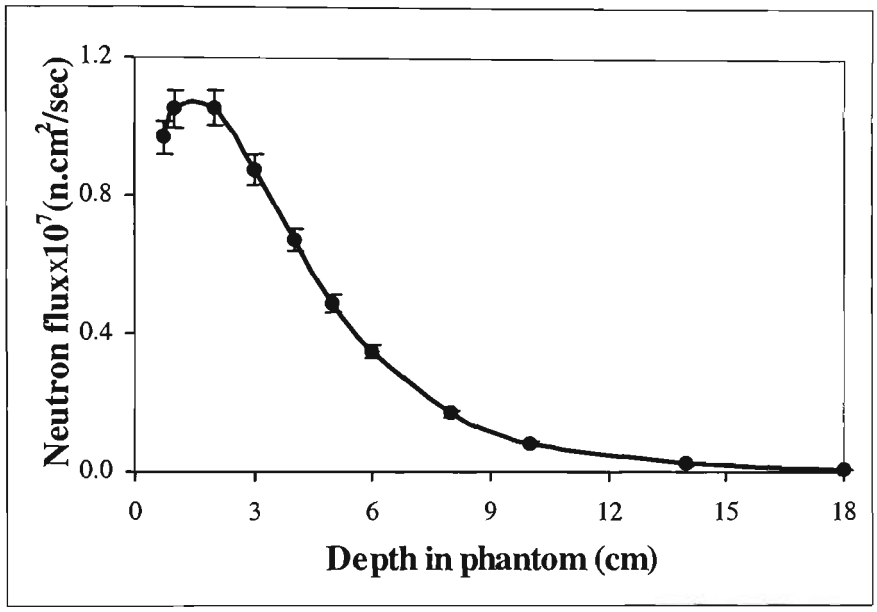

a)

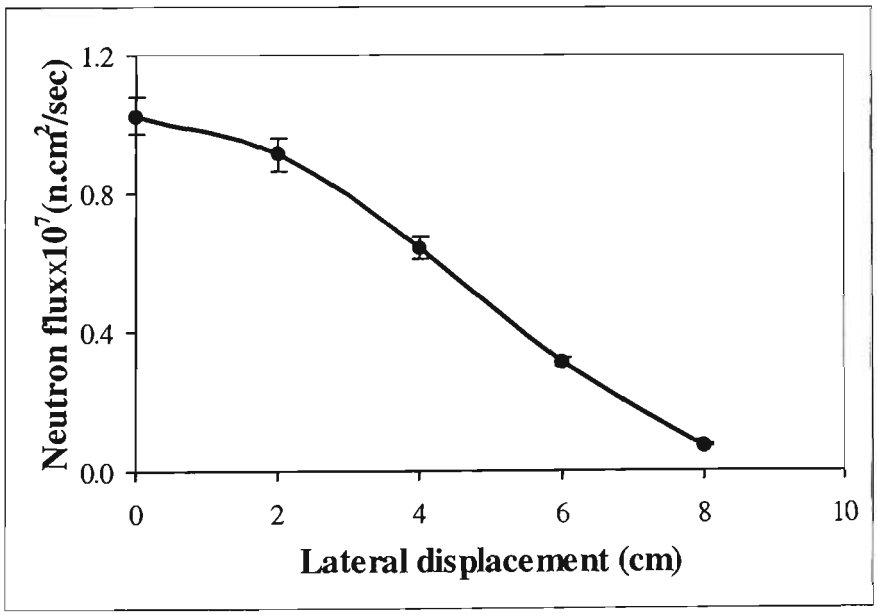

b)

Figure 6-16. Thermal neutron flux rate measured by the fission detector in a 30 cm D_2O filtered BNCT beam at the Osaka reactor. (a) Flux depth measurement

along the phantom axis and (b) in the lateral direction at 2 cm depth. The beam diameter was 10 cm.

The measurements were performed with a step of 1 cm to a depth of 6 cm, and in larger steps for greater depths. Thermal neutron flux depth distribution had a build up region from the surface to 1 cm depth (Figure 6-16a). The maximum in thermal neutron flux distribution was observed at the depth of 1 to 2 cm. The flux rapidly decreased with depth, and at the depth of 5 cm it was less than a half of its maximum value. In comparison with the epithermal beam at the BMRR (Figure 6-15), the depth distribution of the thermal neutron flux of a filtered Kyoto beam has a narrower maximum. The maximum in the thermal neutron flux distribution of a Kyoto beam is closer to the phantom surface than it is for the epithermal beam at BMRR.

The lateral change in thermal neutron flux distribution was measured off the central axis of the beam at a depth of 2 cm in a cylindrical water phantom. The measurements were performed with a step of 2 cm. The beam diameter was 10 cm as was determined by the collimator opening. Thermal neutron flux at 5 centimetres off the central axis was about one third of its value at the centre of the beam (Figure 6-16b). The flux was 7% of the maximum value at 8 centimetres away from the centre. The flux was spread out and had a significant reduction from the centre towards the edges. Two centimetres of water definitely affected the spread of the beam. It was not possible to compare the measurements with

Monte Carlo calculations, because the energy spectrum of the beam was not known.

The consistency of the measurements was checked by repeated measurements at the same points in the phantom. At an initial depth of 0.7 cm the measurements were repeated without moving the detector. The values obtained for thermal neutron flux in two consecutive runs were 9.66×10^6 and 9.70×10^6 neutrons per second. The difference between them was less than half of a percent. After completing measurements of the depth distribution, the detector was moved back to the 2 cm central position, for lateral distribution measurements, and the measurement at 2 cm depth was repeated. The two values of thermal neutron flux were 1.05×10^7 and 1.03×10^7 neutrons per second. The difference was only 2%. The increase in the difference between the repeated measurements at 2 cm depth and at 0.7 cm depth may be partially attributed to the uncertainty of the detector positioning system. The quoted accuracy of the positioning system of ±0.1 mm, might cause an error of 0.8% due to the measured gradient in thermal neutron flux distribution.

6.7. FNT and the feasibility of BNCEFTN

The main aim of the fission detector measurements in the FNT beam of the superconducting cyclotron at Harper Hospital, Detroit, MI, USA was to estimate thermal neutron flux, and, on the basis of the flux, to provide recommendations on the feasibility of boron enhancement of FNT dose in a cyclotron beam.

Description of the Harper Hospital fast neutron therapy facility is in Chapter 3.4.4, page 60. Ion implanted silicon detectors of a surface area of 3 x 3 mm^2 were used in 3 different configurations:

- Bare detector with no converter
- Detector with a ^{235}U fission converter
- Detector with a 1% ^{10}B converter

Application of the uranium-235 fission converter detector in a fast neutron beam has physical and technical limitations which may affect the accuracy and reliability of the measurements. The fast neutron capture cross section of ^{235}U, while being 200 to 300 fold smaller than for thermal neutrons, does not equal zero (Figure 6-2). During application of the fission detector in a predominantly fast neutron beam, some proportion of the fission fragments may originate from decay caused by fast neutrons. Thus the thermal neutron flux, calculated from the uranium-235 fission converter detector data, will also include higher energy neutrons. In this case the calculated value can be treated as an upper limit estimate of thermal neutron flux. Neutron capture cross-section of boron-10 is also energy dependent and it was shown by measurements in epithermal neutron beams (Chapter 6.5.1) that the silicon ^{235}U fission converter detector provides adequate determination of the thermal neutron flux for purposes of boron dose estimation.

A technical problem in the application of a fission detector in a fast neutron beam is the presence of high energy and high LET radiation in the beam. This radiation increases the background count rate in the pulse height spectrum, which leads to

an increase in the uncertainty of the measurements. To reduce the background count level the cyclotron was run at a low current of 0.7 μA. However the lower current caused reduction in flux of all components of neutron beam.

The relative error of thermal neutron flux measurements by the ^{235}U fission converter detector was estimated to be between 20% and 40%. This is similar to the 40% uncertainty in ionisation chamber measurements by Kota *et. al.* (Kota *et al.*, 2000) in the same fast neutron beam. Equation (6-4) from Chapter 6.3.1 was applied to convert the detector count rate to thermal neutron flux. Parameters of the Equation (6-4) had the following numerical values:

Half life of ^{235}U $\tau = 7.1\times10^{8}$ years = 2.2×10^{16} seconds (Turner, 1992)

$p = 0.85$ (Turner, 1992)

$\sigma = 580$ barns = 580×10^{-24} cm^{-2} (Turner, 1992)

$R_\alpha/(R_{La}+R_{Br}) = 0.689$, as established in Chapter 6.5.1

$N_\alpha = 2.26$ counts per second, as calibrated in Chapter 6.4

The thermal neutron flux was calculated per monitoring unit (MU). Measurements in the perspex cube phantom for the fully open collimator, field size 10 cm x 10 cm, were performed at depths of 1.3, 6.2 and 8.7 cm. The corresponding thermal neutron fluence per MU is presented in Table 6-4.

Table 6-4. Thermal neutron flux per MU versus depth in a perspex cube phantom exposed in a FNT beam.

Depth in Phantom	Thermal Neutron Flux ($n \cdot cm^{-2}$)
1.3 cm	1.65×10^8
6.2 cm	1.63×10^8
8.7 cm	1.45×10^8

To compare this data to data obtained from epithermal BNCT, the flux has to be normalised to the dose delivered per single treatment fraction irradiation at each of the modalities. The dose delivered per single fraction in FNT at the Harper Hospital facility is normally 150 MU. The 2.5×10^{10} thermal neutron fluence per FNT fractionation, at 1.3 cm depth in perspex phantom, is significantly less than the thermal neutron fluence of 1.9×10^{12} for a typical 20 minute irradiation at BMRR. Another difference between FNT and epithermal BNCT is that the thermal neutron flux depth distribution is flat. There is no change from depths of 1.3 cm to 6.2 cm in the phantom and then it drops by only 11% at the depth of 8.7 cm.

The thermal neutron flux data in Table 6-4 can be used to calculate of the ^{10}B dose rate in a water phantom per MU of fast neutron beam. The dose rate can be compared to recent measurements by the paired proportional chamber method reported by (Kota *et al.*, 2000) and performed in the same fast neutron therapy beam of the Gershenson Oncology Center at Harper Hospital. The dose rate in this

study (Kota *et al.*, 2000) was measured in cGy per MU for 50 ppm of boron-10 loading.

A radiation dose of 1 Gy is produced when 1 Joule of energy is deposited in 1 kg of medium. In each neutron boron capture reaction approximately E_0 = 2.3 MeV of energy is released in the form of kinetic energy from decay products. Converting this to Joules

$$E_0 = 2.3\times10^{6}\times1.6\times10^{-19} = 3.7\times10^{-13}\ \text{J}$$

This energy is deposited in close proximity to the initial capture site, because the range of the decay products in tissue equivalent material does not exceed 10 μm. One kilogram of medium contains 50 mg of ^{10}B, for a typical therapeutic boron-10 loading concentration of 50 ppm. The number of ^{10}B atoms, N_B, in m gram of boron-10 can be calculated as

$$N_B = \frac{N_A \times m}{m_B}$$
$$= \frac{6.02\times10^{23}\times5\times10^{-2}}{10}$$
$$= 3\times10^{21}\ \text{atoms}$$

where N_A = 6.02×10^{23} is the Avogadro number and m_B = 10 g is weight of 1 mol of ^{10}B.

The boron dose rate D_B is equal to

$$D_B = \Phi \times \sigma \times N_B \times E_0$$

where σ = 3840 barn = 3840 $\times$ 10^{-24} cm^2 and is the boron-10 thermal neutron capture cross section (BNL, 1958). The thermal neutron flux at a depth of 6.2 cm in water phantom $\Phi = 1.63\times10^8$ $n\cdot cm^{-2}\cdot MU^{-1}$. If we substitute the values of the other parameters in the last equation then the boron dose rate can be calculated as

$$D_B = 1.63\times10^8\times3.84\times10^{-21}\times3\times10^{21}\times3.7\times10^{-13}\times10^2$$

$$= 6.9\times10^{-2} \text{ cGy/MU}$$

The boron dose rate measured by a paired proportional counter method by (Kota *et al.*, 2000), for a concentration of ^{10}B of 50 ppm at a depth of 5 cm in the water phantom, was $(4.2 \pm 1.6)\times10^{-2}$ cGy/MU. The uncertainty of that measurement was 40%. The same uncertainty assumed for the fission detector measurement results in the current estimate of the boron dose rate to be $(6.9 \pm 2.7)\times10^{-2}$ cGy/MU. Thus these two measurements agree within the error limits. A reference physical fast neutron dose rate is approximately 1cGy per MU. Therefore the boron dose is about 4-5 % of the total dose. The calculated boron dose is a physical dose and does not take into account the relative biological effectiveness (RBE) of alpha radiation of boron-10 decay alpha particles, which is taken as 3.5 for BNCT dose planning (Coderre & Morris, 1999). The RBE of fast neutrons depends strongly on the cell type and on the dose delivered per fraction. RBE of fast neutrons was measured in various studies as being between 2 to 5 with average value of

approximately 3 (Denekamp, 1974; Denekamp, 1994; Hornsey *et al.*, 1981). Accordingly, boron enhancement of the biological dose in a fast neutron beam exceeds the fast neutron dose by a factor of 3.5 to 3, which is approximately 1.2. As a result, the boron dose enhancement over fast neutrons reaches 6%. This enhancement may provide a boost to the dose delivered to the target volume, especially taking into account that this dose is delivered in the target volume.

While the fission converter measurement gives a higher estimate of the boron dose, partly due to an overestimate of the thermal neutron flux in a fast neutron beam, as discussed earlier in this chapter, the error intervals of these two measurements overlap. We should also note that the value of $(6.9 \pm 2.7)\times10^{-2}$ cGy/MU was obtained at a depth of 6.2 cm in the water phantom, while Kota *et al.* measured the boron dose at a depth of 5 cm. The fraction of thermal neutrons in the fast neutron beam is expected to increase with depth. This increase may result in an increase in boron dose if the change in total neutron flux is relatively small. A detailed Monte Carlo modeling is required to compare both the proportional counter and uranium fission converter measurements with the calculated values. At this stage an accurate Monte Carlo computation cannot be performed for two main reasons. Firstly, experimental neutron interaction cross-sections are rarely available for neutrons with energies in excess of 20 MeV and secondly, the energy spectrum of the fast neutron beam at Harper Hospital has not yet been determined.

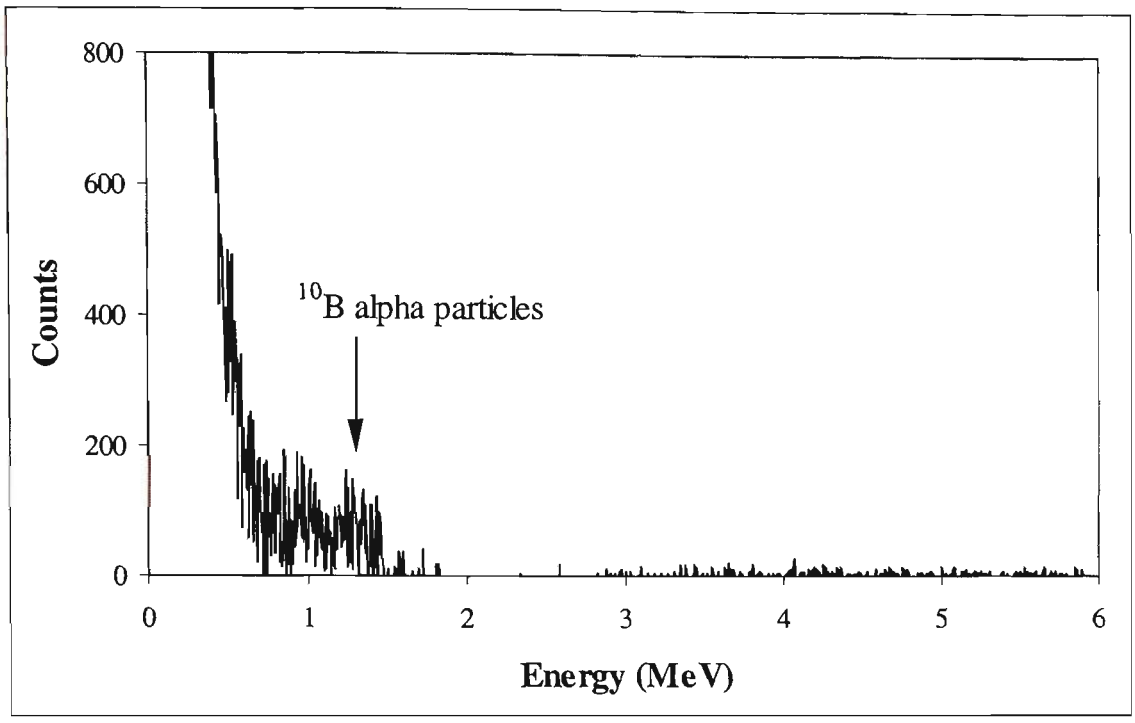

Figure 6-17. Boron difference spectrum at a 1.3 cm depth in a perspex phantom.

Pulse height spectra were measured by an ion implanted detector covered by a plastic converter with 1% ^{10}B. This was done in an effort to directly measure the boron dose. Two spectra were measured at a depth of 1.3 cm in a perpex phantom. One was acquired by a bare detector and the other one by a detector with a ^{10}B converter. The difference spectrum (^{10}B – no boron) is presented in Figure 6-17. A peak corresponding to the alpha particles produced in the boron neutron capture reaction can be seen. The statistics are low and the signal to background ratio shows considerable noise. The boron-10 neutron capture decay alpha particle energy is about 1.5 MeV. The energy of alpha particles reaching the detector may be less and the peak is spread towards lower energies because the alpha particles originate from different depths in the ^{10}B converter, as was discussed previously. There are many other secondary particles, such as protons, in a fast neutron beam which deposit a similar energy in the 300 μm sensitive volume of the silicon ion

implanted detector. These particles produce a large number of background pulses and significantly rarer alpha particle pulses are hidden by this background. Low signal to noise ratio makes the silicon detector with a ^{10}B converter unsuitable for measuring boron dose in boron neutron capture enhanced fast neutron therapy.

Measurements were also performed at a 5 cm depth in the water phantom for an open or partly closed tungsten rod collimator. The field size was adjusted to 15 cm ×15 cm and the beam current was 0.7 μA. The aim of the partial closure of the collimator was to increase the thermal neutron component of the radiation beam. It was found that while the closing of the collimator significantly reduced the total intensity of the beam, the relative contribution of the thermal neutron component of the beam, at a depth in water of 5 cm was increased by about 30%.

6.8. Thermal neutron dosimetry in ^{252}Cf brachytherapy

Brachytherapy was developed well before external beam radiation therapy became available. The first application of brachytherapy was reported in1903 just 5 years after the discovery of radium by Maria Sklodowska Curie. The new cancer treatment therapy began when Pierre Curie gave a vial of radium to Dr. Henri Danlos and suggested that it was inserted into a tumour (Cleaves, 1903). It is interesting to note that a physicist was the first to propose the therapeutic use of ionised radiation.

In the 1920s investigations by C. Regaud proved that low intensity radium needles applied during a period of up to 10 days are efficient in the treatment of some types of cancer, in particular cancer of the uterus (Brady *et al.*, 1995; Regaud, 1926). In the late 1950s and early 1960s new radioisotopes became available as a substitute for radium in brachytherapy. The new isotopes were iodine-125, iridium-192 and cesium-137. As brachytherapy techniques developed they ranged from intracavitary and interstitial loadings in gynaecological cancers to high and low dose remote afterloading devices.

In the 1970s, with the increased use of Cobalt-60 and electron accelerator therapy units, the popularity of brachytherapy started to decline. However it was soon realised that supplementation of external beam therapy with brachytherapy can increase the level of local control of some forms of cancer. This development was accelerated by the introduction of new radioisotopes, new dosimetry, computer modelling and loading methods.

In the 1970s californium-252 was introduced to cancer radiation therapy for intracavitary treatment of cervical cancer (Castro *et al.*, 1973; Maruyama *et al.*, 1991). Californium-252 emits fast neutrons accompanied by gamma rays. Other radioisotopes used in the standard treatment in brachytherapy emit mostly gamma rays. The median energy of neutrons emitted by ^{252}Cf is about 1 MeV. Secondary particles produced by fast neutrons generate dense ionisation tracks in tissue and as a result they have significantly higher LET and RBE than gamma radiation. Neutron damage to a cell is less affected by factors which increase the cell's resistance to radiation such as cell cycle, repair ability and hypoxia (Maruyama,

1984). The main application of californium-252 brachytherapy is in the treatment of gynaecological cancers (Brady *et al.*, 1995; Maruyama *et al.*, 1991).

As pointed out by Mark Rivard (Rivard, 1999), practical dosimetry in ^{252}Cf brachytherapy differs from the recommendations of the American Association of Physicists in Medicine Task Group No. 43 (Nath *et al.*, 1995). The recommendations were made for the gamma and electron emitting isotopes used in brachytherapy. Californium-252 emits fast neutrons and for this reason its dosimetry should be based on the same principles as for the dosimetry of an external fast neutron beam. A comprehensive study of ^{252}Cf dosimetry was published by Mark Rivard (Rivard, 1999), who developed a protocol and performed Monte Carlo MCNP (Briesmeister, 1986) calculations and experimental measurements of ^{252}Cf applicator tubes. The protocol was based on the International Commission on Radiation Units and Measurements report No. 45 on patient dosimetry for external fast neutron beam treatment (ICRU, 1989). The calculations were performed for 11 different materials including water, plastic and body tissues. The measurements were performed by two types of tissue equivalent ionisation chambers and by a GM counter. The GM counter is less sensitive to fast neutrons and was used paired with a tissue equivalent ionisation chamber to separate gamma and neutron doses. To minimise the effect of thermal neutrons, the GM counter was put inside a LiF cap. Neutron and proton dose rates were measured and compared with the calculated values.

Mark Rivard further developed the concept of californium-252 dosimetry in the subsequent paper (Rivard, 2000) where he calculated energy spectra of ^{252}Cf

neutron at different depths in water. The spectrum has two peaks, one peak represents fast neutrons with an average energy of approximately 1 MeV, while the second one corresponds to the thermal neutrons. The ratio of fast neutron to thermal neutron fluxes, at a point of 1 cm away from the source, is approximately 1:5. Fast neutrons are moderated in water and at a distance of 5 cm the ratio becomes 3:1. The thermal neutron flux depends strongly on the water phantom size. The flux at 5 cm depth in a 10 cm diameter water phantom is only approximately one tenth of the thermal neutron flux in a 50 cm water phantom.

Californium-252 brachytherapy can be enhanced by boron-10 neutron capture decay. Boron neutron capture enhancement was first suggested in the early 1990's (Beach *et al.*, 1990; Wierzbicki *et al.*, 1991). The enhancement in a ^{252}Cf radiation field can be achieved in a way similar to that used in a fast neutron therapy beam. The boron dose enhancement was calculated by Monte Carlo (Allen & Ralston, 1997) and measurements of boron dose were performed for 2 types of californium-252 sources by Schmidt *et al.* (Schmidt *et al.*, 1999). They applied a Mg/Ar ionisation chamber coated with a 3 μm thick layer of ^{10}B. One of the californium-252 brachytherapy facilities was at the Harper Hospital, Detroit, USA and the other one was at Chiang Mai Hospital in Thailand. The Harper Hospital ^{252}Cf sources were produced by the Oak Ridge National Laboratory, and the Chiang Mai Hospital sources were produced by the Frontier Technology Corporation. The dose components of the Chiang Mai Hospital source, such as neutron and gamma doses, were measured by a combination of a Mg/Ar ionisation chamber and a GM tube (Wanwilairat *et al.*, 2000).

In this project the thermal neutron flux around a californium-252 source in a water phantom was determined experimentally. The measurements were performed at the Harper Hospital with a source produced by the Oak Ridge National Laboratory. Six sources were placed in a plastic tube and the tube was immersed in water. Each source had approximately 11 μg of ^{252}Cf and in total 66 μg of ^{252}Cf were placed in the tube. The phantom had perspex walls and was of a square prism shape with a 30 × 30 cm^2 base. The water level was also 30 cm. Ion implanted silicon detector probes were used in the same 3 configurations as in FNT measurements at the same hospital:

- Bare detector with no converter
- Detector with a ^{235}U fission converter
- Detector with a 1% ^{10}B converter

A silicon detector was placed in the water phantom at a distance of 5 cm from the source. The centre of the detector was positioned at the same level as the centre of the source tube. All three detectors were placed around the source in the phantom at the same time and the energy spectra were simultaneously acquired from all three detectors by a three input channel spectroscopy system. Each channel used a separate charge sensitive preamplifier, main spectroscopy amplifier and an analogue-digital converter. The settings of the spectroscopy system were calibrated by a reference ^{210}Po alpha source. Two measurements were performed for the same positions of the detectors at the two different acquisition times of 716 sec and 988 sec.

Table 6-5. Thermal neutron flux measured by a ^{235}U fission converter detector at 5 cm distance from the source in a water phantom and normalised per milligram of ^{252}Cf. Boron dose rate calculated for 50 ppm ^{10}B concentration per milligram of ^{252}Cf.

Acquisition Time, sec	Thermal neutron flux, $n \cdot cm^{-2} \cdot s^{-1} \cdot mg^{-1}$	Boron dose rate, $cGy \cdot s^{-1} \cdot mg^{-1}$
716	2.14×10^{7}	9.10×10^{-3}
988	2.17×10^{7}	9.26×10^{-3}

Thermal neutron flux was measured by a silicon detector with a ^{235}U fission converter. The measurements were calibrated to the mass of ^{252}Cf in the radiation source. The results are presented in Table 6-5. The boron dose was calculated from the thermal neutron flux data by the method described in Chapter 6.7. Boron-10 concentration for the calculation was taken as 50 ppm.

The thermal neutron flux data for both measurements are very similar to each other. The difference between the measurements does not exceed 1.5%, therefore it confirms the reproducibility of the fission converter detector measurements. The thermal neutron flux obtained by the silicon ion implanted ^{235}U fission converter detector was compared to Monte Carlo calculations published by Mark Rivard (Rivard, 2000). The measurements were compared to calculations performed for a 15 cm diameter water phantom. The calculated thermal neutron flux was 1.1×10^{7} $n \cdot cm^{-2} \cdot s^{-1} \cdot mg^{-1}$, which is only about one half of the measured value. The calculations were performed in a different geometry than in this experiment, with a detector in the centre, surrounded by several sources. The calculations were very

sensitive to the size of the phantom. Thermal neutron flux was calculated as 1.7×10^{7} $n\cdot cm^{-2}\cdot s^{-1}\cdot mg^{-1}$ for a phantom of 20 cm diameter. This size may be a closer approximation of a 30 × 30 cm^2 square phantom. Thermal neutron flux becomes 2.0×10^{7} $n\cdot cm^{-2}\cdot s^{-1}\cdot mg^{-1}$ for a phantom of 25 cm diameter. Taking into account the difference in the geometry of the sources, geometry of the phantom and a strong dependence of the calculated result on the phantom size, we can conclude that the agreement between the measurements and the calculations was satisfactory.

The boron dose rate for a 50 ppm concentration of ^{10}B was compared to measurements using a ^{10}B loaded Mg/Ar ionisation chamber performed at the Harper Hospital by (Schmidt *et al.*, 1999). Their measurements at 3 cm distance in a water phantom produced a boron dose rate of 8.8×10^{-3} $cGy\cdot s^{-1}\cdot mg^{-1}$. This value is approximately 4% smaller than the measurement obtained using a uranium-235 fission converter. The agreement between the two measurements is good. As previously, a ^{235}U fission converter measurement slightly overestimated the boron dose. This overestimation is related to the difference in energy dependence of the ^{10}B and ^{235}U neutron capture cross-sections.

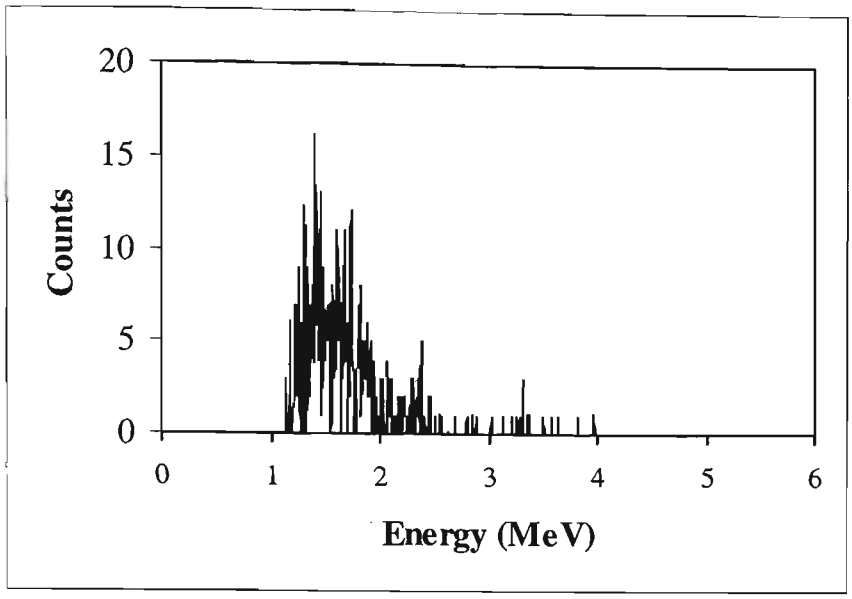

Figure 6-18. A difference spectrum of ion implanted silicon detectors with and without a ^{10}B converter at a distance of 5 cm from a ^{252}Cf source in a water phantom.

Two identical silicon detectors, one with a ^{10}B converter and one with a bare detector without a converter were exposed to ^{252}Cf radiation at 5 cm in the water phantom. The difference spectrum, Figure 6-18, reveals a maximum at 1.5 MeV, which corresponds to the energy of alpha particles released in boron-10 neutron capture decay. The data presented in this chapter confirm the possibility of boron-10 enhancement of californium-252 brachytherapy.

6.9. Conclusions

The uranium-235 fission converter, small size semiconductor detector probe was developed and successfully applied for in-phantom measurements of thermal neutron flux distribution at therapeutic neutron irradiation facilities, such as

epithermal BNCT, thermal BNCT, Fast Neutron Therapy and Californium Brachytherapy. A mathematical model of a detector with a thick fission converter response was derived for absolute measurement of thermal neutron flux.

The agreement between fission detector measurements and Monte Carlo calculated fluxes at the epithermal irradiation facility at BMRR was good. Advantages of the uranium converter fission detector include internal on-line calibration by alpha particles produced by spontaneous decay of uranium-235; fast measurement which requires a single reactor run; small size of the detector (ie smaller that a miniature ionisation chamber), which minimises radiation field perturbation; and the possibility of on-line monitoring of the thermal neutron flux.

The application method and data analysis of the uranium converter silicon detector was developed and validated by comparison with Monte Carlo calculations and reference measurements in an epithermal BNCT beam at the Brookhaven National Laboratory. Thermal neutron flux distribution peaked at a depth range of 1.5 cm to 4 cm in a perspex phantom. The method was applied for measurement of thermal neutron flux in a filtered thermal BNCT beam of the Osaka reactor. Thermal neutron flux peaked at the depth range of 1 cm to approximately 2.5 cm. The lateral distribution of the thermal neutron flux was not uniform, dropping to half of it maximum value at the central axis when measured at about 5 cm off the central axis. The measurements were performed in water.

Calculation of boron dose in the fast neutron therapy beam, based on the thermal neutron flux measurement by the silicon detector with a uranium-235 fission

converter, was in a good agreement with the paired proportional counter method. The boron dose calculated for 50 ppm ^{10}B concentration was within the error limits of the dose measured by a tissue equivalent proportional counter with walls loaded with 50 ppm of ^{10}B. The contribution of the boron dose to the total dose was 4-5%, while the biological dose enhancement, which takes RBE into account, was estimated to reach 30%.

For the boron dose enhancement of FNT to be clinically significant, a neutron radiation beam should contain a substantial thermal neutron component. Modification of the fast neutron beam by a tungsten rod collimator was proposed to increase the thermal neutron component of the beam (Kota *et al.*, 1997). Our measurements showed that the tungsten rod collimator, when it is closed, changes the energy spectrum of neutrons in a water phantom by increasing the relative thermal neutron component. At the same time the relative fast neutron component of the beam is decreased, which may cause a change in the therapeutic properties of the beam. The total intensity of the beam also decreases with the introduction of a tungsten filter.

The suitability of an ion implanted silicon detector with a ^{235}U fission converter as an absolute thermal neutron detector in neutron radiation therapy was confirmed by measurements in a ^{252}Cf radiation field. The measured thermal neutron flux was in agreement with Monte Carlo calculations, while the boron dose was in good agreement with ^{10}B loaded ionisation chamber measurements.

The boron dose distribution in a perspex phantom at the BNCT facility at BNL, as measured by the paired MOSFET dosimeter method, peaks at a depth of 2 to 4 cm. The maximum boron dose corresponds to the peak in thermal neutron flux distribution in the phantom, as measured by a fission converter detector and calculated by Monte Carlo simulation.

The relative dose measured in an epithermal BNCT beam, by both p- and n-channel MOSFET detectors, was in a good agreement between the two types of MOSFETs and with the Monte Carlo calculations.

To improve the accuracy of a fission converter detector, a thinner uranium-235 converter should be used, preferably with a thickness of less than 1 μm. A smaller sized silicon detector will also further reduce the perturbation of the radiation field and thereby improve spatial resolution of the detector.

Chapter 7. Microbeam radiation therapy and radiation dosimetry of x-ray microbeams

Microbeam radiation therapy (MRT) is a new experimental modality which uses an array of 20 μm to 200 μm wide x-ray beams produced by a synchrotron for treatment of brain tumours. MRT takes advantage of the very high tolerance of normal tissue to extreme doses of radiation delivered to a very small volume. The experimental measurement of absorbed dose distribution across the path of a microbeam represents a challenge as it requires a dosimeter with a micron resolution. For this reason, microbeam dosimetry research has focused on Monte Carlo simulations of the absorbed dose. So far no experimental method for measuring the radiation dose across a microbeam has been available. Experimental verification of MRT dose planning calculations is necessary for the validation of dose planning and for progressing this new modality to the stage of clinical trials.

7.1. Aim

The aims of the research into the dosimetry of an x-ray microbeam were

⇒ To develop a new method of high spatial resolution on-line dosimetry using a MOSFET detector

⇒ To evaluate the performance of high spatial resolution radiation detectors within a micron range

⇒ To establish a method for experimental dosimetry of a planar x-ray microbeam

⇒ To experimentally measure the radiation dose profile across a synchrotron planar microbeam used in the development of microbeam radiation therapy

7.2. Current stage of development of MRT

7.2.1. Radiobiology of microbeam irradiation

In the late nineteen fifties and in the nineteen sixties an interest in the biological effects of high energy charged particle microbeams was fostered by manned space fights. It was assumed that a high energy cosmic radiation may adversely affect the astronaut's health.

The neurological effects of high-energy cosmic rays on humans was modelled by micron sized, high energy deuteron (Ordy *et al.*, 1963; Zeman *et al.*, 1961; Zeman *et al.*, 1959) and by x-ray microbeams (Straile & Chase, 1963) irradiation of mice. The findings showed that the threshold absorbed dose for cerebral damage was significantly higher for a microbeam than for a 1 mm beam (Curtis, 1967) and that tolerance of a normal tissue to an absorbed radiation dose increases with a decrease in the irradiated volume. The idea of using a narrow proton beam as a neurosurgical tool was first suggested in 1958 by (Larsson *et al.*, 1958).

The histopathologic effect on a mouse brain of a 22.5 MeV cylindrical deuteron beam was investigated for beam diameters of 1 mm, 250 μm, 75 μm and 25μm (Zeman *et al.*, 1961; Zeman *et al.*, 1959). The effect on a mouse brain of irradiation to 720 Gy by two parallel microbeams of 9 mm × 0.025 mm with 0.5 mm spacing, applied across the neocerebellar cortex, was also studied (Ordy *et al.*, 1963). The dose rate for the cylindrical beams was varied from 150 to 600 Gy per second. The effect of the dose rate on the development of brain lesions was relatively small, while the effect of the beam diameter was found to be highly significant. For a beam diameter of 1 mm, a cavity was produced in the mouse brain within 12 days after irradiation. A dose of approximately 140 Gy was the threshold for histologic effect within 24 days after irradiation by a 1 mm beam. The threshold dose increased to 360 Gy for a 0.25 mm beam, 500 Gy for a 75 μm beam and up to 4,000 Gy for a 25 μm beam. The statistical variation in the threshold dose for different mice was much smaller for 75 and 25 μm beams then for larger beams. Variations in tissue tolerance were observed from animal to animal rather than within a single animal. When both cerebral hemispheres were irradiated, the same reaction was found on the both sides. Therefore, a decrease in variation of radiation effect with a decrease in the beam diameter suggested that variations in the tissue tolerance were due to vascular factors.

For beam diameters of 75 and 25 μm, damage to blood vessels was observed in the first few weeks after irradiation. The damage was reversible since the vessels looked entirely normal in 3 to 6 months after irradiation. The nerve cell bodies,

surrounding the vessels in the path of the microbeam, disappeared permanently. The vascular endothelial cells did not escape radiation damage but were able to regenerate. This regeneration ability was not shared by the nerve cell bodies. In contrast to larger beams, the 25 μm beam, while destroying nerve cell bodies, did not destroy nerve fibres, and interstitial glia cells were partially preserved. Once the nerve cells had disappeared there was no further change and no shrinkage to the irradiated tissue.

An explanation for the dramatic decrease in brain tissue radiation sensitivity is that a microbeam causes predominantly direct radiation damage, while a larger beam produces an additional indirect effect. When a large area is irradiated, the radiation effect includes different forms of vascular disturbances, which play an important role in the pathological development of radiogenic lesions.

An interest in the medical applications of an x-ray microbeam was activated by development of a high intensity synchrotron source of x-ray radiation at the Brookhaven National Laboratory (BNL) (Steenbergen & staff, 1980). The synchrotron source provides a very low divergence beam. The range of secondary delta electrons in tissue is microscopically short for x-rays with energies between 50 to 100 keV. Low divergence and small delta electron ranges make it possible for the synchrotron microbeam to have sharply defined beam edges at a significant depth within the body. The synchrotron high dose rate, of up to 1000 Gy per second, is required for reducing the irradiation time in MRT. The exposure time should be kept short to avoid blurring of the margins of the irradiated zones in the body due to organ movement.

The current interest in microbeam radiation therapy (MRT) has been led by Slatkin *et al* at BNL (Slatkin *et al.*, 1992). Using synchrotron radiation, they have established that induced brain tumours in rats can be controlled by microbeam radiation therapy (Laissue *et al.*, 1998; Slatkin *et al.*, 1995b). An experimental study of the effects of synchrotron microbeam irradiation on the brains of rats (Slatkin *et al.*, 1995b) revealed no brain tissue necrosis after irradiation of up to 10,000 Gy entrance absorbed dose. The irradiation resulted in loss of neuronal and astrocytic nuclei. The principal behind MRT is that normal tissue can tolerate high doses of radiation without leading to necrosis. This is because the survival of capillary cells adjacent to the exposed region of lethally irradiated capillaries allows regeneration, thus avoiding tissue necrosis (Zeman *et al.*, 1961). The high dose delivered in each fraction is sufficient for fast killing of the cells in the path of the microbeam. The exact mechanism of selective tumour suppression by a microbeam is not yet known. At this stage we can only speculate that the difference in growth kinetics between tumour and endothelial cells allows the capillaries to re-grow between the dose fractions.

Apart from a higher tolerance of normal tissue to microbeam radiation, advantages of MRT include a higher precision of delivery of a lethal dose to a tumour region. Stepanek *et al.* (Stepanek *et al.*, 2000) calculated, that by cross-firing of two microbeam arrays, MRT is capable of delivering a peak dose of 84 Gy to a deep adult brain tumour during a single fraction. The dose outside the target zone will not exceed 6 Gy which is within tissue tolerance limits. By contrast, same dose of 84 Gy delivered to a 3 cm lesion with standard radiosurgery by millimetre-

diameter beams will penetrate to approximately 1 cm in normal tissue beyond the target volume (Stepanek *et al.*, 2000).

When implemented, microbeam radiation therapy may be beneficial for treatment of infant brain tumours. Attenuation of the x-rays is considerably reduced in a smaller sized infant's brain. An investigation by Dilmanian *et al.* (Dilmanian *et al.*, 1997) proved that developing brains of suckling rats and 4-day prehatched ducks are much less susceptible to damage from irradiation by a planar microbeam array than by a standard macroscopic x-ray beam.

All of the more recent results on the biological effects of x-ray microbeam radiation were obtained at the National Synchrotron Light Source (NSLS) in BNL. Much of the older data on the biological effects of deuteron and proton beams were also obtained at BNL facilities. BNL scientists, utilising the NSLS, are leading the field in MRT research. More recently a research program in MRT started at the European Synchrotron Radiation Facility in Grenoble in France (Thomlinsons *et al.*, 2000). The research in Grenoble is focused on irradiation of the brains of suckling rats and several-week-old pigs, with an aim to predict the radiation tolerance of human infant brains. Histological studies on the effects of microbeam radiation on animal brains are also being conducted at the Pathology Institute of the University of Bern in Switzerland by (Laissue *et. al.* 1998).

7.2.2. Radiation dosimetry of x-ray microbeams

Experimental measurement of an absorbed dose distribution across the path of a microbeam represents a challenge because it requires a dosimeter with a micron resolution. The difference between the actual and the measured radiation dose can be significant if the size of the dosimeter is comparable or even greater than the width of the beam penumbra. The size of most conventional dosimeters exceeds a few tens of micrometers width of a microbeam penumbra. For this reason, microbeam dosimetry research has focused on Monte Carlo computer simulations of the absorbed radiation dose.

In the first published paper on a microbeam absorbed dose profile Slatkin *et al* (Slatkin *et al.*, 1992) calculated, by using the Monte Carlo method, the absorbed dose distribution for an array of x-ray microbeams. The calculations were performed using an EGS4 computer code (Nelson *et al.*, 1985), a Persliden charged-particle-equilibrium photon code (Persliden, 1983) and an unpublished charged-particle-equilibrium photon code by F. A. Dilmanian of BNL. All the codes were based on a Monte Carlo method. EGS4 is the only one of the three codes that takes secondary electron transport into account. The accuracy of these methods applied to microbeam calculations were compared in the path of a microbeam, in the penumbra region and in the space between the microbeams. It was demonstrated that secondary electron transport is important for accurate calculation of the deposited dose in the penumbra region of the microbeam, where

the dose gradient is steep. The calculations were performed at different depths in a phantom for x-ray energies of 50, 100 and 200 keV. Two profiles of microbeams were used: a cylindrical microbeam of 25 μm in diameter, and a planar microbeam of 25 μm wide by 30 mm high. Different configurations of arrays were substituted into calculations for each microbeam at each energy of x-rays. The calculation proved that the peak-to-valley absorbed dose ratio was increasing with an increase of x-ray energy. With increased depth in the phantom, the peak-to-valley absorbed dose ratio decreased. This ratio also depends on the spacing between the microbeams in an array. For an array of 25 μm wide planar microbeams, with 200 μm centre-to-centre intervals, propagated within the envelope of a 3×3 cm^2 cross-section and with an x-ray energy of 100 kV, the peak-to-valley absorbed dose ratio near the surface of the phantom was 35:1. The ratio decreased to 12.8:1 at a depth of 7.5 cm. The entrance absorbed dose for each microbeam of 111 Gy was reduced to 31 Gy in the path of the microbeam at a depth of 7.5 cm in water. The absorbed dose for the interval between the microbeams was 2 Gy. The threshold for irreversible morphological damage to tissue is about 10 Gy. The absorbed dose in the interspace between the microbeams was considerably less than the threshold, while the dose in the path of the microbeam was significantly greater.

Monte Carlo EGS4 absorbed dose calculations were performed for a 2 cm × 150 μm microbeam of 88 kV Cadmium-108 radiation by Company and Allen (Company & Allen, 1996). More accurate calculations were later performed for the interface absorbed doses (Company & Allen, 1998). The microbeam absorbed dose was calculated for a tissue-lung-tissue phantom. The width of the 150 μm

planar ^{108}Cd microbeam was experimentally measured by a 5 cm diameter NaI(Tl) scintillation detector (Company & Allen, 1996). The integral photon signal was measured versus the micron step displacement of a lead shutter. While providing data on the width of the microbeam, this method was not suffiently accurate to measure the absorbed dose distribution across the microbeam. The integral method does not allow microbeam penumbra measurements.

An upgraded EGS4 code was applied by (Orion *et al.*, 2000). The code was upgraded with a low energy photon scattering expansion package. The package included a polarised photon-bound Compton scattering, linear polarised characteristics and a Doppler broadening effect. The updated code calculated a steeper penumbra than the older version of EGS4.

Another Monte Carlo code, the GEANT, was applied by (Stepanek *et al.*, 2000) for calculations of an x-ray microbeam energy spectrum and absorbed-dose profiles. This method accounted for secondary electron transport and used experimental electron cross-sections and atomic data compiled at the Lawrence Livermore National Laboratory. The results of the calculation of absorbed dose profiles by the GEANT were close to the EGS4 calculations in peak and penumbra areas, but the GEANT predicted a higher dose in the valley region between the two planar microbeams.

A major advantage of the metal-oxide-semiconductor field effect transistor (MOSFET) as a radiation monitor is that the radiation-sensitive region, the oxide film, is very small and thin (Holmes-Siedle, 1974b; Rosenfeld *et al.*, 1995), see

also Chapter 3.1. The sensing volume is much smaller than for other integral dose measuring devices, such as an ionisation chamber, a semiconductor diode or a thermoluminescent dosimeter (TLD). The smallest available liquid ionisation chamber (Dasu *et al.*, 1998) has a dosimetric volume of about 2 mm^3, while the TLD has a volume of approximately 1 mm^3. The semiconductor diode sensitive volume is approximately 0.3 mm^3 (Dasu *et al.*, 1998). The MOSFET's sensitive volume is typically $1 \times 200 \times 200$ micrometers or only 4×10^{-5} mm^3.

The relationship between the size of the sensitive volume and the measured width of the penumbra of a small diameter high energy x-ray beam was recently investigated by (Westermark *et al.*, 2000). Five different detectors were exposed to 4, 8, 14 and 18 mm diameter linac beams with energies of 6 MV and 18 MV. The detectors were:

- Double diode, thickness of active volume 0.06 mm. A pilot sample was made for that study
- Natural diamond, thickness 0.29 mm, volume 4.2 mm^3
- p-type Scanditronix diode, thickness about 0.5 mm
- Liquid ionising chamber, diameter 1.5 mm, thickness 0.6 mm
- Miniature plastic scintillation detector, as described by Beddor *et al* (Beddor *et al.*, 1992), diameter 0.1 mm, thickness 0.1 mm

The spatial resolution of the thinnest detector, the double diode, was found to be the best at all the beam diameters and for both beam energies. It was followed by the diamond, then the p-type diode, the liquid ionising chamber and the plastic

scintillator. With the exception of the plastic scintillator, the detector spatial resolution is determined by the thickness of the sensitive volume. The poor performance of the plastic scintillator was related to light produced in the light guide.

Attention is thus now being turned to the use of MOSFETs, especially where the sensor has to be inserted into a confined space such as a catheter (Gladstone *et al.*, 1994b; Hughes *et al.*, 1988a). The small sensitive volume of the MOSFET also makes it attractive for measurements in a high gradient radiation field, where the gradient mostly depends on a single space co-ordinate, such as resolving dose profiles of x-ray microbeams or depth dose distribution.

7.3. The "edge-on" application of a MOSFET detector in an x-ray microbeam

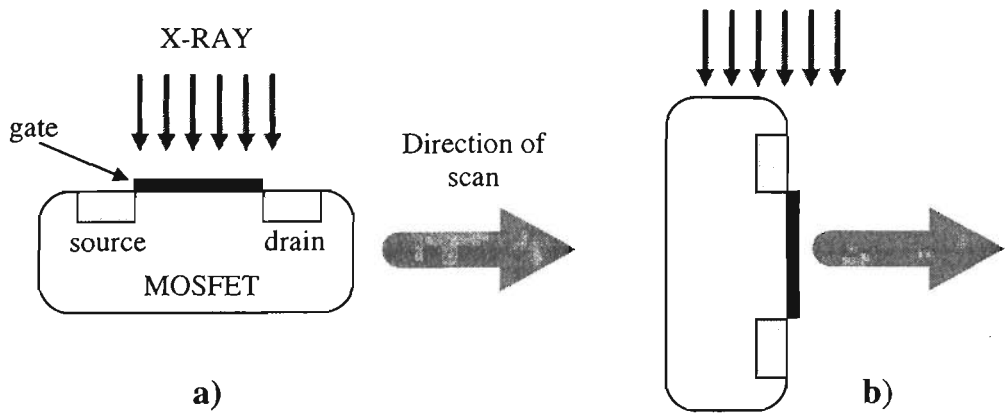

Figure 7-1. MOSFET application in a) "normal" and b) "edge-on" orientations.

A MOSFET dosimeter is typically used with the surface of the silicon chip normal to an incident x-ray beam (Figure 7-1a). The MOSFET has been applied in this orientation in the previous chapters of this thesis and in the available literature. For this mode the spatial resolution is limited by the external dimensions of the MOSFET gate oxide, which is approximately 200 μm × 200 μm for an n-type MOSFET (Figure 3-2) and is of a similar size for a p-type MOSFET or a RADFET. To take advantage of the micron thin sensitive volume of a MOSFET and to apply it in order to increase the spatial resolution of the detector, the detector plane has to be rotated until the oxide film is "edge-on" to the beam (Figure 7-1b). This constitutes a new approach to MOSFET dosimetry. In this orientation, the theoretical limit of resolution is 1 μm, the thickness of the gate oxide.

In order to test the "edge-on" application of a MOSFET and to evaluate the improvement in spatial resolution compared to the traditional application of a MOSFET detector, a very thin x-ray beam was required. A synchrotron microbeam is not available in Australia, therefore the output of an orthovoltage x-ray generator was adapted to provide a narrow beam. A micrometer controlled variable width collimator was obtained from the synchrotron group in Melbourne and attached to a brass adapter to be attached to the end of the applicator of a Therapax DXT300 orthovoltage x-ray machine at the Illawarra Cancer Care Centre (see Chapter 3.4.1 for a description of the x-ray machine).

The slit width of the variable width collimator (Figure 7-2) can be controlled by two micrometer screws. The micrometers control the opening between two steel

plates with lead lining. The plates have wedge shaped edges facing each other. The wedges make the width adjustment more accurate, but, at the same time, x-rays can partly penetrate through the thinner part of the plates blurring the edges of the microbeam.

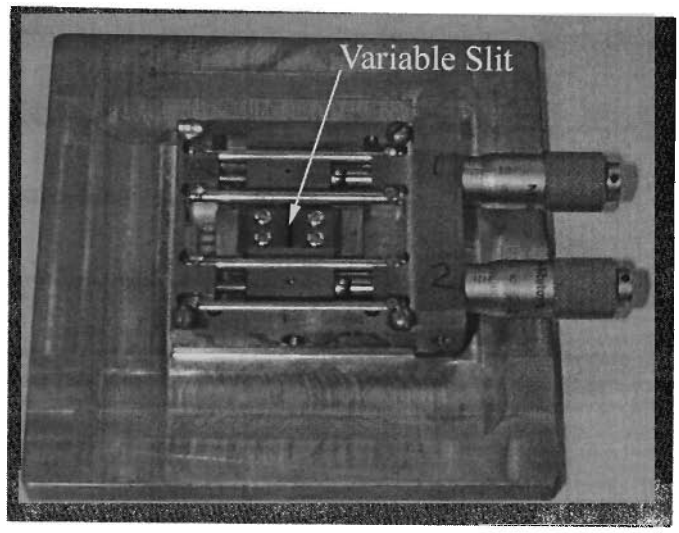

Figure 7-2. Variable slit-collimator for attaching to the applicator of a Therapax DXT300 orthovoltage x-ray machine

The collimator was set to a 200 μm slit width with the a length of 1 cm. The accuracy and uniformity of the slit was checked by a travelling microscope. The slit was attached to the x-ray machine applicator and the x-ray energy was set to 100 kV_p, which corresponded to an effective energy of 39 kV. The effective energy was determined by a half value layers method. Half value layers for aluminium and copper filters were 3.5 mm and 0.15 mm respectively. The energy was determined by application of the energy dependent interaction coefficients for aluminium and copper, as tabulated by Johns and Cunningham (Johns & Cunningham, 1983).

The spatial resolutions of both n- and p-type MOSFETs were tested for the "edge-on" orientation of each detector. The MOSFET dosimeters were exposed to the microbeam in air, i.e. without any build-up material, in "normal" and "edge-on" orientations. The lids of the MOSFET housings were removed and the chips were exposed directly to the x-ray beam. The MOSFET was fixed to the end of a perspex rod, which was attached to a micrometer jig and allowed translational motion with a resolution of 2 micrometers (see Chapter 3.5.2).

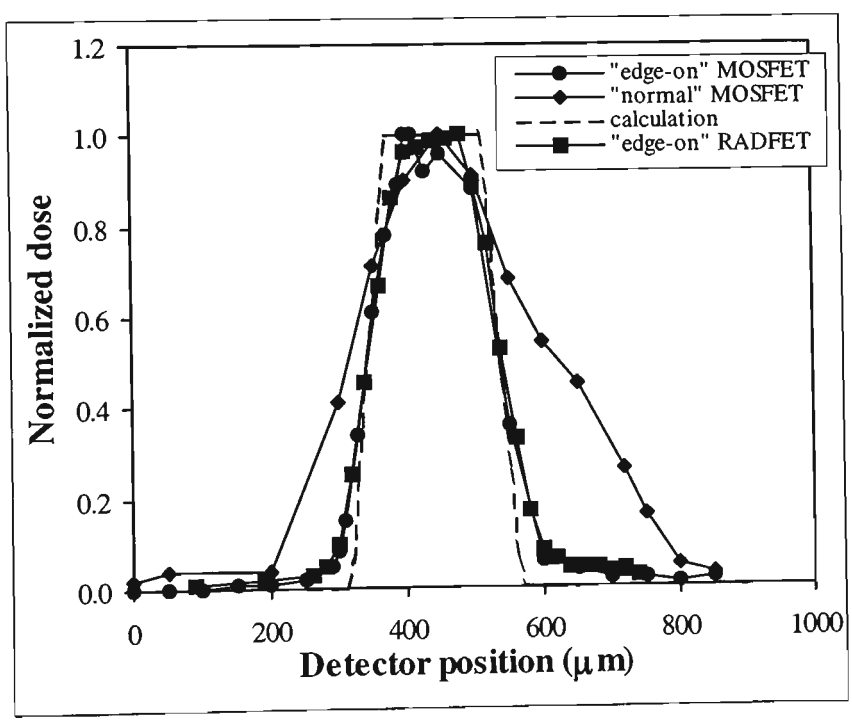

Figure 7-3. Comparison of transverse radiation dose profiles across the 200 μm wide microbeam measured by a MOSFET detector in both "normal" and "edge-on" orientations.

The n-MOSFET dosimeter was exposed to the microbeam in two orientations, "normal" and "edge-on". The p-MOSFET dosimeter was exposed in the "edge-

on" orientation only. The dose delivered to the MOSFET per single irradiation shot in free air geometry was 17 MU, which corresponds to a maximum threshold voltage shift in the centre of the beam of about 150 mV. The readings were normalised to the maximum MOSFET response for each dose profile. The results (Figure 7-3) prove that the spatial resolution of a MOSFET dosimeter is indeed affected by the orientation of the detector in the beam, the resolution being superior in the "edge-on" mode.

The p- and n-MOSFET curves closely follow each other and are nearly identical. The MOSFETs differ by the shape and linear dimensions of their gates, while the thickness of the gates remains the same. The housing material also differs. The RADFET is attached to a plastic computer type board, while the n-type MOSFET was fixed in a Kovar housing. The nearly identical dose distribution profile, measured by both MOSFETs, demonstrates that scattering from the MOSFET housing has a little effect on the resolution of the device for low energy x-rays. It also proves that gate thickness is a critical parameter in determining MOSFET resolution.

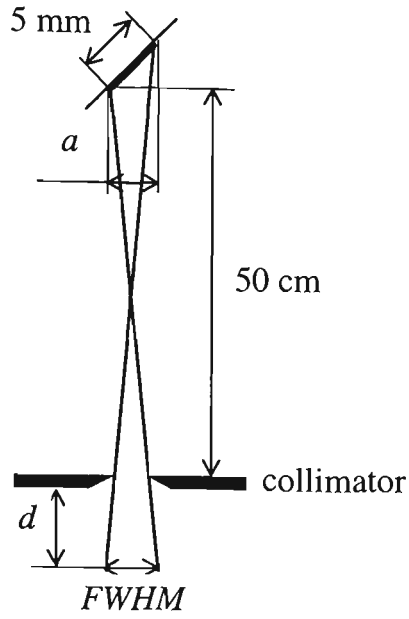

Figure 7-4. Sketch of the geometry of an X-ray beam produced by a Therapax DXT300 orthovoltage accelerator.

A dose distribution profile across a microbeam was calculated for the 200 μm wide slit attached to the Therapax DXT300 applicator. The calculation took into account only geometrical factors of the experimental set up and no physical considerations of x-ray absorption and scattering were made. A simple computer code was written and used in the calculations. A sketch of the x-ray beam geometry of the Therapax DXT300 orthovoltage accelerator is shown in Figure 7-4. The diameter of the anode spot was 0.5 cm and the distance from the spot to the collimator was 50 cm. This geometry was used for beam profile calculations at different detector-to-collimator distances, d, for comparison with experimental data. The electron beam produced by a Therapax DXT300 orthovoltage accelerator hits a target at an angle of 45°. The beam makes a 5 mm diameter spot, p, on the target (Figure 7-4). Thus, the effective size of the x-ray source is $a = p \cdot cos45°$. The distance between the target and the collimator, h, is 50 cm.

The calculated beam profile in air agreed well with both MOSFET and RADFET "edge-on" measurements (Figure 7-3). However, a discrepancy can be noted towards the external edges of the beam penumbra, where the intensity of the measured profile is greater than for that calculated. This discrepancy can be explained by the partial penetration of the x-ray beam through the thinner part of the wedges of the collimator plates (see the schematic presentation on the collimator edges in Figure 7-4).

7.4. High spatial resolution measurements of dose profiles across x-ray microbeams

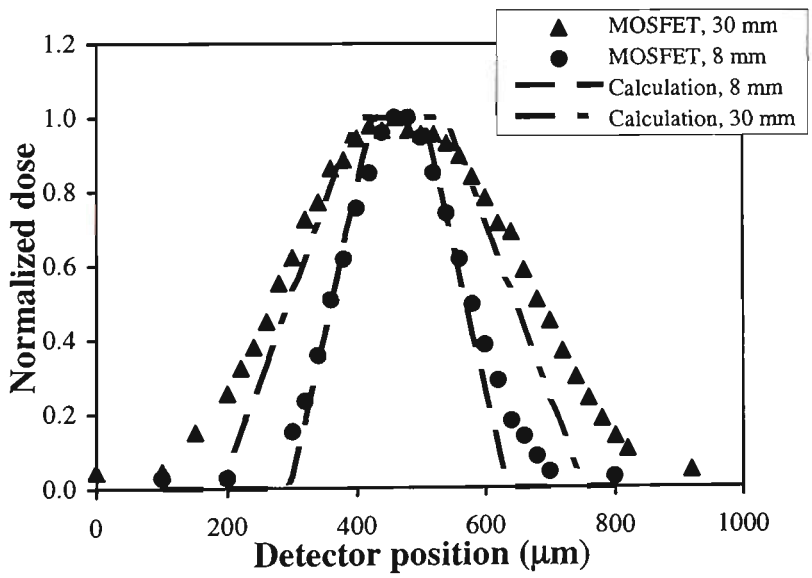

Figure 7-5. Measurement and calculation of transverse microbeam profiles at 0.8 and 3 cm depths in a perspex phantom. Measurement by an n-MOSFET dosimeter in "edge-on" mode.

The measurements of a microbeam in a perspex (PMMA) phantom using the "edge-on" MOSFET method were performed at depths in perspex of 0.8, 3 and 5 cm. Results at depths of 0.8 and 3 cm are shown in Figure 7-5, together with the calculated profiles at the same distance from the collimator. The transverse dose profile at 0.8 cm depth follows the calculated geometrical profile well (Figure 7-5). The full width at half maximum (FWHM) of the calculated and measured beams at a depth of 0.8 cm in the phantom are similar. The experimental FWHM exceeds the geometrical FWHM by less than 5%. As in a free air measurement, there is some discrepancy in the beam penumbra because of the partial penetration of x-rays through the wedge like shapes of the variable width collimator plates (Figure 7-4). Correlation between the calculation and the measurement indicates that at shallow depths the beam spreads out in the phantom, mostly due to the geometric divergence of the beam. However, the scattering effect becomes more significant at the greater depths. For the depth of 3 cm, the experimental FWHM becomes 16% wider than the calculated FWHM.

Gafchromic film was selected for resolution comparison between the MOSFETs. A detailed description of the film can be found in Chapter 3.3. Gafchromic film is a high spatial resolution two-dimensional detector with maximum resolution of the film reported as 1200 lines/mm (McLaughlin *et al.*, 1991). Gafchromic films have been applied previously for a high resolution x-ray dosimetry (Dempsey *et al.*, 2000; Francescon *et al.*, 1998; Sanders *et al.*, 1993; Zhu *et al.*, 1997).

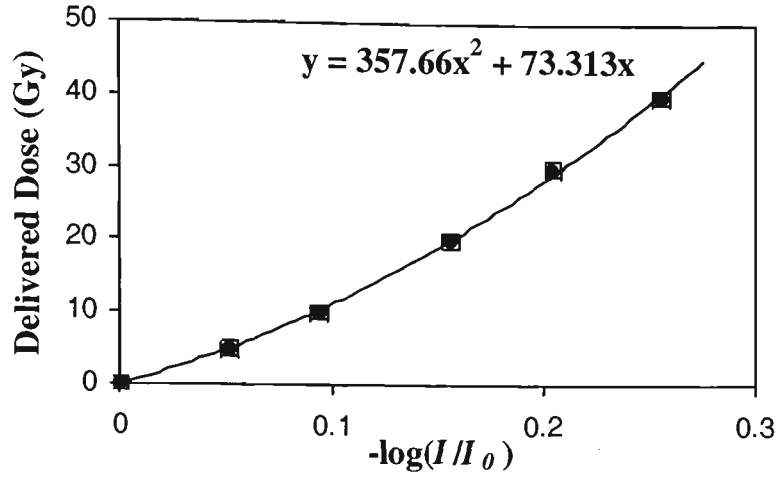

Figure 7-6. Gafchromic film calibration curve in a 100 kV_p x-ray beam.

For calibration of the dose response of Gafchromic film, the 1 cm^2 films were uniformly irradiated in air at doses from 0 to 40 Gy in steps of 5 Gy. For in air measurement, a film strip was suspended between two foam blocks to minimise backscattered radiation. After storing the films at room temperature in a light tight envelope for two days, the relative intensity of the transmitted light through the film was digitised and analysed by a CCD image analysis system (see Chapter 3.3.1). The dose, D, was plotted versus $-\log(I/I_0)$ where I is the intensity of transmitted light through an exposed film and I_0 is the intensity of transmitted light through an unexposed film. The calibration results were best fitted by a second degree polynomial (Figure 7-6).

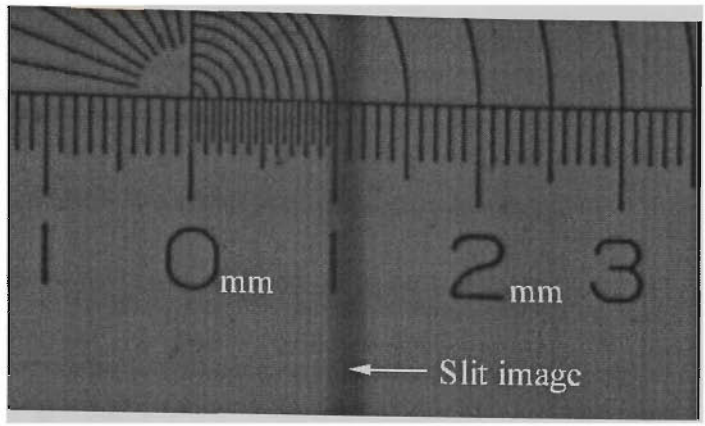

Figure 7-7. Gafchromic film. X-ray image of a 200 μm wide collimator slit. The film was placed on the top surface of a perspex phantom.

Strips of gafchromic film were sandwiched between the plates of 7.5 cm × 7.5 cm perspex phantom (Figure 3-6). The phantom was exposed in a 200 μm wide x-ray beam with an energy of 100 kV_p. The image of the slit is clearly visible in the film (Figure 7-7). The visual width of the x-ray slit is approximately 0.2 mm, which corresponds the 200 μm width of the collimator slit. The films were digitised by the same CCD image analysis system, used for the calibration (see Chapter 3.3.1).

A beam with a low or even nil divergence is important for MRT since overlapping of microbeams at some depth in the tissue must be avoided. The beam divergence is proportional to the distance between the detector and the collimator and is inversely proportional to the distance between the beam source and the collimator. For the Therapax DXT300 the latter distance is only 50 cm. So far the radiobiological aspects of MRT have mostly been studied at the synchrotron at BNL (Laissue *et al.*, 1998; Slatkin *et al.*, 1995a). For the BNL synchrotron, the beam travels 30 m after leaving the synchrotron wiggler before entering the treatment room (see also Chapter 3.4.5). At the BNL MRT facility a specimen for

irradiation is placed close to the therapy multislit collimator (Slatkin *et al.*, 1995a) thus minimising any divergence.

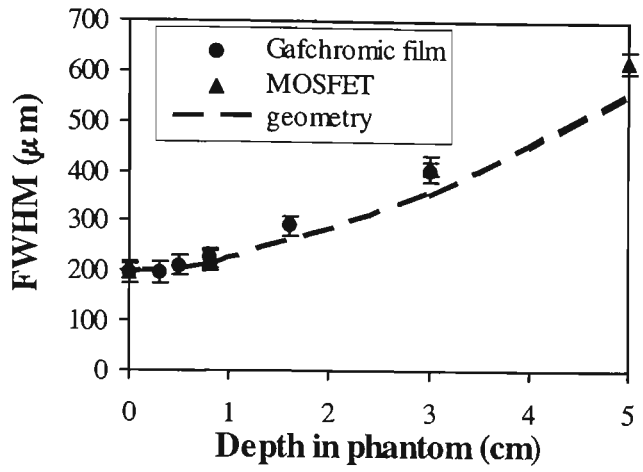

Figure 7-8. Experimentally measured and calculated FWHM of a 200 μm microbeam in a perspex phantom, using Gafchromic film and a MOSFET dosimeter in the "edge-on" mode.

The measured and calculated FWHMs of the 200 μm planar x-ray microbeam are plotted in Figure 7-8 against the depth in the phantom. For depths of less than 1 cm experimental points coincide with the geometry calculated curve which means that the increase in microbeam field size due to in-phantom scattering is negligible for these depths. Perspex has a higher density than tissue, $\rho = 1.18$ g/cm^3, and this has to be taken into account when estimating the scattering effect in tissue. Even when considering the 18% difference in density, scattering is not a significant factor in assessing microbeam width increase for depths in tissue of less than 2 cm.

Both MOSFET and Gafchromic film data are shown in Figure 7-5. The dependence of MOSFET and Gafchromic film response on the energy of x-rays should be noted, with the MOSFETs demonstrating a stronger dependence, (Kron *et al.*, 1998) see also Chapter 4.3. A correction for this energy dependence was not performed because the FWHM was determined from the relative dose measurements at the same depth in the phantom. It can be reasonably assumed that the x-ray spectrum, at a certain depth, did not change with less than 0.1 cm lateral displacement.

7.4.1. Comparison of the spatial resolution of a MOSFET and Gafchromic film

Microbeam measurements by the MOSFET and Gafchromic film show a very similar FWHM. To compare the two detectors, transverse profiles at the same depths of 0.8 and 3 cm in the phantom were measured (Figure 7-9). In both cases, the FWHM was similar and at the smaller depth (Figure 7-9a) both profiles closely follow each other. However, the Gafchromic film data are less uniform and at the greater depth, as a result of a weaker signal (Figure 7-9b), non-uniformity in the Gafchromic film response becomes more significant, reaching as high as 20%. A non-uniformity of optical density, up to 15%, of irradiated Gafchromic film has been previously reported (Meigooni *et al.*, 1996; Zhu *et al.*, 1997). Those measurements were performed on a scale of several millimetres, whereas the measurements in this study are on a smaller scale. Narrow spikes in optical density have previously been observed by (Meigooni *et al.*, 1996). In the

current higher resolution study, it was possible to resolve these spikes with a distance between neighbouring maxima of 40 to 60 μm (see Figure 7-9b).

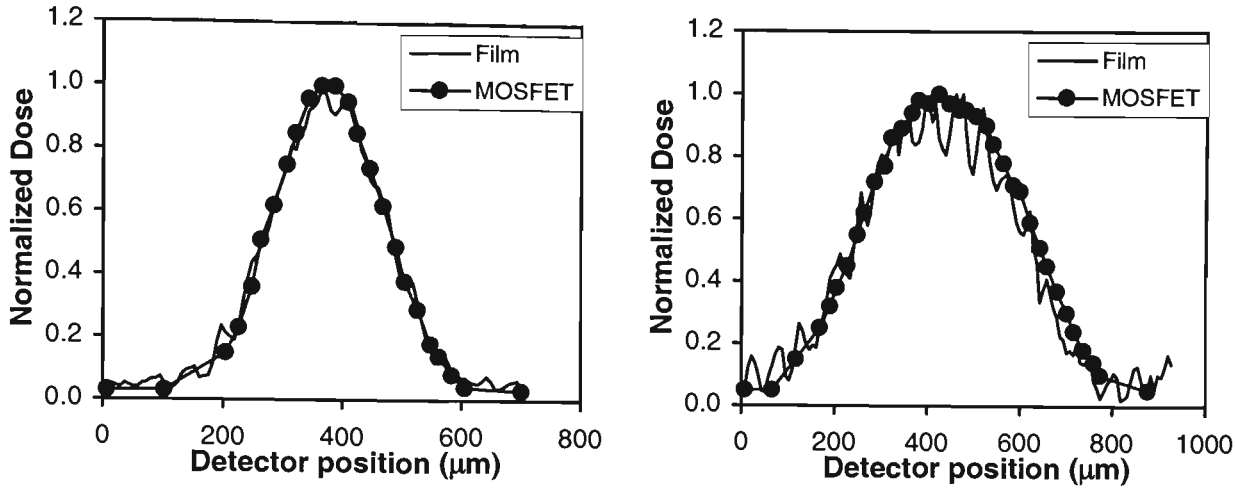

Figure 7-9. Comparison of the transverse microbeam profiles as measured by the MOSFET and Gafchromic film at a) 0.8 cm and b) 3 cm depths in perspex phantom.

The dose profile, as measured by a radiation detector, is a convolution of the true dose profile, detector resolution and the readout system resolution. The "edge-on" MOSFET and Gafchromic film dose profiles were identical (Figure 7-9). The MOSFET detector was shifted across the microbeam with a step of 10 μm which is similar to the film optical readout system resolution of 8 μm (Chapter 3.3.1). The resolution of the film is about 1 μm, thus implying that the MOSFET resolution limit is also about 1 μm. This is consistent with the main physical limitation of the MOSFET resolution which is the 1 μm thickness of the dosimetric volume, the gate oxide and it was confirmed by the measurements

described in the next section. MOSFET resolution can be further improved by using a MOSFET with a 0.1 μm thick oxide layer and by using a scanning system with a sub-micron step. The possibility for further reduction of Gafchromic film spatial resolution is limited.

The error analysis. The accuracy of the MOSFET microbeam measurements depends on accuracy of the detector, threshold voltage measurement, positioning device and consistency of the dose delivery by the Therapax x-ray machine. The consistency in dose delivery was ensured by using a constant set current of the x-ray machine beam and a constant irradiation time, it was also monitored by an in-beam ionisation chamber. It has been reported elsewhere (see for example (Kron *et al.*, 1998)) that the reproducibility of MOSFET measurements is no worse than the accuracy of the threshold voltage measurement. During this study, the MOSFET was irradiated twice with a fully open collimator to a reference dose of 15 MU. The duration of radiation exposure was 15 seconds. In both cases the change in threshold voltage was 117 mV. The combined accuracy of the MOSFET threshold voltage readout system was ±2 mV or 1.5%, for 150 mV change. The accuracy of the micrometry screw on the positioning device was ±1 μm for movement in a forward direction. A screw backlash reduced the accuracy for return movement so microbeam measurements were performed in the forward direction only. All the components of system accuracy, including backlash, were tested by moving the MOSFET 400 μm back and then repeating the measurement. The overall accuracy was found to be 3%.

7.4.2. MOSFET measurement of a dose distribution profile across 30 μm wide synchrotron microbeam

An n-type MOSFET was applied to measurement of the dose profile across an x-ray microbeam produced by the X17B1 beam line of the National Synchrotron Light Source in BNL (see Chapter 3.4.5). The MOSFET was embedded in a 20 cm long perspex rod with square cross-section of 1.5 cm × 1.5 cm. The detector sensitive element was 4.5 mm below the surface of the rod. The perspex rod, with the MOSFET detector in it, was shifted across the microbeam by a precision positioning system. The accuracy of the positioning system was 0.1 μm. The same system was used for rat irradiation at the facility. The measurements in the path of the microbeam were taken with a step of 1 μm. This was the first experimental measurement of a microbeam profile by a radiation detector. Prior to this, the dosimetry of an x-ray microbeam was limited to theoretical calculations.

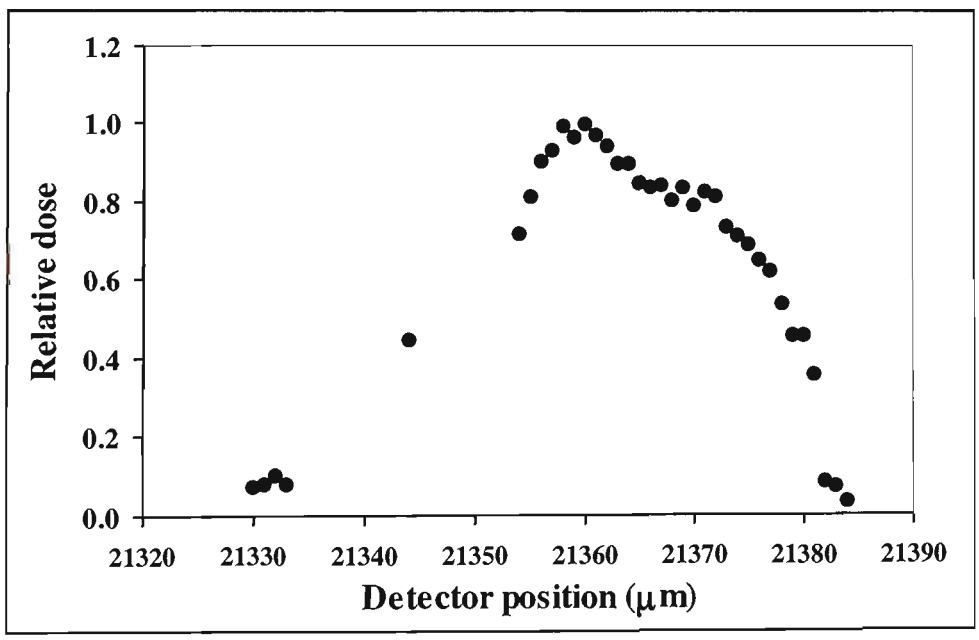

Figure 7-10. "Edge-on" MOSFET measurement of the relative dose profile across a 30 μm wide synchrotron microbeam at the NSLS in BNL.

The dose distribution profile across a 30 μm wide x-ray microbeam is presented in Figure 7-10. The experimental data were within 10% agreement with Monte Carlo calculations by (Orion *et al.*, 2000) for the same microbeam. The experimental points can be fitted by a smooth curve and a more than 10% difference can be observed in the penumbra region between two consecutive MOSFET readings separated by only 1 μm. Thus, the microbeam dose distribution profile confirmed that the "edge-on" MOSFET spatial resolution was 1 micrometer.

7.5. Conclusions

This study has developed a new technique of application of a MOSFET detector using an "edge-on" method that allows a significant increase in spatial resolution. Spatial resolution of the MOSFET detector in an "edge-on" orientation was approximately 1 μm, which equals the thickness of the gate oxide.

Spatial resolution of the MOSFET in an "edge-on" orientation matches the resolution of Gafchromic film but a further increase in MOSFET resolution is possible if a thinner gate oxide is selected. It is not obvious how to increase the spatrial resolution of Gafchromic film. Gafchromic film also demonstrated a significant lateral non-uniformity of response to x-ray irradiation. If should be noted, however, that reduction in gate oxide thickness reduces the sensitivity of the MOSFET dosimeter. A MOSFET with a thinner gate oxide is suitable for high dose rate applications, such as synchrotron MRT. The convenience of remote, on-

line measurement and the new possibilities of large arrays, increases the attractiveness of the MOSFET dosimetry method for measuring microbeams during MRT and radiosurgery.

It was demonstrated in this study that a radiation-sensing MOSFET detector, in the "edge-on" configuration, is highly suitable for scanning the dose profile of a planar x-ray microbeam. The main advantage over conventional dose integrating methods (TLD, film) arises from the ultra-small size of the sensitive element of the MOSFET structure in the "edge-on" configuration. Another advantage is the complete compatibility of the MOSFET with array fabrication, electronic metrology, digitisation of dose data and automation of data collection.

The presence of packaging material around the sensing chip did not seriously affect the spatial resolution of the MOSFET detector at low x-ray energies. Furthermore, in devices designed for "edge-on" scanning, any such effects can be reduced still further eg. by encapsulating in very thin materials, or reducing substrate thickness by machining the chip to optimise silicon dioxide film exposure, etc.

The manual scanning of a MOSFET point detector takes longer than competing measurement techniques, because a separate short irradiation is required for each data point. However, we have demonstrated that the entire measurement, automated data analysis and curve plotting can be completed within one hour. While the Gafchromic film analysis took required at least 24 hours waiting period

between irradiation and measurement followed by the procedure of focusing digital imaging system, scanning and digitising, which required at least 1 hour.

An "edge-on" n-type MOSFET detector was applied for the measurement of the dose distribution profile across a 30 μm wide synchrotron microbeam at the National Synchrotron Light Source in BNL. This was the first experimental measurement of an x-ray microbeam profile used in MRT. The experiment confirmed the micron spatial resolution of the MOSFET detector and the suitability of the detector to validate Monte Carlo calculations of the microbeam dose profile.

Summary

This work is the first comprehensive investigation of the semiconductor dosimetry based on MOSFETs and ion-implanted silicon detectors with and without fission converters in a wide range of radiation oncology modalities. It was clear from the preliminary analysis, that such areas of clinical dosimetry as electron non-equilibrium, x-ray microbeams, which require very high spatial resolution for verification of dose planning, currently are not supported by reliable on-line clinical detectors. There were no detectors available for verification of Monte Carlo dose simulations in a 30 μm wide beam of MRT. In neutron therapy, where the dose distribution and a radiobiological quality of the beam are important, no suitable on-line detector for dose component separation was available. The main issues in neutron therapies are: thermal neutron flux and boron dose distributions, fast neutron dose, gamma dose and microdosimetry with a high spatial resolution. These main issues have been addressed in this work.

Properties of a MOSFET detector

The sensitive element of a MOSFET detector is comprised of a silicon oxide layer underneath an aluminium transistor gate. The electrical signal used as the dosimetric parameter of a MOSFET detector is the "threshold voltage". The threshold voltage is the voltage applied to the MOSFET to achieve a certain current to flow between the MOSFET's drain and the source. Threshold voltage exhibits a shift when the device is irradiated, and a thermal-stable current minimises the threshold voltage change caused by a change in temperature. The

thermal-stable current was determined from the temperature dependent current voltage characteristics of an n-type MOSFET and was in the range of 42 μA to 45 μA.

The sensitivity of a MOSFET detector to x-ray radiation decreased with accumulated change in the MOSFET threshold voltage. This reduction in sensitivity was caused by an accumulation of trapped holes in the SiO_2/Si interface. The electric field of positively charged holes reduces the external electric field in silicon oxide and causes a less efficient separation of electron-hole pairs in the oxide and a reduction in the fractional yield. The sensitivity of the MOSFET detector was reduced by about 2.5% for each 1 V change in threshold voltage.

Dependence of a MOSFET response on x-ray energy, incident angle and the detector housing

X-ray energy and packaging material dependence of the MOSFET response was investigated for MOSFETs with an open silicon chip, or with a chip covered by either a plastic or by metal cap, for an x-ray energy range of up to 6 MV. The maximum enhancement of the MOSFET response was observed for an x-ray energy of approximately 35 keV. No dose enhancement was observed for the x-ray energies above 250 kV_p. The MOSFET response to an x-ray beam of energy above 250 kV was independent of the detector housing when measurements were taken under conditions of electron equilibrium.

Similar to the majority of other integral dose dosimeters, the MOSFET response on the surface of a phantom depends on the angle of the incident x-ray beam with that surface. The angular dependence of the MOSFET response was, however, found to be less significant, when compared with an Attix ionisation chamber. The reduced angular dependence can be explained by the thinner sensitive volume of the MOSFET detector.

The MOSFET sensitivity to alpha radiation

Our initial hypothesis that the threshold voltage change of a MOSFET detector is sensitive to alpha radiation was experimentally proven. It was demonstrated that the MOSFET threshold voltage changes linearly with the fluence of ^{241}Am alpha particles. Americium-241 emits a 60 keV gamma ray during each act of alpha decay and an experiment was designed to demonstrate that most of the MOSFET threshold voltage change, after exposure to ^{241}Am, was caused by alpha radiation. Gamma radiation was responsible for less than 6% change in threshold voltage. These experiments proved that a MOSFET detector can be used successfully as an alpha dosimeter.

Use of the MOSFET drain-substrate p-n junction for a pulse height spectrum measurement. The concept of separation of low and high LET radiation doses by a single MOSFET detector.

Two p-n junctions of a MOSFET structure, the drain-substrate and the source-substrate, were reversed biased and used to acquire pulse height spectra of alpha

particles. Charge collection by each junction separately, or by both of them simultaneously was investigated. The energy spectra of ^{241}Am and ^{210}Po alpha particles were obtained using different connection configurations for the MOSFET dosimeter and analysis of the experimental data revealed the drain-substrate p-n junction to be the most suitable for acquiring energy spectra of alpha particles.

Experiments with alpha, beta and gamma radiation demonstrated that only high LET alpha radiation deposits a measurable amount of energy in the reversed biased p-n junction of a MOSFET detector. Both, low LET gamma radiation and high LET charged particles contribute to a change in MOSFET threshold voltage, therefore simultaneous measurement of the pulse height spectrum and of the threshold voltage chnage can separate doses delivered by low and high LET radiation.

A pulse height spectrum can be acquired by the p-n junction of a MOSFET detector at the same time as measuring the total dose as a change in the detector threshold voltage. Both measurements are performed independently of each other. The MOSFET gate surrounds the drain, with a gap of only a few micrometers between them. Thus the total absorbed dose and the pulse height spectrum are measured in almost the same silicon/silicon oxide volume of the MOSFET detector.

It was shown that low LET gamma and beta radiation deposits very little energy in the thin sensitive volume of the MOSFET drain-substrate p-n junction, while both high and low LET radiation induce a change in the MOSFET threshold voltage.

This makes it possible to separate doses delivered by low and high LET radiation. This approach to dual, high and low LET, dosimetry was tested in the BNCT epithermal neutron beam of the Brookhaven Medical Research Reactor of the Brookhaven National Laboratory.

Microdosimetry by a small silicon volume

A 5.5 MeV alpha particle deposits only a proportion of its energy in the sensitive volume of a MOSFET drain-substrate p-n junction. Although, this is partly the result of energy loss in the detector, it is mostly due to the detector's thin sensitive volume. Therefore, a pulse height spectrum measured by a MOSFET drain-substrate p-n junction is not an energy, E, spectrum, but rather an energy loss, $\frac{dE}{dx}$, spectrum. The effective thickness of the sensitive volume of a MOSFET drain-substrate p-n junction, as measured by an alpha probe, is equal to the range in silicon of an alpha particle with an energy of 4.5 MeV, calculated to be approximately 14 μm. This value is in agreement with a proton edge measurement in a fast neutron beam. A mean chord length of 23.5 μm was calculated from the geomentrical dimensions of the sensitive volume, and was later used for convertion of the deposited energy spectrum to a microdosimetry spectrum. A microdosimetry spectrum can be aqcuired simultaneously with total dose measurement by the same MOSFET detector.

This new approach to microdosimetry was tested in the Fast Neutron Therapy beam of the Superconducting Cyclotron of Harper Hospital, Detroit, USA. The

microdosimetry spectra measured by the MOSFET drain-substrate p-n junction in a FNT beam, correlated well with tissue equivalent gas proportional chamber measurements. The measurements were performed at four different depths in a water tank. The area under the microdosimetry spectra, at each depth, is proportional to neutron dose. The relative neutron dose depth distribution curve coincided with the neutron dose measured by a reference paired ionisation chamber method. The relative total dose depth distribution, measured simultaneously with microdosimetry spectra by MOSFET threshold voltage change, agreed well with the relative total dose measured by an ionisation chamber.

The technique of using paired MOSFET detectors

This research has demonstrated the use of a paired MOSFET detector method for determining a boron dose in BNCT. The paired MOSFET technique consists of applying two idential MOSFET detectors to measure radiation dose. One detector is covered by boron-10 containing plastics and the other is a bare detector. The difference in the detector readings is directly proportional to the boron dose.

The relative boron dose was measured in a BNCT beam of the Brookhaven Medical Research Reactor. The measurements were performed in a perspex phantom and the boron dose peaked at a depth of 2 to 4 cm. The relative dose correlated well with both Monte Carlo calculations and thermal neutron flux measurements.

Thermal neutron and boron dose dosimetry

The uranium-235 fission converter ion-implanted silicon detector was developed and successfully used for in-phantom measurements of thermal neutron flux distribution at epithermal and thermal BNCT, FNT and californium-252 brachytherapy facilities. A theoretical approach was introduced and mathematical calculations were derived for the analysis of data collected by a detector with a thick fission converter.

The agreement between fission detector measurements and Monte Carlo calculated fluxes at the epithermal irradiation facility of BMRR was within 5% accuracy of measurments. Some of the advantages of using a uranium converter fission detector include internal on-line calibration by alpha particles produced by spontaneous decay of uranium-235; fast measurement requiring a single reactor run; small sized detector which minimises radiation field perturbation; and the possibility of on-line monitoring of thermal neutron flux.

The application method and data analysis of using a uranium converter silicon detector was validated by comparison with Monte Carlo calculations and reference measurements in the epithermal BNCT beam at the Brookhaven National Laboratory. Thermal neutron flux distribution peaked at the depth range of 1.5 cm to 4 cm in a perspex phantom. The method was applied for measurement of thermal neutron flux in the filtered thermal BNCT beam of the Osaka reactor. Thermal neutron flux peaked at the depth range of 1 cm to approximately 2.5 cm. The lateral distribution of thermal neutron flux was not

uniform, with the thermal neutron flux dropping to half of its maximum value at the central axis at about 5 cm off the central axis. The measurements were performed in water.

A fission converter detector was applied to measure thermal neutron flux in the FNT beam of the Harper Hospital cyclotron. Calculations of boron dose in the fast neutron therapy beam, based on thermal neutron flux measurements by the detector, agreed within error limits with the paired proportional counter method. The boron dose calculated for 50 ppm ^{10}B concentration was within the error limits of this dose measured by a tissue equivalent proportional counter with the walls loaded with 50 ppm of ^{10}B. The contribution of the boron dose to the total dose was 4-5%, while the biological dose enhancement, which takes into account the relative biological effectivness, was estimated to reach 30%.

The suitability of an ion implanted silicon detector with a ^{235}U fission converter as an absolute thermal neutron detector in neutron radiation therapy was confirmed by measurements in a ^{252}Cf radiation field, with the boron dose correlated with ^{10}B loaded ionisation chamber measurements.

MOSFET application for high spatial resolution x-ray microbeam dosimetry

A new technique of applying the MOSFET dosimeter in an "edge-on" configuration was developed. The "edge-on" technique utilises the ultra thin sensitive volume of the MOSFET detector to achieve a spatial resolution of only 1 μm.

Applications of an "edge-on" MOSFET were tested in a 200 μm wide 100kV$_p$ x-ray beam. The spatial resolution of the MOSFET in an "edge-on" orientation was compared with the resolution of Gafchromic film. Spatial resolution of Gafchromic film is similar to the spatial resolution of a MOSFET in "edge-on" mode for the x-ray beam in this study, however, the Gafchromic film demonstrated a significant lateral non-uniformity at the micron level of response to x-ray irradiation. The convenience of remote, on-line measurements and new possibilities of large arrays increases the attractiveness of the MOSFET dosimetry method for measuring microbeams during microbeam radiation therapy (MRT) and radiosurgery.

The presence of packaging material around the sensing chip of the MOSFET detector did not seriously effect its spatial resolution in a low energy x-ray beam. Furthermore, in devices designed for "edge-on" scanning, any such effects can be reduced still further by encapsulating the chip in very thin material and by reducing the substrate thickness by machining the chip to optimise silicon dioxide film exposure.

An "edge-on" n-type MOSFET detector was applied in the measurement of a dose distribution profile across a 30 μm wide synchrotron microbeam at the National Synchrotron Light Source in BNL. This was the first experimental measurement of an x-ray microbeam profile used in MRT. The experiment confirmed the micron spatial resolution of the MOSFET detector and its suitability in validation of a microbeam dose profile as calculated by the Monte Carlo method.

References

Adams, G.E. (1990). The clinical relevance of tumour hypoxia. *Eur. J. Cancer*, **26,** 420-421.

Adams, L. & Holmes-Siedle, A. (1978). The development of an MOS dosimetry unit for use in space. *IEEE Trans. Nucl. Sci.*, **NS-25,** 1607-1612.

Aitken, J.M. & Young, D.R. (1977). Avalanche injection of holes into SiO_2. *IEEE Trans. Nucl. Sci.*, **NS-24,** 2128-2134.

Alam, F., Bapat, B.V., Soloway, A.H., Barth, R.F., Mafune, N. & Adams, D.M. (1989). Boronated compounds for neutron capture therapy. *Strahlenther. Onkol.*, **165,** 121-123.

Alburger, D.E., Raparia, D. & Zucker, M.S. (1998). Phantoms with $^{10}BF_3$ detectors for boron neutron capture therapy applications. *Medical Physics*, **25,** 1735-1738.

Allen, B.J. & Ralston, A. (1997). Boron dose enhancement for ^{252}Cf brachytherapy. In *Advances in Neutron Capture Therapy*, Larsson, B., Crawford, J. & Weinreich, R. (eds) pp. 271-274. Elsevier: Lausanne.

Asbury, A.K., Orjemann, R.G., Nielsen, S.L. & Sweet, W.H. (1972). Neuropathologic study of fourteen cases of malignant brain tumor treated by boron -10 slow neutron irradiation. *J. Neuropathology and Exp. Neurology*, **31,** 278-303.

August, L.S. (1982). Estimating and reducing errors in MOS dosimeters caused by exposure to different radiation. *IEEE. Trans. Nucl. Sci.*, **NS-29,** 2000-2003.

Baranskiy, P.I., Klochkov, B.L. & Potykevich, I.V. (1975). *Manual of Semiconductor Electronics*. Naukova Dumka (in Russian): Kiev.

Barth, R.F., Johnson, C.W., Wei, W.-Z., Carey, W.E., Soloway, A.H. & McGuire, J. (1982). Neutron capture using boronated monoclonial antibody directed againsttumor-associated antigens. *Cancer Detec. Prevent.*, **5,** 315-323.

Barth, R.F., Soloway, A.H., Goodman, J.H., Gahbauer, R.A., Gupta, N., Blue, T.E., Yang, W. & Tjarks, W. (1999). Boron neutron capture therapy of brain tumors: An emerging therapeutic modality. *Neurosurgery*, **44,** 433-449.

Beach, J.L., Schroy, C.B., Ashtari, M., Harris, M.R. & Maruyama, Y. (1990). Boron neutron capture enhancement of ^{252}Cf brachytherapy. *Int. J. Radiat. Oncol. Biol. Phys.*, **18,** 1421-1427.

Beddor, A.S., Mackie, T.R. & Attix, F.X. (1992). Water equivalent plastic scintillation detectors for high energy beam dosimetry: 1; Physical characteristics and theoretical considerations. 2; properties and measurements. *Phys. Med. Biol.*, **37,** 1883-1913.

Bendel, P., frantz, A., Zilberstein, J., Kabalka, G.W. & Salomon, Y. (1998). Boron-11 NMR of borocaptate: relaxation and *in vivo* detection in melanoma bearing mice. *Magn. Reson. Med.*, **39,** 430-447.

Bendel, P. & Sauerwein, W. (2001). Optimal detection of the neutron capture therapy agent borocaptate sodium (BPS): A comparison between ^{1}H and ^{10}B NMR. *Med. Phys.*, **28,** 178-183.

Blamires, N.G., Totterdell, D.H.J., Holmes-Siedle, A.G. & Adams, L. (1986). pMOS dosimeters: long-term annealing and neutron response. *IEEE Trans. Nucl. Sci.*, **NS-33,** 1310-1315.

Bleuel, D.L., Donahue, R.J., Ludewigt, B.A. & Vujic, J. (1998). Designing accelerator-based epithermal neutron beams for boron neutron capture therapy. *Medical Physics*, **25,** 1725-1734.

BNL. (1958). Report BNL-325. BNL.

Böck, H. & Balcar, E. (1975). Long-time behaviour of regenerating in-core neutron detectors with ^{238}U - ^{239}Pu electrodes during power cycling. *Nucl. Instr. Meth.*, **124,** 563-571.

Boesch, H.E. & McGarrity, J.M. (1976). Charge yield and dose effects in MOS capacitors at 80K. *IEEE Trans. Nucl. Sci.*, **NS-23,** 1520-1525.

Bradley, P.D., Rosenfeld, A.B., Allen, B.J., Coderre, J. & Capala, J. (1999). Performance of silicon microdosimetry detectors in boron neutron capture therapy. *Rad. Research*, **151,** 235-243.

Bradshaw, K.M., Schweizer, M.P., Glover, G.H., Hadley, J.R., Tippets, R., Tang, P.P., Davis, W.L., Heilbrun, M.P., Johnson, S. & Ghanen, T. (1995). BSH distribution in the canine head and human patient using ^{11}B MRI. *Magn. Reson. Med.*, **34,** 48-56.

Brady, L.W., Micaily, B., Miyamoto, C.T., Heilmann, H.-P. & Montemaggi, P. (1995). Innovations in brachytherapy in gynecological oncology. *Cancer*, **76,** 2143-2151.

Briesmeister, J.F. (1986). MCNP-4A General Monte Carlo Code for Neutron and Photon Transport. Los Alamos National Lab.

Brown, D.B. & Dozier, C.M. (1981). Electron-hole recombination in irradiated SiO_2 from a microdosimetry viewpoint. *IEEE Trans. Nucl. Sci.*, **NS28,** 4142-4144.

Brownell, G.L. & Sweet, W.H. (1958). Studies on neutron capture therapy. In *Second United Nations International Conference on Peaceful Uses of Atomic Energy*, Vol. 26. United Nations: Geneva.

Brucker, G.J., Kronenberg, S. & Gentner, F. (1995). Effect of package geometry, materials, and die design on energy dependence of pMOS dosimeters. *IEEE. Trans. Nucl. Sci.*, **42,** 33-40.

Buehler, M.G., Blaes, B.R., Soli, G.A. & Tardio, G.R. (1993). On-chip p-MOSFET dosimetry. *IEEE Trans. Nucl. Sci.*, **40,** 1442-1449.

Busse, P.M., Zamenhoff, R., Madoc-Jones, H., Solares, G., Kiger, S., Riley, K., Chuang, C., Rogers, G. & Harling, O. (1997). Clinical Follow-up of Patients with Melanoma of the Extremity Treated in a Phase I Boron

Neutron Capture Therapy Protocol. In *Advances in Neutron Capture Therapy*, Larsson, B., Crawford, J. & Weinreich, R. (eds), Vol. 1. pp. 60-64. Elseiver: Lausanne.

Butson, M.J., Rosenfeld, A.B., Mathur, J.N., Carolan, M.G., Wong, T.P.Y. & Metcalf, P.E. (1996). A new radiotherapy surface dose detector: the MOSFET. *Med. Phys.*, **23,** 655-658.

Cai, J., Soloway, A.H., Barth, R.F., Adams, D.M., Hariharan, J.A., Wizlic, I.M. & Radcliffe, K. (1997). Boron-containing polyamines as DNA targeting agents for neutron capture therapy of brain tumors: synthesis and biological evaluation. *J. Medicinial Chem.*, **40,** 3887-3896.

Carolan, M.G., Rosenfeld, A.B., Allen, B.J., Mathur, J.N., Meriaty H.A., Stecher-Rasmussen, F., Moss, R.L., Raaijmakers, C.P.J. & Konijnenberg, M.W. (1997). Characterisation and use of MOSFET gamma dosimeters and silicon p-i-n diode neutron dosimeters for epithermal neutron beam dosimetry. In *Advances in Neutron Capture Therapy*, Larsson, B., Crawford, J. & Weinreich, R. (eds) pp. 192-197. Elsevier: Lausanne.

Carolan, M.G., Wallace, S.A., Rosenfeld, A.B., Mathur, J.N. & Allen, B.J. (1994). Validation of Monte Carlo dose planning by epithermal beam dose distribution measurements in phantoms. In *Sixth International Symposium on Neutron Capture Therapy* pp. 12 pages: Kobe, Japan.

Castro, J.R., Oliver, G.D., Withers, H.R. & Almond, P.R. (1973). Experience with californium-252 in clinical radiotherpy. *Am J Roentgenol*, **117,** 172-194.

Catterall, M. (1974). A report on three years' fast neutron therapy from the medical research council's cyclotron at Hammersmith Hospital, London. *Cancer*, **34,** 91-95.

Catterall, M., Bewley, D.K. & Sutherland, I. (1975). First results of a randomized clinical trial of fast neutrons compare to X and gamma rays in treatment of advance tumours of the head and neck. *Brit. Med. J*, **1,** 653-656.

Catterall, M., Bewley, D.K. & Sutherland, I. (1977). Second report on results of a randomized clinical trial of fast neutrons compare with X and gamma rays in treatment of advance tumours of the head and neck. *Brit. Med. J*, **1,** 1642-1644.

Cauchy, A. (1908). Memoire sur la rectification des courbes et la quadrature des sourface courbe. In *Oevres Completes*. Gauthier Villard: Paris.

Chadha, M., Capala, J., Coderre, J.A., Elowitz, E.H., Iwai, J., Joel, D.D., Liu, H.B., Wieloploski, L. & Chanana, A.D. (1998). Boron Neutron Capture Therapy (BNCT) for Glioblastoma Multiform (GBM) Using the Epithermal Neutron Beam at the Brookhaven National Laboratory. *Int. J. Rad. Oncol. Biol. Phys.*, **40,** 829-834.

Chadwick, J. (1932). The existence of a neutron. *Proceedings of the Royal Society of London*, **A136,** 692-708.

Chadwick, J. & Goldhaber, M. (1935). Disintegration by slow neutrons. *Nature*, **135,** 65.

Chapman, J.D. (1988). Biophysical models of mammalian cell inactivation by radiation. In *Radiation biology in cancer research*, Meyn, R.E. & Withers, H.R. (eds) pp. 21-32. Raven Press: New York.

Cleaves, M.A. (1903). Radium Therapy. *Medical Records*, **64,** 601.

Coderre, J.A., Makar, M.S., Micca, P.L., Nawrocky, M.M., Liu, H.B., Joel, D.D., Slatkin, D.N. & Amols, H.I. (1993). Derivation of relative biological effectiveness for the high-LET radiations produced during boron neutron capture irradiationsof the 9L rat gliosarcoma *in vitro* and *in vivo*. *Int. J. Radiat. Oncol. Biol. Phys.*, **27,** 1121-1142.

Coderre, J.A. & Morris, G.M. (1999). The radiation biology of boron neutron capture therapy. *Radiat. Res.*, **151,** 1-18.

Company, F.Z. & Allen, B.J. (1996). Measurements and Monte Carlo Simulations of the Fluence and Dose Characteristics of Microplanar Proton Beam. *Australian Phys. Eng. Sci. in Medicine*, **19,** 217-223.

Company, F.Z. & Allen, B.J. (1998). Calculation of microplanar beam dose profiles in a tissue/lung/tissue phantom. *Phys. Med. Biol.*, **44,** 1-11.

Conneely, C., O'Connell, B.O., Hurley, P., Lane, W. & Adams, L. (1998). Strategies for millirad sensitivity of pMOS dosimeters. *IEEE Trans. on Nucl. Sci.*, **45,** 1475-1480.

Cross, P. (1992). The use of parallel plate ion chambers to determine surface dose in a 6 MV photon beam. *Australasian Physics and Engineering Science in Medicine*, **15,** 208-216.

Curran, W.J., Scott, C.B., Horton, J., Nelson, J.S., Weinstein, A.S., Fischbach, J., Chang, C.H., Rotman, M., Asbell, S.O., Kirsch, R.E. & Nelson, D.F. (1993). Recursive partitioning analysis of prognostic factors in three radiation therapy oncology group malignant gliom trials. *J. Natl. Cancer Inst.*, **85,** 704-710.

Curtis, H.J. (1967). The use of a deuteron microbeam for simulating the biological efects of heavy cosmic-ray particles. *Rad. Res. Suppl.*, **7,** 250-257.

Curtis, O.L., Srour, J.R. & Chiu, K.Y. (1974). Hole and electron transport in SiO_2 films. *J. Appl. Phys.*, **45,** 4506-4513.

Danchenko, V. & Griffin, G.F. (1981). Delayed darkening of radiation-exposed radiochromic dye dosimeter. *IEEE Trans. Nucl. Sci.*, **NS-28,** 4156-4160.

Dasu, A., Löfroth, P.-O. & Wickman, G. (1998). Liquid ionization chamber measurement of dose distribution in small 6 MV photon beam. *Phys. Med. Biol.*, **43,** 21-36.

Deal, B.E. (1980). Standardized terminology for oxide charge associated with thermally oxidized silicon. *IEEE Trans. E.D.*, **ED-27,** 606-607.

DeLuka, F., Campanella, R., Bifone, A. & Maraviglia, B. (1991). Boron-10 double resonance spatial NMR detection. *Chem Phys. Lett.*, **186,** 303-306.

Dempsey, J.F., Low, D.A., Mutic, S., Markman, J., Kirov, A.S., Nussbaum, G.H. & Williamson, J.F. (2000). Validation of a precision radiochromic film dosimetry system for quantitative two-dimentional imaging of acute exposure dose distribution. *Med. Phys.*, **27,** 2462-2475.

Denekamp, J. (1974). The response of a mouse sarcoma to single and divided doses of x-rays and fast neutrons. *Brit. J. Cancer*, **29,** 292-299.

Denekamp, J. (1994). Neutron radiobilogy revisited. *Acta Oncol.*, **33,** 233-240.

Dicello, J.F., Gross, W. & Kraljevic, U. (1972). Radiation quality of californium-252. *Phys. Med. Biol.*, **17,** 345.

Dilmanian, F.A., Wu, X.Y., Huang, X., Kershaw, M., Ren, B., Slatkin, D.N., Trandem, K., Menk, R., Thomlinson, W.C. & Zong, Z. (1997). Microbeam irraidation of duck embryo brains: Relavance to microbeam radiation therapy (MRT) of brain tumors in infants. In *1996 NSLS Activity Report*, Rothman, E.Z. & Hastings, J.B. (eds), Vol. BNL 52517. pp. B-140.

DiMaria, D.J., Weinberg, Z.A. & Aitken, J.M. (1977). Location of positive charges in SiO2 films on Si generated by vuv photons, x ray and high field stressing. *J. Appl. Phys.*, **48,** 898-906.

Djezzar, B., Amrouche, A., Smatti, A. & Kachouane, M. (1999). Electrical characterization of oxide and Si/SiO_2 interface of irradiated nMOS transistors at low radiation doses. *IEEE Trans. Nucl. Sci.*, **46,** 829-833.

Dobelbower, M.C., A.Vest, Reed, M.J. & Blue, T.E. (1999). Experimental verification of in-phantom calculations for an accelerator-based neutron source for boron neutron capture therapy. *Med. Phys.*, **26,** 376-380.

Dozier, C.M. & Brown, D.B. (1981). Effect of photon energy on the response of MOS devices. *IEEE Trans. Nucl. Sci.*, **NS-28,** 4137-4141.

Dozier, C.M., Fleetwood, D.M., Brown, D. & Winokur, P.S. (1987). Evaluation of low-energy x-ray and cobalt-60 irradiations of MOS transistors. *IEEE Trans. Nucl. Sci.*, **34,** 1535-1539.

Edwards, C.R., Green, S., Palethorpe, J.E. & Mountford, P.J. (1997). The response of a MOSFET, p-type semiconductor and LiF LTD to quasi-monoenergetic x-rays. *Phys. Med. Biol.*, **42,** 2383-2391.

Ensell, G., Holmes-Siedle, A. & Adams, L. (1988). Thick oxide pMOSFET dosimeters for high energy radiation. *Nucl. Instr. Meth.*, **A269,** 655-658.

Fairchild, R.G. & Bond, V.P. (1985). Current status of ^{10}B-neutron captureterapy: enhancement of tumor dose via beam filtration and dose rate, and the effect of this parameters on minimum boron content: a theoretical evaluation. *Int. J. Radiat. Oncl. Biol. Phys.*, **11,** 831-840.

Farr, L.E., Robertson, J.S. & Strickley, E.E. (1954a). Physics and physiology of neutron capture therapy. *Proc. Nat. Acad. Sci. USA*, **40,** 1087-1093.

Farr, L.E., Robertson, J.S., Strickley, E.E., Bagnall, H.J., Easterday, O.D. & Kahle, W. (1958). Recent advances in neutron capture therapy. In *Second United Nations International Conference on Peaceful Uses of Atomic Energy*, Vol. 26. pp. 451-456. United Nations: Geneva.

Farr, L.E., Sweet, W.H., Locksley, H.B. & Robertson, J.S. (1954b). Neutron capture therapy of gliomas using boron-10. *Trans. Am. Neurol. Assoc.*, **79.**

Field, S.B. & Hornsey, S. (1971). RBE values for cyclotron neutrons for effect on normal tissue and tumours as a function of dose and dose fractination. *Eur. J. Cancer*, **7,** 161-169.

Fleetwood, D.M. (1992). 'Border traps' in MOS devices. *IEEE Trans. Nucl. Sci*, **39,** 269-271.

Fleetwood, D.M. (1996). Fast and slow border traps in MOS devices. *IEEE Trans. Nucl. Sci.*, **43,** 779-786.

Fleetwood, D.M., Warren, W.L., Schwank, R.J., Winokur, P.S., Shaneyfelt, M.R. & Riewe, L.C. (1995). Effect of interface traps and border traps on MOS postirradiation annealing response. *IEEE Trans. Nucl. Sci.*, **42,** 1698-1702.

Fleetwood, D.M., Winokur, P.S., Lorence, L.J., Beezhold, W., Dressendorfer, P.V. & Schwank, R.J. (1986). The response of MOS devoces to dose-enhanced low-energy radiation. *IEEE Trans. Nucl. Sci.*, **NS-33,** 1245-1251.

Francescon, P., Cora, S., Cavedon, C., Scalchi, P. & Reccanello, S. (1998). Use of a new type of radiochromic film, a new parallel-plate micro-chamber, MOSFETs, and TLD 800 microcubes in the dosimetry of small beams. *Med. Phys.*, **25,** 503-511.

Freeman, R. & Holmes-Siedle, A. (1978). A simple model for predicting radiation effects in MOS devices. *IEEE Trans. Nucl. Sci.*, **NS-26,** 1216-1225.

Fukuda, H., Kobayashi, T., Matsuzava, T., Kanda, K., Ichihashi, M. & Mishima, Y. (1987). RBE of a thermal neutron beam and the 10B(n,α)7Li reaction on cultured B-16 melanoma cells. *Int. J. Radiat. Biol.*, **51,** 167-175.

Gabel, D., Fairchild, R.G. & Larsson, B. (1984). The relative biological effectiveness in V79 Chinese hampster cells of the neutron capture reaction in boron and nitrogen. *Radiat. Res.*, **98,** 307-316.

Gahbauer, R., Fairchild, R.C., Goodman, J.H. & Blue, T.E. (1992). RBE in normal tissue studies. In *Towards Clinical Trials of Glioma Treatment*, Gabel, D. & Moss, R.L. (eds) pp. 123-128. Plenum Press: New York.

Gladstone, D.J. & Chin, L.M. (1991). Automated data collection system for MOSFET radiation detectors. *Med. Phys.*, **18,** 542-548.

Gladstone, D.J., Lu, X.Q., Humm, J.L., Bowam, H.F. & Chin, L.M. (1994a). A miniature MOSFET radiation dosimeter probe. *Med. Phys.*, **21,** 1721-1728.

Gladstone, D.J., Lu, X.Q., Humm, J.L., Bowman, H.F. & Chin, L.M. (1994b). A miniature MOSFET radiation dosimeter probe. *Med. Phys.*, **21,** 1721-1728.

Godwin, J.T., Farr, L.E., Sweet, W.H. & Robertson, J.S. (1955). Pathological study of eight patients with glioblastoma multiform treated by neutron capture therapy using boron-10. *Cancer*, **8.**

Green, D., Sandor, J.E., O'Keeffe, T.W. & Matta, R.K. (1965). Reversible changes in transistor characteristics caused by scanning electron microscope illumination. *Appl. Phys. Lett.*, **6,** 3-4.

Greenberg, D.D. (1997). .

Guerga, D.P., Yanch, J.C. & Shefer, R.E. (2000). Development and construction of a neutron beam line for accelerator-based boron neutron capture synovectomy. *Med. Phys.*, **27,** 203-214.

Gupta, N., Blue, T.E., Kanellitsas, C. & Gahbauer, R. (1994). Effect of head size on ^{10}B dose distribution for a broad field accelerator epithermal neutron source for BNCT. In *Topics in Dosimetry and Treatment Planning for Neutron Capture Therapy*, Zamenhof, R., Solares, G. & Harling, O. (eds) pp. 165-175. Advanced Medical Publ.: Madison, Wisconsin.

Gwen, C.W. (1969). Model for radiation-induced charge trapping and annealing in the oxide layer of MOS devices. *J. Appl. Phys.*, **40,** 4886-4892.

Hardling, O.K., Rogus, R., Choi, J.R., Moulin, D.J., Zamenhof, R.G. & Yanch, J.C. (1994). Dosimetry and dose control for clinical trials of neutron capture therapy at the MITR-II reactor. In *Topics in Dosimetry and Treatment Planning for Neutron Capture Therapy*, Zamenhof, R., Solares, G. & Harling, O. (eds) pp. 67-79. Advanced Medical Publ.: Madison, Wisconsin.

Hatanaka, H. (1975). A revised boron neutron capture therapy for malignant brain tumors. II. Interim clinical result with the patients excluding previous treatment. *J. Neurol.*, **209**.

Hatanaka, H., Kamano, S., Amano, K., Hojo, S., Sano, K., Egawa, S. & Yoshizaki, T. (1986). Clinical experience of boron neutron capture therapy for gliomas- a comparison with conventional chemo-immuno-radiotherapy. In *Boron Neutron Capture Therapy for Tumors*, Hatanaka, H. (ed) pp. 349-379. Nishimura: Niigata, Japan.

Hatanaka, H. & Urano, Y. (1986). Eighteen autopsy cases of malignant brain tumors treated by boron neutron capture therapy between 1968 and 1985. In *Baron Neutron Capture Therapy for Tumors*, Hatanaka, H. (ed) pp. 381-416. Nishimura: Niigata, Japan.

Hayakawa, Y., Harasawa, S., Nakamoto, A., Amano, K., Hatanaka, H. & Egawa, J. (1978). Simultaneous Monitoring System of Thermal Neutron Flux for Boron Neutron Capture Therapy. *Radiation Research*, **75,** 243-251.

Hayakawa, Y., Nakagawa, Y. & Hatanaka, H. (1996). Simultaneous Monitoring System of Neutron Fluence Rate Distribution by Detectors with Multiple Sensitive Heads. In *Cancer Neutron Capture Therapy*, Mishima (ed) pp. 473-477. Plenum Press: New York.

Hei, T.H., Wu, L.J., Liu, S.X., Vannais, D., Waldern, C.A. & Randers-Pehrson, G. (1997). Mutagenic effects of a single and an exact number of α particles in mammalian cells. *Proc. Natl. Acad. Sci. USA*, **94,** 3765-3770.

Holmes-Siedle, A. (1974a). The space charge dosimeter. General principles of a new method of radiation detection. *Nucl. Instr. Methods*, **21,** 169-179.

Holmes-Siedle, A. (1974b). The space-charge dosimeter - General principles of a new method of radiation detection. *Nucl Instr. Meth.*, **121,** 169-179.

Holmes-Siedle, A. (1986). RADFET: a review of the use of metal-oxide-silicon devices as integrating dosimeters. *Radiat. Phys. Chem.*, **28,** 1-10.

Hornsey, S., Morris, C.C., Myers, R. & White, A. (1981). Relative biological effectivness for damage to the central nervous system by neutrons. *Int. J. Rad. Oncol. Biol. Phys.*, **7,** 185-189.

Hughes, R.C. (1977). Time resolved hole transport in α-SiO_2. *Phys. Rev. B*, **15,** 2012-2020.

Hughes, R.C., Huffman, D., Snelling, J.V., Zipperian, T.E., Ricco, A.J. & Kelsey, C.A. (1988a). Miniature radiation dosimeter for in vivo radiation measurements. *Int J Rad Oncol Biol Phys*, **14,** 963-967.

Hughes, R.C., Huffman, D., Snelling, J.V., Zipperian, T.E., Ricco, A.J. & Kelsey, C.A. (1988b). Miniature radiation dosimeter for *in-vivo* radiation measurements. *Int. J. Radiat. Oncol. Biol. Phys.*, **14,** 963-967.

ICRU. (1969). Neutron fluence, neutron spectra and kerma, Vol. Report 13. International Commission on Radiation Units and Measurements: Washington.

ICRU. (1980). Radiation Quantities and Units. International Commission on Radiation Units and Measurements: Bethesda, MD.

ICRU. (1983). Microdosimetry, Vol. Report 36. International Commission on Radiation Units and Measurements: Washington.

ICRU. (1984). *Neutron dosimetry for biology and medicine*. Vol. Report 26. International Commission on Radiation Units and Measurements: Washington.

ICRU. (1989). *Clinical neutron dosimetry, Part 1: Determination of absorbed dose in a patient treated be external beam of fast neutrons*. Vol. Report 45. International Commission on Radiation Units and Measurements: Berthesda, MD.

Javid, M., Brownell, G.L. & Sweet, W.H. (1952). The possible use of neutron-capture isotopes such as boron-10 in the treatment of neoplasms. II. Computation of the radiation energy and estimates of effects in normal and neoplastic brain. *J. Clin. Invest.*, **31,** 603-610.

Johns, H.E. & Cunningham, J.R. (1983). *The Physics of Radiology*. Charles C Thomas Publishers: Springfield Illinois USA.

Kassabov, J., Nedev, N. & Smirnov, N. (1991). Radiation dosimetry based on floating gate MOS transistor. *Radiation Effects and Defects in Solids*, **116,** 155-158.

Kirkpatrik, S. (1979). Modelling diffusion and collection of charge from ionising radiation in silicon devices. *IEEE Trans. Electron Devices*, **26,** 1742-1753.

Klinkowstein, R.E., Shefer, R.E., Yanch, J.C., Howard, W.B., Song, H., Binello, E., Blackburn, B.W., Daigle, J.L., Sears, S.M., Goldie, C.H. & Ledoux, R.J. (1997). Operation of a high current tandem electrostatic accelerator for boron neutron capture threrapy. In *Advances in Neutron Capture Therapy*, Larsson, B., Crawford, J. & Weinreich, R. (eds), Vol. 1. pp. 522-527. Elseiver: Lausanne.

Knoll, M. & Braunig, D. (1988). MOS Dosimeter: USA.

Knudson, A.R., Campbell, A.B., Shapiro, P., Stapor, W.J., Wolicki, E.A., Peterson, E.L., Diehl-Nagle, S.E. & Hauser, J. (1984). Charge collection in multilayer structures. *IEEE Trans. Nucl. Sci.*, **31,** 1149-1154.

Kobayashi, T., Kanda, K., Fujita, Y., Sakurai, Y. & Ono, K. (1997). The upgrade of the heavy water facility of the Kyoto University Reactor for neutron capture therapy. In *Advances in Neutron Capture Therapy*, Larsson, B., Crawford, J. & Weinreich, R. (eds), Vol. 1. pp. 321-325. Elseiver: Lausanne.

Kobayashi, T., Sakurai, Y. & Ishikawa, M. (2000a). A non-invasive dose estimation system for clinical BNCT based on PG-SPECT - conceptual study and fundamental experiments using HPGe and CdTe semiconductor detectors. *Med. Phys.*, **27,** 2124-2132.

Kobayashi, T., Sakurai, Y., Kanda, K., Fujita, Y. & Ono, K. (2000b). The remodelling and basic characteristics of the heavy water neutron radiation

facility of the Kyoto University, manly for neutron capture therapy. *Nuclear Technology*, **131,** 354-378.

Konijnenberg, M.W., Dewit, L.G.H., Mijnheer, B.J., Raaijimakers, C.P.J. & Watkins, P.R.D. (1995). Dose homogeneity in born neutron capture therapy using an epithermal neutron beam. *Radiat. Res.*, **142,** 327-339.

Kooi, E. (1967). *The surface properties of oxidized silicon.* Springer-Verlag: Berlin.

Kota, C., Maughan, R., Tattam, D. & Beyon, T.D. (2000). Use of low-pressure tissue equivalent proportional counters for the disimetry in BNCT and BNCEFNT. *Medical Physics*, **27,** 535-548.

Kota, C., Maughan, R.L., Burmeister, J. & Forman, J.D. (1997). A Modified Fast Neutron Therapy Beam for Boron Neutron Capture Therapy (BNCEFNT). In *Advances in Neutron Capture Therapy*, Larsson, B., Crawford, J. & Weinreich, R. (eds), Vol. 1. pp. 496-500. Elseiver: Lausanne.

Kozlov, S.F., Konorova, E.A., Lebedev, B.A., Bolshakova, V.V., Konoplev, K.A. & Morozov, V.F. (1977). Semiconductor detectors for neutron field investigation. *IEEE Trans. Nucl. Sci.*, **24,** 238-239.

Kron, T., Duggan, L., Smith, T., Rosenfeld, A., Butson, M., Kaplan, G., Howlett, S. & Hyodo, K. (1998). Dose response of various radiation detectors to synchrotron radiation. *Phys Med Biol*, **43,** 3235-3259.

Laissue, J.L., Geiser, G., Spanne, P.O., Dilmanian, F.A., Gebbers, J.-O., Geiser, M., Wu, X.-Y., Makar, M., Micca, P., Nawrocky, M., Joel, D.D. & Slatkin, D.N. (1998). Neuropathology of ablation of rat gliosarcomas and contiguous brain tissues using a microplanar beam of synchrotron-wiggler-generated x rays. *Int. J. Cancer*, **78.**

Lamarsh, J.R. (1966). *Introduction to Nuclear Reactor Theory.* Addison-Westley: Reading, Mass.

Laramore, G.E., Wooton, P., Livesey, J.C., Wilbur, D.S., Risler, R., Phillips, M., Jacky, J., Buchholz, T.A., Griffin, T.W. & Brossard, S. (1994). Boron neutron capture therapy: a mechanism for achieving a concominant tumor boost in fast neutron radiotherapy. *Int. J. Radiat. Oncol. Biol. Phys.*, **5,** 1135-1142.

Larsson, B., Laksell, L., Rexed, B., Sourander, P., Mair, W. & Anderson, B. (1958). The high energy proton beam as a neurosurgical tool. *Nature*, **182,** 1222-1223.

Lauber, A. (1972). Development of miniaturized solid state detectors for the measurement of beta and gamma radiation in superficial and deep parts of living tissue. *Nucl. Instr. Methods*, **101,** 545-550.

Lerche, R.A., Wehring, B.W. & Wyman, M.E. (1972). Effect of UO_2 deposit thickness on fission-fragment double-kinetic-energy measurements. *Nucl. Instr. Meth.*, **101,** 287-293.

Liu, H.B., Brugger, R.M., Greenberg, D.D., Roger, D.C., Hu, J.P. & Hauptman, H.M. (1994). Enhancement of the Epithermal Neutron Beam Used for BNCT at BMRR. *Int. J. of Radiat. Oncol. Biol. Phys.*, **28,** 1149-1156.

Liu, H.B., Greenberg, D.D., Capala, J. & Wheeler, F.J. (1996). An Improved Neutron Collimator for Brain Tumour Irradiation in Clinical BNCT. *Medical Physics*, **23,** 2051-2060.

Locher. (1936). Biological effects and therapeutic possibilities of neutrons. *Am. J. of Roentgenology*, **36,** 1-13.

Locksley, H.B. & Sweet, W.H. (1954). Tissue distribution of boron compounds in relation to neutron capture therapy of cancer. *Proc. Soc. Exp. Biol. Med.*, **86,** 56-63.

Long, D.M., Millward, D.G. & Wallace, J. (1982). Dose enhancement in semiconductor devices. *IEEE Trans. Nucl. Sci.*, **NS-29,** 1980-1984.

Marshak, A. (1939). Effect of fast neutrons on chromosomes in mitosis. *Proc. Soc. Exp. Biol. Med.*, **41,** 176-180.

Maruyama, Y. (1984). Neutron brachytherapy: An advance for bulky localized cancer therapy. *Nucl Sci Appl*, **1,** 677-748.

Maruyama, Y., Nagell, J.R.v., Yoneda, J., Donaldson, E.S., Gallion, H.H., Powell, D. & Kryscio, R.J. (1991). A review of californium-252 neutron brachytherapy for cervical cancer. *Cancer*, **68,** 1189-1197.

Masunaga, S., Ono, K., Sakurai, Y., Suzuki, M., Takagaki, M., Koboyashi, T., Kinashi, Y. & Akaboshi, M. (1998). Responses of total and quiescent cell populations in solid tumors to boron and gadolinium neutron capture reaction using neutrons with two different energy spectra. *Japanese J. Cancer Research*, **89,** 81-89.

Matsumoto, T. & Aizava, O. (1988). Dose measuring system for boron neutron capture therapy. *Nucl. Instr. Meth. Phys. Res.*, **A271,** 662-670.

Maughan, R.C., Kota, C. & Yudelev, M. (1992a). A microdosimetric study of dose enhancement in a fast neutron beam due to boron neutron capture. *Phys. Med. Biol.*, **37,** 1957-1961.

Maughan, R.L. (1992). Radiation science - of molecules, mice and men. *Brit. J. Radiat.*, **Suppl 24.**

Maughan, R.L., Kota, C. & Forman, J.D. (1997). Feasibility of Boron Neutron Capture Enhancement of Fast Neutron Therapy Utilising a Superconducting Cyclotron. In *Advances in Neutron Capture Therapy*, Larsson, B., Crawford, J. & Weinreich, R. (eds), Vol. 1. pp. 490-495. Elsevier: Lausanne.

Maughan, R.L., Kota, C. & Yudelev, M. (1992b). A microdosimetric study of the dose enhancement in a fast neutron beam due to boron neutron capture. *Phys. Med. Biol.*, **37,** 1957-1961.

Maughan, R.L. & M.Yudelev. (1995). Physical Characteristics of a Clinical d(48.5)+Be Neutron Therapy Beam Produced by a Superconducting Cyclotron. *Medical Physics*, **22,** 1459-1465.

Maughan, R.L., Powers, W.E. & Blosser, H.G. (1994). A superconducting cyclotron for neutron radiation therapy. *Medical Physics*, **21,** 779-785.

McGarrity, J.M. (1980). Consideration for hardening MOS devices and circuits for low radiation doses. *IEEE Trans. Nucl. Sci.*, **NS-27,** 1739-1744.

McKenzie, J.M. & Bromley, D.A. (1959). Observation of Charged Particle Reactor Products. *Phys. Rev. Lett.*, **2,** 303-305.

McLaughlin, W.L., Puhl, J.M., Al-Sheikhly, M., Christou, C.A., Miller, A., Kovacs, A., Wojnarovits, L., Dyk, G.V. & Lewis, D.F. (1996). Novel radiochromic films for clinical dosimetry. *Radiat. Prot. Dosim.*, **66,** 263-268.

McLaughlin, W.L., Yun-Dong, C., Soares, C.G., Miller, A., Dyk, G.V. & Lewis, D.F. (1991). Sensitometry of the response of a new radiochromic film dosimeter to gamma radiation and electron beams. *Nucl. Instr. Meth. Phys. Res.*, **A302,** 165-176.

McNulty, P.J., Abdel-Kader, W.G. & Lynch, J.E. (1991). Modelling charge collection and single event upset in microelectronics. *Nucl. Instr. Meth. in Phys. Res.*, **B61,** 52-58.

Meigooni, A.S., Sanders, M.F. & Ibbott, G.S. (1996). Dosimetric characteristics of an improved radiochromic film. *Med. Phys.*, **23,** 1883-1888.

Messenger, G.C. (1982). Collection of charge on junction nodes from ion tracks. *IEEE Trans. Nucl. Sci.*, **29,** 2024-2031.

Miller, R.C., Randers-Pehrson, G., Geard, C.R., Hall, E.J. & Brenner, D.J. (1999). The oncogenic transforming potential of the passage of single alpha particles through mammalian cell nuclei. *Proc. Natl. Acad. Sci. USA*, **96,** 19-22.

Mishima, Y. (1973). Neutron capture treatment of malignant melanoma using ^{10}B-cholorpromazine. *Pigm. Cell*, **1,** 215-231.

Mishima, Y., Ichihashi, M., Tsui, M., Hatta, S., Ueda, M., Honda, C. & Susuki, T. (1989). Treatment of malignant melanoma by single thermal neutron capture therapy with melanoma -seeking ^{10}B-compound. *Lancet*, **2,** 388-389.

Morris, G.M., Coderre, J.A., Hopewell, J.W., Micca, P.L. & Rezvani, M. (1994). Response of rat skin to boron neutron capture therapy with *p*-boronophenylalanine or borocaptate sodium. *Radiother. Oncol.*, **32,** 144-153.

Muench, P.J., Meigooni, A.S., Nath, R. & McLaughlin, W.L. (1991). Photon energy dependence of the sensitivity of radiochromic film and comparison with silver halide film and LiF LTDs used for branchytherapy dosimetry. *Med. Phys.*, **18,** 769-775.

Nakagawa, Y. & Hatanaka, H. (1997). Boron neutron capture therapy: Clinical brain tumor studies. *J. Neutrooncol.*, **33,** 105-115.

Nath, R., Anderson, L.L., Luxton, G., Weaver, K.A., Williamson, J.F. & Meigooni, A.S. (1995). Dosimetry of interstitial brachytherapy sources: Recommendations of the AAPM Radiation Therapy Committee Task Group No. 43. *Med. Phys.*, **22,** 209-234.

Nelson, W.R., Hirayama, H. & Rogers, D.W.O. (1985). The EGS4 code system. SLAC.

Nemec, O.F. & Hofman, Y.V. (1975). *Nuclear Physics Handbook.* Naukova Dumka (in Russian): Kiev.

Nicollian, E.H. & Brews, J.R. (1981). *MOS (metal oxide semiconductor) physics and technology*. Wiley: New York.

Nikanishi, T., Ichihashi, M., Mishima, Y., Matsuzawa, T. & Fukuda, H. (1980). Thermal neutron capture therapy of malignant melanoma: *in vitro* radiobilogical analysis. *Int. J Radiat. Biol.*, **37,** 573-580.

Niroomand-Rad, A., Blackwell, C.R., Coursey, B.M., Gall, K.P., Galvin, J.M., McLaughlin, W.L., Meigooni, A.S., Nath, R., Rodgers, J.E. & Soares, C.G. (1998). Radiochromic film dosimetry: Recommendations of AAPM Radiation Therapy Committee Task Group 55. *Med. Phys.*, **25,** 2093-2115.

Ono, K., Ueda, S., Oda, Y., Nakagawa, Y., Miyatake, S., Takagaki, M., Osawa, M. & Kobayashi, T. (1997). Boron neutron capture therapy for malignant glioma at Kyoto University reactor. In *Advances in Neutron Capture Therapy*, Larsson, B., Crawford, J. & Weinreich, R. (eds), Vol. 1. pp. 39-45. Elseiver: Lausanne.

Ordy, J.M., Barnes, H.W., Samorajaski, T., Curtis, H.J., Wolin, L. & Zeman, W. (1963). Pathologic and behavioral changes in mice after deuteron irradiation of the central nervous system. *Radiat. Res.*, **18,** 31-45.

Orion, I., Rosenfeld, A.B., Dilmanian, F.A., Telang, F., Rent, B. & Namito, Y. (2000). Monte Carlo simulation of dose distribution from a synchrotron-produced microplanar beam array using the EGS4 code system. *Phys. Med. Biol.*, **45,** 2497-2508.

Paretzke, H.G., Goodhead, D.N., Kaplan, I.G. & Terrissol, M. (1995). Track structure quantities. In *IAEA Report: Atomic and Molecular Data for Radiotherapy and Radiation Research*, Vol. IAEA-TECDOC-799. pp. 635-721. International Atomic Energy Agency: Vienna.

Persliden, J. (1983). A Monte Carlo program for photon transport using analogue sampling of scattering angle in coherent and incoherent scattering process. *Comput. Prog. Biomed.*, **17,** 115-128.

Pfeiffer, C.C. & Jenney, E.H. (1950). The pharmacology of boric acid and boron compounds. *Bull. Natl. Formulary Comm.*, **18,** 57-80.

Pignol, J.-P., Cuendent, P., Brassart, N., Fares, G., Colomb, F., Diop, C.M.B., Sabattier, R., Hachem, A. & Prevot, G. (1998). Combined use of FLUKA and MCNP-4A for the Monte-Carlo simulation of the dosimetry of ^{10}B capture enhancement of fast neutron irradiation. *Medical Physics*, **25,** 885-891.

Poch, W.J. & Holmes-Siedle, A. (1970). *RCA Engineer*, **10,** 56.

Pospisil, S., Havrankova, E., Janout, Z., Konicek, J., Macha, I. & Pavlu, J. (1993). Si diode as a small detector of slow neutrons. *Radiat. Prot. Dosim.*, **46,** 115-118.

Raaijmakers, C.P.J., Konijnenberg, M.W. & Mijnheer, B.J. (1997). Clinical dosimetry of an epithermal neutron beam for neutron capture therapy: dose distribution under reference conditions. *Intern. J. Radiat. Oncol. Biol. Phys.*, **37,** 941-951.

Raaijmakers, C.P.J., Konijnenberg, M.W., Verhagen, H.W. & Mijnheer, B.J. (1995). Determination of Dose Components in Phantom Irradiated with an

Epithermal Neutron Beam for Boron Neutron Capture Therapy. *Medical Physics*, **22,** 321-329.

Raaijmakers, C.P.J., Nottelman, E.L., Konijnenberg, M.W. & Mijnheer, B.J. (1996a). Dose monitoring in boron neutron capture therapy using a reactor-based epithermal neutron beam. *Phy. Med. Biol.*, **41,** 2789-2797.

Raaijmakers, C.P.J., Watkins, P.R.D., Nottelman, E.L., Verhagen, H.W., Jansen, J.T.M., J.Zoetelief & Mijnheer, B.J. (1996b). The neutron sensitivity of dosimeters applied to boron neutron capture therapy. *Med. Phys.*, **23,** 1581-1589.

Raju, M.R., Eisen, Y., Carpenter, S. & Inkert, W.C. (1991). Radiobiology of alpha particles. III. Cell inactivation by alpha paticle traversal of the cell nucleus. *Radiat. Res.*, **128,** 204-209.

Ramani, R., Russell, S. & O'Brien, P. (1997). Clinical dosimetry using MOSFETs. *Int. J. Rad. Oncol. Biol. Phys.*, **37,** 959-964.

Reed, R.A., McNulty, P.J., Beauvais, W.J. & Roth, D.R. (1993). Charge collection spectroscopy. *IEEE Trans. Nucl. Sci.*, **40,** 1880-1887.

Regaud, C. (1926). Traitement des cancers du col de l'uterus par les radiations: idee sommaires des methodes et des resultants; indications therapeutique. In *7th Congress of the Societe Internationale dela CHirurgie*, Vol. 1. pp. 35-146.

Reinstein, L.E. & Gluckman, G.R. (1997). Comparison of dose response of radiochromic film measured with He-Ne laser, broadband and filtered light densitometers. *Med. Phys.*, **24,** 1531-1533.

Rivard, M.J. (1999). Dosimetry for ^{252}Cf neutron emitting brachytherapy source: Protocol, measurements, and calculations. *Med. Phys.*, **26,** 1503-1514.

Rivard, M.J. (2000). Dosimetry for a general ^{252}Cf source. *Med. Phys.*, **27,** 2803-2815.

Rofstad, E.K. (1986). Radiation biology of malignant melanoma. *Acta Radiol.*, **25,** 1-10.

Rosenfeld, A.B., Carolan, M.G., Kaplan, G.I., Allen, B.J. & Khivrich, V.I. (1995). MOSFET dosimeters: role of encapsulation on dosimetric characteristics in mixed gamma-neutron and megavoltage x-ray fields. *IEEE Trans. Nucl. Sci.*, **42,** 1870-1877.

Rosenfeld, A.B., Kaplan, G.I., Carolan, M.G., Allen, B.J., Maughan, R.L., Yudelev, M., Kota, C. & Coderre, J.A. (1996). Simultaneous macro and micro dosimetry with MOSFETs. *IEEE Trans. Nucl. Sci.*, **43,** 2693-2700.

Rossi, H.H. & Zaider, M. (1996). *Microdosimetry and its applications*. Springer-Verlag: Berlin, Heidelberg.

Sanders, J.M. (1986). Improvements in characteristics of a solid state dosimeter. *IEEE Trans. Nucl. Sci.*, **33,** 617-619.

Sanders, M., Sayeg, J., Coffey, C., Patel, P. & Walsh, J. (1993). Beam Profile Analysis Using GafChromic Films. *Stereotact. Funct. Neurosurg.*, **61(suppl 1),** 124-129.

Sarrabayrouse, G., Bellaouar, A. & Rossel, P. (1986). Electrical properties of MOS radiation detectors. *Revue Phys. Appl.*, **21,** 283-287.

Sauerwein, W. (1997). The Clinical Project at HFR Petten - a Status Report. In *Advances in Neutron Capture Therapy*, Larsson, B., Crawford, J. & Weinreich, R. (eds), Vol. 1. pp. 77-82. Elseiver: Lausanne.

Sauerwein, W., Moss, R., Rassow, J., Stecher-Rasmussen, F., Hiderherty, K., Wolbers, J.G. & Sack, H. (1999). Organisation and management of the first clinical trial of BNCT in Europe (EORTC Protocol 11961). *Strahlenter. Oncol.*, **175,** 108-111.

Sauerwein, W., Ziegler, W., Olthoff, K., Stroffer, C., Rassow, J. & Sach, H. (1989). Neutron Capture Therapy Using a Fast Neutron Beam: Clinical Considerations and Physical Aspects. *Strahlenther. Onkol.*, **165,** 208-210.

Scalchi, P. & Francescon, P. (1998). Calibration of a MOSFET detection system for 6 MV *in vivo* dosimetry. *Int. J. Oncology Biol. Phys.*, **40,** 987-993.

Scheick, L.Z., McNulty, P.J., Roth, D.R., Davis, M.G. & Mason, B.E. (1999). Maesurements of dose with individual FAMOS transistors. *IEEE Trans. Nucl. Sci.*, **46,** 1751-1756.

Schmidt, R., Maughan, R.L., Yudelev, M., Kota, C. & Wanwilairat, S. (1999). Experimental determination of the thermal neutron flux around two different types of high intensity ^{252}Cf sources. *Med Phys*, **26,** 83-86.

Sexton, F.W., Horn, K.M., Doyle, B.L., Laird, J.S., Cholewa, M., Saint, A. & Legge, G.J.F. (1993). Relationship between IBICC imaging and SEU in CMOS ICs. *IEEE Trans. Nucl. Sci.*, **40,** 1787-1794.

Shaneyfelt, M.R., Schwank, R.J., Fleetwood, D.M. & Winokur, P.S. (1998). Effect of irradiation temperature onMOS radiation response. *IEEE Trans. Nucl. Sci.*, **45,** 1372-1378.

Shröder, O., Schmitz, T. & Pierschel, M. (1992). Microdosimetric dosimeters for individual monitoring based on semiconductor detectors. In *Eleventh Symposium on Microdosimetry*: Gatlinburg, Tennessee.

Shröder, O., Schmitz, T. & Pierschel, M. (1994). Microdosimetric dosimeters for individual monitoring based on semiconductor detectors. *Rad. Prot. Dosimetry*, **52,** 431-434.

Sigmon, T.W., Chu, W.K., Lugujjo, E. & Mayer, J.W. (1974). Stoichiometry of thin silicon oxide layer on silicon. *Appl. Phys. Lett.*, **24,** 105-107.

Slatkin, D.N. (1991). A history of boron neutron capture therapy of brain tumours. *Brain*, **114,** 1609-1629.

Slatkin, D.N., Dilmanian, F.A., Nawrocky, M.M. & Spanne, P. (1995a). Design of a multislit, variable width collimator for microplanar beam radiotherapy. *Rev. Sci. Instrum.*, **66,** 1459-1460.

Slatkin, D.N., McChesney, D.D. & Wallace, D.W. (1986). A retrospective study of 457 neurosurgical patients with cerebral malignant glioma at the Massachusetts General Hospital. In *Second International Symposium on Neutron Capture Therapy*, Hatanaka, H. (ed) pp. 434-446. Nishimura: Niigata, Japan.

Slatkin, D.N., Spanne, P., Dilmanian, F.A., Gebbers, J.-O. & Laissue, J.A. (1995b). Subacute neuropathological effects of microplanar beams of x-ray from a synchrotron wiggler. *Proc. Nat. Acad. Sci. USA*, **92,** 8783-8787.

Slatkin, D.N., Spanne, P., Dilmanian, F.A. & Sandborg, M. (1992). Microbeam radiation therapy. *Med. Phys.*, **19,** 1395-1400.

Snyder, W.S., H.L. Fisher, J., Ford, M.R. & Warner, G.G. (1969). Estimates for absorbed fractions for monoenergetic photon sources uniformly distributed in various organs of a heterogeneuos phantom (Appendix B). *J. Nucl. Medicine, MIRD Supplement No.3,* Pamphlet 5.

Sofar, S.K., Kalef-Ezra, J., Faichild, R.G., Laster, B.H., Fiarman, S. & Ramsay, E. (1990). Epithermal Beam Development at BMMR: Dosimetric Evaluation. In *Neutron Beam Design, Development and Performance for NCT,* Harling, O. & et al. (eds) pp. 307-316. Plenum Press: NY.

Solares, G., Katz, D., Harling, O. & Zamenhof, R. (1997). On-line dosimetry for boron neutron capture therapy at the MIT research reactor. In *Advances in Neutron Capture Therapy,* Larsson, B., Crawford, J. & Weinreich, R. (eds), Vol. 1. pp. 147-152. Elsevier: Lausanne.

Solaris, G.R. & Zamenhof, R.G. (1995). A novel approach to the microdosimetry of neutron capture therapy. *Rad. Research,* **144,** 50-58.

Soloway, A.H., Barth, R.F., Alam, F. & Carey, W.E. (1986). Boron compounds and boronated antibodies for neutron capture therapy. In *Boron Neutron Therapy for Cancer,* Hatanaka, H. (ed) pp. 47-58. Nishimura: Niigata, Japan.

Soloway, A.H., Hatanaka, H. & Davis, M.A. (1967). Penetration of brain and brain tumor. VII. Tumor-binding sulfhydryl boron compounds. *J. Medicinal Chem.*, **10,** 714-717.

Soubra, M., Cygler, J. & Mackay, G. (1994). Evaluation of a dual bias metal oxide-semiconductor field efffect transistor detector as radiation dosimeter. *Med. Phys.*, **21,** 567-572.

Srdoc, D., Goodman, L.J., Marino, S.A., Mills, R.E., Zaider, M. & Rossi, H.H. (1981). Microdosimetry of monoenergetic neutron radiation. In *Seventh Symposium on Microdosimetry,* Booz, J., Ebert, H. & Hartfiel, H. (eds) pp. 765-774. Harwood Academic Publishers: London.

Srour, J.R. & Chiu, K.Y. (1977). MOS hardening approaches for low-temperature applications. *IEEE Trans. Nucl. Sci.*, **NS-24,** 2140-2146.

Srour, J.R., Curtis, O.L. & Chiu, K.Y. (1974). Charge transport studies in SiO_2: processing effects and implications for radiation hardening. *IEEE Trans. Nucl. Sci.*, **NS-21,** 73-80.

Steenbergen, A.V. & staff, N. (1980). The National Synchrotron Light Source basic design and project status. *Nucl. Instr. and Meth.*, **172,** 25-32.

Stelzer, K.J., Lindsley, K.L., Cho, P.S., Laramore, G.E. & Griffin, T.W. (1997). Fast neutron radiotherpy: the University of Washington experience and potential use of concomitant boost with boron neutron capture. *Rad. Protect. Dosimetry,* **70,** 471-475.

Stepanek, J., Blattmann, H., Laissue, J.A., Lyubimova, N., Michiel, M.D. & Slatkin, D.N. (2000). Physics study of microbeam radiation therapy with PSI-version of Monte Carlo cose GEANT as a new computation tool. *Med. Phys.*, **27,** 1664-1675.

Stephens, L.C., Hussey, D.H., Raulstom, G.L., Jardine, J.H., Gray, K.N. & Almond, P.R. (1983). Late effects of 50 $MeV_{d\text{-}Be}$ neutron and cobalt-60 irradiation on rhesus monkey cervical spinal cord. *Int. J. Rad. Oncol. Biol. Phys.*, **9,** 859-864.

Stone, R.S. (1948). Neutron therapy and specific ionization. *Am. J. of Roentgenology*, **59,** 771-788.

Stone, R.S. & Larkin, J.C. (1942). The treatment of cancer with fast neutrons. *Radiology*, **39,** 608-620.

Stone, R.S., Lawrence, J.H. & Aebersold, P.C. (1940). A preliminary report on the use of neutrons in the treatment of malignant diseases. *Radiology*, **35,** 322-327.

Straile, W.E. & Chase, H.B. (1963). The use of elongate microbeams of x-rays for simulating the effects of cosmic rays on tissues: A study of wound healing and hear follicle regeneration. *Radiat. Res.*, **18,** 65-75.

Streubel, G., Dörschel, B., Haniswch, T., Reinhard, J. & Schoop, K. (1989). Properties of MOS sensors for application in neutron field monitoring. *Nucl. Instr. Meth.*, **A274,** 194-202.

Sullivan, P.R., Hasson, B.F., Grossman, C.H. & Simpson, L.D. (2000). Optical density changes of Gafchromic MD-55 film resulting from laser light exposure at wavelengths of 671 nm and 633 nm. *Med. Phys.*, **27,** 245-251.

Sweet, W.H. (1951). The use of nuclear disintegrations in the diagnosis and treatment of brain tumour. *N. Engl. J. Med.*, **245,** 875-878.

Sweet, W.H. (1986). Preface. In *Second International Symposium on Neutron Capture Therapy*, Hatanaka, H. (ed). Nishimura: Niigata, Japan.

Sweet, W.H., Soloway, A.H. & Brownell, G.L. (1963). Boron-slow neutron capture therapy of gliomas. *Acta Radiol. Ther.*, **1,** 114-121.

Szedon, J.R. & Sandor, J.E. (1965). The effect of low-energy electron irradiation of metal-oxide-semiconductor structures. *Appl. Phys. Lett.*, **6,** 181-182.

Takagaki, M., Oda, Y., Miyatake, S., Kikuchi, H., Kobayashi, T., Sakurai, Y., Osawa, M., Mori, K. & Ono, K. (1997). Boron neutron capture therapy: preliminary study of BNCT with sodium borocaptate ($Na_2B_{12}H_{11}SH$) on glioblastoma. *J. Neuro-Oncl.*, **35,** 177-185.

Tallon, R.W., Kemp, W.T., Ackermann, M.R., Owen, M.H. & Hoffland, A.H. (1987). Radiation damage in MOS transistors as a function of the angle betweeen an applied electric field and various incident radiations (protons, electrons, and C0-60 gamma rays). *IEEE Trans. Nucl. Sci.*, **NS-34,** 1208-1213.

Tarr, N.G., Mackay, G.F., Shortt, K. & I.Thomson. (1998). A floating gate MOSFET dosimeter requiring no external bias supply. *IEEE Trans. Nucl. Sci.*, **45,** 1470-1474.

Tarr, N.G., Plett, C., Yeaton, A., Mackay, G.F. & I.Thomson. (1996). Limitations on MOSFET dosimeter resolution imposed by $1/f$ noise. *IEEE Trans. Nucl. Sci.*, **43,** 2492-2495.

Tattam, D.A., Allen, D.A., Beynon, T.D., Constantine, G., Green, S. & Scott, M.C. (1998). In-phantom neutron fluence measurements in the orthogonal

Birmingham boron neutron capture therapy beam. *Med. Phys.*, **25,** 1964-1966.

Taylor, J.H. & Goldhaber, M. (1935). Detection of nuclear disintegration in a photographic emulsion. *Nature*, **135,** 341.

Thomlinsons, W., Berkvens, P., Berruyer, G., Bertrand, B., Blattmann, H., Brauer-Krisch, E., Brochard, T., Charvet, A.M., Corde, S., Dimichiel, M., Elleaume, H., Esteve, F., Fiedler, S., Laissue, J.A., LeBas, J.F., LeDuc, G., Lyubimova, N., Nemoz, C., Renier, M., Slatikn, D.N., Spanne, P. & Suortti, P. (2000). Research at the European synhrotron radiation facility medical beamline. *Cell. Moll. Biol.*, **46,** 1053-1063.

Thomson, I., Thomas, R.E. & Berndt, L.P. (1984). Radiation dosimetry with MOS sensors. *Rad. Protect. Dosimetry*, **6,** 121-124.

Tommasino, L., Klein, N. & Solomon, P. (1977). *Nucl. Track. Detect.*, **1,** 63.

Turner, J.E. (1992). *Atoms, Radiation and Radiation Protection.* McGraw-Hill Inc.

Vanitsky, S.M., Miller, D.W., Moyers, M.F., Levy, R.P., Schulte, R.W., Slater, J.D. & Slater, J.M. (1999). Dosimetry techniques for narrow protn beam radiosurgery. *Phys. Med. Biol.*, **44,** 2789-2801.

Wambersie, A., Richard, F. & Bretteau, N. (1994). Development of fast neutron therapy worlwide. *Acta Oncol.*, **33,** 261-274.

Wanwilairat, S., Schmidt, R., Vilaithong, T., V.Lorvidhaya & Hoffmann, W. (2000). Measurement of the dose components of fast and thermal neutrons and photons from 0.1 mg 252Cf source in water for brachytherapy treatment planning. *Med. Phys.*, **27,** 2357-2362.

Westermark, M., Arndt, J. & Brahme, A. (2000). Comparative dosimetry in narrow high-energy photon beams. *Phys. Med.Biol.*, **45,** 685-702.

Wierzbicki, J.G., Maruyama, Y. & Alexander, C.W. (1991). ^{252}Cf for teletherapy and thermalized ^{252}Cf neutrons for brachytherapy. *Nucl. Sci. Appl.*, **4,** 331-336.

Winokur, P., Kerris, K.G. & Harper, L. (1983). Predicting CMOS inverter response in nuclear and space environments. *IEEE. Trans. Nucl. Sci.*, **NS-30,** 4326-4332.

Woodruff, R.L. & Rudeck, P.J. (1993). Three-dimentional numerical simulation of single event upset of a SRAM cell. *IEEE Trans. Nucl. Sci.*, **40,** 1795-1803.

Woods, M.H. & Williams, R. (1976). Hole traps in silicon dioxide. *J. Appl. Phys.*, **47,** 1082-1089.

Woollard, J.E., Albertson, B.J., Reed, M.K., Blue, T.E., Capala, J., Gupta, N. & Gahbauer, R.A. (2001). A comparission of neutron beams for BNCT based on in-phantom neutron field assessment paraments. *Med. Phys.*, **28,** 184-193.

Wuu, C.S., Almos, H.I., Kliauga, P., Reinstein, L.E. & Saraf, S. (1992). Microdosimetry for boron neutron capture therapy. *Rad. Research*, **130,** 355-359.

Yanch, J.C., Shefer, R.E., Klinkowstein, R.E., Song, H., Blackburn, B.W. & Howard, W.B. (1997). Use of 9Be(d,n) nuclear reaction for BNCT: simulation and experimental measurement. In *Advances in Neutron Capture Therapy*, Larsson, B., Crawford, J. & Weinreich, R. (eds), Vol. 1. pp. 564-569. Elseiver: Lausanne.

Zeman, W., Curtis, H.J. & Baker, C.P. (1961). Histopathologic effects of high-energy-particle microbeams on the visual cortex of the mouse brain. *Radiat. Res.*, **15,** 189-495.

Zeman, W., Curtis, H.J., Gebhard, E.L. & Haymaker, W. (1959). Tolerance of mouse brain tissue to high-energy deuterons. *Science*, **130,** 1760-1761.

Zhu, Y., Kirov, A.S., Mishra, V., Meigooni, A.S. & Williamson, J.F. (1997). Quantitative evaluation of radiochromic film response for two-dimensional dosimetry. *Med. Phys.*, **24,** 223-231.

Ziegler, J.F., Biersack, J.P. & U.Littmark. (1985). *The stopping and range of ions in solids*. Pergamon Press: New York.